Rock magnetic exploration of cold seep system and associated shallow methane hydrate from the Bay of Bengal

A THESIS SUBMITTED IN PARTIAL FULFILLMENT FOR THE DEGREE OF

DOCTOR OF PHILOSOPHY

IN THE School of Earth, Ocean, and Atmospheric Sciences

GOA UNIVERSITY

By

Virsen Vishwanath Gaikwad
CSIR-National Institute of Oceanography, Goa, India

AUGUST 2022

Rock Magnetic Exploration of Cold Seep System and Associated Shallow Methane Hydrate from the Bay of Bengal

Virsen Gaikwad

Ph.D. 2022

Rock magnetic exploration of cold seep system and associated shallow methane hydrate from the Bay of Bengal

A THESIS SUBMITTED IN PARTIAL FULFILLMENT FOR THE DEGREE OF

DOCTOR OF PHILOSOPHY

IN THE School of Earth, Ocean, and Atmospheric Sciences

GOA UNIVERSITY

By

Virsen Vishwanath Gaikwad

CSIR-National Institute of Oceanography, Goa, India

AUGUST 2022

DECLARATION

I, Mr. Virsen Vishwanath Gaikwad hereby declare that this thesis represents work which has been carried out by me and that it has not been submitted, either in part or full, to any other University or Institution for the award of any research degree.

Place: Taleigao Plateau.

Date: **Mr. Virsen Vishwanath Gaikwad**

Certificate

This is to certify that the thesis entitled, **"Rock magnetic exploration of cold seep system and associated shallow methane hydrate from the Bay of Bengal"**, submitted by **Mr. Virsen Vishwanath Gaikwad** for the award of the Degree of Doctor of Philosophy in Earth Science. I hereby certify that the above declaration of the candidate, name of the candidate is true and the work was carried out under my/our supervision.

Place: Goa University

Date:

Dr. Firoz K. Badesab	**Dr. Mahender Kotha**
(Research Guide) Senior Scientist CSIR-National Institute of Oceanography, Goa, India.	(Research Co-guide) Professor, Goa University, Taleigao, Goa, India.

Contents

Dedicated to Dr. B.R. Ambedkar

Acknowledgments

This thesis owes its existence to the help, support and inspiration of several people. Firstly, I would like to express my sincere appreciation and gratitude to my research guide Dr. Firoz Badesab who introduced me to the subject and the field of research and for willing to guide me. His support, guidance, constructive criticism and inspiring suggestions have been precious for the development of this thesis content. I strongly believe that existence of this work is only because of his motivation, inspiring nature, supervision, and valuable guidance. I am greatly indebted to him.

I am grateful to my to my research co-guide Dr. Mahender Kotha for all his efforts, support, guidance, and patience at all times.

My sincere thanks to Dr. Pawan Dewangan, Senior Principal Scientist, NIO, Goa and Prof. VM Matta Vice-Chancellors Nominee, for their constructive criticism and support which improved the quality of the thesis.

My sincere thanks to Director Prof. Sunil Kumar Singh, of CSIR-NIO, Goa for providing all the necessary research facilities and encouragement.

The Director of the Centre for Advanced Marine Core Research (CMCR), Kochi University, Japan is thanked for allowing access to the Paleomagnetic laboratory during a research visit of Dr. Firoz Badesab as a part of the INSA-JSPS fellowship.

Dr. Myriam Kars and Chisa Nishimori is thanked for providing timely support to Dr. Firoz Badesab during the fellowship period at CMCR.

I am very much thankful to Sh. T. Ramprasad, project leader of Gas Hydrate Research Group for his constant encouragement, providing financial support for the research work, valuable advice and encouragement and for being a great mentor.

I also wish to thank Dr. NH Khadge, Dr. Samir Damare, and Dr. Maria Brenda Mascarenhas-Periera for their timely support and encouragement.

I thank Mr. Girish A. Prabhu, and Mr. Areef Sardar for providing technical support during the various measurements.

I thank Omkar Naik-Gaonkar, Kaveri Salunke, and Prem Piyush Panda for their support in carrying out magnetic and mineralogical analyses.

I thank Prof. R. G. Sonkawade, Co-ordinator, Sophisticated Analytical Instrument Facilities (SAIF) Shivaji University, Kolhapur, and Mr. Sunny Gurav for their support in carrying out Transmission Electron Microscopy at Shivaji University, Kolhapur.

I show appreciation towards my colleagues and friends Nitin Kadam, Walsh Fernandes, Piyush Dahake, Rakesh Sahoo, Pabitra Singha, Sagar Pujari, Aditya Kumar, Delcy Nazareth, Nitisha Sangodkar, Geetanjali Dakara, Diksha Shetty, Ramakrishna Reddy and many more who have helped me directly or indirectly. Thank you for your priceless company which made my work easier.

My profound gratitude to my father, to my mother, to my wife, to my daughters, to my sister, to my brother, and all other family members, who were there for me through thick and thin; words will fall short for their constant support, encouragement and the sacrifices they made for me. This accomplishment would not have been possible without them.

Thank you.

List of Publications

Publications from the thesis

1) **Gaikwad V**, Badesab F, Dewangan P and Kotha M (2021). Diagenesis of magnetic minerals in active/relict methane seep: constraints from rock magnetism and mineralogical records from Bay of Bengal. Frontiers in Earth Science,9, 60. https://doi.org/10.3389/feart.2021.638594
2) **Gaikwad V**, Badesab F, and Kotha M (2022). Diagenetic analysis of shallow and deep-seated gas hydrate systems from the Bay of Bengal. Marine Geology, 448, https://doi.org/10.1016/j.margeo.2022.106824
3) Badesab, F., **Gaikwad, V**., Venkateshwarlu, M., Kadam, N., & João, H. M. (2022). Diagenetic dissolution, maghemitization and sulphidization of magnetic minerals in rapidly deposited gas hydrate bearing sediments from the Bay of Bengal. Marine and Petroleum Geology, 139, 105585. https://doi.org/10.1016/j.marpetgeo.2022.105585

Other Publications

1) Badesab, F., **Gaikwad, V.**, Venkateshwarlu, M., Kadam, N. (2023). Genesis and preservation of authigenic magnetite and greigite in the cold seep sediments, Bay of Bengal. Marine and Petroleum Geology, 151, 106212. https://doi.org/10.1016/j.marpetgeo.2023.106212
2) Kadam, N., Badesab, F., **Gaikwad, V.**, Kotha, M., Fernandes, L. L., & Venkateshwarlu, M. (2022). Sedimentary response to the contrasting provenance and oceanographic conditions on the continental shelf of India. Continental Shelf Research, 248, 104853. https://doi.org/10.1016/j.csr.2022.104853
3) F. Badesab, **V. Gaikwad**, B. N. Nath, M. Venkateshwarlu, P. Aiswarya, A. Tyagi, K. Salunke, W. Fernandes, N. Kadam, S. Sangode, A. Sardar, and G. Prabhu (2021). Controls of contrasting provenance and fractionation on the sediment magnetic records from the Bay of Bengal. Marine Geology, 437, 106515. https://doi.org/10.1016/j.margeo.2021.106515
4) F. Badesab, M.B.L. Mascarenhas-Periera, **V. Gaikwad**, P. Dewangan, P.P. Panda, K. Deenadayalan, K. Salunke, B. Augastian, J. R. Patil, and B.V. Lakshmi (2021). Rock Magnetic Evidence of Tectonic Control on the Sedimentation and Diagenesis in the

Andaman Sea over ~ 1 Million Years. Marine and Petroleum Geology, 130, 105150. https://doi.org/10.1016/j.marpetgeo.2021.105150

5) João, H. M., F. Badesab, **V. Gaikwad**, M. Kocherla, and K. Deenadayalan (2021). Controls of mass transport deposit and magnetic mineral diagenesis on the sediment magnetic record from the Bay of Bengal. Marine and Petroleum Geology, 128, 104994. https://doi.org/10.1016/j.marpetgeo.2021.104994
6) Badesab F, Dewangan P and **Gaikwad V** (2020). Magnetic Mineral Diagenesis in a Newly Discovered Active Cold Seep Site in the Bay of Bengal. Frontiers in Earth Science, 8, 592557 https://doi.org/10.3389/feart.2020.592557
7) Badesab, F., Dewangan, P., **Gaikwad, V.**, Sebastian, J. G., & Venkateshwarlu, M. (2020) A rock magnetic perspective of gas hydrate occurrences in a high-energy depositional system in the Krishna-Godavari basin, Bay of Bengal. Geo-Marine Letters, 1-15. https://doi.org/10.1007/s00367-020-00646-8
8) Firoz Badesab, **Virsen Gaikwad**, Pawan Dewangan (2019). Controls on greigite preservation in a gas-hydrate system off Krishna-Godavari basin, Bay of Bengal. Geo-marine Letters, 40(4), 439-452. https://doi.org/10.1007/s00367-019-00604-z
9) Firoz Badesab, Pawan Dewangan, **Virsen Gaikwad**, Myriam Kars, Muralidhar Kocherla, Kolluru S. Krishna, Satish J. Sangode, Kannan Deenadayalan, Pushpendra Kumar, Omkar Naikgaonkar, Mohammad Ismaiel, and Aarbaz Khan (2019). Magnetic-mineralogical approach for exploration of gas hydrates in the Bay of Bengal. Journal of Geophysical Research: Solid Earth, 124(5), 4428-4451 https://doi.org/10.1029/2019JB017466
10) Mazumdar, A.; Dewangan, P.; Peketi, A.; Sriram, G.; M.S. Kalpana; Naik, G.P.; D. Shetty ; S. Pujari ; S. P. Pillutla ; **V. V. Gaikwad** ; D. Nazareth ; N. S. Sangodkar ; G. Dakara; A. Kumar ; C. K. Mishra ; P. Singha ; and R. Reddy (2019). The first record of active methane (cold) seep ecosystem from the Indian EEZ. Journal of Earth System Science, 128:18, 1-8. https://doi.org/10.1007/s12040-018-1044-y
11) F. Badesab, **V. Gaikwad**, T. R. Gireeshkumar, O. Naikgaonkar, K. Deenadayalan, S. V. Samiksha, P. K. Dinesh Kumar, V. J. Loveson, S. D. Iyer, A. Khan, P. B. Udayakrishnan, and A. Sardar (2018). Magnetic tracing of sediment dynamics of mudbanks off southwest

coast of India. Environmental Earth Sciences, 77:625, 1-16. https://doi.org/10.1007/s12665-018-7807-6

12) A. Usapkar, P. Dewangan, A. Mazumdar, K.S. Krishna, T. Ramprasad, F.K. Badesab, M. Patil, and **V.V. Gaikwad** (2018). Paleomagnetic record for the past 80 ka from the Mahanadi basin, Bay of Bengal. Journal of Asian Earth Sciences, 151, 226–239. https://doi.org/10.1016/j.jseaes.2017.10.024

Papers presented at national and international conferences

1. An oral presentation entitled "*Diagenetic analysis of methane seep (active vs. inactive) sediments from the Bay of Bengal*" was delivered during the IAGA-IASPEI Joint Scientific Assembly (JSA) 2021, 21st – 27th August 2021 (Virtual) organized by CSIR-National Geophysical Research Institute, India.

2. A poster titled "*Diagenesis of magnetic minerals at newly discovered active methane seep in Bay of Bengal*" was presented during the 57th Annual Convention of Indian Geophysical Union (IGU) 2021, 2-4th Feb 2021(Virtual) organized jointly by IGU and CSIR-National Institute of Oceanography, Goa.

3. A poster entitled "*A comparative diagenetic analysis of shallow and deep-seated gas hydrate systems from the Bay of Bengal*" was presented during the 58th Annual Convention of IGU "Recent Advances in Earth Sciences with Special Emphasis – Natural Hazards" jointly organized by Indian Geophysical Union and North-Eastern Hill University, Shillong between 2nd and 4th February 2022.

List of Tables

List of Figures

2.15. Rigaku X-Ray Diffractometer (Ultima IV) housed at CSIR-NIO, Goa, India.2.16. Laser Particle Size Analyzer (Malvern Mastersizer 2000) at CSIR-NIO.

2.16. Laser Particle Size Analyzer (Malvern Mastersizer 2000) housed at CSIR-NIO, Goa, India.

3.1. (a) Map showing the location of active (SSD-45/Stn-4), relict (SSD-45/Stn-11/GC-02) and paleo (MD161/Stn-08) seep sites in the Krishna-Godavari (K-G) basin, Bay of Bengal. High-resolution seismic profile (P1) highlighting (b) the normal faults (blue dashed lines), subsurface chimney-like feature (solid red lines), and water column imaging showing gas flares (orange). Regional toe-thrust fault (yellow dashed line), feasible BSR (white dashed line), and subsurface horizons (solid black lines) are marked on the seismic section (modified after Dewangan et al., 2020). The spade sediment cores SPC-01, SPC-02, SPC-03, SPC-04, SPC-05, and SPC-06 were retrieved from active seep site SSD-45/Stn-4 and gravity core GC-02 was retrieved from relict site SSD-45/Stn-11. The location of the sediment core from the paleo-seep site (MD161/Stn-8) is also marked. Bathymetry data of the studied area was obtained from GEBCO Compilation Group665 (2020) GEBCO 2020 Grid (doi: 10.5285/a29c5465-b138-234d-e053-6c86abc040b9).

3.2. Down-core variations of selected rock magnetic data of spade (a-e): SPC-01, (f-j): SPC-02, (k-o): SPC-03, (p-t): SPC-04, (u-y): SPC-05, (z-a4): SPC-06, and gravity sediment cores (a5-a9): GC-02. Based on magnetic susceptibility variations, two sedimentary magnetic zones Z-I and Z-II are demarcated. Z-I highlighted with gray shading. (Please note that χlf = low frequency magnetic susceptibility, ARM = anhysteretic remanent magnetization, and SIRM = saturation isothermal remanent magnetization, χfd % = frequency-dependent susceptibility). Depth of carbonate occurrence are highlighted in solid black arrows (horizontal). The depth of greigite occurrence is marked by "G". Sediment magnetic zones (Z-I, Z-II) in each profile are marked.

3.3. Thermomagnetic profiles of selected representative samples representing two sedimentary magnetic zones of the studied spade sediment cores. (a-b): SPC-01, (c-d): SPC-02, (e-f): SPC-03, and (g-h): SPC-05. Solid red lines indicate heating curves, and blue lines indicate cooling curves respectively.

3.4. First-order reversal curve diagrams for selected representative samples from spade cores. (A-D): SPC-01, (E-H): SPC-02, (I-J): SPC-03, (K-L): SPC-05, and (M-N): SPC-06.

3.5. Low-temperature magnetization curves for selected representative samples from the two spade cores (A-C): SPC-01 and (D-F): SPC-02. FC = field-cooled, RTSIRM = saturation isothermal remanent magnetization at room temperature, ZFC = zero field-cooled. The corresponding values of Verwey transition (*Tv*) are placed near the first derivative of magnetization curves.

3.6. X-ray diffraction spectra for magnetic minerals extracted from different sediment core depth intervals of spade cores. (A-C): SPC-01, (D-F): SPC-02, (G-I): SPC-03, (J-K): SPC-04, and (L-M): SPC-05. TM = titanomagnetite, P = pyrite, Qz = quartz, and G = greigite.

3.7. Scanning electron microscopy on magnetic extracts from different sediment core depth intervals. Energy dispersive x-ray spectroscopy spectra are placed adjacent to the respective images. (A-C): SPC-01, (D-F): SPC-02, (G-I): SPC-03, and (J-L): SPC-04. Iron (Fe), titanium (Ti), sulfur (S), oxygen (O), calcium (Ca), silicon (Si), carbon (C), aluminium (Al), potassium (K), magnesium (Mg), and manganese (Mn) peaks are indicated.

3.8. Grain size distribution and magnetic susceptibility data of all spade (SPC-01 to SPC-06) sediment cores retrieved from active methane seep site SSD-45/Stn-4. Depths of carbonate occurrence are highlighted in solid red arrows (vertical). The depth of greigite occurrence is marked by "G". Sediment magnetic zones (Z-I, Z-II) in each profile are marked.

3.9. Photographs showing occurrence of (A, B, C, E): Bathymodiolus sp., (D): Decapod crustaceans (squat lobsters), (F): Acharax sp. found at the spade core (surface) locations, (G) calyptogena sp., shell fragment, and (H) authigenic carbonates found at 48 cmbsf in GC-02 location. (I–P): Scanning electron microscopy on magnetic extracts from different sediment core depth intervals (Relict seep site: SSD-45/Stn-11/GC-02). TM = titanomagnetite, TH = titanohematite, and G = greigite).

3.10. (A–D) Bivariate scatter plots of magnetic parameters magnetic susceptibility (χlf), saturation isothermal remanent magnetization (IRM1T), IRM1T/χ, S-ratio, ARM/IRM1T and mean grain size for spade cores (SPC-01 to SPC-06) from active (SSD-45/Stn-4) and gravity core (GC-02) from relict seep site (SSD-45/Stn-11) in the Krishna-Godavari (K-G) basin, Bay of Bengal. The gray arrows are used to highlight the trends in plots.

3.11. Comparative FORC diagrams of greigite bearing sediment intervals from (A-B): active (SSD-45/Stn-4/SPC-01) and (C-D) of paleo-seep location (MD161-Station-08; modified from Badesab et al., 2020a) in the Krishna-Godavari (K-G) basin, Bay of Bengal. The dashed (black) lines along Bc axis highlights the negative region on the horizontal axis.

3.12. Conceptual model explaining the structural and diagenetic controls on the evolution of magnetic mineralogies at active and relict methane seep site in the Krishna-Godavari (K-G) basin, Bay of Bengal.

3.13. (A-D) X-ray diffraction spectra for magnetic minerals extracted from different sediment intervals of relict seep site: SSD-45/ Stn-11/GC-02. TM = titanomagnetite, H = hematite, Py= pyrite, and G = greigite

3.14. Photographs showing methane-derived authigenic carbonates found in an active seep sites SSD-45/Stn-04/SPC-01, SPC-04 and SPC-06. Respective depths of the carbonate occurrence are mentioned.

3.15. Sediment core locations map of NGHP-01-20A (present study), NGHP-01-10D, MD161/Stn-8, NGHP-01-03B, NGHP-01-05C, NGHP-01-14A, NGHP-01-15A, NGHP-01-16A and NGHP-01-07B, in the Krishna-Godavari (K-G) basin, Bay of Bengal. Bathymetry data of the studied area was obtained from GEBCO Compilation Group665 (2020) GEBCO 2020 Grid (10.5285/a29c5465-b138-234d-e053-6c86abc040b9).

3.16. Depth variations of (a–e) selected magnetic and (f–h) geochemical parameters for sediment core NGHP-01-20A. Three magnetite-rich bands exhibiting higher values of magnetic susceptibility have been identified. Magnetite-rich band in sediment magnetic zones Z– II, Z-III and Z-V are highlighted by pink, green and yellow color shading respectively. The depth of sulfate-methane transition zone (SMTZ) is marked by blue

arrow. The sediment depth intervals of pyrite nodules occurrence are highlighted in solid black arrows (horizontal). (Please note that χ_{lf} = low frequency magnetic susceptibility; ARM = anhysteretic remanent magnetization; and SIRM = saturation isothermal remanent magnetization).

3.17. (a–n) Temperature dependence of magnetic susceptibility (χ-T) for selected representative samples from the five sediment zones (Z-I, Z-II, Z-III, Z-IV, Z-V) of the studied sediment core NGHP-01-20A are presented. Solid red and blue lines indicate heating and cooling curves respectively. The respective magnetic minerals titanomagnetite (TM) and pyrite (Py) identified based on the χ-T curves are mentioned in the plot.

3.18. (a–f) Bivariate scatter plots of magnetic parameters: magnetic susceptibility (χ_{lf}), saturation isothermal remanent magnetization (SIRM), ARM/$IRM_{2.5T}$, SIRM/χlf, total organic carbon (TOC), calcium carbonate ($CaCO_3$) and Day plot of NGHP-01-20A from the Krishna-Godavari (K-G) basin, Bay of Bengal. The gray arrows are used only to highlight the observed trends in plots.

3.19. (a–b) Scanning electron microscopy (SEM) images of magnetic particles extracted from sediment magnetic zone (Z-I) of the sediment core NGHP-01-20A. (a-b) well-preserved detrital titanomagnetite (TM) grain. The blue color square represents the area selected for generation of energy dispersive X-ray spectra (EDS).

3.20. (a–d) Scanning electron microscopy (SEM) images of magnetic particles extracted from sediment magnetic zone (Z-II) of the sediment core NGHP-01-20A. (a,d) Diagenetically altered titanomagnetite (TM) grains exhibiting dissolution features. Signatures of minor low-temperature oxidation are noticed, (b) Detrital titanomagnetite (TM) grain showing partial dissolution, and (c) Diagnetically formed iron-sulfides (pyrite; Py) occur as individual fine-grained crystals on the surface of titanomagnetite (TM) grain. The blue color square represents the area selected for generation of energy dispersive X-ray spectra (EDS).

3.21. (a–f) Scanning electron microscopy (SEM) images of magnetic particles extracted from sediment magnetic zone (Z-III) of the sediment core NGHP-01-20A. (a,d,f)

Titanohematite (TH) grains exhibiting skeletal and lamellae like structure resulting from oxidation of titanomagnetite, (b) Well-preserved detrital titanomagnetite (TM) grains, (c,e) Titanomaghemite (TMG) grains exhibiting shrinkage cracks typical features linked with low-temperature maghemitization. The blue color square represents the area selected for generation of energy dispersive X-ray spectra (EDS).

3.22. (a–c) Scanning electron microscopy (SEM) images of magnetic particles extracted from sediment magnetic zone (Z-III) of the sediment core NGHP-01-20A (a) Titanomaghemite (TMG) grain characterized by shrinkage cracks formed due to low-temperature maghemitization, (b,c) Titanohematite (TH) grains exhibiting lamellae-like features reflecting pervasive oxidation of titanomagnetite. The blue color square represents the area selected for generation of energy dispersive X-ray spectra (EDS).

3.23. (a–b) Scanning electron microscopy (SEM) images of magnetic particles extracted from sediment magnetic zone (Z-IV) of the sediment core NGHP-01-20A. (a,b) Well-preserved detrital titanomagnetite (TM) grains. The blue color square represents the area selected for generation of energy dispersive X-ray spectra (EDS).

3.24. (a–c) Scanning electron microscopy (SEM) images of magnetic particles extracted from sediment magnetic zone (Z-V) of the sediment core NGHP-01-20A. (a,b) Titanomagnetite (TM) grains of detrital origin. Few grains showed signature of low-temperature maghemitization, (b) Titanohematite (TH) grains exhibiting lamellae-like features resulting from oxidation of titanomagnetite, (c) Well-preserved detrital titanomagnetite (TM) grains. The blue color square represents the area selected for generation of energy dispersive X-ray spectra (EDS).

3.25. (a – l) Optical microscopic images of the pyrite nodules separated from the sediment core NGHP-01-20A. The overgrowth (orange-reddish color) of pyrite on the magnetite grains is highlighted using arrows (white color).

3.26. (a–l) Optical microscopic images of the representative coarse fractions (>63 μm) from the different magnetic zones of sediment core NGHP-01-20A are presented. Fine-grained magnetic inclusion within host silicate minerals (>63 μm) fractions are marked (see red arrows).

3.27. Conceptual model explaining the constraints of detrital, diagenetic, authigenic, maghemitization and sulphidization processes on the evolution of magnetic mineralogies at Site NGHP-01-20. The arrows (red color) on the magnetic susceptibility profile of core NGHP-01-20A represent the carbonate occurrence depths.

4.1. (a) Map showing the sediment core location of shallow (active seep, Core ID: SSD-45/Stn-4/GC-01, marked by red star) and deep-seated (Core ID: NGHP-01-15A, marked by blue star) gas-hydrate site. The location of proximal and distal sediment cores (NGHP-01-20A, NGHP-01-10D, NGHP-01-3B, NGHP-01-5C, NGHP-01-14A, NGHP-01-15A, and NGHP-01-7B) collected during National Gas hydrate Expedition -01 (modified from Collett et al., 2014) from the Krishna-Godavari (K-G) basin, Bay of Bengal are shown. High-resolution seismic profile of the active seep site (SSD-45/Stn-4/GC-01) (P-1) is highlighted in purple color and the deep-seated gas-hydrate site (NGHP-01-15A) (P-2) is highlighted in light blue color (b) High-resolution seismic profile highlighting the normal faults (green dashed lines), subsurface chimney-like feature (solid blue lines) and gas flares (purple). Regional toe-thrust fault (yellow dashed line), feasible BSR (white dashed line), and subsurface horizons (solid black lines) are marked on the seismic section from the active cold seep location (Core ID: SSD-45/Stn-4/GC-01) (modified from Dewangan et al., 2021) (c) High-resolution seismic profile of site NGHP-01-15 highlighting the sediment core location and bottom simulating reflector (BSR) with the blue color arrow (modified from Kumar et al. 2014).

4.2. Depth variations of selected rock magnetic data for sediment cores (a–f) shallow (active cold seep, Core ID: SSD-45/Stn-4/GC-01), and (g–l) deep-seated (Core ID: NGHP-01-15A) gas hydrate site. Based on the variation in magnetic susceptibility (χ_{lf}), two sediment magnetic zones (Z-I, Z-II) of shallow (active cold seep) and five sediment magnetic zones (Z-I, Z-II, Z-III, Z-IV, Z-V) of deep-seated gas hydrate site in the Krishna-Godavari (K-G) basin, Bay of Bengal are marked. (Please note that χ_{lf} = low frequency magnetic susceptibility; ARM = anhysteretic remanent magnetization; and SIRM = isothermal remanent magnetization).

4.3. (a-g) Downcore variations of magnetic susceptibility (χ_{lf}) in the sediment cores (NGHP-01-20A, NGHP-01-10D, NGHP-01-03B, NGHP-01-05C, NGHP-01-14A, NGHP-01-

4.9. Transmission electron microscope (TEM) images of magnetic particles representing different sediment magnetic zones of cores (a–b) from shallow (active cold seep, Core ID: SSD-45/Stn-4/GC-01) and (c–d) deep-seated (Core ID: NGHP-01-15A) gas-hydrate site in the Krishna-Godavari (K-G) basin, Bay of Bengal. Energy dispersive X-ray spectroscopy (EDS) spectra of image a and c presented in e-f respectively. Iron (Fe), oxygen (O), titanium (Ti), silicon (Si), carbon (C), aluminium (Al), and magnesium (Mg) peaks are indicated.

4.10. X-ray diffraction spectra for extracted minerals from different sediment zones of cores (a–f) from shallow (active cold seep, Core ID: SSD-45/Stn-4/GC-01) and (g–l) deep-seated (Core ID: NGHP-01-15A) gas hydrate site in the Krishna-Godavari (K-G) basin, Bay of Bengal. TM = titanomagnetite, G = greigite, Py = pyrite, Qz = quartz.

4.11. Photographs showing methane-derived authigenic carbonates from different depth intervals of shallow (active cold seep, Core ID: SSD45/Stn-4/GC-01) gas hydrate core: Z-I (a) 0.02 mbsf, (b) 0.18 mbsf, (c) 0.25 mbsf, (d) 0.77 mbsf, (e) 1.01 mbsf, (f) 1.25 mbsf, (g) 1.57 mbsf, chemosynthetic communities from sea floor (h) Bathymodiolus Sp., (i) Calyptogena Sp., (j) Acharax Sp., (k) Decapod crustaceans (Squat lobster), and (l) fracture (vein) filled gas hydrates (2.23 mbsf) recovered from active cold seep site in the Krishna-Godavari (K-G) basin, Bay of Bengal.

4.12. (a–d) Petrographic thin sections of methane-derived authigenic carbonates from shallow (active cold seep, Core ID: SSD-45/Stn-4/GC-01) gas hydrate site in the Krishna-Godavari (K-G) basin, Bay of Bengal. The thin sections were observed under plane-polarized light (Please note that arrow used to highlight the structures and mineral types).

4.13. (a–c) Bivariate scatter plots of magnetic parameters: magnetic susceptibility (χ_{lf}), saturation isothermal remanent magnetization (SIRM), SIRM/χ_{lf}, S-ratio, and (d) Day plot for samples from shallow (active cold seep, Core ID: SSD-45/Stn-4/GC-01) and deep-seated gas (Core ID: NGHP-01-15A) hydrate site in the Krishna-Godavari (K-G) basin, Bay of Bengal. (Please note that the gray arrow is used in plot (c) to highlight the trend).

Preface

Krishna-Godavari (K-G) basin is a proven petroliferous, located in the eastern central continental margin of India. The sediments in the basin are fed by the peninsular Krishna and Godavari Rivers and their tributaries. Both the rivers drain through the Late Cretaceous Deccan Basalts (DcB), Archean-Proterozoic Gneissic Complexes (APGC), and recent sediments and deliver a large amount of detrital (magnetite-rich) sediments to the K-G basin (Sangode et al., 2007; Ramesh and Subramanian 1988). Geophysical and geological studies have confirmed the existence of active and paleo-cold (methane) seep associated with shallow and deep-seated methane hydrates in the K-G basin. (Collett et al., 2008; Mazumdar et al., 2009; Mazumdar et al., 2019; Dewangan et al., 2021).

Magnetic minerals are widespread and indicative of sedimentary constituents, and their associated magnetic signals can reflect primary depositional and secondary diagenetic and authigenic processes (Canfield, 1989). Sedimentation rate, sediment provenance, transportation, and depositional conditions determine the concentration, grain size, and mineralogy of magnetic minerals and can significantly affect sediment magnetic records (Thompson & Oldfield, 1986). In marine cold seep and methane hydrate bearing sedimentary system, anaerobic oxidation of methane (AOM) is an important biogeochemical process that results from the interaction of rising methane flux and downward diffusing sulfate concentrations (Knittel & Boetius, 2009). AOM process coupled with organoclastic sulfate reduction (OSR) generates hydrogen sulfide in the pore-waters of the host sediments. The released hydrogen sulfide reacts further with dissolved iron to form magnetic iron sulfides, thereby creating distinct secondary magnetic signals in the AOM zone (Berner, 1970; Canfield & Berner, 1987; Dewangan et al., 2013; Jørgensen et al., 2004; Riedinger et al., 2005). The rock magnetic investigation can help to characterize the primary and secondary magnetic signals and secondary signals originating from the detrital as well as diagenetic/authigenic minerals in gas hydrate depositional environments.

Magnetic minerals are valuable recorders of the geological and methane-related geochemical processes and provide important insights on the methane seepage dynamics and diagenetic processes in marine gas hydrate sedimentary system (Musgrave et al., 2006; Larrasoaña et al., 2007; Kars and Kodama, 2015; Badesab et al., 2019). The linkage between rock magnetism, pore-water geochemistry, methane-related magnetic mineral diagenesis, and

authigenesis has been well-established (Roberts, 2015). For example, in Cascadia Margin (Musgrave et al., 2006; Larrasoaña et al., 2007), Mackenzie Delta, Canada (Enkin et al., 2007), Arctic Vestnesa Ridge, offshore western Svalbard (Johnson et al., 2014), Nankai Trough (Kars and Kodama, 2015; Shi et al., 2017), offshore Shimokita Peninsula Japan (Phillips et al., 2017), Bay of Bengal (Dewangan et al., 2013; Badesab et al., 2019; Johnson et al., 2021), West Siberian Sea (Rudmin et al., 2018), offshore Taiwan (Horng, 2018), Izu-Bonin rear arc (Musgrave et al., 2019), Mediterranean continental shelf (Amiel et al., 2020), Northwestern Weddell Sea (Reilly et al., 2020), South China Sea (Lin et al., 2021), and Hikurangi Margin, New Zealand (Greve et al., 2021; Kars et al., 2021). Despite of extensive environmental and rock magnetic research focussing on understanding magnetic mineral diagenesis in the marine gas hydrate sedimentary system, there is no systematic study till date which addresses three key questions. (a) how magnetic minerals selectively respond to a range of diagenetic processes in the sulfidic and methanic environments respectively, (b) compare the diagenetic analysis of two different (shallow versus deep-seated) marine gas hydrate systems in the K-G basin, (c) delineate the complex diagenetic (early and late) processes constrained by the variability in methane fluxes and underlying fault/fractures at active and relict seep dominated sedimentary systems.

The K-G basin represents an ideal natural laboratory representing highly dynamic depositional (high sedimentation rates, shale-tectonism) sedimentary environment and with its unique presence of active, relict and paleo-cold (methane) seep linked with the presence of shallow and deep-seated gas hydrate systems provides an opportunity and to obtain a comprehensive view of the methane-related diagenetic and authigenic processes. Sediment cores retrieved from active, relict and paleo-cold seep sites linked with shallow gas hydrates and deep-seated gas hydrates during CSIR-National Institute of Oceanography (NIO) gas hydrate discovery cruise (SSD-045 onboard R/V Sindhu Sadhana; 2018, Mazumdar et al., 2019) and first Indian National Gas Hydrate Drilling Expedition (NGHP-Exp-01; 2006, Collet et al., 2008; Kumar et al., 2014) were utilized to accomplish the following objectives of the PhD thesis:

1. Unravel the magnetic mineral assemblages in methane hydrate-bearing cold seep system from Krishna-Godavari basin, Bay of Bengal.
2. Comparative diagenetic analysis of shallow and deep-seated marine gas hydrates system from the Bay of Bengal.

In this study, rock magnetic, sedimentological, mineralogical, and petrological methods were employed on the sediment cores representing different type of methanic environments from the Bay of Bengal. In this study, two sediment gravity cores and six spade cores collected during CSIR-NIO's gas hydrate exploration cruise (SSD-045) and two drilled cores (NGHP-01-15A, NGHP-01-20A) recovered during the first NGHP expedition-01 were investigated. The research work carried out for this doctoral thesis is presented in five chapters. The scientific results of this study achieve two objective of the PhD thesis and are published in peer-reviewed international journals. The chapter-wise content of the thesis is listed below-

Chapter 1: Introduction

This chapter provides a brief introduction on the marine cold (methane) seep and different types (active, relict, paleo) linked with shallow and deep-seated gas hydrates, geological (detrital) and geochemical (diagenetic/authigenic) processes. Introduction on rock magnetic methods, parameters (concentration, grain size, mineralogy) and its usefulness in resolving the research problems related to magnetic mineral diagenesis and authigenesis in methanic and gas hydrate bearing sediments are included in this chapter. Considering published research and what is known, chapter 1 summarizes the rationale for conducting research and describes the objectives in detail.

Chapter 2: Methodology

In this chapter, a detailed information on the study area, geology, materials and methods employed in this study are provided. An introduction on the various analytical instruments utilized to conduct rock magnetic, sedimentological, mineralogical and petrological analyses on the sediment cores, magnetic particles and methane-derived authigenic carbonates is included. Two sediment gravity cores SSD-45/Stn-4/GC-01 (active methane seep, shallow gas hydrate system), SSD-45/Stn-11/GC-02 (relict seep), and six spade cores SSD-45/Stn-4/SPC-01 to SPC-06 (active methane seep) retrieved onboard R/V Sindhu Sadhana (Cruise No: SSD-045) and long-drilled sediment core NGHP-01-15A, NGHP-01-20A (deep-seated gas hydrate system) recovered onboard D/V JOIDES Resolution (Expedition No: NGHP-Exp-01) were utilized in this study. The sediment cores were sub-sampled and stored at cold repository of CSIR-National Institute of Oceanography, Goa, India prior to the analyses.

2.1: Sampling and measurements

For rock magnetic analyses, sediment sub samples of were dried, weighed, and packed in cylindrical sample (plastic) bottles. The magnetic susceptibility was measured at low (χ_{lf}) and high (χ_{hf}) frequencies 0.47 kHz and 4.7 kHz respectively using a Bartington Instruments MS2B dual-frequency susceptibility meter. The frequency-dependent susceptibility was calculated by using the formulae-

$$\chi fd\ \% = \frac{\chi lf - \chi hf)}{\chi lf} X100$$

Anhysteretic remanent magnetization (ARM) was imparted using 100mT alternating magnetic field superimposed on a fixed direct current (DC) bias field of 50 μT. In the forward direction, an isothermal remanent magnetization (IRM) was applied in an inducing field of +1T and +2.5T and demagnetized by DC backfields, respectively −20, −30, −100, and −300 mT using a MMPM10 pulse magnetizer. All remanent magnetizations were measured using AGICO JR-6A spinner magnetometer. Mass normalized IRM acquired at a peak field of 2.5T is assumed as the saturation IRM (SIRM). S-ratio is calculated as the ratio between the IRM at −300 mT and SIRM (Bloemendal et al., 1992).

$$S - ratio = \frac{IRM - 300mT}{SIRM}$$

The inter-parametric ratios ARM/SIRM and SIRM/χ_{lf} were also calculated. Curie temperature is determined for selected samples using a Natsuhara Giken (Model NMB-89) magnetic balance. In order to analyze the samples were heated up to 700°C and subsequently cooled back to room temperature and the sediment magnetization acquired by the sample at different temperatures was recorded. First-order reversal curves (FORC) diagrams provided additional information on the type of magnetic minerals and their domain states. Magnetic hysteresis loops, FORC, and back-field demagnetization curves of selected samples were measured using the vibrating sample magnetometer (VSM). FORCinel software was used to process the FORC diagrams (Harrison & Feinberg, 2008). Quantum Design Magnetic Properties Measurement System (MPMS) was used to conduct low-temperature magnetic measurements on

the selected sediment samples. Low-temperature Verwey transition (T_v) is typically used to detect the magnetite and Besnus transition (T_{Bes}) for pyrrhotite.

A magnetic minerals extraction method was used to separate the magnetic particles from the bulk sediments (Petersen et al., 1986). For determination of magnetic mineralogies, the scanning electron microscopy coupled with energy dispersive spectrum (SEM-EDS) (SEM; JEOL JSM-5800 LV) and X-ray Diffraction (Rigaku X-Ray Diffractometer Ultima IV) analyses were conducted on magnetic particles. Optical microscopy on separated >63 μm fractions representing different sediment intervals was carried out using Olympus microscope (BX41). The polished thin sections (26 x 46 mm) of methane-derived authigenic carbonates were analyzed on a petrographic trinocular microscope (Model No. BX51TRF).

Chapter 3: Origin of magnetic minerals and its fate in sulfidic and methanic environments.

A comprehensive inventory of magnetic minerals originating from detrital, diagenetic, authigenic and biogenic sources are developed based on the large set of rock magnetic, mineralogical and sedimentological data generated on the sediment cores from active, relict, paleo-cold seep sites manifested by the shallow and deep-seated marine gas hydrate systems from the Bay of Bengal. In general, sediment magnetism is mainly carried by complex magnetic mineral assemblages of detrital (titanomagnetite, titanohematite, titanomaghemite), diagenetic (pyrite), authigenic (magnetite, greigite) and biogenic (magnetite) minerals. In addition, silicate-hosted fine-grained magnetic inclusions which survived time-varying diagenetic fronts also contributed to the bulk sediment magnetic signal.

Rock magnetic and mineralogical methods helped to characterize magnetic assemblages in a complex active cold seep and methane-hydrate bearing marine sedimentary system with different sources (detrital, diagenetic, authigenic) of the magnetic particles. In this study, we conducted systematic investigation on a sediment core from the Bay of Bengal by combining bulk rock magnetic analyses and SEM-EDS observations to unravel the effect of range of diagenetic processes on the magnetic minerals in the sulfidic and methanic sediments. The sediment magnetic zones were demarcated into sulfidic (uppermost) and methanic (lowermost) based on the depth of expected sulfate methane transition zone as evident through distinct

minima in magnetic susceptibility. The degree of influence of each magnetic mineral phase in the studied sediment core varied within sulfidic and methanic sedimentary zones is clearly evident in rock magnetic and mineralogical records. Progressive diagenetic dissolution of primary iron oxide and consequent formation of iron sulfide in the uppermost sulfidic zone is clearly mirrored in the magnetic susceptibility (χlf) profile. Enrichment of superparamagnetic (SP) size magnetic particles marked by higher values of authigenic iron sulfide proxy (SIRM/χ_{lf}) and coercivity (S-ratio) in the sulfidic environment is linked with the growth of fine-grained ferrimagnetic iron sulfides like greigite. Lower values of magnetic grain size diagnostic proxy (ARM/SIRM) in the uppermost sulfidic zones (Z-I, Z-II) is attributed to the preferential dissolution of fine-grained magnetite. Elevated values of ARM/SIRM proxy in the methanic zones of studied sediment cores indicates the presence of authigenic magnetite formed via microbial iron-reduction process (Vigderovich et al., 2019; Lin et al., 2021).

A comprehensive analysis of SEM-EDS observations on the magnetic particles from the sulfidic, methanic, and gas hydrate bearing sediment zones provided evidence on the detrital and methane-related diagenetic processes. Detrital titanomagnetite were noticed in the sulfidic as well as methanic zone. Less-altered with angular, irregular, spherical and well-defined octahedral micron sized magnetic particles in all sediment cores are mainly derived from Deccan Volcanic Province (DVP) and dominates the bulk sediment magnetic signal. Several evidence of diagenetic dissolution, sulphidization and maghemitization of magnetic particles in the sulfidic and methanic zones are presented in this study.

Chapter 4: Comparative diagenetic analysis of shallow and deep-seated marine gas systems from the Bay of Bengal.

This chapter presents the first systematic study of high-resolution rock magnetism complemented by mineralogical and petrological observations conducted on two sediment cores representing shallow (active methane seep; SSD-45/Stn-4/GC-01) and deep-seated (NGHP-01-15A) gas hydrate systems in the Bay of Bengal. Two key questions are addressed in this study. Firstly, how magnetic minerals respond to the geochemical environment at two different diagenetic settings experiencing variable fluid sequence, and secondly elucidate the control on the magnetite and greigite authigenesis in sulfidic, methanic, and gas hydrate bearing sediments.

Comprehensive rock magnetic measurements complemented by mineralogical and petrological observation on sediment samples revealed that detrital titanomagnetite is the dominant magnetic mineral along with diagenetically formed pyrite, authigenic formed magnetite, and greigite minerals in both sediment cores. Magnetic granulometric proxies (ARM/SIRM and SIRM/χ_{lf}) provided useful insights on the diagenetic dissolution and authigenic formation of magnetic minerals in the sulfidic, methanic and gas hydrate-bearing zones. The presence of authigenic greigite and magnetite in both the studied cores is confirmed by the rock magnetic and mineralogical data sets. The mechanisms of formation of authigenic greigite and magnetite in shallow and deep-seated gas hydrate-bearing sedimentary systems in the Bay of Bengal is clearly explained. Multiple occurrences of authigenic carbonate provided evidence on the episodic intensification of anaerobic oxidation of methane (AOM) at active seep (shallow hydrate) site. In contrast, silicate weathering coupled to microbial methanogenesis is the major process responsible for the formation of Fe-rich carbonates in deep-seated gas hydrate core. Our findings are summarized into a conceptual model explaining the constraints on the formation and preservation of diagenetic and authigenic minerals in two different diagenetic systems.

Chapter 5: Summary and conclusions

The conclusion of the present thesis and the scope of future research are presented in this chapter. A set of comprehensive rock magnetic, mineralogical and sedimentological data of the studied sediment cores helped to develop a magnetic mineral inventory for the marine gas hydrate systems from the Bay of Bengal. Several lines of evidences provided vital information on the evolution of different magnetic mineralogies constrained by variable diagenetic and authigenic processes in the studied sediment cores. The usefulness of employing rock magnetic methods in combination with focussed electron microscope analyses for unravelling the mineralogy, genesis and state of preservation of magnetic particles in the sulfidic and methanic environments has been demonstrated in this study.

A reference list of the literature cited in the thesis is presented in alphabetical order at the end.

प्रस्तावना

कृष्णा-गोदावरी (के-जी) खोरे भारताच्या पूर्व-मध्य महाद्वीपीय समासामध्ये स्थित एक सिद्ध पेट्रोलियमयुक्त आहे. खोऱ्यातील गाळ द्वीपकल्पीय कृष्णा आणि गोदावरी नद्या आणि त्यांच्या उपनद्या द्वारे वाहून आणला जातो. दोन्ही नद्या लेट क्रेटेशियस डेक्कन बेसाल्ट्स (डे.बे.), आर्कियन-प्रोटेरोझोइक ग्नेसिक कॉम्प्लेक्सेस (एपीजिसी) आणि अलीकडील गाळातून वाहून जातात आणि के-जी खोऱ्यामध्ये मोठ्या प्रमाणात मूळ खडकांचे सूक्ष्मकण (मॅग्नेटाइट-समृद्ध) गाळ वितरीत करतात (सांगोडे एट अल., २००७; रमेश आणि सुब्रमण्यम १९८८). भूभौतिकीय आणि भूगर्भशास्त्रीय अभ्यासांनी के-जी बेसिनमध्ये उथळ आणि खोल-बसलेल्या मिथेन हायड्रेट्सशी संबंधित सक्रिय आणि पॅलेओ-कोल्ड (मिथेन) सीपच्या अस्तित्वाची पुष्टी केली आहे. (कोलेट एट अल., २००८; मुझुमदार एट अल., २००९, २०१९; देवांगन एट अल., २०२१).

चुंबकीय खनिजे व्यापक आहेत आणि गाळाच्या घटकांचे सूचक आहेत आणि त्यांच्याशी संबंधित चुंबकीय सिग्नल प्राथमिक निक्षेपण आणि दुय्यम डायजेनेटिक आणि ऑथिजेनिक प्रक्रिया प्रतिबिंबित करू शकतात (कॅनफिल्ड, १९८९). अवसादन दर, गाळाचा उगम, वाहतूक आणि निक्षेपीय परिस्थिती चुंबकीय खनिजांची एकाग्रता, सूक्ष्म कणांचा आकार आणि खनिजशास्त्र निर्धारित करतात आणि गाळाच्या चुंबकीय नोंदींवर लक्षणीय परिणाम करू शकतात (थॉम्पसन आणि ओल्डफिल्ड, १९८६). सागरी कोल्ड सीप आणि मिथेन हायड्रेट समावेश असलेल्या गाळाच्या प्रणालीमध्ये, मिथेनचे ॲनारोबिक ऑक्सिडेशन (एओएम) ही एक महत्त्वाची जैव-रासायनिक प्रक्रिया आहे जी वाढत्या मिथेन प्रवाह आणि खालच्या दिशेने पसरणाऱ्या सल्फेट सांद्रता (निटेल आणि बोएटियस, २००९) यांच्या परस्परसंवादामुळे होते. ऑर्गनोक्लास्टिक सल्फेट रिडक्शन (ओएसआर) सह एओएम प्रक्रिया यजमान गाळाच्या छिद्र-पाण्यात हायड्रोजन सल्फाइड तयार करते. सोडलेला हायड्रोजन सल्फाइड चुंबकीय लोह सल्फाइड तयार करण्यासाठी विरघळलेल्या लोखंडावर आणखी प्रतिक्रिया देतो, ज्यामुळे एओएम झोनमध्ये वेगळे दुय्यम चुंबकीय सिग्नल तयार होतात (बर्नर, १९७०; कॅनफिल्ड आणि बर्नर, १९८७; दिवांगन एट अल., २०१३; जोर्गेनसेन एट अल., २००४; रिडिंजर एट अल., २००५). रॉक मॅग्नेटिक तपासामुळे गॅस हायड्रेट डिपॉझिशनल वातावरणात मूळ खडकांचे सूक्ष्मकण तसेच डायजेनेटिक/ऑथिजेनिक खनिजांपासून उद्भवणारे प्राथमिक आणि दुय्यम चुंबकीय सिग्नल आणि दुय्यम सिग्नल वैशिष्ट्यीकृत करण्यात मदत होऊ शकते.

चुंबकीय खनिजे भूगर्भशास्त्रीय आणि मिथेन-संबंधित भू-रासायनिक प्रक्रियांचे मौल्यवान रेकॉर्डर आहेत आणि सागरी वायू हायड्रेट गाळाच्या प्रणालीमध्ये मिथेन सीपेज डायनॅमिक्स आणि डायजेनेटिक प्रक्रियांबद्दल महत्त्वपूर्ण अंतर्दृष्टी प्रदान करतात (मुस्ग्रेव्ह एट अल., २००६; लारासोआना एट अल., २००७, २०१५; बडेसाब एट अल.,२०१९). रॉक मॅग्नेटिझम, पोअर-वॉटर जिओकेमिस्ट्री, मिथेन-संबंधित चुंबकीय खनिज डायजेनेसिस आणि ऑथिजेनेसिस यांच्यातील संबंध चांगल्या प्रकारे स्थापित केले गेले आहेत (रॉबर्ट्स, २०१५). उदाहरणार्थ, कॅस्केडिया मार्जिन (मुस्ग्रेव्ह एट अल., २००६; लारासोआना, २००७), मॅकेन्झी डेल्टा, कॅनडा (अँकीन एट अल., २००७), आर्क्टिक वेस्टनेसा रिज, ऑफशोअर वेस्टर्न स्वालबार्ड (जॉन्सन एट अल., २०१४), नानकाई ट्रफ (कार्स आणि कोडामा, २०१५; शि एट अल., २०१७), ऑफशोअर शिमोकिता प्रायद्वीप जपान (फिलिप्स एट अल., २०१७), बंगालचा उपसागर (दिवांगन एट अल., २०१३; बडेसाब एट अल., २०१९; जॉनसन एट अल., २०२१), पश्चिम सायबेरियन समुद्र (रुडमिन एट अल., २०१८), ऑफशोअर तैवान (हॉर्नग, २०१८), इझु-बोनिन रियर आर्क (मुस्ग्रेव्ह

एट अल., २०१९), भूमध्य महाद्वीपीय शेल्फ (आमिल एट अल., २०२०), नॉर्थवेस्टर्न वेडेल सी (रेली एट अल., २०२०), दक्षिण चीन समुद्र (लिन एट अल., २०२१), आणि हिकुरंगी मार्जिन, न्यूझीलंड (ग्रीव्ह एट अल., २०२१; कार्स एट अल., २०२१). सागरी वायू हायड्रेट सेडमेंटरी सिस्टीममधील चुंबकीय खनिज डायजेनेसिस समजून घेण्यावर लक्ष केंद्रित करून व्यापक पर्यावरणीय आणि खडक चुंबकीय संशोधन असूनही, तीन प्रमुख प्रश्नांना संबोधित करणारा कोणताही पद्धतशीर अभ्यास आजपर्यंत झालेला नाही. (अ) चुंबकीय खनिजे क्रमशः सल्फिडिक आणि मेथॅनिक वातावरणातील डायजेनेटिक प्रक्रियांच्या श्रेणीला निवडक प्रतिसाद कसा देतात, (ब) के-जी खोऱ्यातील दोन भिन्न (उथळ विरुद्ध खोल बसलेल्या) सागरी वायू हायड्रेट प्रणालींच्या डायजेनेटिक विश्लेषणाची तुलना, (क) मिथेन फ्लक्सेसमधील परिवर्तनशीलता आणि सक्रिय आणि अवशेष सीप वर्चस्व असलेल्या गाळ प्रणालींमध्ये अंतर्निहित दोष/फ्रॅक्चरमुळे प्रतिबंधित जटिल डायजेनेटिक (लवकर आणि उशीरा) प्रक्रियांचे वर्णन करा.

के-जी खोऱ्यातील एक आदर्श नैसर्गिक प्रयोगशाळा दर्शवते जी अत्यंत गतिमान निक्षेपण (उच्च अवक्षेपण दर, शेल-टेक्टोनिझम) गाळाच्या वातावरणाचे प्रतिनिधित्व करते आणि त्यात सक्रिय, अवशेष आणि पॅलेओ-कोल्ड (मिथेन) गळतीची अनोखी उपस्थिती उथळ आणि खोलवर बसलेली असते. गॅस हायड्रेट सिस्टीम मिथेन-संबंधित डायजेनेटिक आणि ऑथिजेनिक प्रक्रियांचे सर्वसमावेशक दृश्य मिळविण्याची संधी प्रदान करते. सी.एस.आय.आर.-नॅशनल इन्स्टिट्यूट ऑफ ओशनोग्राफी (एन.आय.ओ.) गॅस हायड्रेट डिस्कवरी क्रूझ (एस.एस.डी.- ०४५ ऑनबोर्ड आर/व्ही सिंधू साधना, २०१८) दरम्यान उथळ गॅस हायड्रेट्स आणि खोल बसलेल्या गॅस हायड्रेट्सशी जोडलेल्या सक्रिय, अवशेष आणि पॅलेओ-कोल्ड सीप साइट्समधून सेडिमेंट कोर पुनर्प्राप्त केले गेले (मझुमदार एट अल., २०१९) आणि पहिली भारतीय राष्ट्रीय गॅस हायड्रेट ड्रिलिंग मोहीम (एन.जि.एच.पी एक्सपि.-१; २००६, कोलेट एट अल., २००८; कुमार एट अल., २०१४) पी.एच.डी.ची खालील उद्दिष्टे पूर्ण करण्यासाठी वापरली गेली:

१. बंगालच्या उपसागरातील कृष्णा-गोदावरी खोऱ्यातील मिथेन हायड्रेट-बेअरिंग कोल्ड सीप सिस्टीममधील चुंबकीय खनिज एकत्रीकरणे उलगडून दाखवा.

२. बंगालच्या उपसागरातून उथळ आणि खोल बसलेल्या सागरी वायू हायड्रेट्स प्रणालीचे तुलनात्मक डायजेनेटिक विश्लेषण.

या अभ्यासात, बंगालच्या उपसागरातील विविध प्रकारच्या मिथेनिक वातावरणाचे प्रतिनिधित्व करणाऱ्या गाळाच्या कोरांवर रॉक मॅग्नेटिक, सेडिमेंटोलॉजिकल, मिनरॉलॉजिकल आणि पेट्रोलॉजिकल पद्धती वापरल्या गेल्या. या अभ्यासात, सी.एस.आय.आर.-एन.आय.ओ. च्या गॅस हायड्रेट एक्सप्लोरेशन क्रूझ (एस.एस.डी.- ०४५) दरम्यान गोळा केलेले दोन सेडिमेंट ग्रॅव्हिटी कोर आणि सहा स्पेड कोर आणि पहिल्या एन.जि.एच.पी. मोहिमेदरम्यान दोन ड्रिल केलेले कोर (एन.जि.एच.पी.-०१-१५ए, एन.जि.एच.पी.-०१-२०ए) यांचे संशोधन करण्यात आले. या डॉक्टरेट प्रबंधासाठी केलेले संशोधन कार्य पाच प्रकरणांमध्ये मांडण्यात आले आहे. या अभ्यासाचे वैज्ञानिक परिणाम पी.एच.डी. प्रबंधाचे दोन उद्दिष्ट साध्य करतात आणि पीअर-रिव्ह्यू केलेल्या आंतरराष्ट्रीय जर्नल्समध्ये प्रकाशित केले आहेत. प्रबंधाचा प्रकरण -वार मजकूर खाली सूचीबद्ध आहे-

प्रकरण १: परिचय

या प्रकरणामध्ये सागरी शीत (मिथेन) गळती आणि उथळ आणि खोल बसलेल्या वायू हायड्रेट्स, भूगर्भीय (अपायकारक) आणि भू-रासायनिक (डायजेनेटिक/ऑथिजेनिक) प्रक्रियांशी जोडलेले विविध प्रकार (सक्रिय, अवशेष, पॅलेओ) यांचा थोडक्यात परिचय देतो. या प्रकरणात रॉक मॅग्नेटिक पद्धती, मापदंड (एकाग्रता, धान्य आकार, खनिजशास्त्र) आणि चुंबकीय खनिज डायजेनेसिस आणि मेथॅनिक आणि गॅस हायड्रेट बेअरिंग सेडिमेंट्समधील ऑथिजेनेसिसशी संबंधित संशोधन समस्यांचे निराकरण करण्यासाठी त्याची उपयुक्तता या विषयावर माहिती दिली आहे. प्रकाशित संशोधन आणि काय ज्ञात आहे याचा विचार करून, धडा १ संशोधन आयोजित करण्याच्या तर्काचा सारांश देतो आणि उद्दिष्टांचे तपशीलवार वर्णन करतो.

प्रकरण २: पद्धती

या प्रकरणामध्ये, अभ्यास क्षेत्र, भूविज्ञान, साहित्य आणि या अभ्यासात वापरल्या जाणाऱ्या पद्धतींची तपशीलवार माहिती दिली आहे. रॉक मॅग्नेटिक, सेडिमेंटलॉजिकल, मिनरॉलॉजिकल आणि पेट्रोलॉजिकल विश्लेषणे करण्यासाठी वापरल्या जाणाऱ्या विविध विश्लेषणात्मक साधनांचा परिचय गाळाच्या कोर, चुंबकीय कण आणि मिथेन-व्युत्पन्न ऑथिजेनिक कार्बोनेटवर समाविष्ट केला आहे. दोन सेडिमेंट ग्रॅव्हिटी कोर एस.एस.डी.-०४५/स्टेशन-४/ग्रा.को.-०१ (सक्रिय मिथेन सीप, उथळ गॅस हायड्रेट सिस्टम), एस.एस.डी.-०४५/स्टेशन-११/ग्रा.को.-०२ (अवशेष सीप), आणि सहा स्पेड कोर एस.एस.डी.-०४५/स्टेशन-४/एस पी सी -०१ ते एस पी सी -०६ (सक्रिय मिथेन सीप) ऑनबोर्ड आर/व्ही सिंधू साधना (क्रूझ क्रमांक: एस.एस.डी.-०४५) आणि लाँग-ड्रिल्ड सेडिमेंट कोर एन.जि.एच.पी.-०१-१५ए, एन.जि.एच.पी.-०१-२०ए (खोल) पुनर्प्राप्त -सीट गॅस हायड्रेट सिस्टीम) ऑनबोर्ड ड्री/व्हे जॉइड्स रिझोल्यूशन (एक्सपेडिशन क्र: एनजीएचपी-एक्सप-०१) या अभ्यासात वापरण्यात आले. विश्लेषणापूर्वी गाळाचे कोर उप-नमुने घेतले आणि सी.एस.आय.आर.-नॅशनल इन्स्टिट्यूट ऑफ ओशनोग्राफी, गोवा, भारताच्या शीत भांडारात साठवले गेले.

२. १: नमुना आणि मोजमाप

खडक चुंबकीय विश्लेषणासाठी, गाळाचे उपनमुने वाळवले गेले, वजन केले गेले आणि दंडगोलाकार नमुना (प्लास्टिक) बाटल्यांमध्ये पॅक केले गेले. चुंबकीय संवेदनशीलता कमी (χlf) आणि उच्च (χhf) फ्रिक्वेन्सी अनुक्रमे ०.४७ kHz आणि ४.७ kHz. वर बारटिंग्टन इन्स्ट्रुमेंट्स एम.एस. २ बी. ड्युअल-फ्रिक्वेंसी संवेदनशीलता मीटर वापरून मोजली गेली. वारंवारता-आश्रित संवेदनशीलता सूत्र वापरून मोजली गेली-

$$\chi fd\ \% = \frac{\chi lf - \chi hf)}{\chi lf} X100$$

५०μT च्या फिक्स्ड डायरेक्ट करंट (डीसी) बायस फील्डवर १००mT वैकल्पिक चुंबकीय क्षेत्र वापरून एनहिस्टेरेटिक रेमनेंट मॅग्नेटायझेशन (एआरएम) प्रदान केले गेले. पुढे दिशेने, +१T आणि +२. ५T च्या इंडिकिंग फील्डमध्ये एक समतापीय अवशेष चुंबकीकरण (आईआरएम) लागू केले गेले आणि डीसी बॅकफिल्डद्वारे अनुक्रमे -२०, -३०, -१००, आणि -३०० mT एमएमपीएम १० पल्स मॅग्नेटायझर वापरून डिमॅग्नेटाइज केले गेले. अजिको जेआर ६ ए स्पिनर मॅग्नेटोमीटर वापरून सर्व उर्वरित चुंबकीकरण मोजले गेले. २. ५T च्या पीक फील्डवर अधिग्रहित वस्तुमान सामान्यीकृत आईआरएम हे संपृक्तता आईआरएम (एसआईआरएम) म्हणून गृहीत धरले जाते. S-गुणोत्तर -

३०० mT आणि एसआईआरएम (ब्लोएमेण्डल इट अल., १९९२) मधील आईआरएम मधील गुणोत्तर म्हणून मोजले जाते.

$$S - ratio = \frac{IRM - 300mT}{SIRM}$$

आंतर-पॅरामेट्रिक गुणोत्तर एआरएम/एसआईआरएम आणि एसआईआरएम /χlf देखील मोजले गेले. नटसुहारा गिकेन (मॉडेल एनएमबी -८९) चुंबकीय समतोल वापरून निवडलेल्या नमुन्यांसाठी क्युरी तापमान निर्धारित केले जाते. विश्लेषण करण्यासाठी नमुने ७०० डिग्री सेल्सिअस पर्यंत गरम केले गेले आणि नंतर खोलीच्या तपमानावर परत थंड केले गेले आणि वेगवेगळ्या तापमानात नमुन्याद्वारे प्राप्त केलेले गाळाचे चुंबकीकरण नोंदवले गेले. फर्स्ट-ऑर्डर रिव्हर्सल वक्र (फोर्क) आकृत्यांनी चुंबकीय खनिजांच्या प्रकारावर आणि त्यांच्या डोमेन स्थितीबद्दल अतिरिक्त माहिती प्रदान केली आहे. चुंबकीय हिस्टेरेसिस लूप, फोर्क आणि निवडलेल्या नमुन्यांचे बॅक-फील्ड डिमॅग्नेटायझेशन वक्र व्हायब्रेटिंग सॅम्पल मॅग्नेटोमीटर (व्हीएसएम) वापरून मोजले गेले. FORCinel सॉफ्टवेअरचा वापर फोर्क आकृत्यांवर प्रक्रिया करण्यासाठी केला गेला (हॅरिसन आणि फीनबर्ग, 2008). क्वांटम डिझाइन मॅग्नेटिक प्रॉपर्टीज मेजरमेंट सिस्टम (एमपीएमएस) चा वापर निवडलेल्या गाळाच्या नमुन्यांवर कमी-तापमान चुंबकीय मोजमाप करण्यासाठी केला गेला. कमी-तापमान वर्वे संक्रमण (टीव्ही) सामान्यत: मॅग्नेटाइट आणि बेसनस संक्रमण (टिबेस) शोधण्यासाठी पायरोटाईट साठी वापरले जाते.

चुंबकीय खनिजे काढण्याची पद्धत मोठ्या प्रमाणात गाळापासून चुंबकीय कण वेगळे करण्यासाठी वापरली गेली (पीटरसन एट अल., १९८६). चुंबकीय खनिजांच्या निर्धारणासाठी, स्कॅनिंग इलेक्ट्रॉन मायक्रोस्कोपीसह ऊर्जा पसरवणारा स्पेक्ट्रम (एसईएम - ईडीएस) (जेईओएल-जेएसएम ५८०० एलव्ही) आणि एक्स-रे डिफ्रॅक्शन (रिगाकू एक्स-रे डिफ्रॅक्टोमीटर अल्टिमा IV) विश्लेषणे मॅग्नेटिक पार्टल्सवर आयोजित केली गेली. ऑलिंपस मायक्रोस्कोप (बीएक्स ४१) वापरून विभक्त >६३ μm अपूर्णांकांवर ऑप्टिकल मायक्रोस्कोपी केली गेली. पेट्रोग्राफिक ट्रायनोक्युलर मायक्रोस्कोप (मॉडेल क्र. बीएक्स ५१टिआरएफ) वर मिथेन-व्युत्पन्न ऑथिजेनिक कार्बोनेटचे पॉलिश केलेले पातळ विभाग (२६ X ४६ मिमी) विश्लेषित केले गेले.

प्रकरण ३: चुंबकीय खनिजांची उत्पत्ती आणि सल्फिडिक आणि मिथेनिक वातावरणात त्याचे भविष्य.

डेट्रिटल, डायजेनेटिक, ऑथिजेनिक आणि बायोजेनिक स्त्रोतांपासून उद्भवलेल्या चुंबकीय खनिजांची सर्वसमावेशक यादी सक्रिय, अवशेष, पॅलेओ-कोल्ड सीप साइट्सद्वारे शेडमेंट कोरवर तयार केलेल्या रॉक मॅग्नेटिक, मिनरॉलॉजिकल आणि सेडिमेंटलॉजिकल डेटाच्या मोठ्या संचाच्या आधारे विकसित केली जाते. आणि बंगालच्या उपसागरातून खोलवर बसलेल्या सागरी वायू हायड्रेट प्रणाली. सर्वसाधारणपणे, गाळाचे चुंबकत्व हे मुख्यत्वे डेट्रिटल (टायटानोमॅग्नेटाइट, टायटॅनोहेमॅटाइट, टायटॅनोमॅगेमाइट), डायजेनेटिक (पायराइट), ऑथिजेनिक (मॅग्नेटाइट, ग्रेगाइट) आणि बायोजेनिक (मॅग्नेटाइट) खनिजांच्या जटिल चुंबकीय खनिज संयोजनांद्वारे वाहून नेले जाते. याव्यतिरिक्त, सिलिकेट-होस्ट केलेले सूक्ष्म-दाणेदार चुंबकीय समावेश जे कालांतराने टिकून राहिलेल्या डायजेनेटिक फ्रंट्सने देखील बल्क सेडिमेंट चुंबकीय सिग्नलमध्ये योगदान दिले.

रॉक मॅग्नेटिक आणि मिनरॉलॉजिकल पद्धतींनी चुंबकीय कणांच्या वेगवेगळ्या स्त्रोतांसह (डेट्रिटल, डायजेनेटिक, ऑथिजेनिक) जटिल सक्रिय कोल्ड सीप आणि मिथेन-हायड्रेट बेअरिंग सागरी गाळ प्रणालीमध्ये

चुंबकीय असेंबलेज वैशिष्ट्यीकृत करण्यात मदत केली. या अभ्यासात, आम्ही सल्फिडिक आणि मिथेनिक गाळातील चुंबकीय खनिजांवर डायजेनेटिक प्रक्रियेच्या श्रेणीचा प्रभाव उलगडण्यासाठी बल्क रॉक चुंबकीय विश्लेषण आणि एसईएम-ईडीएस निरीक्षणे एकत्रित करून बंगालच्या उपसागरातील गाळाच्या गाभ्यावर पद्धतशीर तपासणी केली. अपेक्षित सल्फेट मिथेन संक्रमण क्षेत्राच्या खोलीच्या आधारावर गाळाचे चुंबकीय क्षेत्र सल्फिडिक (वरच्या) आणि मिथेनिक (सर्वात खालच्या) मध्ये सीमांकित केले गेले. सल्फिडिक आणि मिथेनिक सेडमेंटरी झोनमध्ये वेगवेगळ्या अभ्यास केलेल्या गाळाच्या गाभ्यामध्ये प्रत्येक चुंबकीय खनिज टप्प्याच्या प्रभावाची डिग्री रॉक मॅग्नेटिक आणि मिनरॉलॉजिकल रेकॉर्डमध्ये स्पष्टपणे दिसून येते. प्राथमिक लोह ऑक्साईडचे प्रगतीशील डायजेनेटिक विघटन आणि परिणामी सर्वात वरच्या सल्फिडिक झोनमध्ये लोह सल्फाइडची निर्मिती चुंबकीय संवेदनशीलता (χlf) प्रोफाइलमध्ये स्पष्टपणे प्रतिबिंबित केली जाते. सल्फिडिक वातावरणात ऑथिजेनिक आयर्न सल्फाइड प्रॉक्सी (एसआईआरएम/χlf) आणि कोरसिव्हिटी (S-गुणोत्तर) च्या उच्च मूल्यांनी चिन्हांकित केलेल्या सुपरपरामॅग्नेटिक (एसपी) आकाराच्या चुंबकीय कणांचे संवर्धन ग्रेगाइट सारख्या सूक्ष्म-दाणेदार फेरिमॅग्नेटिक लोह सल्फाइडच्या वाढीशी जोडलेले आहे. सर्वात वरच्या सल्फिडिक झोनमध्ये (झेड -I, झेड -II) चुंबकीय धान्य आकार डायग्नोस्टिक प्रॉक्सी (एआरएम/एसआईआरएम) ची निम्न मूल्ये सूक्ष्मकण मॅग्नेटाइटच्या प्राधान्य विघटनास कारणीभूत आहेत. अभ्यास केलेल्या सेडिमेंट कोरच्या मेथॅनिक झोनमध्ये एआरएम/एसआयआरएम प्रॉक्सीची उन्नत मूल्ये मायक्रोबियल आयर्न-रिडक्शन प्रक्रियेद्वारे तयार झालेल्या ऑथिजेनिक मॅग्नेटाइटची उपस्थिती दर्शवतात (विग्डेरोविच एट अल., २०१९; लिन एट अल., २०२१).

सल्फिडिक, मिथेनिक आणि गॅस हायड्रेट बेअरिंग सेडिमेंट झोनमधील चुंबकीय कणांवरील एसईएम - ईडीएस निरीक्षणांचे सर्वसमावेशक विश्लेषण हानिकारक आणि मिथेन-संबंधित डायजेनेटिक प्रक्रियांचे पुरावे प्रदान करते. सल्फिडिक तसेच मिथेनिक झोनमध्ये डेट्रिटल टायटॅनोमॅग्नेटाइट आढळले. कोनीय, अनियमित, गोलाकार आणि चांगल्या-परिभाषित ऑक्टाहेड्रल मायक्रोन आकाराच्या चुंबकीय कणांसह कमी-बदललेले सर्व गाळाच्या कोरमध्ये प्रामुख्याने डेक्कन व्होल्कॅनिक प्रोव्हिन्स मधून आलेले असतात आणि मोठ्या प्रमाणात गाळाच्या चुंबकीय सिग्नलवर वर्चस्व गाजवतात. या अभ्यासात सल्फिडिक आणि मिथेनिक झोनमधील चुंबकीय कणांचे डायजेनेटिक विघटन, सल्फिडायझेशन आणि मॅग्हेमिटायझेशनचे अनेक पुरावे सादर केले आहेत.

प्रकरण ४: बंगालच्या उपसागरातील उथळ आणि खोल बसलेल्या सागरी वायू प्रणालींचे तुलनात्मक डायजेनेटिक विश्लेषण.

हा धडा उथळ (सक्रिय मिथेन सीप; एस.एस.डी.-०४५/स्टेशन-४/ग्रा.को.-०१) आणि खोल-आसन (एन.जि.एच.पी.-०१-१५ए) बंगालच्या उपसागरातील गॅस हायड्रेट प्रणाली प्रतिनिधित्व करणाऱ्या दोन गाळाच्या कोरांवर आयोजित केलेल्या खनिज आणि पेट्रोलॉजिकल निरीक्षणांद्वारे पूरक उच्च-रिझोल्यूशन रॉक चुंबकत्वाचा पहिला पद्धतशीर अभ्यास सादर करतो. या अभ्यासात दोन महत्त्वाचे प्रश्न हाताळले आहेत. प्रथम, चुंबकीय खनिजे दोन भिन्न डायजेनेटिक सेटिंग्जमध्ये भू-रासायनिक वातावरणास कसा प्रतिसाद देतात, ज्यामध्ये परिवर्तनीय द्रवपदार्थाचा अनुक्रम अनुभवला जातो आणि दुसरे म्हणजे सल्फिडिक, मेथॅनिक आणि गॅस हायड्रेट बेअरिंग सेडिमेंट्समधील मॅग्नेटाइट आणि ग्रेगाइट ऑथिजेनेसिसवरील नियंत्रण स्पष्ट करा.

गाळाच्या नमुन्यांवरील खनिज आणि पेट्रोलॉजिकल निरीक्षणाद्वारे पूरक असलेल्या व्यापक खडक चुंबकीय मोजमापांवरून असे दिसून आले की डेट्रिटल टायटॅनोमॅग्नेटाइट हे डायजेनेटिकली तयार झालेले पायराइट, ऑथिजेनिक बनलेले मॅग्नेटाइट आणि दोन्ही गाळातील ग्रेगाइट खनिजांसह प्रबळ चुंबकीय खनिज आहे. चुंबकीय ग्रॅन्युलोमेट्रिक प्रॉक्सी (एआरएम/एसआईआरएम आणि एसआईआरएम /χlf) ने सल्फिडिक, मिथेनिक आणि गॅस हायड्रेट-बेअरिंग झोनमध्ये डायजेनेटिक विघटन आणि चुंबकीय खनिजांच्या ऑथिजेनिक निर्मितीवर उपयुक्त अंतर्दृष्टी प्रदान केली. दोन्ही अभ्यास केलेल्या कोरमध्ये ऑथिजेनिक ग्रेगाइट आणि मॅग्नेटाइटची उपस्थिती रॉक मॅग्नेटिक आणि मिनरॉलॉजिकल डेटा सेटद्वारे पुष्टी केली जाते. बंगालच्या उपसागरातील उथळ आणि खोल-सीट गॅस हायड्रेट-बेअरिंग गाळ प्रणालींमध्ये ऑथिजेनिक ग्रेगाइट आणि मॅग्नेटाइट तयार करण्याची यंत्रणा स्पष्टपणे स्पष्ट केली आहे. ऑथिजेनिक कार्बोनेटच्या अनेक घटनांनी सक्रिय सीप (उथळ हायड्रेट) साइटवर मिथेन (एओएम) च्या ऍनेरोबिक ऑक्सिडेशनच्या एपिसोडिक तीव्रतेचा पुरावा प्रदान केला. याउलट, सिलिकेट वेदरिंग आणि मायक्रोबियल मेथॅनोजेनेसिस ही मुख्य प्रक्रिया आहे जी खोल-सीट गॅस हायड्रेट कोरमध्ये लोहयुक्त कार्बोनेटच्या निर्मितीसाठी जबाबदार आहे. आमचे निष्कर्ष दोन भिन्न डायजेनेटिक प्रणालींमध्ये डायजेनेटिक आणि ऑथिजेनिक खनिजांच्या निर्मिती आणि संरक्षणावरील मर्यादा स्पष्ट करणाऱ्या संकल्पनात्मक मॉडेलमध्ये सारांशित केले आहेत.

प्रकरण ५: सारांश आणि निष्कर्ष

सध्याच्या प्रबंधाचा निष्कर्ष आणि भविष्यातील संशोधनाची व्याप्ती या प्रकरणामध्ये मांडण्यात आली आहे. अभ्यास केलेल्या गाळाच्या कोरांच्या सर्वसमावेशक रॉक चुंबकीय, खनिज आणि अवसादशास्त्रीय डेटाच्या संचाने बंगालच्या उपसागरातून सागरी वायू हायड्रेट सिस्टमसाठी चुंबकीय खनिज यादी विकसित करण्यास मदत केली. पुराव्याच्या अनेक ओळींनी अभ्यास केलेल्या सेडमेंट कोअर्समधील परिवर्तनीय डायजेनेटिक आणि ऑथिजेनिक प्रक्रियांद्वारे प्रतिबंधित वेगवेगळ्या चुंबकीय खनिजांच्या उत्क्रांतीबद्दल महत्त्वपूर्ण माहिती प्रदान केली. सल्फिडिक आणि मिथेनिक वातावरणातील चुंबकीय कणांचे खनिजशास्त्र, उत्पत्ती आणि संरक्षणाची स्थिती उलगडण्यासाठी केंद्रित इलेक्ट्रॉन सूक्ष्मदर्शकाच्या विश्लेषणासह रॉक मॅग्नेटिक पद्धती वापरण्याची उपयुक्तता या अभ्यासात दर्शविली गेली आहे.

प्रबंधात उद्धृत केलेल्या साहित्याची संदर्भ सूची शेवटी वर्णक्रमानुसार सादर केली आहे.

Chapter 1:
Introduction

1.1. Cold seep and methane hydrates in marine sediments: Occurrence, Distribution, and Controls

Cold seeps are hot spots of hydrocarbon gases, liquids, and sedimentary material which gets released through the seafloor and enters the water column on the passive and convergent continental margins (Linke et al., 2010; Suess, 2014). The first cold seep was discovered in 1983 by Charles Paull and colleagues in the Gulf of Mexico at a water depth of 3200 meters (Paull et al., 1984). Groundwater, brine, and hydrocarbon seeps are the three significant types of cold seeps (Judd and Hovland, 2007). Methane is the most common hydrocarbon gas expulsed through the sediments into the water column at the seep site. Methane emissions at the cold seep are either of biogenic, microbial, or thermogenic origin (Whiticar, 1999). At cold (methane) seeps, the sustenance of unique ecosystem is primarily constrained by the methane and sulphate flux at the sediment-water interface (Sibuet and Olu, 1998; Levin, 2005; Portail et al., 2015). The characteristics of cold seep including lifespan, sediment impact, and biogeochemical environment are highly influenced by the geologic setting (Suess, 2014). Cold seeps occur globally along active plate margins (oceanic and continental plate convergence, oceanic and oceanic plate convergence, and transform plate boundaries), passive continental margins, and transform margins (Figure 1.1). Furthermore, seepage occurs at transform plate boundaries, where the movement of plates is often accompanied by earthquakes, which may trigger the migration of deep fluids (Suess, 2014). Many seepage systems within various geologic settings also occur along passive margins (Figure 1.1; Berndt, 2005; Suess, 2014). Over the years, cold seeps have been discovered not only in oceans, but also found in permafrost settings (You et al., 2019).

Passive continental margins are characterized by the large variety of geological settings, the mechanism of fluid expulsion, and the occurrence of cold seeps worldwide (Figure 1.1). On the continental shelves and slopes, pockmarks represent seep from submerged aquifers, hydrocarbon, and brine-rich formations, or rapidly deposited sediments rich in water. Sediment loading, differential compaction, overpressure, and facies changes are the major driving mechanisms triggering fluid expulsion at passive margins. Rapidly accumulating water-rich sediments produce cold seeps and mud volcanoes in deltas, deep-sea fans, and marginal seas. Change in fluid permeability caused by intersection of faults and fracture in turbidites, sands, silts, drifted

sediments, and even buried reefs allow fluid to escape from the deeper reservoirs and reach the seafloor forming cold seep (Suess, 2014).

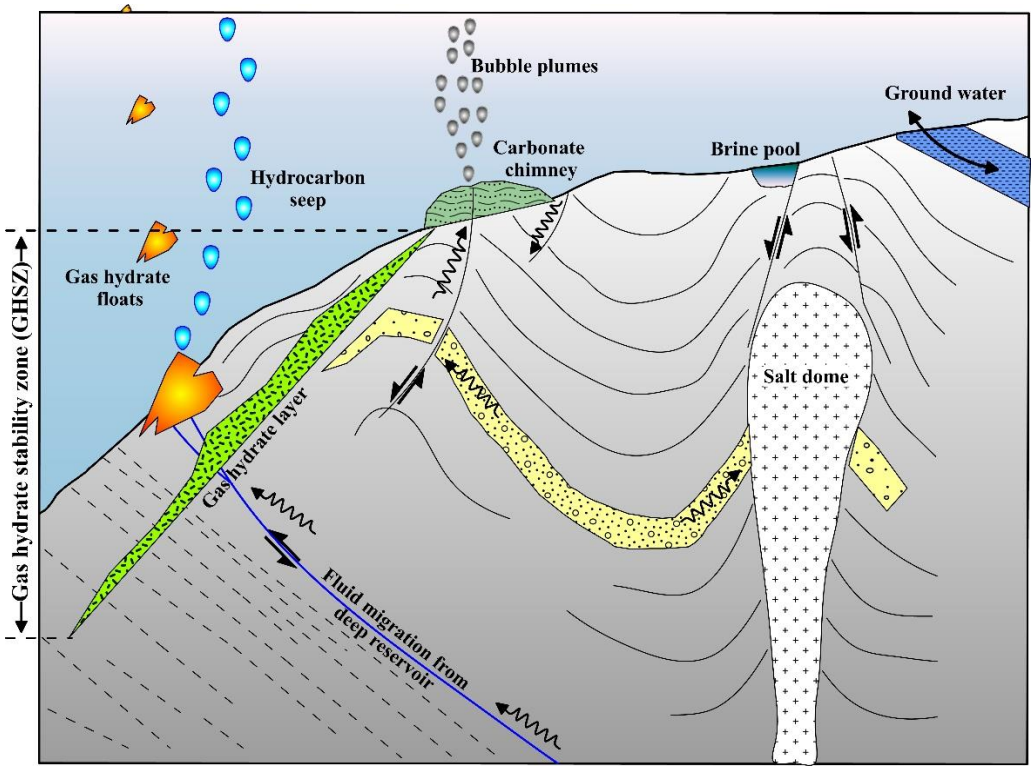

Figure 1.1: *Schematic diagram illustrating the geological settings and the mechanisms of fluid expulsion at cold seeps along the passive continental margin (modified after Suess, 2014).*

Presence of marine cold seeps and associated ecosystems have been reported from many sites around the world (Figure 1.2). Few of the cold seeps recorded from active margin includes Gulf of Izmit (Alpar, 1999), Hikurangi margin (Greinert et al., 2010), Makran accretionary prism (Delisle et al., 2002), Marmara Sea (Bayrakci et al., 2014; Dupr´e et al., 2015), Nankai accretionary wedge (Le Pichon et al., 1987; Henry et al., 2002), Nankai trough (Tsunogai et al., 2012), Oregon subduction zone (Moore et al., 1990; Crutchley et al., 2013), and Southern California (Rudolph and Manga, 2010). In passive margins, some of the examples include Congo basin (Wenau et al., 2018), Gulf of Mexico (Ruppel et al., 2005) Hikurangi margin (Faure et al., 2006), Nile deep-sea fan (Loncke and Mascle, 2004), North Sea (Hovland and Judd, 1988), offshore Oregon (Paull et al., 2002), south-west Barent Sea (Foucher et al., 2010), west Svalbard margin (Plaza-Faverola et al., 2015), and Krishna-Godavari basin, Bay of Bengal (Mazumdar et al., 2019; Dewangan et al., 2020).

Neo-tectonic activities along the continental margins result in the formation of geomorphic structures including shale diapirs, mounds, and faults. Migration of methane through the fault system provides conducive environment for the formation of gas hydrate deposits (Dewangan et al., 2010). Fracture-controlled fluid migration has been well-reported at cold seeps, for example in Vestnesa Ridge (Yao et al., 2019), Harstad Basin, southwest Barents Sea (Vadakkepuliyambatta et al., 2013; Crémière et al., 2018), Hydrate Ridge (Torres et al., 2002; Weinberger and Brown, 2006), Blake Ridge (Egeberg and Dickens, 1999), and Central Chile (Geersen et al., 2016). Faults/fractures facilitate efficient transport of methane-rich fluids from greater depth to shallower depth, and sometimes methane escapes from the sediment-water interface forming gas flares (Berndt et al., 2014; Sahling et al., 2014).

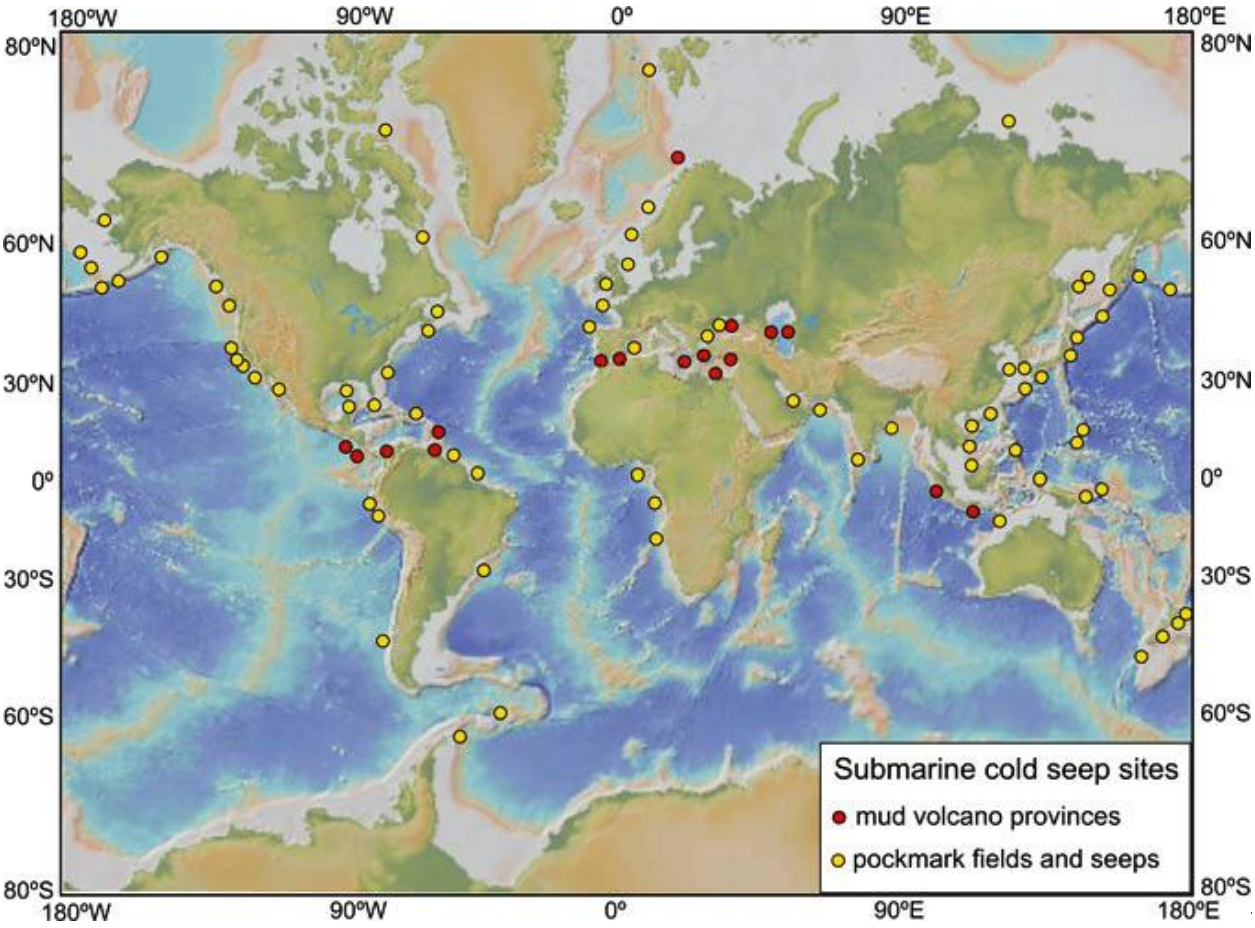

Figure 1.2: *Map showing the global distribution of cold seeps (modified from Milkov 2000; Kopf 2002).*

Gas-hydrates are naturally occurring crystalline, non-stoichiometric substance comprised of a guest molecule, predominantly methane (CH_4), encased within a solid lattice of water molecules (Figure 1.3a; Kvenvolden, 1995; Sloan and Koh, 2007; Boswell and Collett, 2011). Smaller molecules, such as nitrogen (N_2), carbon dioxide (CO_2), hydrogen sulphide (H_2S), ethane (C_2H_6), and propane (C_3H_8) can also occupy water cages as a guest molecule in the structure to form gas-hydrate (Sloan, 2003). Gas-hydrates formed solely from methane are known as methane hydrates or methane clathrates (Figure 1.3) and remains stable at suitable temperature-pressure conditions (Kvenvolden, 1993; Sloan, 1998; Kvenvolden and Lorenson, 2001; Milkov et al., 2003). Methane-hydrates are distributed widely in oceanic and permafrost regions and store large amount of methane gas (Figure 1.4; Kvenvolden, 1993). Geodynamics, tectonism, global climatic change, sea level fluctuations, and variable sedimentation rate can significantly affect the development of gas hydrate systems in marine sediments (Milkov and Sassen, 2002; Herbozo et al., 2013; Moore et al., 2015). For example, neotectonic activity can potentially alter the base of the gas hydrate stability zone, causing dissociation of gas hydrates and consequently intensify methane expulsion/seepage events (Dewangan et al., 2008; Riedel et al., 2011). Rapid sediment loading triggered by abrupt tectono-climatic changes and increased sediment input from major river systems can generate overpressured sedimentary strata, thereby creating an efficient fluid migration system and sedimentary reservoir for trapping of methane and gas hydrate formation (Torres et al., 2008; Yu et al., 2014; Karstens et al., 2018).

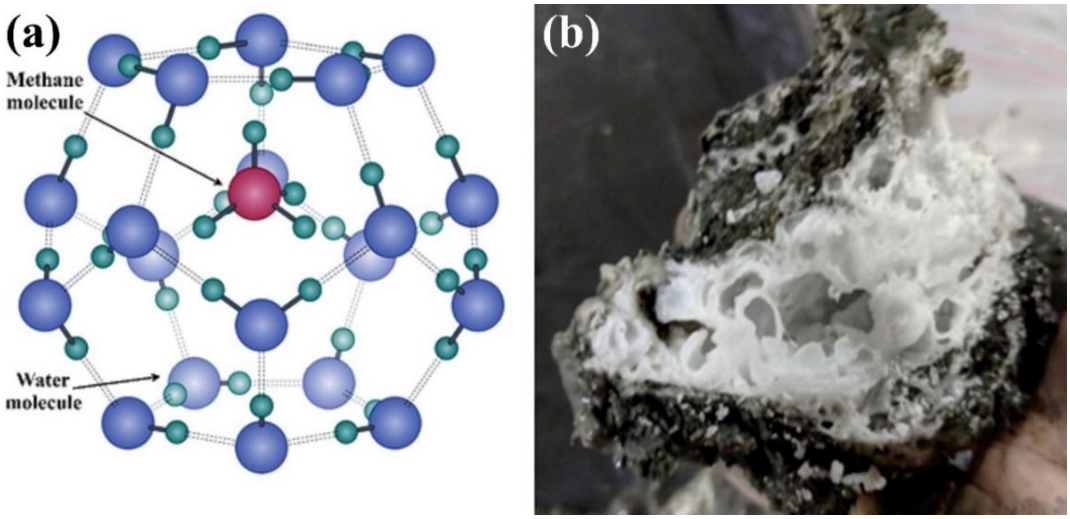

Figure 1.3: (a) *Molecular structure of methane hydrate (b) methane-hydrate recovered from the K-G basin, Bay of Bengal.*

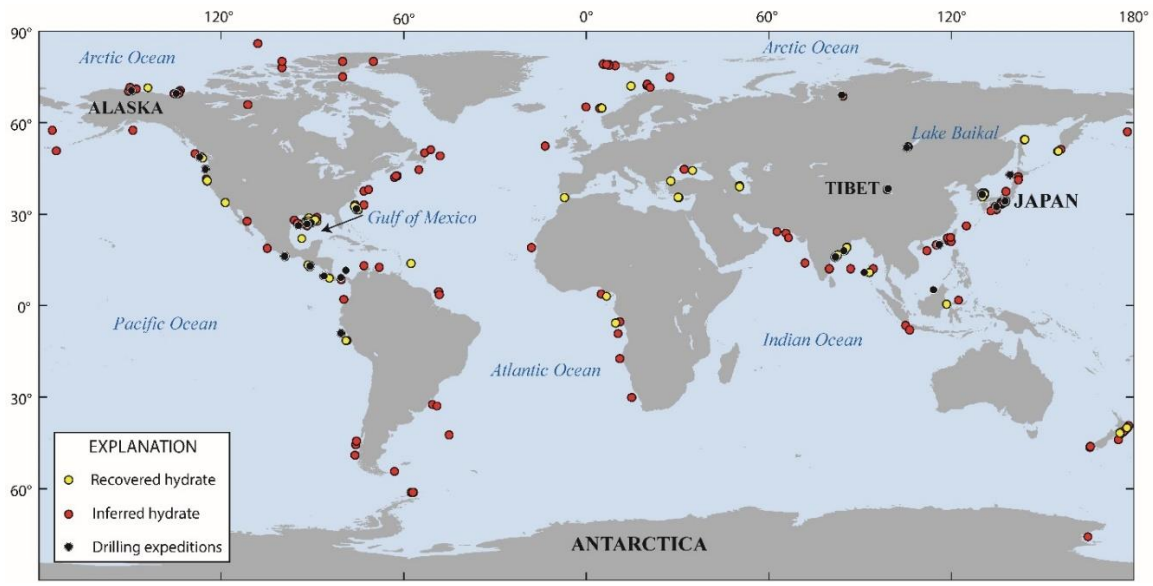

Figure 1.4: *Global map showing the location of inferred and recovered gas hydrates and drilling expeditions completed for gas-hydrate exploration. (Image courtesy: www.usgs.gov).*

1.2. Diagenesis and authigenesis of magnetic minerals in cold seep and methane hydrate-bearing marine sedimentary system

Marine cold-seep system associated with shallow methane-hydrate is a unique ecosystem characterized by ebullition of methane-rich fluids through the seafloor (Suess, 2014). Delineating the changes in the past methane fluxes and gas hydrate (formation/dissociation) and cold seep dynamics, however remains difficult as there are few reliable proxies which endure through geologic time. Magnetic minerals at marine cold (methane) seeps are potential archive of past fluid flow and could provide important constraints on the evolution of paleo-methane seepage dynamics and gas hydrate system through time. At active methane seeps, sulphate-reduction driven by anaerobic oxidation of methane (AOM) releases sufficient amount of hydrogen sulphide into the surrounding pore waters (Jørgensen et al., 2004). The released hydrogen sulphide facilitates dissolution of primary detrital magnetic minerals and transform them into stable non-magnetic pyrite or intermediate ferrimagnetic greigite, thereby inducing secondary magnetic signals in the host sediments which can be easily detected by rock magnetic methods (Housen and Musgrave, 1996; Larrasoaña et al., 2007; Roberts et al., 2015). These magnetic minerals serve as an excellent

geological archive to record the past-methane seepage, and help in understanding the evolution of marine cold seeps and associated shallow/deep gas hydrate system through time.

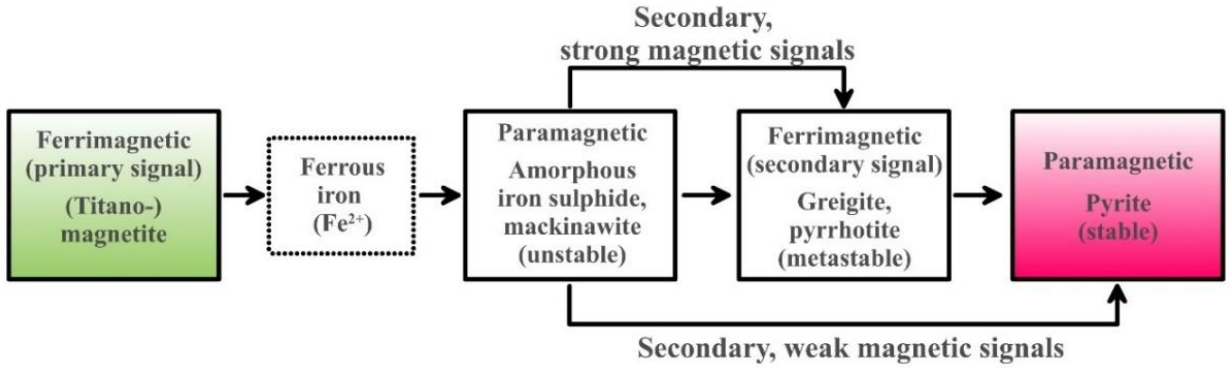

Figure 1.5: *Flow diagram explaining major pathways of the conversion of iron-oxides to iron-sulphides in the anoxic marine environment, (modified from Riedinger, 2005).*

The fluid evicted at cold seeps is enriched in methane, hydrogen sulphide, and bicarbonate resulting in the precipitation of calcium carbonates and pyrite at or below the sediment-water interface. Generally, in marine sediments, organoclastic reduction of sulphate (ORS) accounts for the bulk of the organic matter mineralization through anaerobic pathways, which is represented as:

$$2CH_2O + SO_2^- \rightarrow 2HCO_3^- + H^+ + HS^- \quad \ldots\ldots\ldots\ldots\ldots\ldots (1)$$

The AOM process also controls sulphate-reduction, which can be attributed to a consortia of sulphate-reducing bacteria (SRB) and methane-oxidizing archaea (Borowski et al., 1996; Boetius et al., 2000) and represented as,

$$CH_4 + SO_4^{2-} \rightarrow HCO_3^- + H^- + H_2O \quad \ldots\ldots\ldots\ldots\ldots\ldots (2)$$

The hydrogen sulphide (HS^-) produced by the organo-clastic/AOM coupled sulphate reduction pathways (presented in equation (1) and (2)) react with the magnetic minerals leading to their reductive dissolution (Berner, 1970; Poulton et al., 2004),

$$Fe_2O_3 + HS^- + 5H^+ \rightarrow 2Fe^{2+} + S^0 + 3H_2O \quad \ldots\ldots\ldots\ldots\ldots\ldots (3)$$

$$Fe_3O_4 + HS^- + 7H^+ \rightarrow 3Fe^{2+} + S^0 + 4H_2O \quad \ldots\ldots\ldots\ldots\ldots\ldots (4)$$

The dissolved ferrous iron ($Fe2^{+}$) further reacts with hydrogen sulphide (HS^{-}) to form iron monosulphide (FeS),

$$Fe^{2+} + HS^{-} \rightarrow Fes_{(s)} + H^{+} \text{ …….. (5)}$$

A mechanism for the conversion of iron monosulphide to pyrite with metastable greigite was proposed by Sweeney and Kaplan (1973) and can be represented as:

$$3FeS + S^{0} \rightarrow Fe_3S_4 + 2S^{0} \rightarrow 3FeS_2 \text{ …….. (6)}$$

The geochemical reactions presented above plays a crucial role in the diagenesis and authigenesis of magnetic minerals in methanic and sulphidic environment. The diagenetic process releases dissolved manganese (Mn^{2+}), iron (Fe^{2+}), hydrogen sulphide (H_2S), and methane (CH_4) into the pore waters which provide suitable reactants for authigenesis of minerals. In the geological record, authigenic magnetic minerals indicate past diagenetic conditions (Berner, 1981). Oxic respiration, denitrification, manganese reduction, iron reduction, sulphate reduction, and methanogenesis are important reactions which takes place during organic matter remineralization and produce three major diagenetic zones (Figure 1.6).

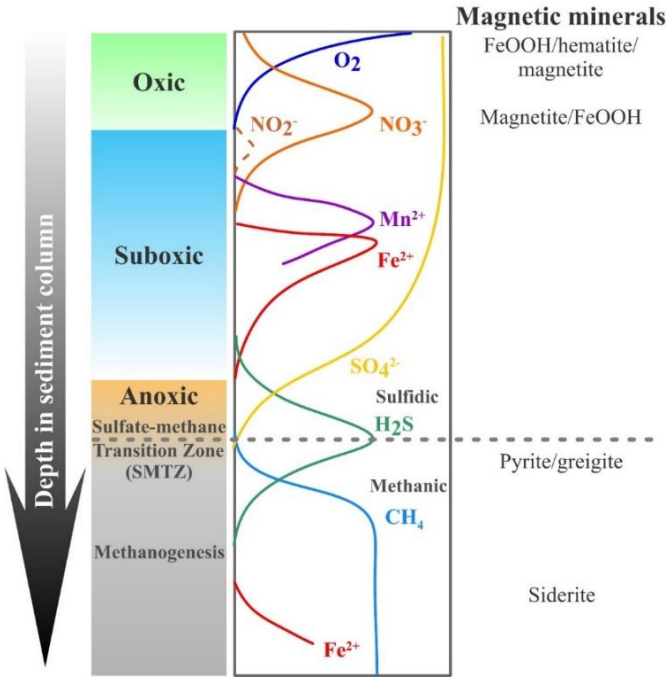

Figure 1.6: *Schematic diagram summarizing biogeochemical zones in marine sediment column (modified from Berner (1981), Canfield and Thamdrup (2009), and Jørgensen and Kasten (2006).*

The diagenetic zones produced by the above-mentioned reactions have been explained below: (i) oxic zone: the upper sediment layer in which organic matter respiration occurs under the presence of measurable concentrations of oxygen and the terminal electron acceptor linked with organic matter degradation is oxygen; (ii) suboxic zone: the intermediate region in which neither oxygen nor dissolved sulphide are present in measurable concentrations. In the same zone, nitrate, manganese, and iron gets successively reduced, and (iii) anoxic: the lowermost region, where oxygen is strictly excluded and is often sub-demarcated into an upper sulphidic zone and a lower methanic zone wherein pore-water sulphide concentrations have been reduced to zero (Froelich et al., 1979).

1.3. Application of rock magnetism in gas (methane) hydrate studies

Magnetic minerals are ubiquitous and originate from diverse sources including terrestrial, atmospheric, lacustrine as well as an extraterrestrial (cosmic flux) and submarine (lithogenic, biogenic, diagenetic, and authigenic) sources (Figure 1.7; Thompson and Oldfield, 1986). Magnetite minerals are potentially useful tracers of geological and methane-related geochemical processes and can provide crucial information on the methane seepage dynamics and diagenetic/authigenic processes in marine gas-hydrate sedimentary systems (Musgrave et al., 2006; Larrasoaña et al., 2007; Roberts, 2015; Badesab et al., 2019). The significant advantages of employing rock magnetic techniques include the non-destructive nature, relatively rapid measurements and the applicability to a wide range of materials.

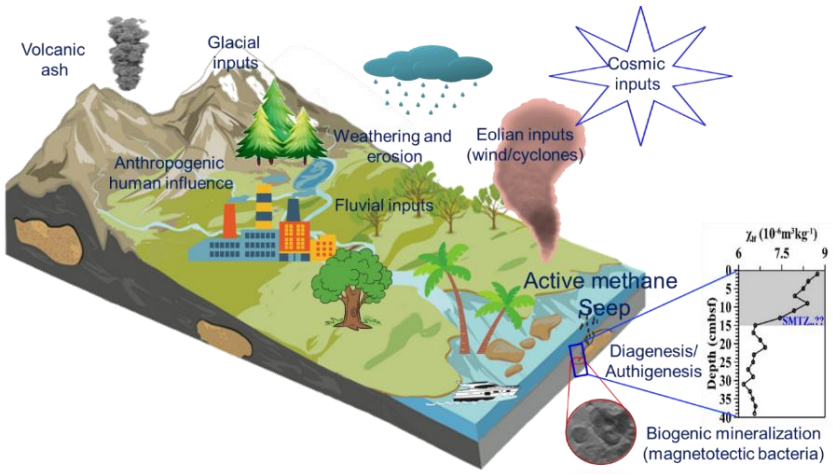

Figure 1.7: *Schematic diagram illustrating the transport modes of magnetic minerals from different sources of marine sediments. (Modified after Frederichs et al., 1999).*

In cold seep and methane-hydrate bearing sedimentary systems, AOM is an important biogeochemical process that results from the interaction of upward methane flux and downward sulphate flux (Treude et al., 2005; Knittel and Boetius, 2009). Geochemical processes linked with fluid (methane) migration, gas hydrate formation/dissociation favor the growth of iron sulphides which induce a distinct magnetic signature in the host sediments and can be easily detected using rock magnetic methods (Esteban et al., 2008). For example, sulphate-reduction driven by anaerobic oxidation of methane (AOM) generates hydrogen sulfide in the pore water via bacterial activities (Canfield and Berner 1987). In terms of concentration, grain size, and mineralogy, magnetic methods complemented by XRD, SEM and TEM analyses can precisely characterize the detrital, diagenetic, authigenic, and biogenic magnetic minerals (Esteban et al., 2008). The linkage between rock magnetism, mineralogy, pore-water geochemistry, and methane-related magnetic mineral diagenesis and authigenesis has been well-established (Roberts, 2015). Authigenic formation of ferrimagnetic (greigite, magnetite) and non-magnetic (pyrite) iron sulfides in the methanic sediments are influenced by the history of fluid sequence and gas hydrate dynamics (Dewangan et al., 2013; Kars and Kodama, 2015; Roberts, 2015; Badesab et al., 2020). Previous rock magnetic studies dealing with magnetic mineral diagenesis in methanic and gas hydrate bearing sediments has established the linkage between methane-related geochemical and microbial processes and sediment magnetism. For example, in Mackenzie Delta, Canada (Enkin et al., 2007), Mediterranean continental shelf (Amiel et al., 2020), Northwestern Weddell Sea (Reilly et al., 2020), South China Sea (Lin et al., 2021), Hikurangi Margin, New Zealand (Greve et al., 2021; Kars et al., 2021), Izu-Bonin rear arc (Musgrave et al., 2019), Nankai Trough (Kars and Kodama, 2015; Shi et al., 2017) and offshore Shimokita Peninsula (Phillips et al., 2017) Japan, offshore Taiwan (Horng, 2018), Cascadia Margin (Musgrave et al., 2006; Larrasoaña et al., 2007), Arctic Vestnesa Ridge, offshore western Svalbard (Johnson et al., 2014), West Siberian Sea (Rudmin et al., 2018), and offshore Taiwan (Horng, 2018).

1.4 Authigenic seep carbonates: Potential archives of fluid flow

Microbially-mediated sulphate driven AOM produces vast amount of methane in sediments along continental margins. AOM is the important process at cold (methane) seeps and mediated by a joint microbial consortium comprised of anaerobic methane-oxidizing archaea and sulphate-reducing bacteria (Boetius et al., 2000; Hinrichs and Boetius, 2002).

$$CH_4 + SO_4^{2-} \rightarrow HCO_3^- + H^- + H_2O \ldots\ldots \text{(AOM)}$$

Bicarbonates generated during AOM process leads to enhancement in pore water alkalinity, resulting in the precipitation of seep-related methane derived authigenic carbonates (Aloisi et al., 2000; Teichert et al., 2014).

$$2HCO_3\text{-} + Ca^{2+} \leftrightarrow CaCO_3 + CO_2 + H_2O \text{ (carbonate precipitation)}$$

Occurrence of active methane seep are often associated with shallow and deep-seated methane hydrates and presence of methane-derived authigenic carbonates (Figure 1.8) and has been well documented worldwide. Hence, the authigenically formed carbonates are considered as potential archives of fluid flow (Bohrmann et al., 1998; Feng and Chen, 2015).

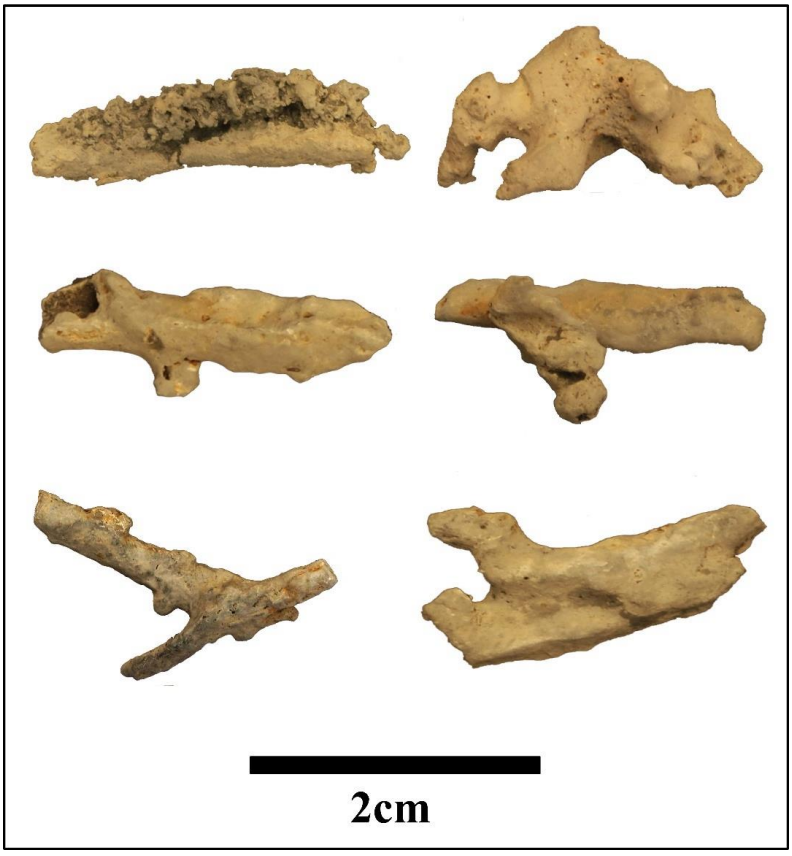

Figure 1.8: *Photographs showing methane-derived authigenic carbonates found in an active methane seep sites from the K-G basin, Bay of Bengal.*

1.5. Motivation and objectives

The K-G basin is characterized by a highly dynamic depositional (high sedimentation rates, shale-tectonism, active cold seeps, shallow, and deep-seated gas hydrates) conditions and represents a suitable sedimentary environment to study geological and geochemical controls on the magnetic mineral diagenesis and authigenesis. Gas hydrate exploration cruise of CSIR-National Institute of Oceanography (CSIR-NIO) in 2018 onboard R/V Sindhu Sadhana discovered the presence of active seep associated with shallow gas hydrate deposits from the K-G basin, Bay of Bengal (Mazumdar et al., 2019). The active seep site manifested by the shallow methane hydrate is characterized by the gas flares, higher methane flux in the water column and presence of living chemosynthetic community at the seafloor, increased concentration of hydrogen sulphide and methane-derived authigenic carbonates on the sea floor and throughout the sediment core (Mazumdar et al., 2019; Dewangan et al., 2020). As a part of first Indian National Gas Hydrate Program (NGHP-01), drilling and coring activities onboard D/V JOIDES Resolution in 2005 marked the discovery of fracture-filled gas hydrates in the K-G basin. Two long-drilled cores (NGHP-01-15A, NGHP-01-20A) were retrieved from the potential gas hydrate bearing sites in the K-G basin during NGHP-01.

Magnetic minerals at marine cold (methane) seep sites and sub-surface sediments are potential archive of past fluid flow and provide important constraints on the evolution of past methane seepage dynamics, gas hydrate formation, and diagenetic and authigenic processes over geologic time (Musgrave et al., 2006; Larrasoaña et al., 2007; Kars and Kodama, 2015; Roberts, 2015; Badesab et al., 2019). Past rock magnetic studies on sediment cores overlying the gas hydrate deposits in the K-G basin mainly focussed on delineating the magnetic signatures of detrital and diagenetic processes associated with evolution of gas-hydrate system (Dewangan et al., 2013; Badesab et al., 2017), exploring linkages between magnetic iron sulfides and gas hydrates (Housen and Musgrave, 1996; Kars and Kodama, 2015), deciphering controls on gas hydrate system evolution (Badesab et al., 2017), rock magnetic properties of gas hydrate bearing sediments (Kars and Kodama, 2015), and developing proxies for tracking paleomethane seepage events (Novosel et al., 2005; Panieri et al., 2016), and paleo sulfate-methane transition zone (SMTZ) boundaries (Johnson et al., 2014; Peketi et al., 2012). Despite of extensive rock magnetic research focussing on understanding magnetic mineral diagenesis in the marine gas hydrate sedimentary system, there was no dedicated rock magnetic study which (a) elucidated how magnetic minerals selectively respond to a range of diagenetic processes in the sulphidic and methanic environments

respectively, and (b) compared the diagenetic processes at two different (shallow versus deep-seated) marine gas hydrate systems in the K-G basin.

The K-G basin represents an ideal natural laboratory to undertake the rock magnetic focussing on diagenesis and authigenesis of magnetic minerals research in the methanic sediments as the basin hosts presence of abundant methane, active and paleo-cold seeps linked with shallow and deep-seated methane hydrates, and presence of chemosynthetic ecosystem, seismic chimneys for efficient transport of fluids/gas from deep-seated gas reservoirs, and high concentration of hydrogen sulfides needed for magnetic mineral diagenesis/authigenesis. The present study focusses on establishing a magnetic mineral inventory of the sediments at active/relict methane seep sites and sub-surface gas hydrate deposits and understand the methane-related diagenetic and authigenic processes at active seep, shallow and deep-seated gas-hydrate systems from the K-G basin, Bay of Bengal. Rock magnetic methods complemented by mineralogical, sedimentological and petrological analyses were employed on the sediments cores from cold (active, relict) seep (SPC-01 to SPC-06; Stn-11/GC-02; Table. 2.1) and methane-hydrate (shallow and deep-seated; SSD-45/Stn-4/GC-01; NGHP-01-15A; NGHP-01-20A; Table. 2.1) sites from the K-G basin, Bay of Bengal to accomplish the following objectives:

1. Unravel the magnetic mineral assemblages in methane hydrate-bearing cold seep system from the Krishna-Godavari basin, Bay of Bengal.

2. Comparative diagenetic analysis of shallow and deep-seated marine gas-hydrates system from the Bay of Bengal.

Sr. No.	Magnetic parameters	Units	Applications	References
1.	Low field magnetic susceptibility χ_{lf}	S.I or m^3/kg	Concentration of strongly magnetic iron oxides (for example: magnetite, maghemite, titanomagnetite)	Hunt, et al. (1995); Walden et al. (1999)
2.	Frequency dependent magnetic susceptibility (χ_{fd})	%	Concentration of superparamagnetic (SP) particles (for example: magnetite, greigite, maghemite)	Eyre, (1997); Worm 1998)
3.	Anhysteretic remanent magnetization (ARM)	Am^2/kg	High values indicate higher concentration of magnetically stable single domain (SD) magnetite/maghemite grains	Maher, (1988); Dunlop and Özdemir (1997); Egli and Lowrie, (2002)
4.	Saturation isothermal remanent magnetization (SIRM)	Am^2/kg	Concentration of remanence carrying fraction of the magnetic minerals	Thompson and Oldfield (1986); Peters and Dekkers (2003)
5.	SIRM/χ_{lf}	A/m	Magnetic grain size proxy for ferrimagnetic iron sulphide (greigite, pyrrhotite). High SIRM/χ_{lf} values indicate the presence of smaller (SD) grains	Thompson and Oldfield (1986); Peters and Dekkers (2003); Kars and Kodama, 2015
6.	ARM/SIRM	Dimensionless	Magnetic grain size proxy for ferrimagnetic iron oxides (magnetite, titanomagnetite, maghemite). High ARM/SIRM values suggest finer size magnetic grains	Peters and Dekkers, 2003; Liu et al., 2012; Lin et al., 2020
7.	S-ratio	Dimensionless	Relative contribution of magnetically soft to hard remanence carrying mineral phases.	Thompson and Oldfield (1986); Peters and Dekkers (2003)
8.	Temperature dependant magnetic susceptibility (χ-*T*)	°C	Determination of magnetic mineralogy diagnostic "Curie Temperature"	Dunlop et al., 1997

9.	Low-temperature magnetometry	K	Determination of magnetic mineralogy diagnostic Curie, Verwey, Neel, and Besnus transition	Tarduno, 1995; Passier and Dekkers, 2002
10.	First order reversal curves (FORC) diagram	T	Magnetic mineralogy and their domain states.	Roberts et al., 2000

Table 1.1: *Summary of rock magnetic parameters, their units, and application (modified from Jordanova et al., 2016).*

Chapter 2:
Methodology

2.1. Study area and location of sediment cores

The study area lies on the continental slope of the Krishna-Godavari (K-G) basin, Bay of Bengal (Figure 1), which is a proven petroliferous basin of India (Bastia, 2007). The K-G basin is a pericratonic rift basin situated in the central eastern continental margin of India. Sediment thicknesses of 3–5 km in the onshore region and about 8 km in the offshore region have been reported (Bastia, 2007*;* Prabhakar and Zutshi, 1993). The Krishna and Godavari river systems deliver most of the sediment to this basin. Holocene-Pleistocene sedimentary deposits in the K-G basin are dominated by smectite-bearing Godavari clay formations (Rao, 2001). The estimated annual sediment transport of the Krishna and Godavari rivers is around 67.7 and 170 × 106 t, respectively (Biksham and Subramanian, 1988; Ramesh and Subramanian, 1988). The presence of cold seep (active, relict, paleo) and subsurface gas hydrate (shallow, deep-seated) deposits in the K-G basin has been confirmed through drilling and sediment coring (Collett et al., 2008; Mazumdar et al., 2009, 2019; Dewangan et al., 2020). Neotectonic activity in the K-G basin led to the formation of different types of geomorphic structures on the sea floor, including shale diapirs, faults, and mounds. The fault systems associated with bathymetric mounds facilitate fluid/gas migration and provide favorable sedimentary structures for the formation of cold seep and gas hydrates in the K-G basin (Dewangan et al., 2010).

Gas hydrate exploration cruise of CSIR-National Institute of Oceanography (CSIR-NIO) in 2018 onboard R/V Sindhu Sadhana discovered the presence of active seep associated with shallow gas hydrate deposits from the K-G basin, Bay of Bengal (Mazumdar et al., 2019). The active seep site manifested by the shallow methane hydrate is characterized by the gas flares, higher methane flux in the water column and presence of living chemosynthetic community at the seafloor and methane-derived authigenic carbonates throughout the sediment core (Mazumdar et al., 2019; Dewangan et al., 2020). As a part of first Indian National Gas Hydrate Program (NGHP-01), drilling and coring activities onboard D/V JOIDES Resolution in 2005 marked the discovery of fracture-filled gas hydrates in the K-G basin (Collet et al., 2008). The sediment cores analyzed in the present study were collected from active, relict, paleo cold seep and potential gas hydrate bearing (shallow and deep-seated) sites from the K-G basin, Bay of Bengal (Figure 2.1). The sediment cores are located at the edge of the sedimentary ridge.

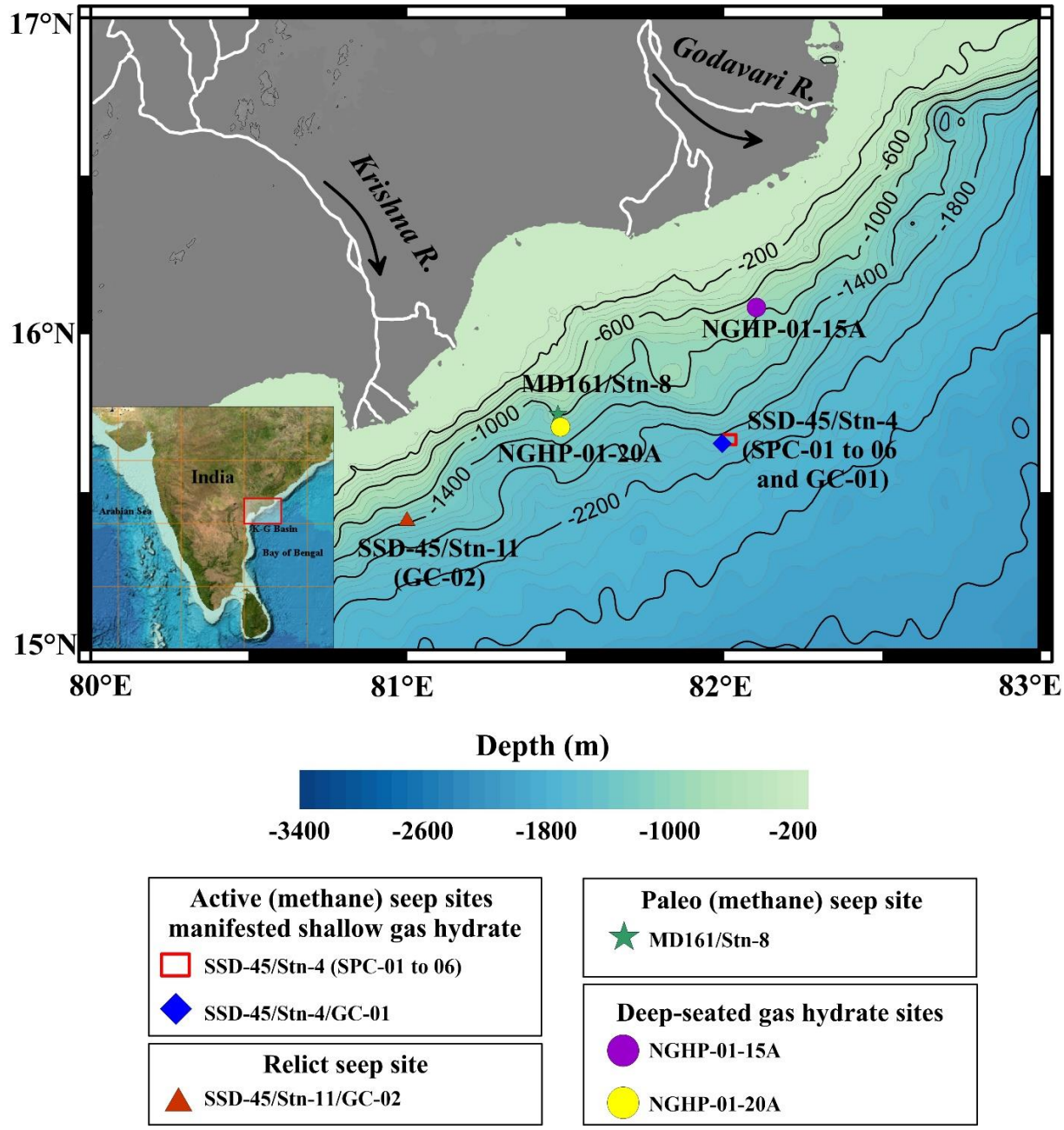

Figure 2.1: *Location of sediment cores in the Krishna-Godavari (K-G) basin, Bay of Bengal. Bathymetry data of the studied area was obtained from GEBCO Compilation Group 665 (2020) GEBCO 2020 Grid (10.5285/a29c5465-b138-234d-e053-6c86abc040b9). Please note that following abbreviations: SSD-045 = cruise no. R/V Sindhu Sadhana - 045, SPC= Spade core, GC= Gravity core, MD161= cruise no. R/V Marion Dufresne - 161, NGHP-01= National Gas Hydrate Program expedition-01 onboard D/V JOIDES Resolution.*

2.2. Geological setting

The Krishna-Godavari (K-G) basin is situated in the central Eastern Continental Margin of India (ECMI) (Figure 2.2). The Krishna-Godavari rivers originate in the Western Ghats and drain through Late Cretaceous Deccan basalt (DcB), Dharwar, and Bastar cratons of Archean Proterozoic peninsular gneissic complexes (APGC), Gondwana rocks of the Godavari graben and

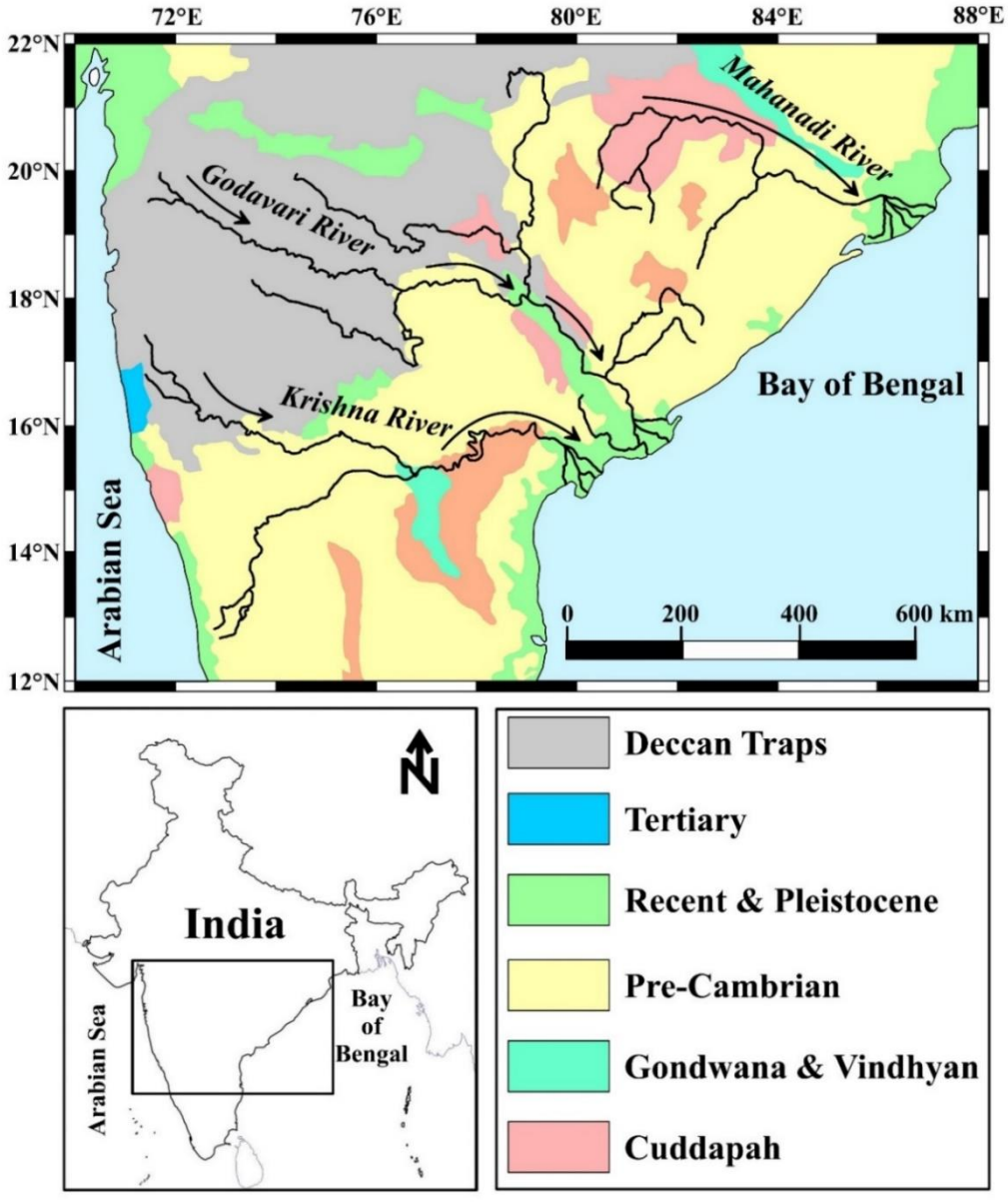

Figure 2.2: *Geological map showing the lithology of Krishna and Godavari River drainage basin (modified after Badesab et al., 2021).*

the Eastern Ghats belt. These formations contain rocks rich in magnetic minerals (for example, mafic volcanic, Fe-rich schists, and iron formations) and are a potential source of detrital magnetic minerals to the K-G basin (Biksham and Subramanian, 1988; Mukhopadhyay et al., 2010; Mazumdar et al., 2015). The stratigraphy of the K-G basin generally covers the sediments from the Early Cretaceous to Recent (Rao, 1993). Raghavpuram shales containing organic-rich sediments overlain by a sequence of interbedded sand and shale were deposited during the Early Cretaceous. Subsequently, Chintalapalu shale were deposited in the Late Cretaceous, followed by the Paleocene-Eocene argillaceous facies. The Ravva formation containing interbedded sand and shale were deposited during the Miocene-Pliocene. The youngest Godavari clay (youngest stratigraphic unit) was formed during the Quaternary Period. The sediments are composed of a majority of montmorillonite along with a minor amount of illite and kaolinite clay (Rao, 1991).

2.3. Sampling of sediment cores (spade, gravity, drilled)

The sediment samples used in this study were collected from the K-G basin using spade and gravity coring techniques during a dedicated gas-hydrate exploration cruise (SSD-45) of CSIR-NIO onboard R/V Sindhu Sadhana in 2018. Drilled sediment cores were retrieved during the first Indian National Gas Hydrate Expedition in 2005 (NGHP, Exp-01; Collett et al., 2008) onboard D/V JOIDES Resolution from the K-G basin. In this study, total of six short spade cores, two gravity cores, and two long drilled sediment cores (Figure 2.1; Table 2.1) representing cold (active, relict, paleo) seep sites were utilized for the detailed rock magnetic, mineralogical, sedimentological, microscopic, and petrographical analyses. Six short spade cores (SPC-01 to SPC-06) and one gravity core (GC-01) were retrieved from the active seep site (SSD-45/Stn-4) and one gravity core (Stn-11/GC-02) from the relict seep site from the K-G basin (Figure 2.1). The detailed information on the sediment cores is provided in Table 2.1. Magnetic samples were taken onboard immediately after the collection of pore water samples to minimize sediment alteration due to warmer temperatures and oxygen exposure. The sediment cores were sub-sampled in the presence of high purity nitrogen flushing to minimize the exposure of samples to atmospheric conditions, which could oxidize hydrogen sulphide or iron mono-sulphide. Samples for magnetic

analysis were collected by pushing non-magnetic plastic bottles into the split halves at ~ 2 cm intervals. After sub-sampling, magnetic samples were transferred to a cold room (4°C) for storage.

Two long drilled sediment cores NGHP-01-15A (196.45 m) and NGHP-01-20A (148.8 m) were retrieved onboard DV JOIDES Resolution at the water depth of 926 m and 1146 m respectively from the K-G basin, Bay of Bengal (Figure 2.1; Table 2.1). The sediment cores were sub-sampled at intervals of 1.5 – 6 m on every 9.6 m long section onboard. The sub-samples were later transported and stored in the cold storage facility of CSIR-National Institute of Oceanography (NIO), Goa, India at ~5–6°C. The sub-sampled bulk sediments were dried, weighed, and packed in the 25 mm plastic (non-magnetic) sample bottles for the rock magnetic measurements. Rock magnetic measurements were carried out on sediment samples at the Paleomagnetic Laboratory of CSIR-NIO. Specialized magnetic measurements were conducted at the Center for Advanced Marine Core Research (CMCR), Kochi University, Japan.

Marine System	**Core No.**	**Type of coring operation**	**Expedition/ Cruise No.**	**Research Vessel**	**Water Depth (m)**	**Core recovery (m)**
Active methane seep sites + shallow gas hydrates	SSD-045 Stn-4 SPC-01	Spade core	SSD-045	R/V Sindhu Sadhana	1755.0	0.30
	SSD-045 Stn-4 SPC-02	Spade core	SSD-045	R/V Sindhu Sadhana	1756.5	0.43
	SSD-045 Stn-4 SPC-03	Spade core	SSD-045	R/V Sindhu Sadhana	1754.0	0.40
	SSD-045 Stn-4 SPC-04	Spade core	SSD-045	R/V Sindhu Sadhana	1756.4	0.25
	SSD-045 Stn-4 SPC-05	Spade core	SSD-045	R/V Sindhu Sadhana	1750.0	0.20
	SSD-045 Stn-4 SPC-06	Spade core	SSD-045	R/V Sindhu Sadhana	1754.0	0.25
	SSD-045 Stn-4 GC-01	Gravity core	SSD-045	R/V Sindhu Sadhana	1803.0	2.23
Relict methane seep site	SSD-045 Stn-11 GC-02	Gravity core	SSD-045	R/V Sindhu Sadhana	1354.0	0.63
Paleo cold seep site	MD161/Stn-8	Piston core	MD161	R/V Marion Dufresne	1033.0	30.05
Deep-seated gas hydrate sites	NGHP-01-15A	Drilled core	NGHP-Exp. 01	D/V JOIDES-Resolution	926.0	196.45
	NGHP-01-20A	Drilled core	NGHP-Exp. 01	D/V JOIDES-Resolution	1146.0	148.8

Table 2.1: *Detailed information on spade, gravity, piston, and drilled sediment cores retrieved from an active seep, relict seep, paleo cold seep, shallow and deep-seated gas-hydrate sites from the Krishna-Godavari (K-G) basin, Bay of Bengal.*

2.4. Analytical techniques

2.4.1. Frequency-dependent magnetic susceptibility measurements

Magnetic susceptibility (χ) is one of the most widely used magnetic parameter to address a range of geoscientific questions (Verosub and Roberts, 1995; Liu et al., 2012). It measures the response of magnetic material to the applied magnetic field. It indicates the quantitative estimates of the concentration of magnetic minerals in the rocks, sediments, soil, and dust samples. The magnetic susceptibility was measured at low (lf) and high (hf) frequencies χ_{lf} = 0.47 kHz and χ_{hf} = 4.7 kHz respectively. Low-field magnetic susceptibility measurements on sediment samples were carried out using a Bartington Instruments MS2B dual-frequency susceptibility meter (Figure 2.3). Mass-specific magnetic susceptibilities values of χ_{lf} and χ_{hf} were normalized by the weight of the sample. The frequency-dependent susceptibility was calculated by using the formulae: $\chi fd\,\% = \frac{(\chi lf - \chi hf)}{\chi lf} X100$

Figure 2.3: *Bartington MS2B dual frequency magnetic susceptibility meter housed at Paleomagnetic laboratory CSIR-NIO, Goa, India.*

2.4.2. Rock magnetic measurements

Rock magnetic measurements were carried out on sediment samples at the Paleomagnetic Laboratory of CSIR-NIO, Goa, India. All remanent magnetizations were measured using an AGICO JR-6A automatic spinner magnetometer (Figure 2.4). In terms of remanent magnetization, the JR-6A spinner magnetometer is the most sensitive and accurate instrument. Samples are inserted manually in the JR-6A sample holder for measuring the remanent magnetizations. It has both manual and automatic settings for changing the sample positions. Inside a pair of coils is the pick-up unit, a specimen of defined size and shape that rotates at a constant angular speed. The coils induce an AC voltage whose magnitude and phase depend on the magnitude and direction of the remanent magnetization (RM) vector of the specimen and the voltage is amplified, filtered, and digitized. The computer calculates two rectangular components of the projection of the RM vector into a plane perpendicular to the rotation axis using harmonic analysis.

Figure 2.4: *AGICO JR-6A spinner magnetometer housed at Paleomagnetic laboratory CSIR-NIO, Goa, India.*

An anhysteretic remanent magnetization (ARM) was measured by using a Molspin AF demagnetizer (Figure 2.5). ARM was imparted using a 100 mT alternating magnetic field superimposed on a fixed direct current (DC) bias field of 50 μT. The ARM value was then mass normalized by dividing the weight of the sample. An isothermal remanent magnetization (IRM)

was applied in an inducing field of +1T, +2T, and +2.5T in the forward direction and was further demagnetized by applying DC backfields at −20, −30, −100, and −300 mT using an MMPM10 pulse magnetizer (Figure 2.6). Mass-normalized IRM acquired at a peak field of 2.5T was considered as the saturation IRM (SIRM). S-ratio was calculated as the ratio between the IRM at −300 mT and SIRM (Thompson and Oldfield 1986). The S-ratio was calculated by using the formulae-

$$S - \text{ratio} = \frac{\text{IRM} - 300\text{mT}}{\text{SIRM}}$$

Figure 2.5: *Molspin Alternating Field (AF)-Demagnetizer with p-ARM attachment housed at Paleomagnetic laboratory CSIR-NIO, Goa, India.*

Figure 2.6: *Magnetic Measurements Pulse magnetizer (MMPM 10) housed at Paleomagnetic laboratory CSIR-NIO, Goa, India.*

2.4.3. Specialized magnetic measurements

2.4.3.1. Thermomagnetic analyses

Specialized rock magnetic measurements were carried out on the dried sediment samples at the Center for Advanced Marine Core Research (CMCR), Kochi University, Japan. Thermomagnetic analyses were conducted on a Natsuhara Giken (Model NMB-89) magnetic balance (Figure 2.7). Samples were heated from room temperature to 700°C with a heating rate of 10°C/min in a 0.3-T field at the Paleo and Rock Magnetism Laboratory of CMCR. Thermomagnetic curves (k-T curves) were used to determine the mineralogy of the sample by the standard Curie temperature (T_C) of the magnetic minerals. In thermomagnetic analysis, a magnetic dipole moment in a zero or applied field was sensitively measured as a function of temperature. Temperature dependence is necessary for a correct interpretation of magnetic moments and anisotropy energies. In general, temperature dependences are derived from bulk magnetic properties. However, the magnetic properties of small particles are strongly affected by surface effects related to low-temperature oxidation, reduced spin coordination, and interactions with molecules surrounding them (Egli, 2009).

Figure 2.7: *Natsuhara Giken (Model NMB-89) magnetic balance housed at Paleo and Rock Magnetism Laboratory of CMCR, Kochi, Japan.*

2.4.3.2. First-order reversal curves (FORC) measurements

Magnetic hysteresis loops, first-order reversal curves (FORC), and back-field demagnetization curves were measured by Vibrating Sample Magnetometer (VSM) at Paleo and Rock Magnetism Laboratory of CMCR (Figure 2.8). A saturating field of 1T, field increment of 4 mT, slew rate limit of 1 T/s, and averaging time of 200 ms at the CMCR. Processing of FORC diagrams was done using the FORCinel software (smoothing factor (SF) = 4 – 5; Harrison and Feinberg, 2008). FORC diagrams provided useful insights into the characterization of coercivities, domain states, magnetostatic interactions, and the type of magnetic minerals (Egli et al., 2006; Pike et al., 1999; Roberts et al., 2000, 2014).

Figure 2.8: *Vibrating Sample Magnetometer (VSM) housed at Paleo and Rock Magnetism Laboratory of CMCR, Kochi, Japan.*

2.4.3.3. Low-temperature magnetometry

Low-temperature magnetic measurements of the sediment samples were conducted using Quantum Design Magnetic Properties Measurement System (MPMS) at CMCR (Figure 2.9). A room temperature SIRM (RT-SIRM) was applied at room temperature (300 K) in a 2.5 T. Samples were further cooled to 5 K and warmed back again to 300 K in a zero magnetic field. An LT-SIRM was then imparted at 5 K in 2.5 T. Samples were further warmed up to 300 K in a zero magnetic field ("ZFC" for zero field-cooled). Samples were then cooled to 5 K in the presence of a 2.5 T magnetic field. An LT-SIRM was again induced at 5 K, and samples were warmed to 300 K in a zero magnetic field (FC= for field-cooled). The low-temperature magnetic measurements contributed to a better understanding of the magnetic domain states and mineralogy. The typical Verwey transition (Tv) is a low-temperature phase widely used to determine the presence of magnetite in the sample. In low-temperature SIRM warming curves, the presence of monoclinic pyrrhotite is indicated by the Besnus magnetic transition at ~34 K.

Figure 2.9: *Magnetic Property Measurement System (MPMS) housed at Paleo and Rock Magnetism Laboratory of CMCR, Kochi, Japan.*

2.4.4. Magnetic mineral extraction

Magnetic particles were extracted from the bulk sediment samples using a magnetic mineral extraction method developed by Petersen et al. (1986). The sediment was dispersed with sodium hexa-meta phosphate and the sediment slurry was poured into a magnetic extraction unit and circulated continuously for 24 hours with the help of a peristaltic pump. The magnetic particles got attracted to the magnetic probe during the continuous circulation of the sediment and the extracted magnetic minerals were collected and washed with distilled water. To prevent the oxidation, the extracted magnetic particles were placed in to the vacuum desiccator prior to drying in the hot air oven. These dried magnetic particles from the different sediment intervals were further used for the x-ray diffraction (XRD), scanning electron microscope (SEM), and transmission electron microscopy (TEM) analyses.

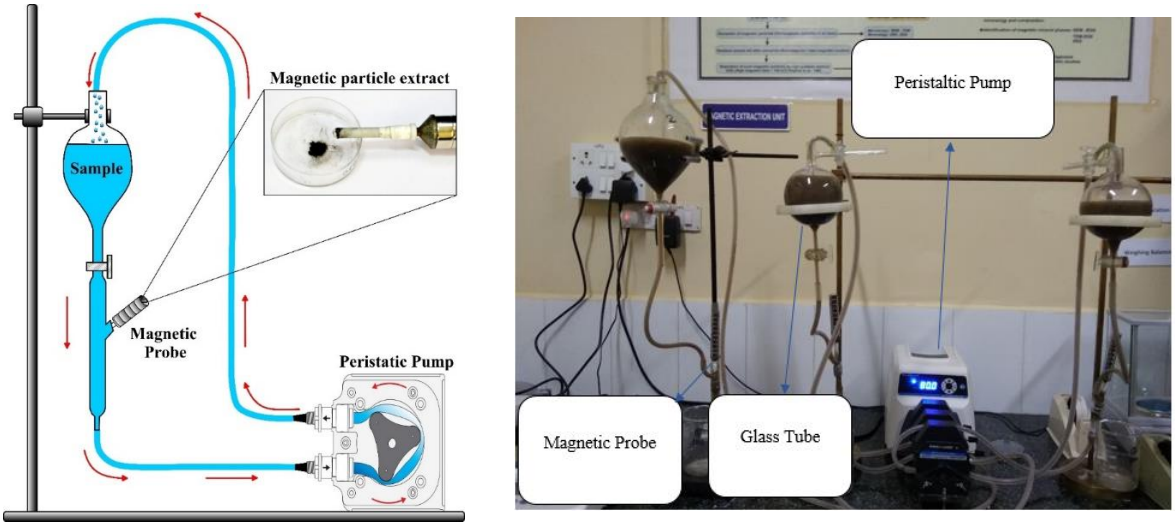

Figure 2.10: *Schematic diagram of the magnetic mineral extraction unit housed at CSIR-NIO, Goa, India. (The red arrow indicates the flow direction of the sediment slurry).*

2.4.5. Microscopy

2.4.5.1. Scanning electron microscopy and energy-dispersive x-ray spectroscopy (SEM-EDS)

Magnetic particles extracted from bulk sediment samples were mounted on copper stubs and carbon coated for imaging. A scanning electron microscope (SEM; JEOL JSM-5800 LV) at CSIR-NIO was used to capture the images of the magnetic particles in a secondary electron imaging mode at energy levels between 15 and 20 keV. To determine the composition of magnetic

particles, an energy-dispersive X-ray spectroscopy (EDS) probe attached to the microscope was used.

Figure 2.11: *JEOL JSM-5800 LV Scanning Electron Microscope (SEM) housed at CSIR-NIO, Goa, India.*

2.4.5.2. Transmission electron microscopy and energy-dispersive x-ray spectroscopy (TEM-EDS)

The morphology of the finer magnetic particles was examined using a transmission electron microscope (TEM). TEM imaging analyses was performed on a JOEL JEM-2100 *plus* housed at the sophisticated analytical instrument facility (SAIF), Shivaji University, Kolhapur, Maharashtra, India. The extracted magnetic particles were dispersed in methanol and ultrasonicated for 15 minutes to get the sample in the suspension. A small drop of the extracted particles was pipetted onto the copper TEM grid and the methanol was later allowed to evaporate. To minimize the oxidation of magnetic particles, samples were straight away placed in the vacuum desiccator. The elemental composition of the components were determined by energy dispersive x-ray spectrometry (EDS). The analyses were performed with a JEOL JEM 2100 *plus* TEM (run with 200 kV acceleration voltages) at the SAIF, Shivaji University, Kolhapur, Maharashtra, India.

Figure 2.12: *JEOL JEM-2100 Plus Transmission Electron Microscope (TEM) housed at Sophisticated Analytical Instrument Facility (SAIF), Shivaji University, Kolhapur, Maharashtra, India.*

2.4.5.3 Optical microscopy

The bulk sediment samples were wet sieved with >63 μm size sieve and the separated coarse-grained particles were analyzed to obtain the microscopic images of fine-grained magnetic inclusions present in the silicate grains. Optical microscopy was conducted on separated >63 μm fraction using Nikon SMZ 18 Stereo Zoom Microscope. The microscope employs a single-zoom optical path with a large diameter, which is optimized to collect light with revolutionary efficiency and resolution at all magnifications.

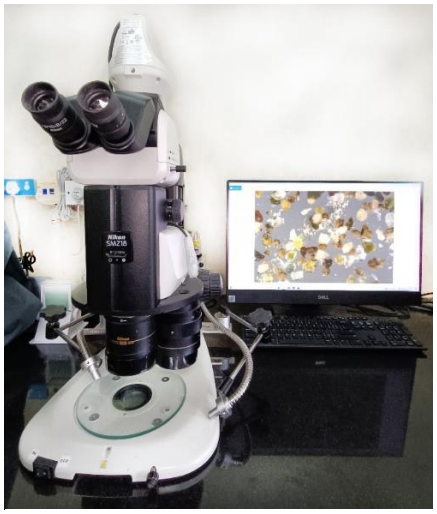

Figure 2.13: *Nikon Zoom Microscope (Model No.- SMZ 18 Stereo) housed at CSIR-NIO, Goa, India.*

2.4.5.4 Petrography of authigenic carbonates

Methane-derived authigenic carbonate (MDAC) were picked up from the SSD-45/Stn-4/GC-01 (active seep) sediment core during sub-sampling. The polished thin sections (26 X 46 mm) of MDAC were prepared and further examined using a petrographic Trinocular Microscope (Model No.-BX51TRF) housed at the Petrology Laboratory of CSIR-NIO, Goa, India.

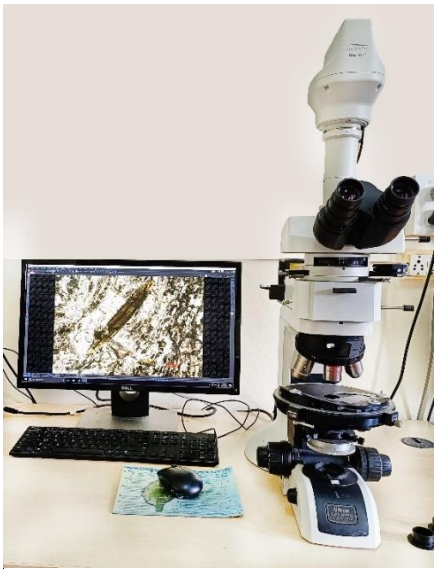

Figure 2.14: *Petrographic trinocular microscope (Model No.-BX51TRF) housed at the Petrology Laboratory of CSIR-NIO, Goa, India.*

2.4.6. Mineralogical analyses

2.4.6.1. X-ray diffraction analyses

Sediment magnetic mineralogy was determined using a Rigaku X-Ray Diffractometer (Ultima IV). The samples were allowed to run from 15° to 65° of 2θ at 1°/min scan speed using Cu Kα radiation (λ = 1.5414 Å). The raw data were processed using a Match software for identification of mineral phases following the crystallography open database (COD).

Figure 2.15: *Rigaku X-Ray Diffractometer (Ultima IV) housed at CSIR-NIO, Goa, India.*

2.4.7. Sedimentological analyses

2.4.7.1. Sediment grain size distribution

Sediment grain size measurements were carried out using a Malvern Mastersizer 2000 Laser Particle Size Analyzer (LPSA) at CSIR-NIO, Goa, India. Desalination of sediment samples was carried out by washing repetitively with deionized water, followed by decarbonization using dilute HCl (1N) acid prior to the analysis. For removal of organic carbon, samples were treated with 10% H_2O_2, and later, sodium hexametaphosphate was added to the sediment solution for better dispersal of the individual sediment fractions. Grain size values are reported as volume%.

Figure 2.16: *Laser Particle Size Analyzer (Malvern Mastersizer 2000) housed at CSIR-NIO, Goa, India.*

Chapter 3:
Origin of magnetic minerals and its fate in sulfidic and methanic environments

3.1. General Introduction

Cold seep ecosystems are peculiar ecosystem characterized by ebullition of methane-rich fluids through the seafloor (Suess, 2014). Methane seeps are also associated with shallow gas (methane) hydrates deposits (Bohrmann et al., 1998; Greinert et al., 2001). During the development of the cold seep system, the sub-surface methane hydrate deposits experience several episodes of formation and dissociation to sustain themselves within the sediment column (Chuvilin et al., 2018). Increase in sedimentation, burial and tectonic activities alter the pressure and temperature which could destabilize the sub-surface methane hydrates. Consequently, vast amount of methane released from the dissociating hydrates/deep reservoir may rise up to seafloor and form cold seep (Henriet et al., 1998; Sultan et al., 2004; Handwerger et al., 2017). At active methane seeps, sulfate reduction driven by anaerobic oxidation of methane (AOM) generates large amount of hydrogen sulfide into the pore waters of the host sediments (Borowski et al., 1996; Jørgensen et al., 2004) to sustain chemosynthetic communities. The hydrogen sulfide causes dissolution of primary detrital magnetic minerals and further transform them into stable non-magnetic pyrite or intermediate ferrimagnetic greigite; thereby, generating secondary magnetic signals in the host sediments (Housen and Musgrave, 1996; Roberts et al., 2015). These magnetic minerals serve as an excellent geological archive to record past methane seepage and help in understanding the geochemical processes that favor diagenesis of magnetic minerals and may also influence the gas hydrate dynamics (formation and dissociation) (Housen and Musgrave et al., 2006; Larrasoaña et al., 2007).

In this study, we conducted a systematic evaluation of rock magnetism, mineralogical, and sedimentological records of sediment cores and delineated the controls of structural and diagenetic (early vs. late) processes on the sediment magnetism in active, relic, and paleo-cold seep sites in the Bay of Bengal. A comprehensive inventory of magnetic minerals originating from detrital, diagenetic, authigenic, and biogenic sources is developed based on the large set of rock magnetic, mineralogical, and sedimentological data generated on the sediment cores retrieved from active, relict, and paleo-cold seep sites linked with the presence of shallow and deep-seated marine gas-hydrate systems from the Bay of Bengal. Rock magnetic and mineralogical methods helped to characterize magnetic assemblages originating from different

sources (detrital, diagenetic, authigenic) in a geologically complex marine cold seep system. This chapter comprised of two parts: 1) Diagenesis of magnetic minerals in an active/relict methane seep sites: Constraints from rock magnetism and mineralogical records from the Bay of Bengal, and 2) Diagenetic dissolution, maghemitization, and sulphidization of magnetic minerals in a rapidly deposited gas-hydrate-bearing sediments from the Bay of Bengal.

Part 1: Diagenesis of magnetic minerals in active/relict methane seep: constraints from rock magnetism and mineralogical records from the Bay of Bengal

3.2. Introduction

At active cold seeps, methane and hydrogen sulphide fluids expel from the seafloor. These fluids led to diagenesis and authigenesis of magnetic minerals at or below the sediment-water interface, wherein primary detrital iron-bearing magnetic minerals undergo reductive dissolution and are further converted into iron sulphides, for example, greigite, pyrrhotite, pyrite (Canfield and Berner, 1987; Boetius et al., 2000; Jørgensen et al., 2004; Riedinger et al., 2005; Rowan et al., 2009; Dewangan et al., 2013; Suess, 2014; Kars and Kodama 2015; Roberts, 2015; Lin et al., 2017; Amiel et al., 2020). Rock magnetic properties of methanic sediments from active cold seep and methane hydrate-dominated sedimentary systems have been widely studied to understand the magnetic mineral diagenesis, for example, in the continental margin off Argentina and Uruguay (Riedinger et al., 2005), Bullseye vent off Vancouver Island, Canada (Novosel et al., 2005), continental margin offshore of south-western Taiwan (Horng and Chen, 2006), Niger deep-sea fan (Dillon and Bleil, 2006), Cascadia Margin (Housen and Musgrave, 1996; Larrasoaña et al., 2007), Nankai trough, Japan (Kars and Kodama, 2015), Bay of Bengal (Badesab et al., 2017, 2019, 2020a,b,c), Southern Eastern Mediterranean continental shelf (Amiel et al., 2020), and North-western Weddell Sea (Reilly et al., 2020).

Structural control on methane seepage at cold seep sites has been well reported using high-resolution seismic and bathymetry data. For example, Lomvi pockmark, Vestnesa Ridge, offshore Svalbard (Berndt et al., 2014; Bünz et al., 2012; Yao et al., 2019), Harstad Basin, southwest Barents Sea (Crémière et al., 2018), Bay of Bengal (Dewangan et al., 2020), Concepción Methane Seep Area, offshore Central Chile (Geersen et al., 2016), Taixinan Basin, South China Sea (Wang, et al., 2018) Central Nile deep-sea fan (Römer et al., 2014), Nankai

accretionary prism (Henry et al., 2002), Congo basin (Wenau et al., 2015) and Black Sea (Bohrmann et al., 2003). Extensive geological and geophysical studies established the presence of fracture-filled and massive-type gas-hydrate deposits in the Krishna-Godavari (K-G) basin (Collett et al., 2008; Dewangan et al., 2010; Dewangan et al., 2011; Kumar et al., 2014; Shankar and Riedel, 2010). Fractures/faults generated from shale-tectonism provide an efficient gas plumbing system in the K-G basin (Dewangan et al., 2010). Fluid migration through these fractures/faults led to the occurrence of paleo-cold seeps in the K-G basin (Dewangan et al., 2010; Mazumdar et al., 2009). In some active faults, methane migrates up to the seafloor and forms an active/relict cold seep system associated with shallow gas-hydrates (Gullapalli et al., 2019; Mazumdar et al., 2019; Figure 3.1).

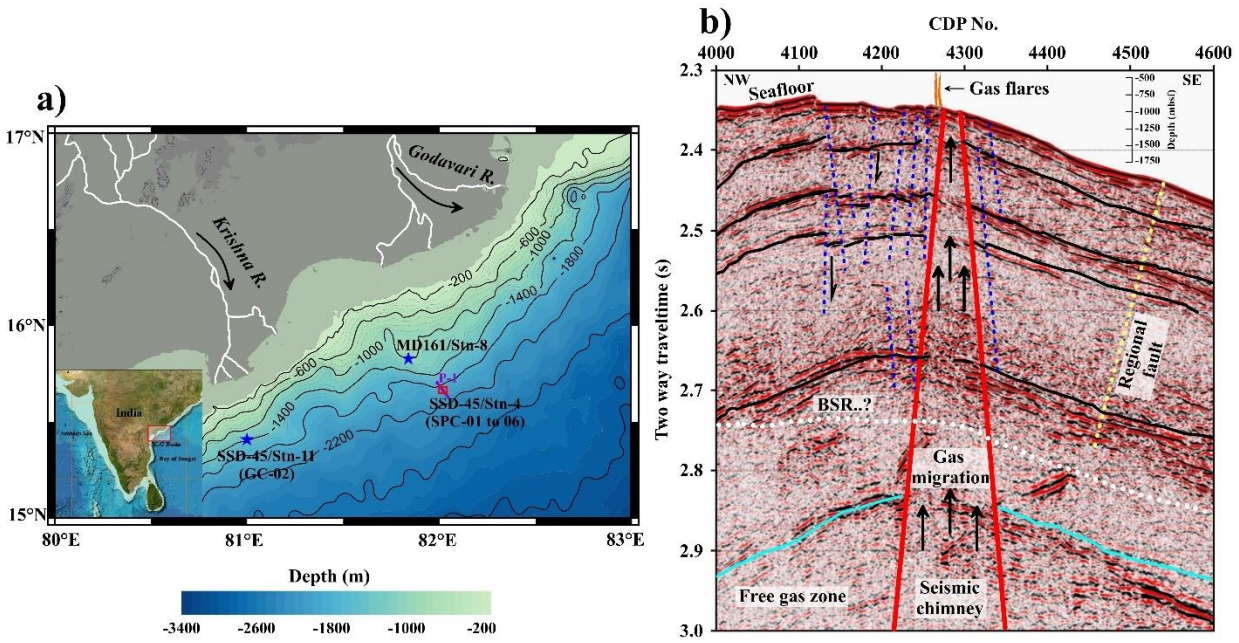

Figure 3.1: *(a) Map showing the location of active (SSD-45/Stn-4), relict (SSD-45/Stn-11/GC-02) and paleo (MD161/Stn-08) seep sites in the Krishna-Godavari (K-G) basin, Bay of Bengal. High-resolution seismic profile (P1) highlighting (b) the normal faults (blue dashed lines), subsurface chimney-like feature (solid red lines), and water column imaging showing gas flares (orange). Regional toe-thrust fault (yellow dashed line), feasible BSR (white dashed line), and subsurface horizons (solid black lines) are marked on the seismic section (modified after Dewangan et al., 2020). The spade sediment cores SPC-01, SPC-02, SPC-03, SPC-04, SPC-05, and SPC-06 were retrieved from active seep site SSD-45/Stn-4 and gravity core GC-02 was*

retrieved from relict site SSD-45/Stn-11. The location of the sediment core from the paleo-seep site (MD161/Stn-8) is also marked. Bathymetry data of the studied area was obtained from GEBCO Compilation Group665 (2020) GEBCO 2020 Grid (doi: 10.5285/a29c5465-b138-234d-e053-6c86abc040b9).

Methane migrates from deep-seated gas reservoirs and interacts with downward diffusing seawater sulfate to trigger multiple zones of anaerobic oxidation of methane (AOM) (Jørgensen et al., 2004; Knittel and Boetius, 2009; Lin et al., 2018) driven by sulfate reduction (Mazumdar et al., 2019). At seep sites, non-steady and multiple diagenetic fronts would yield a complex pattern of magnetic mineral assemblages (Reilly et al., 2020; Roberts, 2015). A recent study by Reilly et al. (2020) provides new insights on magnetic mineral diagenesis through a shallow sulfate-methane transition zone (SMTZ) in a sediment core from Perseverance Drift, Northwestern Weddell Sea, Antarctica. They reported that non-steady-state disturbances, including fluctuations in carbon flux and sedimentation, can shift the pore-water geochemical profiles resulting in the preservation of authigenic ferrimagnetic iron sulphides. In contrast, steady-state diagenetic processes at relict sites would lead to the dissolution of detrital magnetic minerals, followed by the subsequent diagenetic formation of iron sulphide (pyrite), which can significantly reduce magnetic susceptibility of the bulk sediments (Amiel et al., 2020; Canfield and Berner, 1987; Kars and Kodama, 2015; Mohamed et al., 2011; Reilly et al., 2020; Roberts et al., 2005; Roberts, 2015; Roberts and Weaver, 2005, Lin et al., 2020).

Magnetic minerals are potential recorders of the geological and methane-related geochemical processes and provide vital information on the methane seepage dynamics and diagenetic processes in marine gas-hydrate sedimentary system (Badesab et al., 2019a; Kars and Kodama, 2015; Larrasoaña et al., 2007; Musgrave et al., 2006; Roberts, 2015). Previous rock magnetic studies on sediment cores overlying shallow and deep-seated gas-hydrate deposits in the K-G basin mainly aimed at delineating the magnetic signatures of detrital and diagenetic processes associated with the evolution of the gas-hydrate system (Badesab et al., 2017; Dewangan et al., 2013). For example, a magnetic-based proxy for deciphering paleo-methane seepage events and sediment dispersal patterns, tracking the rapid sedimentation events, and its control on the magnetic mineral diagenesis and evolution of gas-hydrate deposits were developed (Badesab et al., 2017; 2019a; 2020b; Usapkar et al., 2014). Furthermore, the mechanism of

formation and preservation of greigite in deep methanic sediments was unraveled by Badesab et al., 2020c. The occurrence of silicate-hosted greigite inclusion was reported by Badesab et al., 2020a. They further highlighted its importance in understanding the magnetic mineral diagenesis in the gas-hydrate system. More recently, Badesab et al. (2020c) conducted a comprehensive rock magnetic and mineralogical investigation on a seep-impacted sediment core from a newly discovered site and successfully delineated the processes governing the methane seepage dynamics and evolution of shallow gas-hydrate (2-3 mbsf) system in the K-G basin. However, a dedicated rock magnetic study focusing on understanding the complex diagenetic (early and late) processes controlled by variability in methane fluxes and underlying fault/fractures at active and relict seep-dominated sedimentary systems was still lacking.

Sediment cores retrieved during a gas-hydrate discovery cruise in 2018 in the K-G basin provided an excellent opportunity to establish a magnetic mineral inventory and investigate the diagenetic processes at active/relict and paleo-seep sites associated with shallow and deep-seated marine gas-hydrates, respectively. The active seep sites (SPC-01 to SPC-06) were mainly characterized by gas flares as observed in the water-column images, higher methane flux, and the presence of live chemosynthesis-dependent organisms, predominantly Bivalvia, Gastropods, and Polychaete (Dewangan et al., 2020; Mazumdar et al., 2019). The absence of gas flares characterize the relict seep site (Stn-11/GC-02), the presence of non-living shell fragments, Calyptogena Sp. and light brown colored authigenic carbonates at 48 cm below seafloor at this site. Contrastingly, the paleo-seep site (MD161/Stn-8) was marked by the presence of methane-derived carbonates, non-living with chemosynthetic clams (*Calyptogena sp.*), and authigenic carbonates within 17-23 mbsf in this core which provided evidence of seepage of methane and sulphide-bearing fluids to the seafloor in the geological past (Mazumdar et al., 2009). In this section, a comprehensive evaluation of rock magnetic, mineralogical, and sedimentological records of sediment cores supplemented by high-resolution seismic data was conducted to elucidate the controls of structural and diagenetic (early versus late) processes on the sediment magnetism in an active (SSD-45/Stn-4/SPC-01 to SPC-06) and relict (SSD-45/Stn-11/GC-02) cold seep sites in the Bay of.

3.3. Results

3.3.1. Down-Core Changes in Rock magnetic Parameters

The magnetic susceptibility (χ_{lf}) profile of all spade cores (SPC-01 to SPC-06) from active seep and a gravity core from relict (SSD-45/Stn-11/GC-02) sites along with SIRM, ARM/SIRM, SIRM/χ_{lf} and S-ratio are shown in Figure 3.2. Two distinct sediment magnetic zones (Z-I and Z-II) were defined based on down-core variations of χ_{lf} in all cores (Figures 3.2a, g, m, s, y, a5, a11). In active methane-seep influenced sediment cores, Z-I is marked by relatively higher values of χ_{lf} and SIRM, indicating a high concentration of magnetic minerals as compared to that observed in Z-II. Magnetic grain size diagnostic proxy (ARM/SIRM) showed variations in Z-I and Z-II of all analyzed sediment cores. (Figure 3.2; Maher and Thompson, 1999; Peters and Dekkers, 2003). A general trend of downcore decrease in ARM/SIRM, suggested coarsening in magnetic grain size till the bottom of Z-I in all cores except SPC-02 (Figure 3.2i). In SPC-01, SPC-03, SPC-04, SPC-06, and GC-02 ARM/SIRM first decreased probably due to preferential dissolution of fine-grained magnetite in Z-I and rised downcore in response to the authigenic formation of greigite (Figures 3.2c, o, u, a7, a13) or fine-grained magnetite (Lin et al., 2020) in Z-II. A mixed trend of ARM/SIRM in SPC-02 and SPC-05 reflects the dominance of both fine and coarse magnetic particles in Z-II (Figures 3.2i, a1). Two distinct patterns in grain size indicator of magnetic iron sulphides (SIRM/χ_{lf}) are observed (Figure 3.2; Maher and Thompson, 1999; Peters and Dekkers, 2003; Snowball, 1991; Snowball and Thompson, 1990). A trend of the initial rise in SIRM/χ_{lf} values were noticed in Z-I of cores SPC-01, SPC-02, SPC-03, SPC-05, and GC-02, suggesting the presence of fine-grained magnetic particles (Figures 3.2d, j, p, a2). After the initial rise, a gradual decline in SIRM/χ_{lf} values till the end of Z-II of the same cores were noticed (Figures 3.2d, j, p, a2, a14). Overall, S-ratios vared between 0.82 and 0.99 for the majority of the samples suggesting that bulk magnetic mineralogy is characterized by both soft as well as hard coercive minerals in the cores from active seep sites (Figures 3.2e, k, q, w, a3, a9; Frank and Nowaczyk, 2008). A systematic downcore decrease in χ_{fd} (%) is seen in all cores from active sites (Figures 3.2f, l, r, x, a4, a10). High values in Z-I indicate a higher concentration of fine-grained magnetic particles, while relatively lower values in Z-II suggest the relative dominance of coarse magnetic particles. Interestingly, an opposite

trend in χ_{fd} (%) profile of the relict site was noticed. Lower χ_{fd} (%) values were found in Z-I and vice-versa (Figure 3.2 a16).

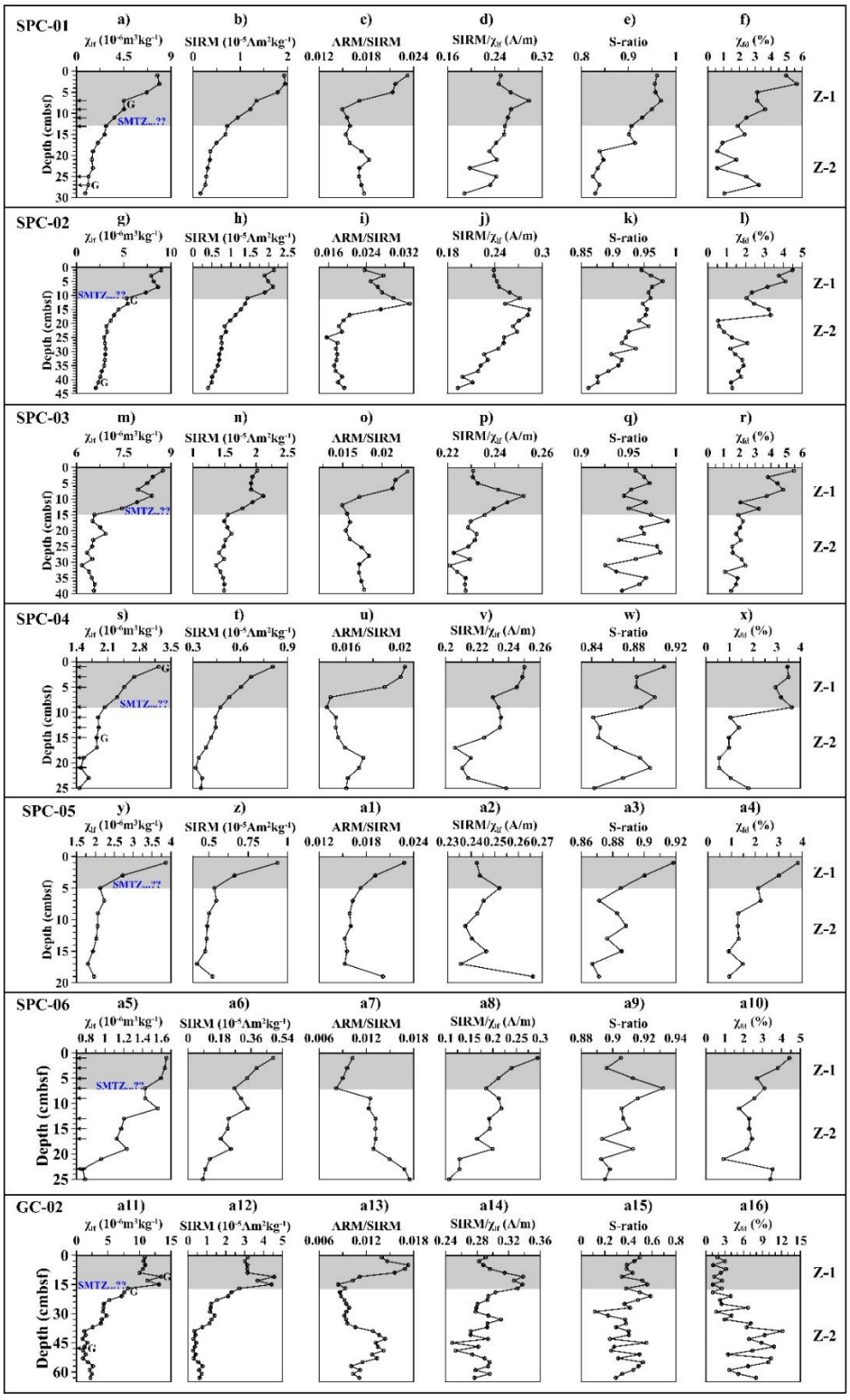

Figure 3.2 *Down-core variations of selected rock magnetic data of spade (a-e): SPC-01, (f-j): SPC-02, (k-o): SPC-03, (p-t): SPC-04, (u-y): SPC-05, (z-a4): SPC-06, and gravity sediment cores (a5-a9): GC-02. Based on magnetic susceptibility variations, two sedimentary magnetic zones Z-I and Z-II are demarcated. Z-I highlighted with gray shading. (Please note that χ_{lf} = low frequency magnetic susceptibility, ARM = anhysteretic remanent magnetization, and SIRM = saturation isothermal remanent magnetization, χ_{fd} % = frequency-dependent susceptibility). Depth of carbonate occurrence are highlighted in solid black arrows (horizontal). The depth of greigite occurrence is marked by "G". Sediment magnetic zones (Z-I, Z-II) in each profile are marked.*

The magnetic record of the relict site (SSD-45/Stn-11/GC-02) showed similar magnetic zonation (Z-I, Z-II), but exhibited different downcore trends in ARM/SIRM, SIRM/χ_{lf}, and S-ratio (Figures 3.2a11-a16). Three sediment intervals (11 cmbsf, 13 cmbsf, and 15 cmbsf) within Z-I showed higher χ_{lf}, SIRM, and SIRM/χ_{lf} suggesting the presence of fine-grained ferrimagnetic iron sulphides in these samples (Figures 3.2a11, a12, a14). An anomalous increase in ARM/SIRM between 39 – 57 cmbsf suggested the dominance of fine-grained magnetic particles in this interval (Figure 3.2a13). A significant shift in S-ratio at 29 cmbsf followed by a minor rise in SIRM downcore (29 – 33 cmbsf) indicated that the relict site has a much higher concentration of high-coercive (coarse-grained) minerals (Figures 3.2a12, a15) as compared to other sites.

3.3.2. Magnetic Mineralogy and Grain Size Diagnostic Parameters

3.3.2.1. Thermomagnetic Measurements

Figures 3.3a-h show the thermomagnetic curves of the representative sediment samples from Z-I and Z-II of cores SPC-01/02/03/05. A steady decrease in χ between 552°C and 633°C in the majority of the samples implies that the bulk magnetic mineralogy is mainly governed by magnetite (Dunlop et al., 1997). Two samples from SPC-01(21 cmbsf) (Figure 3.3b) and SPC-02 (41 cmbsf) (Figure 3.3d) showed a significant drop in χ at 695°C and 673°C respectively. A minor increase in χ between 357°C and 473°C for most of the samples could be either due to the presence of titanomagnetite with a wide range of Ti-contents (Lattard et al., 2006) or because of the conversion of paramagnetic minerals into magnetite during heating process (Hirt and Gehring, 1991; Pan et al., 2000; Passier et al., 2001; Figures 3.3a-h).

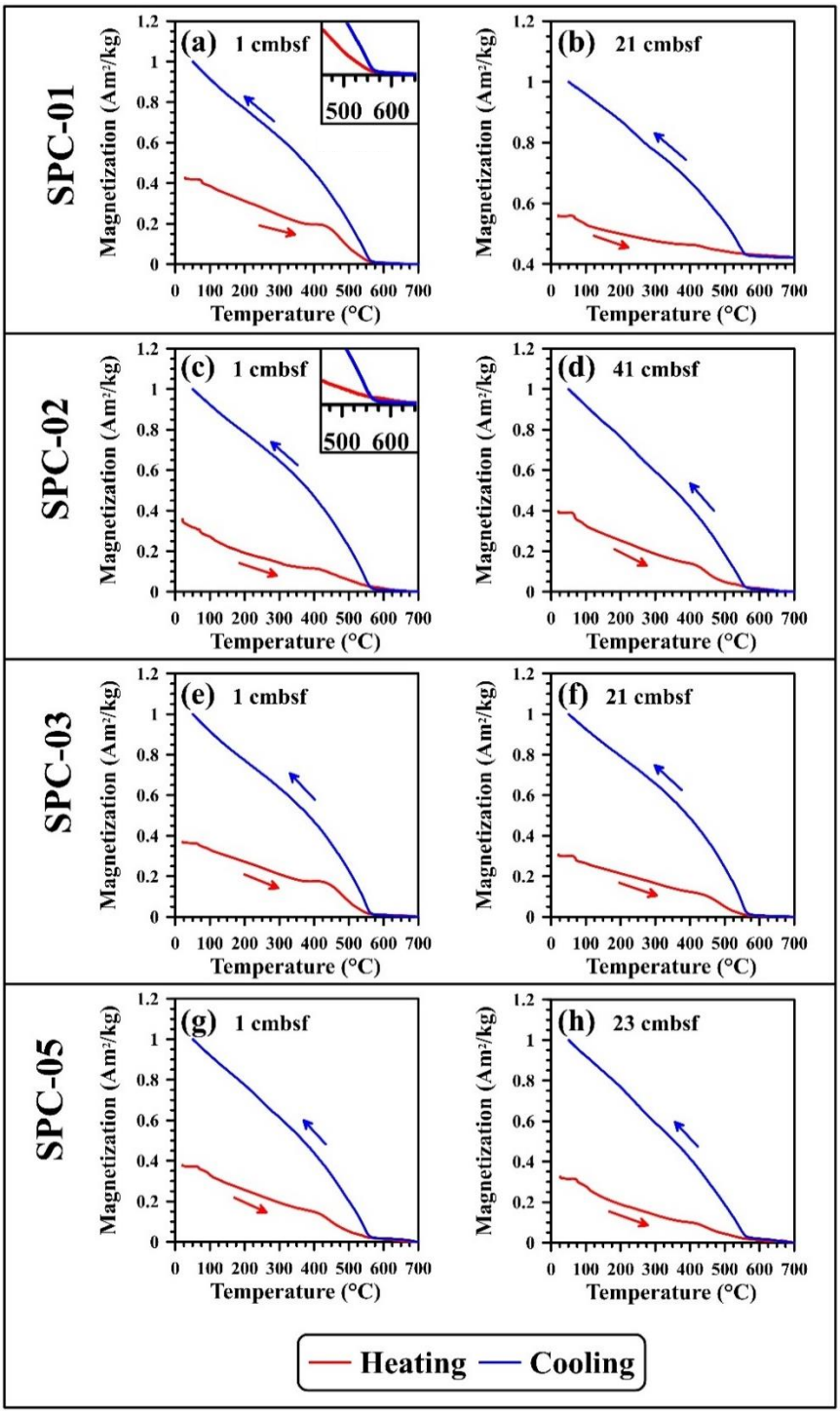

Figure 3.3: *Thermomagnetic profiles of selected representative samples representing two sedimentary magnetic zones of the studied spade sediment cores. (a-b): SPC-01, (c-d): SPC-02, (e-f): SPC-03, and (g-h): SPC-05. Solid red lines indicate heating curves, and blue lines indicate cooling curves respectively.*

3.3.2.2. FORC diagrams

The FORC diagram provided additional information on the type of magnetic minerals and their domain states. Representative FORC diagrams for Z-I and Z-II samples of cores SPC-01/02/03/06 are shown in Figures 3.4a-n. In the majority of the samples, FORC distributions were characterized by closed contours with a peak at Bc ~ 10 – 12 mT indicating that magnetic particles exhibited vortex state to multidomain (MD) type behavior (Figures 3.4a–n; Lascu et al., 2018; Roberts et al., 2000; Roberts et al., 2017)

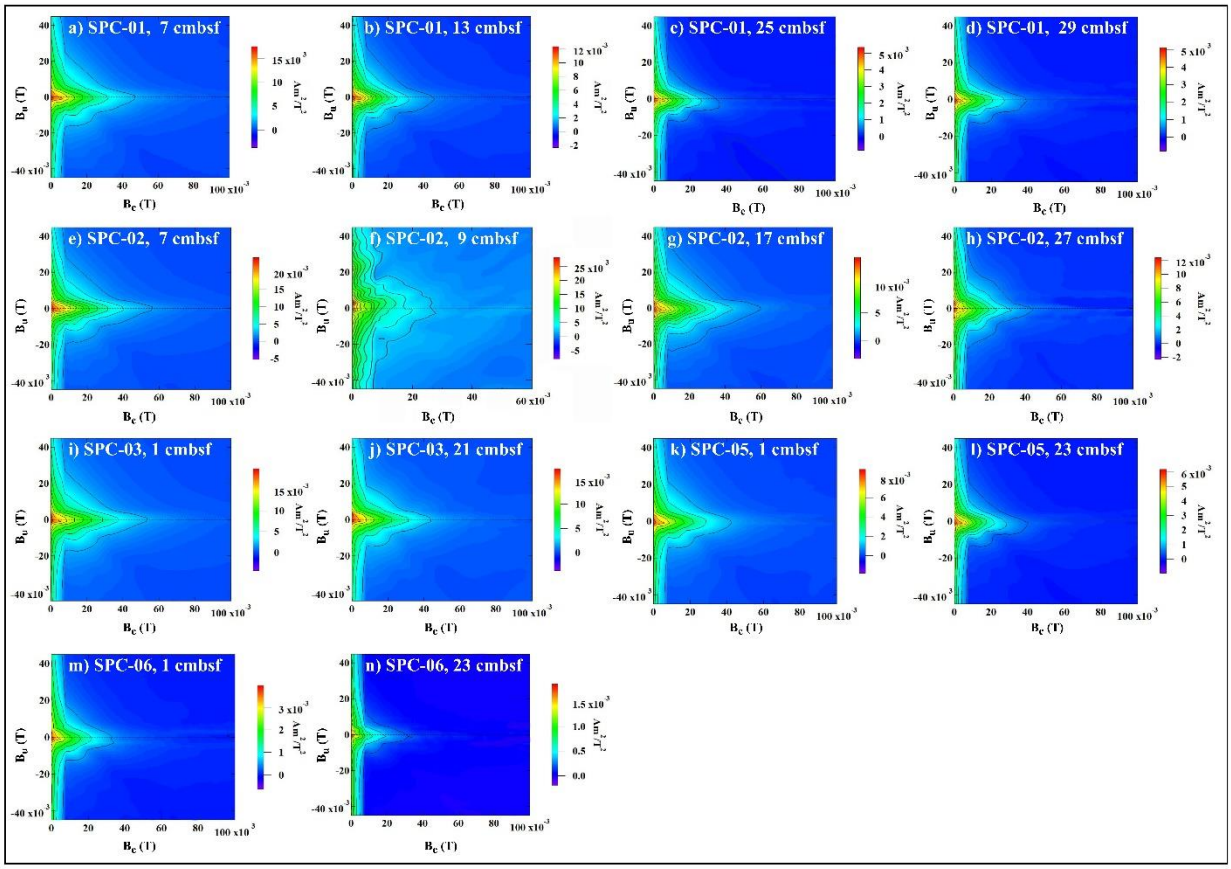

Figure 3.4: *First-order reversal curve diagrams for selected representative samples from spade cores. (a-d): SPC-01, (e-h): SPC-02, (i-j): SPC-03, (k-l): SPC-05, and (m-n): SPC-06.*

3.3.2.3. Low-temperature magnetometry

Results of the low-temperature magnetic measurements displaying characteristic magnetic signatures with respect to the sediment magnetic zones (Z-I, Z-II) are shown in Figure

3.5. A typical Verwey transition (*Tv*) temperature indicative of the presence of magnetite (Figures 3.5a, b, d, e, f) is noticed in RT-SIRM, ZFC-FC, and in the first derivative of magnetization curves (Chang et al., 2016; Özdemir et al., 2002; Verwey, 1939, 1947). Samples from the magnetically reduced zone (Z-II) did not exhibit any *Tv*. The displayed LT magnetization curve (Figure 3.5c) at 29 cmbsf of core SPC-01 indicated the presence of maghemite (Özdemir and Dunlop, 2010). Approximately 62% loss of RT-SIRM induced at 5K was seen during warming between 5 and 30 k (Figure 3.5c) indicating the presence of SP-size magnetic particles. Besnus transition was not observed in the studied samples (typical for pyrrhotite; Besnus and Meyer, 1964; Dekkers, 1989; Larrasoaña et al., 2007).

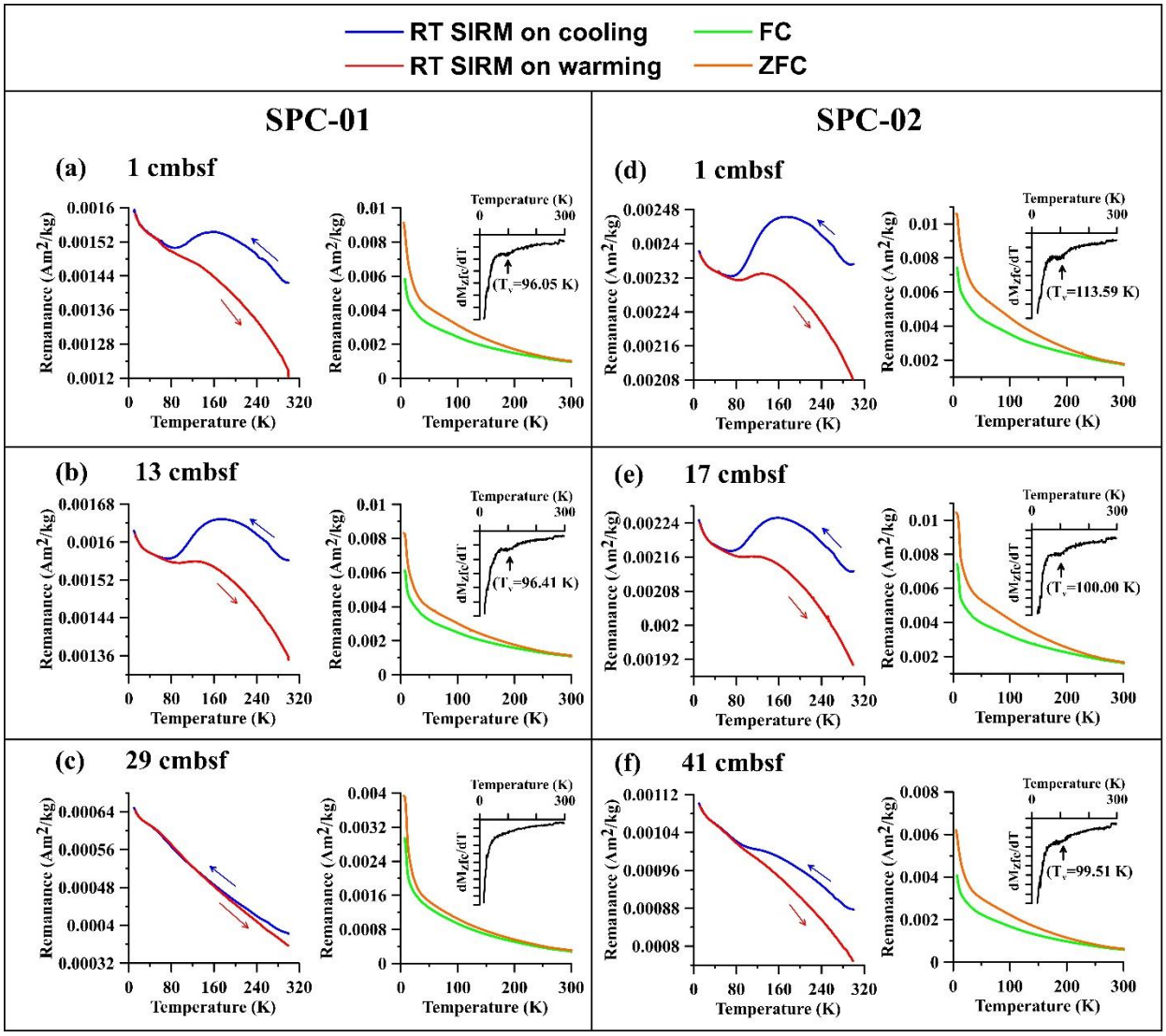

Figure 3.5: *Low-temperature magnetization curves for selected representative samples from the two spade cores (a-c): SPC-01 and (d-f): SPC-02. FC = field-cooled, RTSIRM = saturation isothermal remanent magnetization at room temperature, ZFC = zero field-cooled. The corresponding values of Verwey transition (Tv) are placed near the first derivative of magnetization curves.*

3.3.3. Identification of magnetic mineralogy using m-ray diffraction analysis and scanning electron microscopy

Titano-magnetite and greigite were the dominant magnetic minerals identified in all the sediment magnetic zones (Figures 3.6a-m). Greigite was present in both magnetic zones (Z-I and Z-II) of the cores SPC-01(Figures 3.6b, c), SPC-02 (Figures 3.6e, f), and SPC-04 (Figures 3.6j, k). The electron microscopic images and respective EDS spectra of magnetic particles extracted from different sediment depth intervals of spade cores SPC-01-04 are presented in Figures 3.7a-l. Ferrimagnetic iron oxides (detrital) and sulphides (diagenetic) minerals of different sizes and shapes were identified in all spade cores (Figures 3.7a-l). Well-preserved (Figures 3.7a, d, g, i), as well as diagenetically altered (Figures 3.7c, h) titanomagnetite grains, were found in both sediment magnetic zones. EDS data for these grains indicated the presence of titanium, iron, and oxygen with a minor amount of silicon, aluminum, calcium, potassium, manganese, and magnesium. Numerous diagenetically formed iron sulphides occurring as framboidal crystals and individual grains were observed (Figures 3.7b, k, l) and EDS data indicated the presence of sulfur and iron along with minor amounts of aluminum and silicon (Figures 3.7a-l). Greigite was found to occur as fine-grained minerals only in a few samples and the EDS results of these grains showed the presence of sulfur and iron with minor traces of calcium, potassium, silicon, aluminum, and magnesium (Figures 3.7e, f, j). The titanomagnetite grains in figures 3.7c and 3.7l showed shrinkage cracks typical of low-temperature maghemitization (Nowaczyk, 2011). The cracks on the grains most likely indicated the areas where dissolution might have started. In the relict seep core (GC-02), magnetic mineralogy was carried by titanomagnetite, titanohematite, and greigite particles (Figures 3.9i-p). Z-I was dominated by coarse-grained titanomagnetite and titanohematite grains. A skeletal type of titanohematite grains exhibiting the dissolution features were observed in Z-I (Figure 3.9j) and Z-II (Figures 3.9m, o, p). Numerous

titanomagnetite grains showing the overgrowth of fine-grained greigite particles were noticed in Z-I (Figures 3.9k, l) and Z-II (Figure 3.9o).

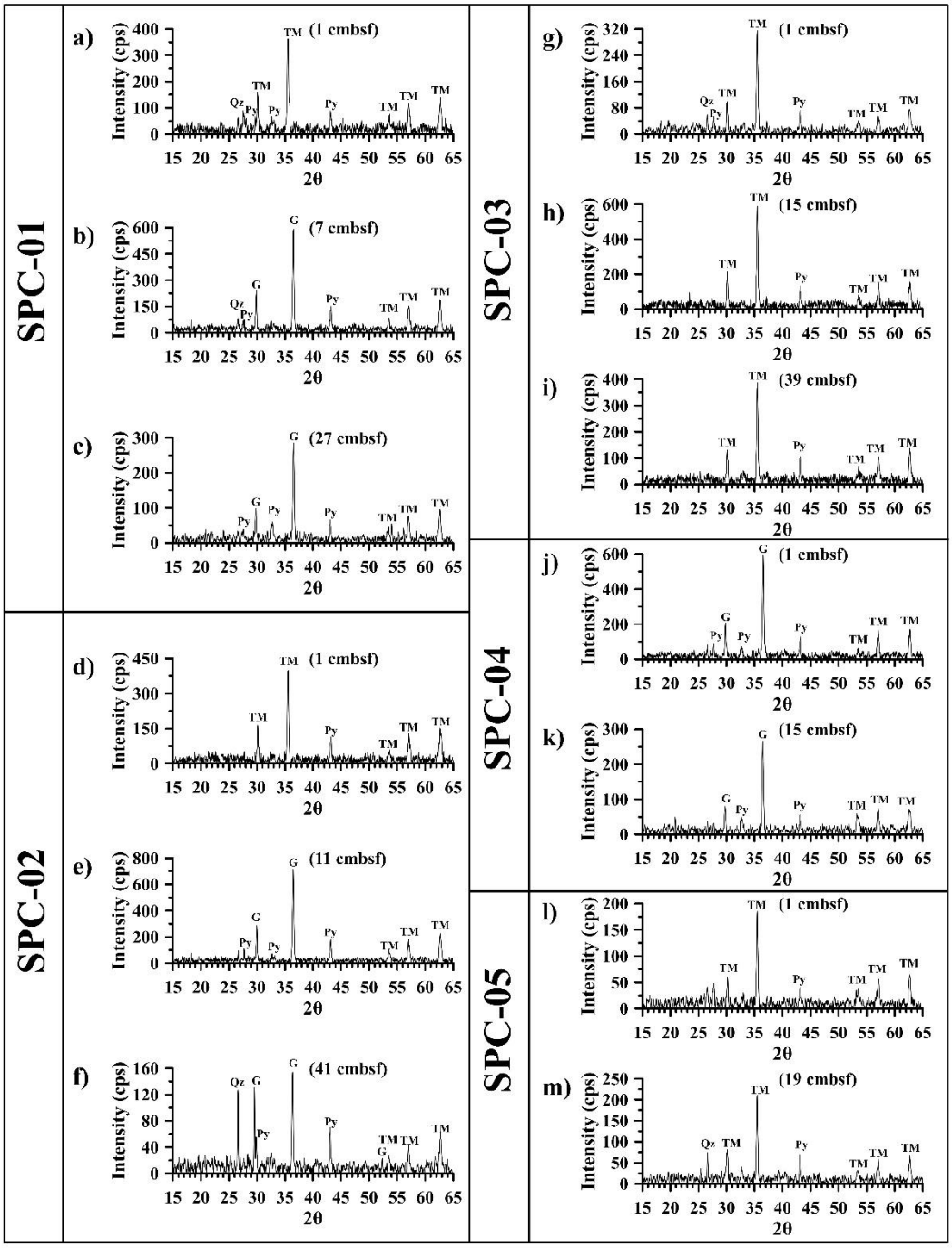

Figure 3.6: *X-ray diffraction spectra for magnetic minerals extracted from different sediment core depth intervals of spade cores. (a-c): SPC-01, (d-f): SPC-02, (g-i): SPC-03, (j-k): SPC-04, and (l-m): SPC-05. TM = titanomagnetite, P = pyrite, Qz = quartz, and G = greigite.*

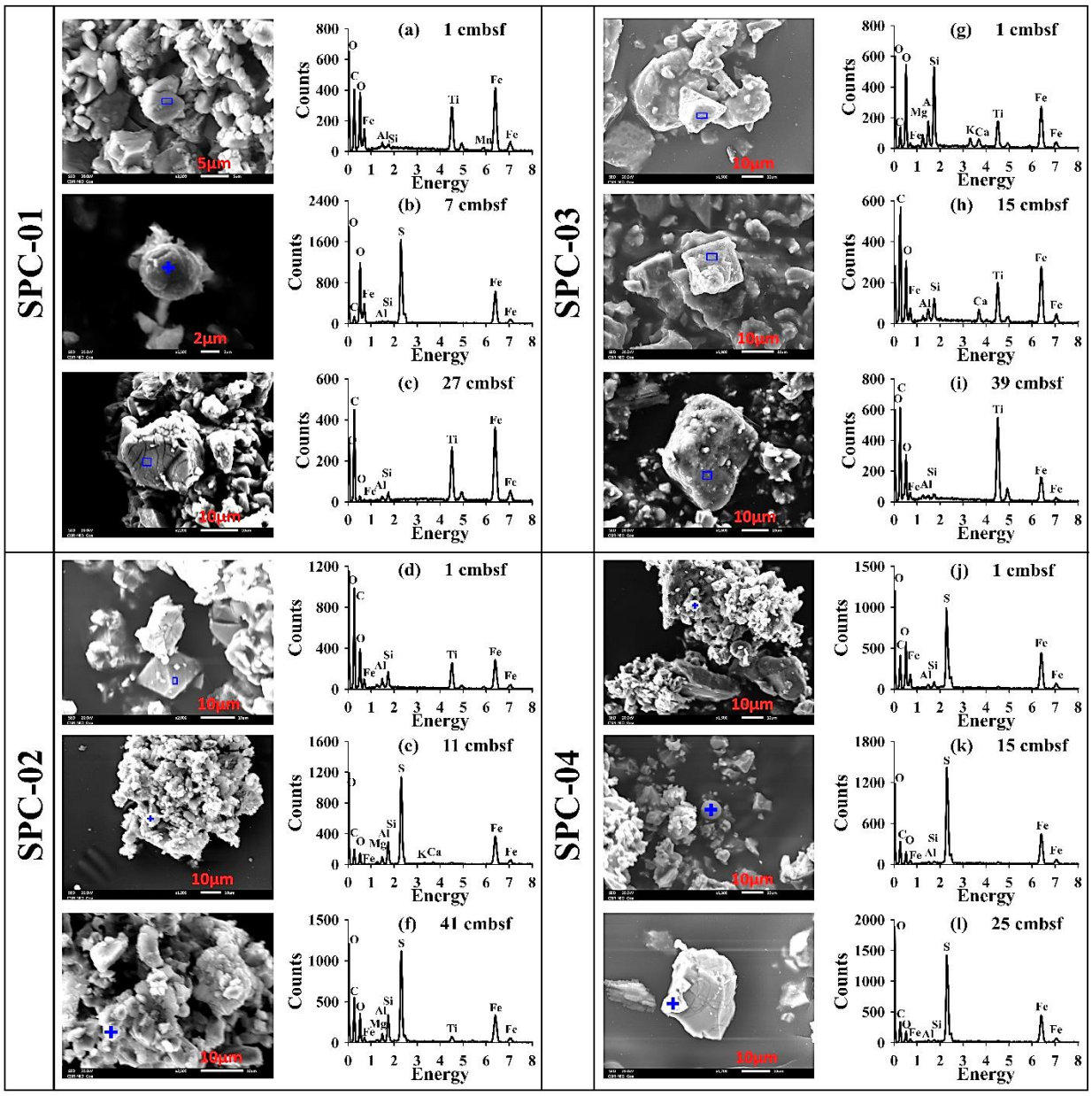

Figure 3.7: *Scanning electron microscopy on magnetic extracts from different sediment core depth intervals. Energy dispersive x-ray spectroscopy spectra are placed adjacent to the respective images. (a-c): SPC-01, (d-f): SPC-02, (g-i): SPC-03, and (j-l): SPC-04. Iron (Fe), titanium (Ti), sulfur (S), oxygen (O), calcium (Ca), silicon (Si), carbon (C), aluminium (Al), potassium (K), magnesium (Mg), and manganese (Mn) peaks are indicated.*

3.3.4. Grain size distributions of sediments, chemosynthetic communities, and authigenic carbonates

Bulk sediment grain size in the studied cores were mainly composed of silt and clay size fractions (Figure 3.8). Sand content was relatively low and varied between 0.99 to 18.58 vol%. Sand-bearing sediment layers were observed throughout the core only in SPC-04/05/06 (Figures 3.8d-f). Higher magnetic susceptibility was found only in silt and clay size fractions (Figures 3.8a-f). Characteristic chemosynthetic living communities (Mazumdar et al., 2019) including *Bathymodiolus sp.*, (Figures 3.9a, b, c, e), *Acharax sp.* shell (Figure 3.9f), and Decapod crustaceans (squat lobsters) belonging to the family Galatheidae and Munidopsidae (Figure 3.9d) were abundantly found at the active methane seep sites. At the relict seep site (SSD-45/Stn-11/GC-02), light brown colored authigenic carbonates showing various morphologies and non-living shell fragments (Calyptogena sp.) were found at 48 cmbsf (Z-II) in this core (Figures 3.9g, h).

3.3.5. Correlation between magnetic parameters of active and relict methane-seep sites

A clear distinction in terms of magnetic mineral concentration, grain size, and mineralogy was seen between active and relict seep sites (Figure 3.10). A positive correlation between χ_{lf} and SIRM was observed in all the samples, but showed different slopes which was attributed to the presence of different magnetic mineralogies (Figure 3.10a). Contrastingly, anomalous lower values (0.11 - 0.55) of S-ratio and a wide range of χ_{lf} displayed by samples from the relict site indicated the predominance of highly coercive minerals (Figure 3.10c). Coupling between magnetic grain size (ARM/SIRM) and physical grain size was noticed in the majority of samples from active and relict seep sites (Figure 3.10d). Two populations A and B were observed. The samples from group-A showed uniformity in physical grain size, but exhibited a wide range of magnetic grain sizes, while group-B samples followed the equivalent trend and showed slight variation in magnetic and large scattering in physical grain size (Figure 3.10d).

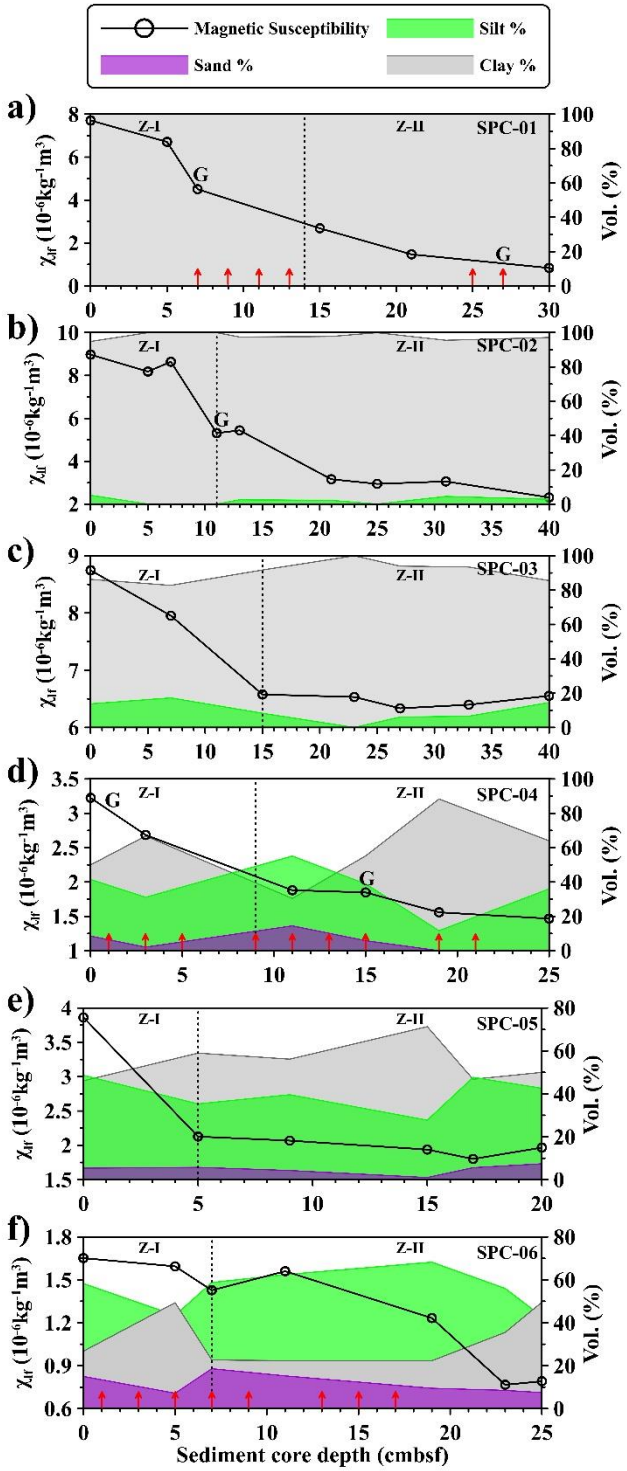

Figure 3.8: *Grain size distribution and magnetic susceptibility data of all spade (SPC-01 to SPC-06) sediment cores retrieved from active methane seep site SSD-45/Stn-4. Depths of*

carbonate occurrence are highlighted in solid red arrows (vertical). The depth of greigite occurrence is marked by "G". Sediment magnetic zones (Z-I, Z-II) in each profile are marked.

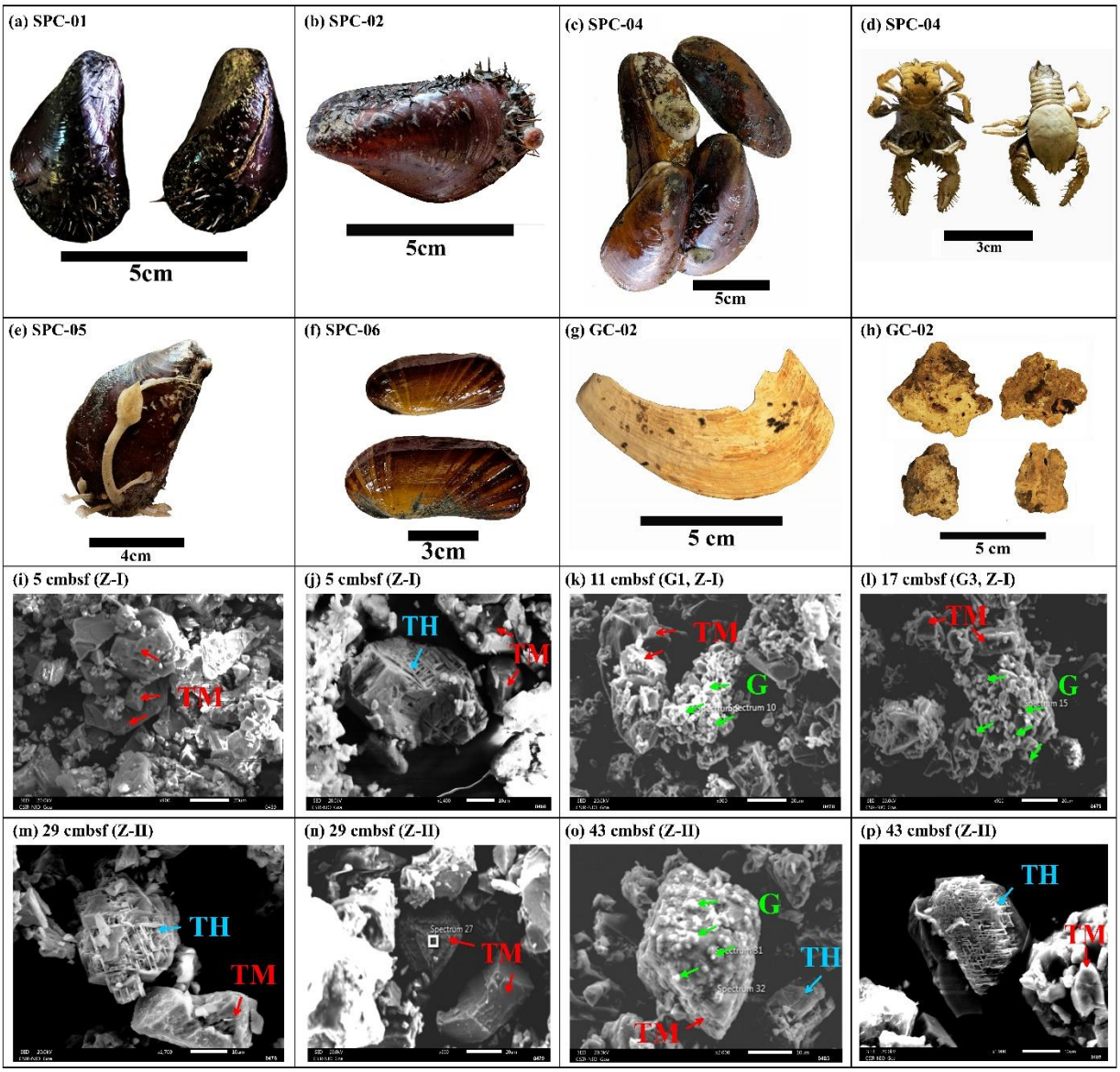

Figure 3.9: *Photographs showing occurrence of (a, b, c, e): Bathymodiolus sp., (d): Decapod crustaceans (squat lobsters), (f): Acharax sp. found at the spade core (surface) locations, (g) calyptogena sp., shell fragment, and (h) authigenic carbonates found at 48 cmbsf in GC-02 location. (i–p): Scanning electron microscopy on magnetic extracts from different sediment core depth intervals (Relict seep site: SSD-45/Stn-11/GC-02). TM = titanomagnetite, TH = titanohematite, and G = greigite).*

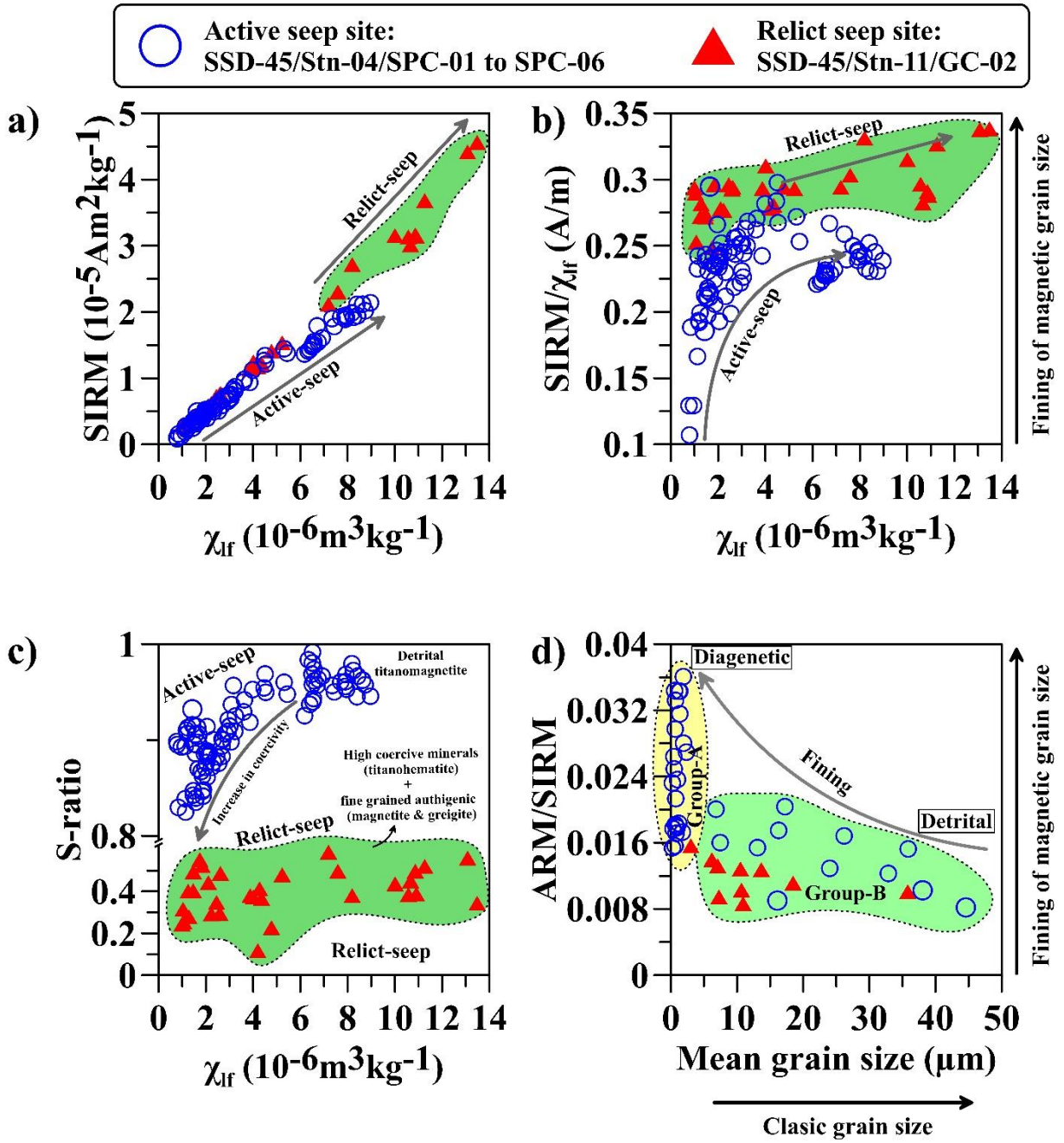

Figure 3.10: *(a–d) Bivariate scatter plots of magnetic parameters magnetic susceptibility (χ_{lf}), saturation isothermal remanent magnetization (SIRM), SIRM/χ_{lf}, S-ratio, ARM/SIRM and mean grain size for spade cores (SPC-01 to SPC-06) from active (SSD-45/Stn-4) and gravity core (GC-02) from relict seep site (SSD-45/Stn-11) in the Krishna-Godavari (K-G) basin, Bay of Bengal. The gray arrows are used to highlight the trends in plots.*

3.4. Discussion

Room, low and high temperature-based rock magnetic data, FORC diagrams, XRD and SEM-EDS observations provided vital information about complex magnetic mineral assemblages in the studied cores. Data revealed that the sediment cores from active seep sites had undergone significant diagenetic dissolution in Z-I, while authigenically formed fine-grained magnetite and greigite was predominant in Z-II. Contrastingly, sulfidic (Z-I) and methanic (Z-II) zones of the relict core were devoid of authigenic magnetite and mainly dominated by a large amount of coarse-grained titanomagnetite and highly coercive (titanohematite) grains of detrital origin which most likely survived the diagenetic dissolution and remained preserved in these zones (Figures 3.9i-p). We utilized the analyzed information to successfully delineate the controls of structural and diagenetic (early versus late) processes on the sediment magnetic signals in active/relict cold seep sites in the Bay of Bengal.

3.4.1. Magnetic mineral inventory of sediments at active/relict cold seep sites in the K-G Basin

Magnetic mineral assemblages in the sediment cores from active and relict seep sites from the K-G basin, primarily comprised of detrital (titanomagnetite, titanohematite), diagenetic (greigite/pyrite) and authigenic (magnetite) origin and were present in various proportions (Figures 3.2,3.3,3.5,3.6,3.7,3.9i-p). Higher values of χ_{lf} in Z-I was attributed to the presence of a mixture of fine and coarse-grained detrital titanomagnetite and titanohematite primarily sourced from Deccan trap basalts (Badesab et al., 2019; Ramesh and Subramanian, 1988; Sangode et al., 2001; Figures 3.2,3.7,3.9i-p). Higher values of grain size indicative (ARM/SIRM) ratio (Maher, 1988) in Z-II of cores SPC-01/03/04/06, and GC-02 revealed high concentrations of fine SD/PSD magnetite (Figures 3.2c, o, u, a7, a13). ARM/SIRM first decreased because of preferential dissolution of fine-grained magnetite in the upper part of the reduced zone (Z-I) and increased later in response to the authigenic formation of fine-grained authigenic magnetite (Lin et al., 2020) and greigite in deeper positions downcore (Z-II). Diagenetically formed magnetic iron sulphide (greigite) were also found to co-exist with detrital titanomagnetite grains and were spatially distributed in both sediment magnetic zones (Z-I and Z-II) of cores from active and relict seep sites (Figures 3.6,3.7,3.9i-p, 3.13). These was explained based on the fact that few

titanomagnetite grains might have survived the early diagenetic dissolution and got rapidly buried and remain preserved due to increased sedimentation.

Verwey transition (*Tv*) temperatures has been successfully utilized as a diagnostic for discriminating detrital magnetite in sulfidic marine sedimentary systems. For example, in Oman continental margin (Chang et al., 2016), offshore of Western Australia (Heslop et al., 2013), and Ria de Vigo, Spain (Mohamed et al., 2011). Low-temperature magnetic data of SPC-01 and SPC-02 revealed the presence of magnetite (Figures 3.5a, b, d, e, f; Chang et al., 2013, 2014 2016; Moskowitz et al., 1993; Moskowitz et al., 1993; Muxworthy and McClelland, 2000; Özdemir et al., 1993; Prozorov et al., 2007; Verwey et al., 1947). At the relict seep site (GC-02), magnetic mineralogy in the high χ_{lf} zone (Z-I) comprised of abundant detrital coarse-grained titanomagnetite and titanohematite particles (Figures 3.9i-j). Within the sulfidic zone, the minor peak of high χ_{lf}, χ_{fd}%, and SIRM/χ_{lf} between 11-13 cmbsf indicated the diagenetic formation of greigite in this interval (Figures 3.2a11, a14, a16, 3.9k-l). Reduced methane flux due to either closure of underlying fractures/fault or cut-off in the supply of downward diffusing sulfate concentrations most likely interrupted the reductive diagenetic process and rather favored the formation and preservation of greigite by limiting H_2S production at this site (Jørgensen et al., 2004; Neretin et al., 2004). Overgrowth of sub-micron-sized particles on the larger titanomagnetite grain in Z-II indicated the authigenic growth of greigite probably due to the weakening of anaerobic oxidation of methane (AOM) process in GC-02 (Figure 3.9o).

Magnetic granulometry (ARM/SIRM, SIRM/χ_{lf}; Maher and Thompson, 1999; Nowaczyk et al., 2012; Roberts, 1995; Sagnotti and Winkler, 1999; Snowball and Thompson, 1990) and mineralogy (S-ratio; Bloemendal et al., 1992) diagnostic parameters exhibited different trends in Z-1 and Z-II, respectively (Figure 3.2). A trend of down-core decrease of ARM/SIRM in SPC-01/03/04/05/06 and GC-02 indicated the increase in abundance of coarser magnetic particles in Z-I (Figures 3.2c, o, u, a1, a7, a13). The loss of finer magnetic fraction in Z-I can be explained by the selective diagenetic dissolution of fine-grained magnetic minerals due to their high reactivity and large surface area (Karlin and Levi, 1983; Tarduno, 1995). In contrast, core SPC-02 showed an opposite trend of down-core increase in ARM/SIRM up to 11 cmbsf in Z-I (Figure 3.2i). Fining of magnetic particles in Z-I (Figure 3.2i) was attributed to the diagenetically-induced fining mechanism (Chang et al., 2016) or due to the increased production of ultra-fine

magnetic grains during magnetite reduction processes (Tarduno, 1995). The titanomagnetite grain in Z-II (Figures 3.7c, 3.7l) showed shrinkage cracks typical of low-temperature maghemitization (Nowaczyk, 2011). The cracks on the grains indicated the areas where dissolution might have started. Hence, the fining mechanism in methanic Z-II can also be linked to the partial dissolution of large titanomagnetite grains (Nowaczyk, 2011). Down-core variations in χ_{lf} and SIRM/χ_{lf} illustrate the spatial distribution of magnetic iron sulphides in the studied spade and gravity cores (Figure 3.2). The apparent linkage between high SIRM/χ_{lf}, χ_{fd}%, and greigite occurrence was clearly observed for SPC-01/02/04 (Figures 3.2d, f, l, x, j, v; 3.6b, c, e, f, j, k; 3.7b, e, f, j, k, l). Several peaks of SIRM/χ_{lf} and χ_{fd}%, predominantly in Z-I manifested by the presence of non-uniformly distributed greigite (confirmed through SEM-EDS and XRD; Fu et al., 2008; Peters and Dekkers, 2003; Rowan et al., 2009; Figures 3.2, 3.6, and 3.7) can be attributed to non-steady-state magnetic mineral diagenesis driven by fluctuations in diffusive methane flux at these sites.

Variability in rock magnetic parameters in each core reflected the different degrees of diagenetic disturbances created by methane seepage within the studied sites in the K-G basin. Similar observations were reported from Vestnesa Ridge, Svalbard margin (Sztybor and Rasmussen, 2017), and Oregon continental margin (Karlin, 1990). Variations in S-ratio can be attributed to the changes in magnetic mineralogy (Figures 3.2e, k, q, w, a3, a9, a15). The high S-ratio in Z-I is due to the presence of detrital titanomagnetite (Figures 3.2e, k, q, w, a3, a9, a15, 3.6a, d, g, j, l, 3.7a, d, g). In spade cores (SPC-01 to SPC-06), SEM-EDS and XRD data did not exhibit any signature of higher coercivity (hematite) minerals (Figures 3.6 and 3.7). In fact, XRD data confirmed the presence of greigite in samples exhibiting low S-ratio in both Z-I and Z-II (Figures 3.6b, c, e, f, k). The S-ratio drop in Z-II of the relict core was well-explained by the occurrence of numerous titanohematite grains (Figure 3.2a15, 3.9e, o, p). Preservation of titanomagnetite grains (Figures 3.9m-p) in Z-II could be either due to weakened AOM (Reidinger et al., 2005) or higher resistance against dissolution (Nowaczyk, 2011) which might have hindered the early diagenetic processes and led to the preservation of detrital magnetic particles. A significant drop in S-ratio (Figure 3.2a15) followed by high χ_{fd}% (Figure 3.2a16) in Z-II of relict core (SSD-45/Stn-11/GC-02) was attributed to the presence of a mixture of detrital titanohematite (Figures 3.9m, o, p), authigenic greigite (Larrasoaña et al., 2007; Dillon and Bleil,

2006) and hexagonal 3C pyrrhotite (Horng, 2018; Horng and Roberts, 2018). Similar observations were recently reported from Perseverance Drift, North-western Weddell Sea (Reilly et al., 2020).

Authigenically formed ferrimagnetic iron sulphides (greigite and pyrrhotite) are well-reported in the methane-rich sedimentary system, for instance in Nankai Trough (Horng, 2018; Kars and Kodama, 2015), Hydrate Ridge (Larrasoaña et al., 2007), and offshore Taiwan (Horng and Roberts, 2018). FORC diagrams and low-temperature magnetic measurements provided additional constraints on the magnetic mineralogy and domain states. FORC distributions showed the mixture of the vortex to multi-domain magnetic particles (Figures 3.4a–n). In a natural system, greigite can commonly occur as magnetostatically interacting framboids. A micromagnetic modeling study involving hysteresis and FORC simulations demonstrated that magnetostatic interactions could remarkably alter the FORC response of greigite framboids and can form patterns similar to vortex and MD (Valdez-Grijalva et al., 2020). It is quite possible that greigite clusters observed in SPC-02 (Figures 3.7e-f) and SPC-04 (Figure 3.7j) might have be contributed significantly toward the observed FORC (vortex to multi-domain) distributions. Low-temperature magnetic data indicated the presence of magnetite in Z-I and Z-II (Figures 3.5a, b, d, e, f). Similar to findings of the present study, Korff et al. (2016) reported cyclic magnetite dissolution and preservation of detrital magnetite in methanic sediments of the abyssal northwest Pacific Ocean. Sample from the zone of reduced magnetic susceptibility (Z-II) of SPC-01 did not show any indication of a Verwey transition in RT-SIRM, ZFC-FC, and the first derivative of magnetization curves (Figures 3.5c). In the figure 3.5c we observed that nearly 62 % of the LT-SIRM applied at 5K was lost during warming between 5 and 30 K. This observation indicated the presence of superparamagnetic (SP) magnetic particles in these samples (Tarduno, 1995; Passier and Dekkers, 2002). Similar to the observation of the present study, Kars and Kodama (2015) reported a related pattern of sudden decrease in LT-SIRM from 5 to ∼30 K and about ∼50–60% loss of the applied remanence in the sediment core samples from Nankai Trough, offshore Japan. They linked the loss of remanence to the presence of SP particles which get unblocked very rapidly. The SP magnetic particles in this sample (Figure 3.5c) was most likely iron sulphides like greigite, pyrrhotite, and titanohematite (Horng, 2018; Roberts et al., 2020). This interpretation was explained considering the fact that fine-grained magnetic particles

in this sample would have got readily dissolved in the sulfidic environment (as seen through the lowest χ_{lf} in Z-II). Contrastingly, the SP greigite and pyrrhotite nanoparticles are thermodynamically more stable compared to the SP magnetite nanoparticles and would rather remain preserved (Rowan et al., 2009; Roberts et al., 2018). The lack of LT transitions in the magnetization derivation curves in this sample (Figure 3.5c) is persistent and further confirmed the presence of greigite (through high χ_{fd}%, Figure 3.2f) and pyrrhotite (Chang et al., 2009; Roberts et al., 2011).

3.4.2. Early versus late diagenesis of magnetic minerals in active and relict methane seep sites in the Bay of Bengal: Constraints from rock magnetism and mineralogical proxies

In an active cold seep sedimentary system, temporal movement of diagenetic fronts due to variability in methane fluxes and sulfate reduction rates favors non-steady-state diagenesis. Such a process could generate complex magnetic signatures in sediments involving magnetite reduction and authigenic formation of magnetite (Amiel et al., 2020; Lin et al., 2020; Riedinger et al., 2005) and iron sulphides (Canfield and Berner, 1987; Larrasoana et al., 2003; Liu et al., 2012; Riedinger et al., 2014; Roberts, 2015). Rock magnetic data showed progressive downcore dissolution of magnetite in sediment cores from active (Figures 3.2a-a10) and relict (Figures 3.2a11-a16; Karlin and Levi, 1983) sites in the K-G basin. A gradual downcore decrease in ARM/SIRM and χ_{lf} within Z-I in cores SPC-01/03/04/05/06 suggested substantial dissolution of fine-grained magnetic particles due to early diagenesis (Figures 3.2c, o, u, a1, a7). A slight increase in ARM/SIRM in Z-II of SPC-01/03/04/06 (Figures 3.2c, o, u, a7) was attributed to the presence of fine-grained authigenic magnetite (Karlin et al., 1987; Lin et al., 2020; Roberts, 2015; Roberts et al., 2018). A similar steady increase of ARM/SIRM in the sulfidic zone of sediment cores from the deep methanic zone of the Southern Eastern Mediterranean continental shelf (Amiel et al., 2020) and Niger deep-sea fan was attributed to the gradual authigenic growth of SD magnetite (Dillon and Bleil, 2006). A downcore increase in ARM/IRM_{1T} in Z-II of active seep sites (SPC-01/03/04/06) could also be due to the presence of authigenic magnetite formed as a result of the microbial iron reduction process in methanic sediments which might have permitted the newly formed magnetite to survive the sulfidic dissolution and favored preservation (Lin et al., 2020; Figure 3.2c, o, u, a7). SEM-EDS and XRD data of cores showed the presence of greigite in the methanic zone (Z-II) from active seep sites (Figure 3.6c, e, f, k, 7e,

f, k, l). Following the concept proposed by Lin et al., 2020, the mechanism was proposed for authigenic greigite formation in Z-II of active seep sites. Increased supply of reactive iron (secondary iron oxyhydr) oxides produced during iron-sulphide mineral oxidation due to decline in methane seepage intensities (Lin et al., 2016; 2020) and limitation of sulphide in the methanic zone (below SMTZ) probably favored the greigite formation in this zone.

During early diagenesis, sulfate gets readily depleted through the decomposition of organic matter (Karlin, 1990a). Taking into consideration, the plausible mechanism is proposed for the preservation of fine-grained authigenic magnetite in Z-II as seen through a trend of high ARM/SIRM in SPC-01/03/04/06 (Figure 3.2c, o, u, a7). Fine-grained magnetite (SD-type) might have occurred as magnetic inclusions in silicates which most likely protected the magnetite from diagenetic dissolution (Chang et al., 2016a, b; Feinberg et al., 2005; Hounslow and Morton 2004; Muxworthy and Evans, 2013; Tarduno et al., 2006) and could explain the preservation of fine-grained magnetite in Z-II. Another possibility is that authigenic magnetite formation coupled with microbial iron reduction (Lin et al., 2020) within methanic sediments might have allowed the freshly formed fine-grained magnetite to survive sulfidic dissolution fronts and rather favored preservation as evident through high ARM/SIRM values in Z-II (methanic) of cores SPC-01/03/04/06 from active seep sites. However, the presence of fine-grained titanomagnetite in Z-II cannot be ruled out. Similar findings were reported from rock magnetic studies on sediment cores from the continental margin of Oman north-western Arabian Sea (Chang et al., 2016) and the northeast part of the Japan Sea (Yamazaki et al., 2003). At the relict site, an anomalous (39 – 57 cmbsf) interval within (Z-II) showed increased ARM/SIRM values and a significant drop in S-ratio (29 – 63 cmbsf) indicating the preservation of numerous highly coercive magnetic particles as confirmed through SEM observations (Figures 3.2a13, a15, 3.9m-p). An increased SIRM/χ_{lf} (Figure 3.2a14) might have been caused by the overgrowth of sub-micron-sized authigenically formed SP greigite particles on larger titanomagnetite grains (at 43 cmbsf, Figure 9o). The presence of SP greigite is further confirmed by the observed increase in χ_{fd}% in Z-II of GC-02 (Figure 3.2a16).

Magnetic iron sulphides including greigite and pyrrhotite formed within the sulfidic pore water produced by upward migrating SMTZ fronts (Kasten et al., 1998; Horng, 2018). Significant downcore decrease in magnetite concentration (χ_{lf}) and grain size (ARM/SIRM)

diagnostic parameters in SPC-01/03/04/05/06 and GC-02 suggested that fine-grained magnetic particles were selectively removed by diagenetic dissolution (Figures 3.2a, c, m, o, s, u, y, a1, a5, a7, a11, a13; Chang et al., 1987; Karlin et al., 1987; Lin et al., 2020; Roberts, 2015). Rock magnetic (Figure 3.2), SEM-EDS (Figures 3.7, 3.9i-p) observations, and mineralogical (Figures 3.6, 3.13) records provided evidence of the spatial distribution of diagenetically formed iron sulphides (greigite, pyrite) in Z-I and Z-II of all analyzed cores. A noticeable high SIRM/χ_{lf} and χ_{fd}% values in samples from Z-I were exhibited by fine-grained greigite particles formed during early diagenesis (Figure 3.2). FORC diagrams for the majority of samples provided evidence of two important magnetic (fine-grained, SD+SP) populations in Z-I and Z-II (Figures 3.4a-n). SP-sized ultra-fine authigenically formed ferrimagnetic greigite particles (as seen through high χ_{fd}% and rapid decrease of ZFC and FC remanences upon warming from 5 to 30K (Banerjee et al., 1993; Muxworthy and Roberts, 2007; Figure 3.2, 3.5c) and SD-type (as seen through negative regions in the horizontal axis, Roberts et al., 2011; Rowan and Roberts, 2006; Sagnotti et al., 2005, 2010; Figures 3.4a-m) indicated the preservation of fine-grained SD magnetite particles.

Reduced magnetization at gas-hydrate vents has been established in Cascadia's accretionary margin off Vancouver Island (Novosel et al., 2015). At active seep sites, methane is being transported from the deep-seated gas reservoir up to the seafloor and the intensities of methane flux govern the SMTZ location. The presence of abundant live chemosynthetic communities (*Bathymodiolus sp.* and *Acharax sp.*) provided evidence of active methane seepage at the studied site (Figures 3.9a-f). Elevated methane flux shifted the SMTZ fronts upward and vice-versa (Borowski et al., 1996). Production of hydrogen sulphide via AOM at SMTZ caused the dissolution of iron oxides, and precipitation of iron sulphides (Reidinger et al., 2005). Diagenetic dissolution of magnetite followed by the subsequent transformation to pyrite created a distinct χ_{lf} minima compared to ferrimagnetic greigite which would significantly increase χ_{lf} (Badesab et al., 2019; Dewangan et al., 2013; Kars and Kodama, 2015). Several researchers established that variability in the SMTZ depth can be used to quantify methane flux (Housen and Musgrave, 1996; Larrasoaña et al., 2007; Musgrave et al., 2006; Neretin et al., 2004; Novosel et al., 2005; Reidinger et al., 2005; Roberts, 2015). A close linkage between the depth of SMTZ and minima in χ_{lf} has been well-established and increasingly utilized as a proxy for detecting SMTZ fronts in methanic sediments for example in the Cascadia margin (Housen and Musgrave,

1996; Larrasoaña et al., 2007), offshore of Argentina and Uruguay (Riedinger et al., 2005), Nankai trough, Japan (Kars and Kodama, 2015), and offshore New Zealand (Rowan and Roberts, 2006). In the analyzed sediment cores, the distinct χ_{lf} minima most probably reflected the recent SMTZ front, which varied between 5 cmbsf and 16 cmbsf (Figure 3.2). The shallowest χ_{lf} minima was noticed in active seep core SPC-05 (Figure 3.2y) and deepest at SPC-03 (Figure 3.2m) and relict site GC-02 (Figure 3.2a11), respectively. Such variability in SMTZ depth provided evidence of the differential rate of diagenesis constrained by fluctuations in methane fluxes. In such a non-steady-state diagenetic scenario, for instance at active seep sites (SPC-01 to SPC-06), different degrees of diagenetic disturbances created by changing methane flux had modified and preserve the primary magnetic mineral assemblages in sediments. SEM observations indicated the presence of abundant coarse-grained titanomagnetite and titanohematite in Z-I (Figures 3.7a, d, g, 9i-p) and Z-II (Figures 3.7c, i, 3.9m-p). More recently Amiel et al. (2020) conducted a detailed magnetic investigation on the sediment cores from SE Mediterranean Continental Shelf to examine the influence of early diagenesis in the methanic environment. They reported that rapid sedimentation and non-steady-state conditions triggered by variability in methane flux favored the survival of abundant iron-oxide minerals in the sulfidic and deep methanic zone (Riedinger et al., 2005). In the present study, the survival and preservation of these minerals in Z-I and Z-II was explained by the fact that titanohematite and titanomagnetite are more stable and offers strong resistance to reductive dissolution induced by early and late diagenetic processes (Channell and Hawthorne, 1990; Nowaczyk, 2011; Poulton et al., 2004) or due to increased sedimentation (Amiel et al., 2020, Riedinger et al., 2005). Stability against diagenetic alteration increased together with elevated Ti content and in turn resulted in higher magnetic stability. Dissolution of titano-hematite involved a noticeably slower reaction compared to magnetite (Cornell and Schwertmann, 1996; Liu et al., 2004; Yamazaki et al., 2003). Previous studies had demonstrated that increasing titanium content stabilizes titanomagnetite compounds because Ti^{4+} substitution correspondingly reduces the number of Fe^{3+}, the acting electron acceptor under anaerobic conditions (Karlin, 1990b; Garming et al., 2005). During non-steady diagenesis, the formation of secondary minerals takes place whenever pore-water chemistry changes due to upward or downward diffusion of dissolved hydrogen sulphide (Roberts and Weaver, 2005) and could lead to the formation and preservation of

authigenic magnetite and greigite. Microbial iron reduction within methanic sediments is the most likely mechanism for authigenic magnetite formation (Lin et al., 2020).

More recently Reilly et al. (2020) revealed that high coercivity magnetic minerals respond slowly to the diagenetic dissolution through the entire SMTZ and can be a potential source for ferric iron via microbial iron reduction process coupled to AOM (Amiel et al., 2020; Beal et al., 2009; Riedinger et al., 2014). They further concluded that increased concentration of high coercivity minerals in the methanic zone (below SMTZ) produced a large amount of ferric (Fe^{3+}) via iron reduction where sulphide is limited and favored the authigenic precipitation of greigite. In the relict core (SSD-45/Stn-11/GC-02) greigite and titanohematite particlers were found to occur throughout the sulfidic (Z-I) and methanic (Z-II) (Figure 3.2a11, a16, 3.9i-p, 3.13a-d). It is highly possible that diagenetic dissolution of titanohematite during iron reduction generated enough (Fe^{3+}) and provided a conducive environment for greigite formation in the intervals where sulphide got exhausted in core SSD-45/Stn-11/GC-02. The SEM (Figures 3.9k, l, o) and XRD (Figures 3.13 b, c) observations of the present study followed by high values of χ_{fd}% (Figure 3.2a16) supported the findings of Reilly et al. (2020). Bivariate magnetic plots (Figure 3.10) and FORC diagrams (Figure 3.11) also helped to evaluate the influence of steady and non-steady state diagenetic processes on the magnetic record of sediment cores from active (SPC-01 to SPC-06), relict (Stn-11/GC-02) and paleo (MD161/Stn-8; Mazumdar et al., 2009) seep sites in the K-G basin. Scattered data plot between IRM_{1T}/χ_{lf} and χ_{lf} indicated a broad range of SP greigite (Figure 3.2a16, 3.9k, l, o) particles and larger variations in their concentrations (Figure 3.10b). A scattered plot between magnetic (ARM/IRM_{1T}) and physical (mean) grain size showed a systematic pattern of fining in magnetic grain size with the increase in diagenetic dissolution of detrital magnetic minerals (Figure 3.10d).

Non-steady state diagenetic processes can potentially affect the sediment magnetic parameters. For example, abrupt change in the sedimentation rate can cause migration of the SMTZ (e.g., Riedinger et al., 2005; Fu et al., 2008), and temporal changes in the organic matter load into the sediment can affect the depths of the different respiration processes (Larrasoaña et al., 2003; Rowan et al., 2009), changes in the sediment composition can lead to the accumulation of magnetic minerals in the sediment and change in the magnetic parameters. These mechanisms require time variations in the flux of the sediments from the Krishna and Godavari rivers, which

are the main sources of detrital magnetic particles in the studied area. Multiple layers of mass transport deposits (MTD's) generated as a result of frequently occurring high sedimentation events have been identified in the shallow and deep offshore regions of the K-G basin (Ramana et al., 2007; Ramprasad et al., 2011; Yamamoto et al., 2018). Recently Badesab et al., 2019 reported a high-resolution sediment magnetic record of high sedimentation events in the K-G basin. Samples from the relict site (SSD-45/Stn-11/GC-02) showed remarkably high χ_{lf} and IRM_{1T} (Figures 3.2A11-A12) compared to active seep sites (SPC-01 to SPC-06) probably due to non-steady-state-diagenesis-driven by high sedimentation events. It is most likely that coarse titanomagnetite and titanohematite grains survived diagenesis due to (1) their inherent property to resist dissolution (Nowaczyk, 2011), and (2) rapid burial due to increased sedimentation (Badesab et al., 2019). Detailed rock magnetic and microscope analyses conducted on the sediment cores from the continental margin of Oman and northern California by Rowan et al. (2009) reported that newly formed greigite particles are small initially and would display thermally unstable SP behavior unless it grows fully through the stable SD blocking volume. They attributed the magnetic enhancement to the late diagenetic growth of magnetically stable greigite. Greigite can display both SD-type behavior (Roberts, 1995) as well as ultrafine-grained SP (Rowan and Roberts, 2006; Rowan et al., 2009).

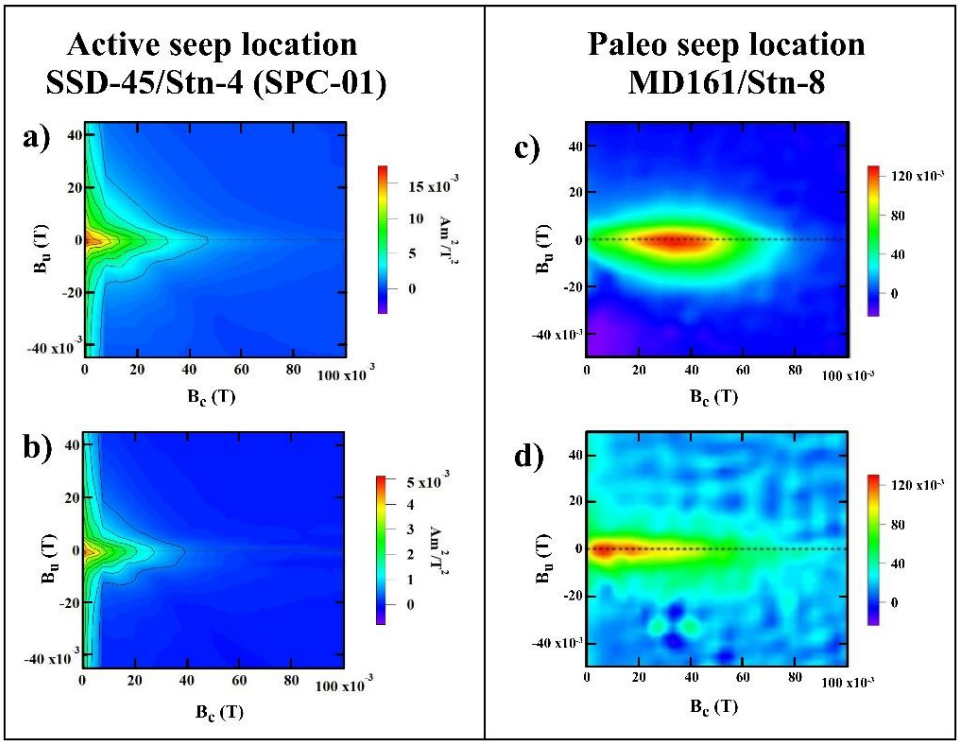

Figure 3.11: *Comparative FORC diagrams of greigite bearing sediment intervals from (a-b): active (SSD-45/Stn-4/SPC-01) and (c-d) of paleo-seep location (MD161-Station-08; modified from Badesab et al., 2020a) in the Krishna-Godavari (K-G) basin, Bay of Bengal. The dashed (black) lines along Bc axis highlights the negative region on the horizontal axis.*

Differences in the growth of greigite particles from active (SPC-01 to SPC-06) and paleo (MD161/Stn-8; Badesab et al., 2020a) samples were clearly reflected in the FORC diagrams (Figures 3.11a-d). FORC diagram of samples from the active seep site (SPC-01) showed that the magnetic particles exhibited a mixed (vortex state to multidomain) type behavior (Figure 3.11a, b; Roberts et al., 2000; Roberts et al., 2017). In contrast, FORC diagrams of paleo-seep samples showed broad distribution with concentric and elongated contours indicative of the presence of magnetically stable greigite probably formed as a result of late diagenetic growth (Figure 3.11c; Rowan et al., 2009) and biogenic mineralization (Figure 3.11d; Badesab et al., 2020a) at site MD161/Stn-8.

3.4.3. Structural Control on the Formation and Preservation of Greigite

Methane venting episodes linked to active and paleo-cold seeps are well documented in the K-G basin (Dewangan et al., 2020; Mazumdar et al., 2009). High-resolution seismic data across active seep site (SSD-45/Stn-4; present study) showed the presence of well-developed seismic chimney and faults, which facilitated the migration of deep-seated gas through the gas-hydrate stability zone (GHSZ) up to the sea floor and favored gas-hydrate accumulation in the K-G basin (Dewangan et al., 2020; Figure 3.1B). At the same site, shallow (2-3 mbsf) gas-hydrates were recovered during a gas-hydrate exploration cruise in 2018 (Mazumdar et al., 2019). Vertical migration of methane through the sedimentary column produces multiple AOM's resulting in the growth of diagenetic minerals including pyrite, greigite, and pyrrhotite (Roberts, 2015). The interplay between the rates of downward diffusing sulfate and upward migrating methane concentrations controls the amount of hydrogen sulphide, which is a key factor constraining the greigite formation (Jørgensen et al., 2004; Kasten et al.,1998; Neretin et al., 2004). For instance, enhanced methane flux would generate a large amount of hydrogen sulphide which could drive the pyritization process to complete resulting in the precipitation of pyrite, while limitation of sulphide due to decline in methane would favor greigite/pyrrhotite formation (Liu et al., 2004).

At the active site, the presence of greigite in both sediment magnetic zones of cores SPC-01/02/04 was confirmed through SEM-EDS and XRD data (Figures 3.2, 3.6, 3.7). In this study, an attempt was made to investigate the structural control on the variability in methane fluxes and subsequent diagenetic formation of greigite in the studied cores. Control of opening and closing dynamics of the underlying fracture/fault system on methane migration in the K-G basin has been well-established (Dewangan et al., 2011; 2020;). The spatial distribution of authigenic carbonates in cores SPC-01, SPC-04, and SPC-06 (Figure 3.14) provided evidence of several AOM's indicative of past fluctuations in methane fluxes. The following plausible mechanisms explained the formation and preservation of greigite in Z-I and Z-II: (1) decline in methane flux either due to massive hydrate accumulation (Dewangan et al., 2020; Mazumdar et al., 2019) or hindering of upward migrating fluid/gas by the carbonate layers in the subsurface sediments most likely resulted in low sulphide production and preferentially favored formation and preservation of greigite in the Z-I. Similar observations were reported in fault-controlled cold seep-hydrate Woolsey Mound in the Northern Gulf of Mexico (Simonetti et al., 2013), gas-hydrate field offshore Vancouver Island (Riedel et al., 2002), Vestnesa Ridge, W-Svalbard Margin (Singhroha et al., 2020), and in the K-G basin (Badesab et al., 2017; Dewangan et al., 2011). They explained that plugging of an active fault system due to massive hydrate formation can also cause a significant drop in methane flux (2) occurrence of greigite below the carbonate layers in cores SPC-01, SPC-04, and SPC-06 (Figure 3.14) in Z-II suggested that the supply of downward diffusing sulphide was most likely hindered and subsequently a sulphide deficient zone is formed below the carbonate layer which inhibited the pyritization and rather favored the formation and preservation of greigite. A detailed rock magnetic analysis of a 30 m long sediment core from the paleo-seep site in the Bay of Bengal reported the presence of both diagenetic and biogenic greigite (within 17-23 mbsf) i.e., beneath a thick layer of the authigenic carbonate formed as a result of intense methane seepage event (Badesab et al., 2020a; Dewangan et al., 2013; Mazumdar et al., 2009). A more recent study demonstrated that an elevated supply of Fe^{2+} via iron reduction produced by high coercivity minerals in sulphide limited zone (Z-II) can also favor the authigenic growth of greigite (Reilly et al., 2020). Greigite presence in low S-ratio intervals of Z-II in relict core (SSD-45/Stn-11/GC-02) was linked with such a process (Figure 3.2a15, 3.9o, 3.13c-d). The presence of greigite was further confirmed by the observed

increase in χ_{fd}% (Figure 3.2a16). However additional geochemical and microbiological data are warranted to resolve the mechanism.

A conceptual model explaining the evolution of magnetic mineralogies at active (Stn-4/SPC-01 to SPC-06) and relict (Stn-11/GC-02) seep sites was developed (Figure 3.12). Shallow gas-hydrates (2-3 mbsf) and authigenic carbonates (throughout the cores) were recovered at active seep sites (Figure 3.14; Mazumdar et al., 2019). In sulfidic (Z-I), detrital magnetic particles minerals supplied through Krishna and Godavari River systems reacted with the H2S produced by bacterial activity via organic matter decomposition and AOM-coupled sulfate reduction which led to the diagenetic dissolution of magnetic particles and subsequent precipitation of iron sulphide (pyrite) with intermediate precursors such as greigite and pyrrhotite (Berner, 1984; Karlin, 1990a). SEM-EDS and XRD data coupled with χ_{fd}% confirmed the presence of greigite in both sulfidic (Z-I) and methanic (Z-II) (Figure 3.2, 3.6, 3.7). The most likely mechanism which explained the formation and preservation of greigite in Z-I and Z-II is as follows. A decline in methane flux due to massive hydrate accumulation along with the active fault system and formation of authigenic carbonate crust in the sub-surface sediments hindered the supply of upward migrating fluid/gas and limited the sulphide production which preferentially enhanced greigite formation in Z-I. Secondly, a restricted supply of downward diffusing sulphide by the carbonate layers in the uppermost sediments is a responsible process for creating a sulphide deficient zone beneath. These might have inhibited the pyritization process and rather favored the formation of greigite in the methanic zone (Z-II). Samples from the relict site (SSD-45/Stn-11/GC-02) showed notably high χ_{lf} and SIRM (Figures 3.2 a11-a12) compared to active seep sites which is most probably due to non-steady-state diagenesis driven by high sedimentation events in the K-G basin. Coarse titanomagnetite and titanohematite grains survived the diagenesis either due to their inherent property to resist dissolution (Nowaczyk, 2011) or because of rapid burial due to increased sedimentation (Badesab et al., 2019).

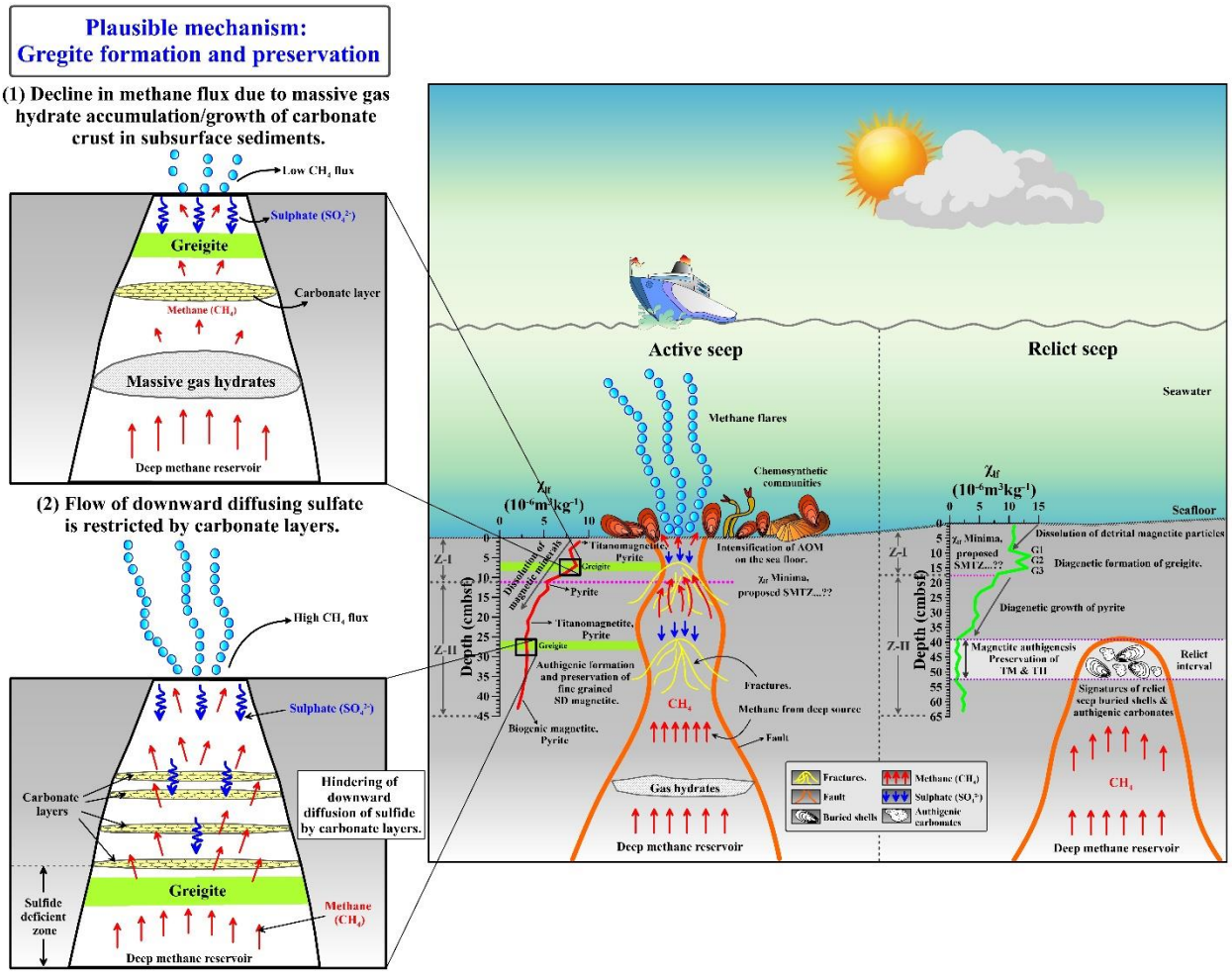

Figure 3.12: *Conceptual model explaining the structural and diagenetic controls on the evolution of magnetic mineralogies at active and relict methane seep site in the Krishna-Godavari (K-G) basin, Bay of Bengal.*

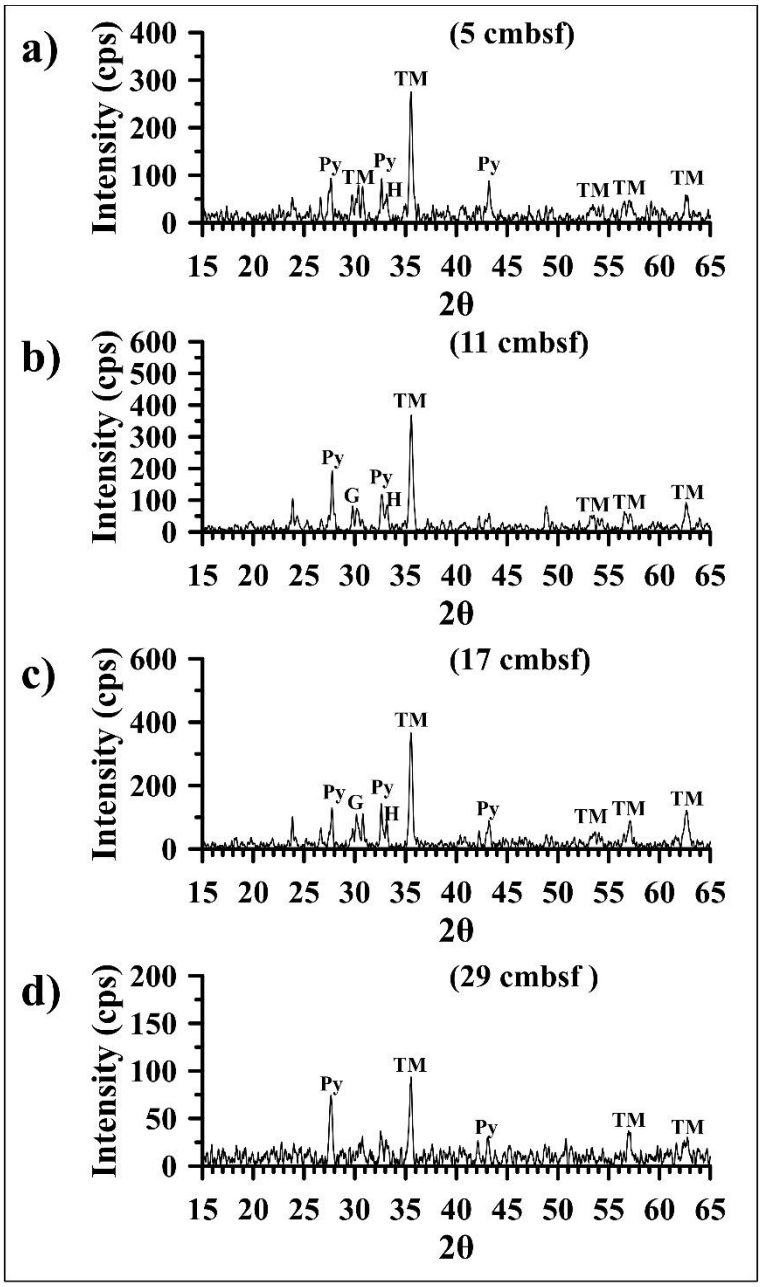

Figure 3.13: *(a-d) X-ray diffraction spectra for magnetic minerals extracted from different sediment intervals of relict seep site: SSD-45/ Stn-11/GC-02. TM = titanomagnetite, H = hematite, Py= pyrite, and G = greigite*

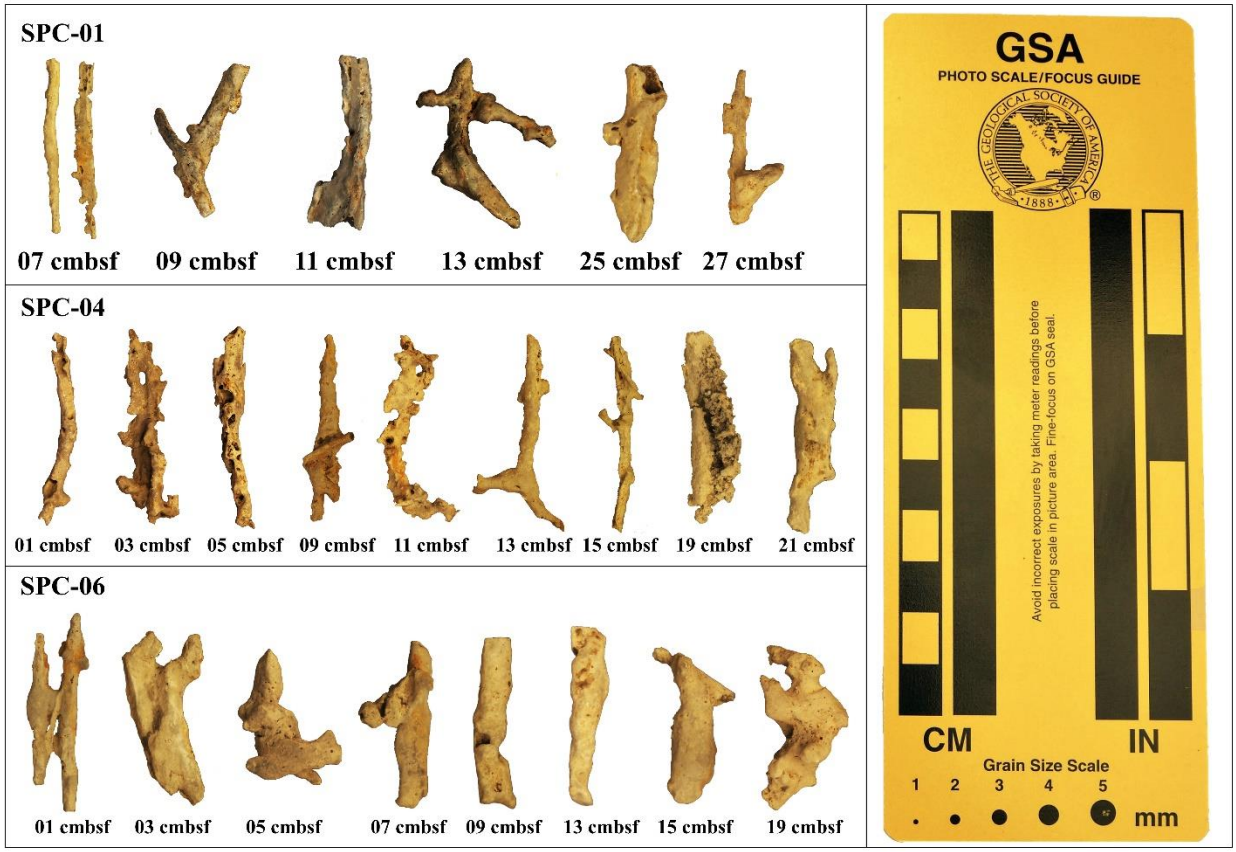

Figure 3.14: *Photographs showing methane-derived authigenic carbonates found in an active seep sites SSD-45/Stn-04/SPC-01, SPC-04 and SPC-06. Respective depths of the carbonate occurrence are mentioned.*

Part 2: Diagenetic dissolution, maghemitization, and sulphidization of magnetic minerals in a rapidly deposited gas-hydrate-bearing sediments from the Bay of Bengal.

3.5. Introduction

Magnetic minerals are sensitive to sedimentary redox conditions and effectively record the diagenetic effects ranging from subtle to pervasive through geologic time (Canfield, 1989; Roberts, 2015). Magnetic mineral diagenesis in oxic environments incorporates surface oxidation and precipitation of Fe^{3+} bearing minerals from solution. In anoxic environments, the detrital iron mineral undergoes dissolution and releases Fe^{2+} which is readily available for diagenetic reactions (Jørgensen et al., 2004; Liu et al., 2012; Raiswell and Canfield, 2012). Anaerobic oxidation of methane (AOM) is a vital biogeochemical process that results from the interaction of rising methane flux and downward diffusing sulfate concentration (Treude et al., 2005; Knittel and Boetius, 2009). AOM is achieved by a syntrophic consortium of methane-oxidizing archaea and sulfate-reducing bacteria (Boetius et al., 2000). Organoclastic sulfate reduction (OSR) coupled with AOM process produces large amounts of hydrogen sulphide in pore waters of the host sediment (Canfield and Berner, 1987; Riedinger et al., 2005). In the sulphidic environment, iron-bearing minerals undergo severe diagenetic alterations. Dissolved Fe^{2+} released from detrital iron oxides reacts with dissolved hydrogen sulphide produce during OSR and AOM to form sedimentary iron sulphides, mainly pyrite (Berner, 1984; Canfield and Berner, 1987; Roberts and Turner, 1993; Neretin et al., 2004; Rowan et al., 2009; Johnson et al., 2021). Such processes give rise to the consumption of pore-water methane and sulfate to depletion and this zone is widely recognized as the sulfate-methane transition zone (SMTZ). Several researchers have successfully established the linkage between distinct minima and maxima in the sediment magnetic susceptibility at SMTZ with the dissolution of magnetite and secondary formation of paramagnetic pyrite and intermediate ferrimagnetic greigite respectively (Garming et al., 2005; Riedinger et al., 2005; Larrasoaña et al., 2007; Roberts, 2015; Badesab et al., 2019).

Sedimentation can significantly influence the diagenesis and authigenesis of magnetic minerals in methanic/marine sediments (Borowski et al., 1996; Kasten et al., 2003; Garming et al., 2005; Riedinger et al., 2005; Roberts, 2015; Kars et al., 2021; Koster et al., 2021). The rate of magnetite dissolution is strongly dependent on the sedimentation rate, sulfate reduction rate,

concentration of dissolved sulphide, and the contact time between the magnetic particles and sulphidic pore-fluids (Roberts and Turner, 1993; Channell and Stoner, 2002; Riedinger et al., 2005; Amiel et al., 2020). Rapid burial of magnetic particles due to increased sediment supply restricts the production of pore-water sulphide and thereby enhances the preservation of magnetic particles (Kao et al., 2004; Kawamura et al., 2007; Kars et al., 2014). For example, uniform sediment supply and reactive organic matter will drive steady-state diagenetic reactions towards completion resulting in a significant loss of iron-bearing minerals through subsequent conversion into paramagnetic iron sulphides. Such mineral transformations can be easily tracked using magnetic proxies (Roberts and Weaver, 2005; Roberts, 2015; Reilly et al., 2020). Contrastingly, non-steady diagenesis arises when sedimentation supply changes rapidly through geologic time and the diagenetic reactions get significantly affected resulting in a complex pattern of magnetic mineral assemblages (Roberts et al., 1996; Ao et al., 2010; Nowaczyk, 2011). For example, mass transport deposits in the continental slope of the K-G basin, Bay of Bengal were generated as a result of slumping/sliding events triggered by the rapid sedimentation, gas-hydrate dissociation, and neotectonic events (Ramana et al., 2007; Dewangan et al., 2008; Ramprasad et al., 2011; Joao et al., 2021). Rock magnetic studies on the sediment cores from active and relict cold seep (Gaikwad et al., 2021), shallow gas-hydrate (Dewangan et al., 2013; Badesab et al., 2019; Badesab et al., 2020), and deep-seated gas-hydrate sites (NGHP-01-10D, NGHP-01-03B, NGHP-01-05C, NGHP-01-7B; NGHP-01-14A Figure 3.15; Badesab et al., 2017; 2019; 2020a) in the Bay of Bengal highlighted the impact of mass transport deposits (MTD's) on the gas-hydrate related biogeochemical processes and the evolution of complex magnetic mineralogies at these sites.

Diagenesis and authigenesis of magnetic minerals in active, relict cold seeps and gas-hydrate-bearing sediments has been extensively studied worldwide. For example, K-G basin, Bay of Bengal (Dewangan et al., 2013; Badesab et al., 2017, 2019, 2020; Gaikwad et al., 2021; Johnson et al., 2021), Nankai Trough, Japan (Kars and Kodama 2015a,b; Musgrave et al., 2019), Cascadia Margin, offshore Oregon (Musgrave,1996; Novosel et al., 2005; Housen and Larrasoaña et al., 2007; Esteban et al., 2008), offshore western Svalbard (Johnson et al., 2014; Panieri et al., 2016), Continental margin off Argentina and Uruguay (Riedinger et al., 2005), and Yungan Ridge, offshore southwestern Taiwan (Horng, C.S. 2018). More recently, Johnson et al.

(2021) developed a new approach based on heavy mineral proxy and X-ray fluorescence (Zr/Rb) data for isolating the detrital and diagenetic signals in methanic sediments from the K-G basin**.** Impact of low and high temperature diagenesis on magnetic mineral assemblages in methane hydrate bearing marine sediments from the Nankai Trough was investigated by Kars et al (2018, 2021). Their work revealed that changes in sediment input and organic matter supply, burial temperature and tectonic fluid circulation through geologic time constrained the sediment magnetic signals. Evolution of long-term changes in the biogeochemical processes and the associated diagenetic overprinting of the primary magnetic mineral assemblages in the Nankai trough offshore Japan was reconstructed using rock magnetic**,** solid phase, and porewater data (Koster et al., 2021). In similar context, a focused rock magnetic study by Musgrave et al. (2019) on a 1,800m long sediment sequence in a volcano-bounded basin on the Izu rear arc, Japan clearly demonstrated how episodes of multiple fluid inputs and pyritization processes controlled the progressive and punctuated magnetic mineral diagenesis.

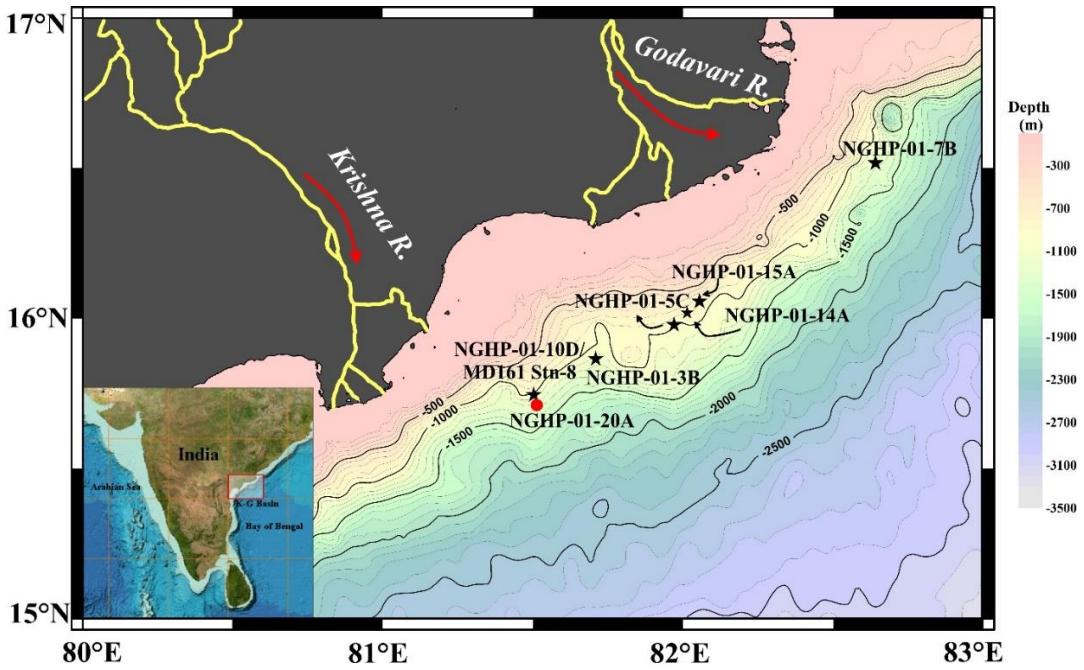

Figure 3.15: *Sediment core locations map of NGHP-01-20A (present study), NGHP-01-10D, MD161/Stn-8, NGHP-01-03B, NGHP-01-05C, NGHP-01-14A, NGHP-01-15A, NGHP-01-16A and NGHP-01-07B, in the Krishna-Godavari (K-G) basin, Bay of Bengal. Bathymetry data of the studied area was obtained from GEBCO Compilation Group665 (2020) GEBCO 2020 Grid (10.5285/a29c5465-b138-234d-e053-6c86abc040b9).*

Despite of extensive environmental and rock magnetic research focussing on understanding magnetic mineral diagenesis in the marine gas-hydrate sedimentary system, there is no systematic study till date which examines how magnetic minerals selectively respond to a range of diagenetic processes in the sulfidic and methanic environments respectively. The K-G basin is characterized by highly dynamic depositional (high sedimentation rates, shale-tectonism, active cold seeps, shallow and deep-seated gas-hydrates) conditions and represents a suitable sedimentary environment to study geological and geochemical controls on the magnetic mineral diagenesis. The sediment core (NGHP-01-20A) retrieved from the region prone to high sedimentation in the K-G basin provided a suitable environment to investigate how a range of diagenetic processes in the sulfidic and methanic conditions modify the sediment magnetic signals. In the present study, a 148.8 m long sediment core (NGHP-01-20A) retrieved from the K-G basin during the first Indian National Gas-hydrate Drilling Expedition (NGHP-Exp-01) offered an excellent opportunity to evaluate the impact of progressive diagenetic dissolution, maghemitization, and sulphidization of detrital magnetic particles on the sediment rock magnetic properties in the marine gas-hydrate system using rock magnetic method. A comprehensive SEM-EDS analysis was employed to systematically visualize the mechanisms of diagenetic alterations and the selective response of magnetic particles in the sulfidic and methanic sediments. For site selection, our assessment regarding the impact of detrital sedimentation and diagenesis on the rock magnetic sediment record of the core NGHP-01-20A was based on the recent findings of Johnson et al (2021) which successfully isolated the detrital and diagenetic signals based on the good correlation between Zr/Rb and χ records of methane-bearing marine sediment cores. The studied sites (NGHP-01-16A, NGHP-01-10D; Johnson et al., 2021) are proximal to the core location (NGHP-01-20A; present study) in the K-G basin, Bay of Bengal.

3.6. Results

3.6.1. Rock magnetic and geochemical properties of sediment core NGHP-01-20A

Five distinct sediment magnetic zones (Z-I to Z-V) were defined based on the down-core variations in χ_{lf} and SIRM (Figure 3.16). A trend of downcore reduction in χ_{lf} and SIRM in the uppermost zone (Z-I: 3.5 to 8.5 mbsf) indicated decline in magnetic mineral content (Figure

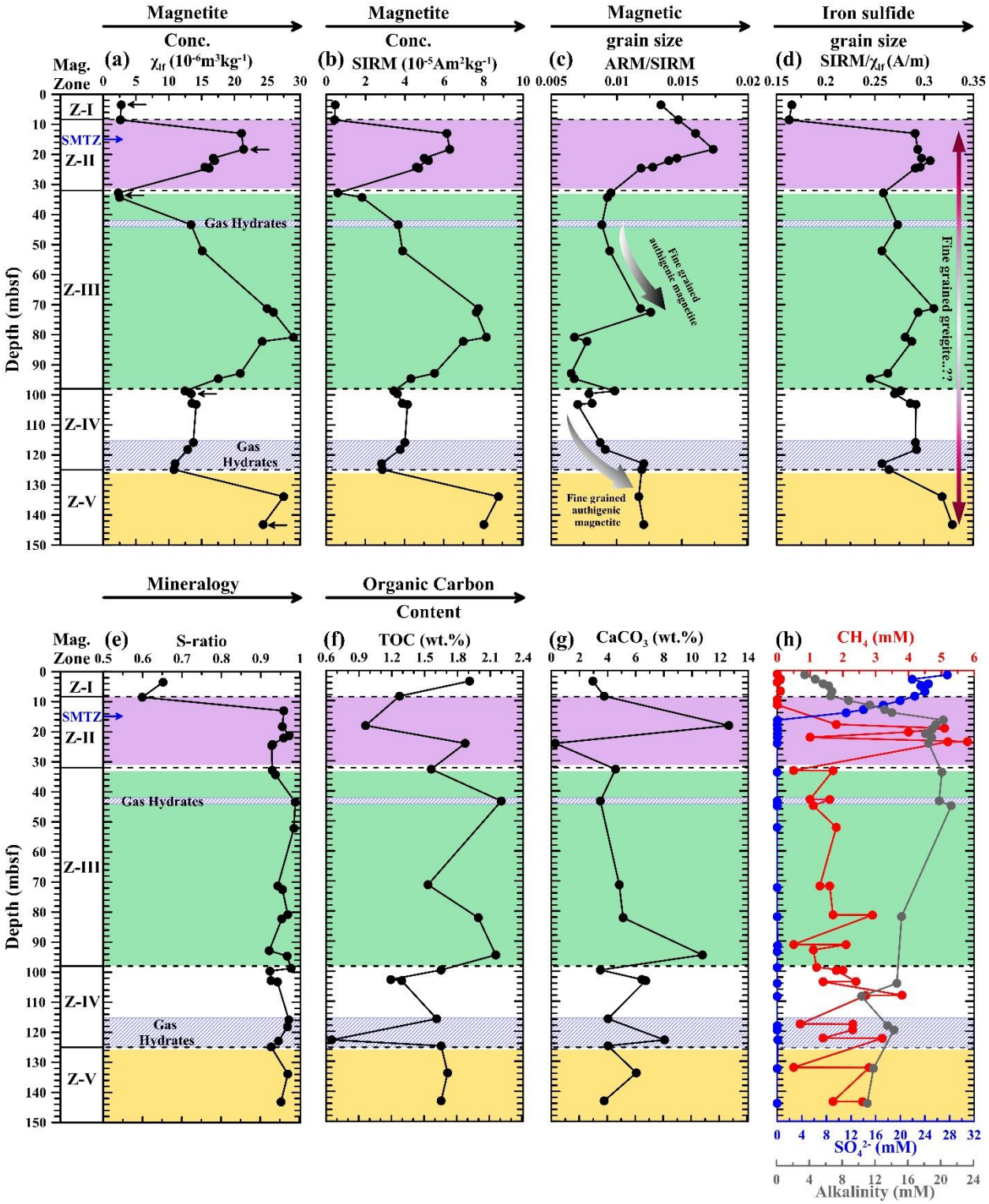

Figure 3.16: *Depth variations of (a–e) selected magnetic and (f–h) geochemical parameters for sediment core NGHP-01-20A. Three magnetite-rich bands exhibiting higher values of magnetic susceptibility have been identified. Magnetite-rich band in sediment magnetic zones Z– II, Z-III,*

and Z-V are highlighted by pink, green and yellow color shading respectively. The depth of sulfate-methane transition zone (SMTZ) is marked by blue arrow. The sediment depth intervals of pyrite nodules occurrence are highlighted in solid black arrows (horizontal). (Please note that χ_{lf} = low frequency magnetic susceptibility; ARM = anhysteretic remanent magnetization; and SIRM = saturation isothermal remanent magnetization).

3.16a, b). The Z-II (13.0 to 32.81 mbsf), Z-III (34.29 to 98.71 mbsf), and Z-V (99.62 to 124.83 mbsf) were marked by a notable enhancement in χ_{lf} and SIRM, but exhibit different trends in ARM/SIRM profile (Figure 3.16a-c). The Z-IV (133.87 to 143.19 mbsf) was marked by relatively lower χ_{lf} and SIRM compared to Z-III and Z-V. A trend of rise in magnetic grain size proxy (ARM/SIRM) in Z-IV and Z-V suggested the presence of fine-grained magnetic particles (Figure 3.16c; Peters and Dekkers, 2003). A gradual downcore rise in ARM/SIRM in Z-II (8.5 to 18.29 mbsf), Z-III (43.4 to 72.53 mbsf), and Z-V (122.9 to 143.19 mbsf) suggested the dominance of fine-grained authigenic magnetite or greigite (Figure 3.16c; Rodelli et al., 2019; Lin et al., 2021). S-ratio is a magnetic mineralogy diagnostic proxy and provides information on the relative proportion of ferri- and antiferromagnetic particles in the sediment sample (Liu et al., 2012). Overall, the S-ratio profile showed uniformity and close to unity, but exhibit a distinct shift between Z-I and other zones (Figure 3.16e). This observation suggested that bulk magnetic mineralogy of Z-II to Z-V is unequivocally characterized by ferrimagnetic minerals. Comparatively, Z-I is dominated by the presence of hard coercive minerals as seen through a drop in S-ratio (Figure 3.16e). Magnetic iron sulphide diagnostic proxy (SIRM/χ_{lf}; Larrasoaña et al., 2007) mimicked the S-ratio profile and showed a marked shift at the end of Z-I suggesting a significant increase in the proportion of ferrimagnetic (greigite, pyrrhotite) iron sulphides (Figure 3.16e; Snowball and Thompson, 1990; Maher and Thompson, 1999; Peters and Dekkers, 2003). In general, TOC and $CaCO_3$ content showed large fluctuations throughout the core (Figure 3.16f, g). Initially, TOC decreased from 3.5 mbsf to 18.19 mbsf in Z-I and later increased downcore from 24.2 mbsf to 94.63 mbsf except in Z-IV (Figure 3.16f). The $CaCO_3$ profile showed peak in Z-II and did not exhibit any specific trends in other zones (Figure 3.16g).

3.6.2. Temperature-dependent magnetic susceptibility (χ-T) Curves and Day Plot

The χ-T data has been utilized for determining the changes in magnetic mineral composition of marine sediments (Liu et al., 2005). The χ-T curves for selected bulk sediment samples representing different magnetic zones are shown in Figure 3.17a-n. A major decline in magnetization between 419°C and 644°C in majority of the samples indicated that the bulk magnetic mineralogy is governed by titanomagnetite (Figure 3.17; Dunlop et al., 1997).

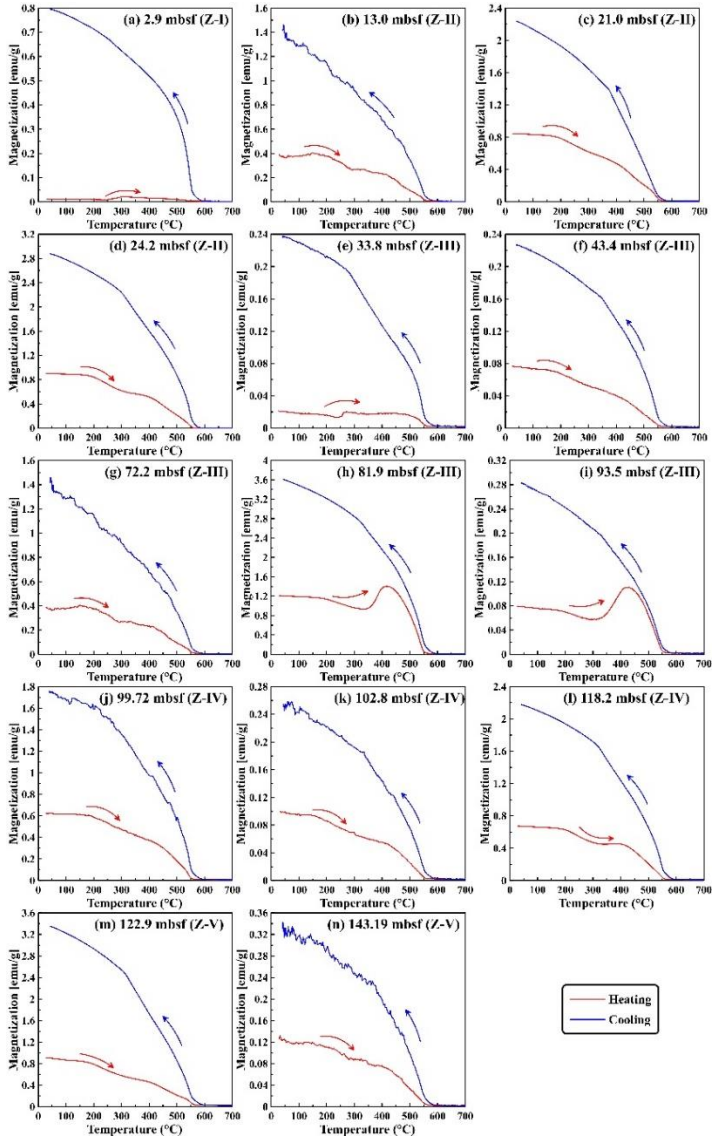

Figure 3.17: ***(a–n)*** *Temperature dependence of magnetic susceptibility (χ-T) for selected representative samples from the five sediment zones (Z-I, Z-II, Z-III, Z-IV, Z-V) of the studied sediment core NGHP-01-20A are presented. Solid red and blue lines indicate heating and*

cooling curves respectively. The respective magnetic minerals titanomagnetite (TM) and pyrite (Py) identified based on the χ-T curves are mentioned in the plot.

A minor rise in χ between 270°C and 492°C suggested the dominance of either titanomagnetite particles possessing wide range of Ti-contents (Lattard et al., 2006), or conversion of pyrite into magnetite due to heating (Figure 3.17; Passier et al., 2001). The day plot showed that all the samples lie on the SD-MD mixing line (Day et al., 1977; Dunlop, 2002) (Figure 3.18d).

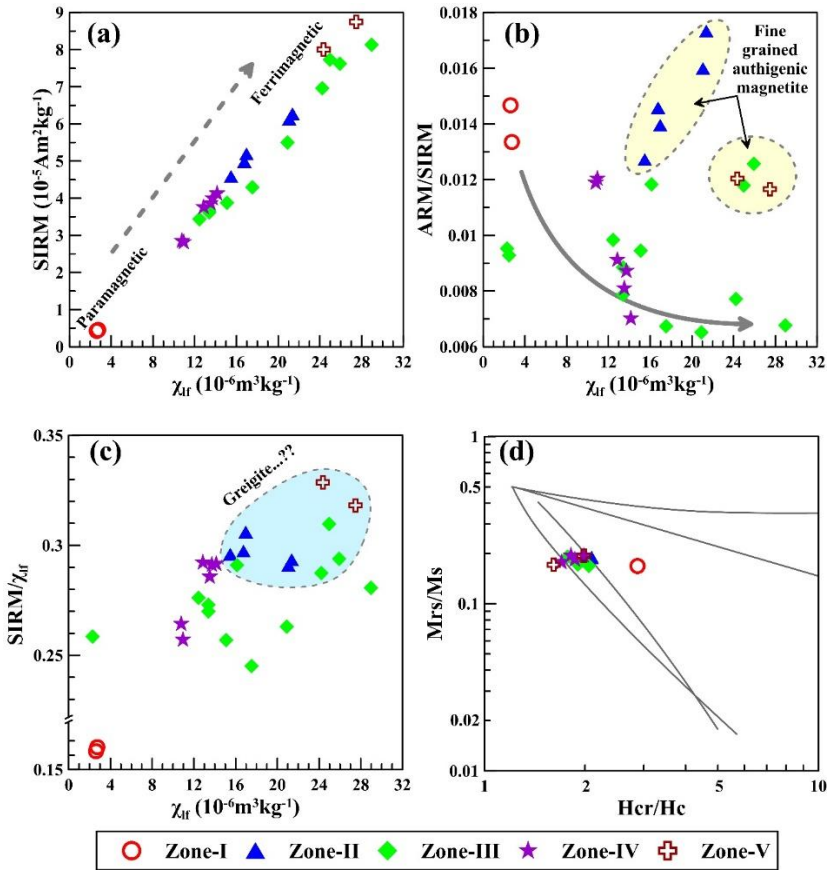

Figure 3.18: ***(a–f)*** *Bivariate scatter plots of magnetic parameters: magnetic susceptibility (χ_{lf}), saturation isothermal remanent magnetization (SIRM), ARM/SIRM, SIRM/χlf, total organic carbon (TOC), calcium carbonate ($CaCO_3$) and Day plot of NGHP-01-20A from the Krishna-Godavari (K-G) basin, Bay of Bengal. The gray arrows are used only to highlight the observed trends in plots.*

3.6.3. Mineralogical analyses of magnetic particles and optical microscopy

SEM-EDS analyses complemented the rock magnetic observations and further confirmed that titanomagnetite was the major magnetic mineral in the studied core (Figures 3.19-3.24). Based on the composition and morphology, detrital ferrimagnetic (titanomagnetite), altered (titanomaghemite, titanohematite) and diagenetically formed iron sulphide (pyrite) grains of various sizes and shapes in the different sediment magnetic zones were identified (Figures 3.19-3.24). Detrital titanomagnetite grains in the uppermost zone (Z-I) appear fresh and well-preserved (Figure 3.19). Signatures of diagenetic dissolution and low-temperature maghemitization of detrital titanomagnetite particles including etching, pits, skeleton lamellae, and distinct shrinkage cracks were noticed (Figures 3.21-3.22). Few titanohematite particles showed lamellae-like features reflecting pervasive oxidation of primary titanomagnetite (Figure 3.22b-c). Diagenetically formed pyrite occurs as individual crystals on the surface of Fe-Ti grains (Figures 3.20-3.24) in the methanic zones (Z-II to Z-V). Several bands of diagenetically formed pyrite nodules of various sizes and shapes were found to occur throughout the core (Figure 3.25).

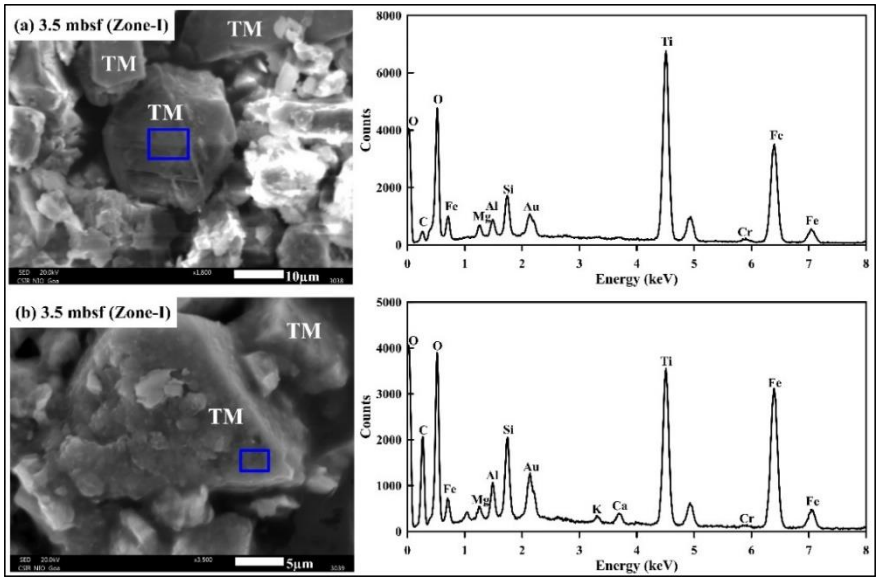

Figure 3.19: ***(a–b)*** *Scanning electron microscopy (SEM) images of magnetic particles extracted from sediment magnetic zone (Z-I) of the sediment core NGHP-01-20A. (a-b) well-preserved detrital titanomagnetite (TM) grain. The blue color square represents the area selected for generation of energy dispersive X-ray spectra (EDS).*

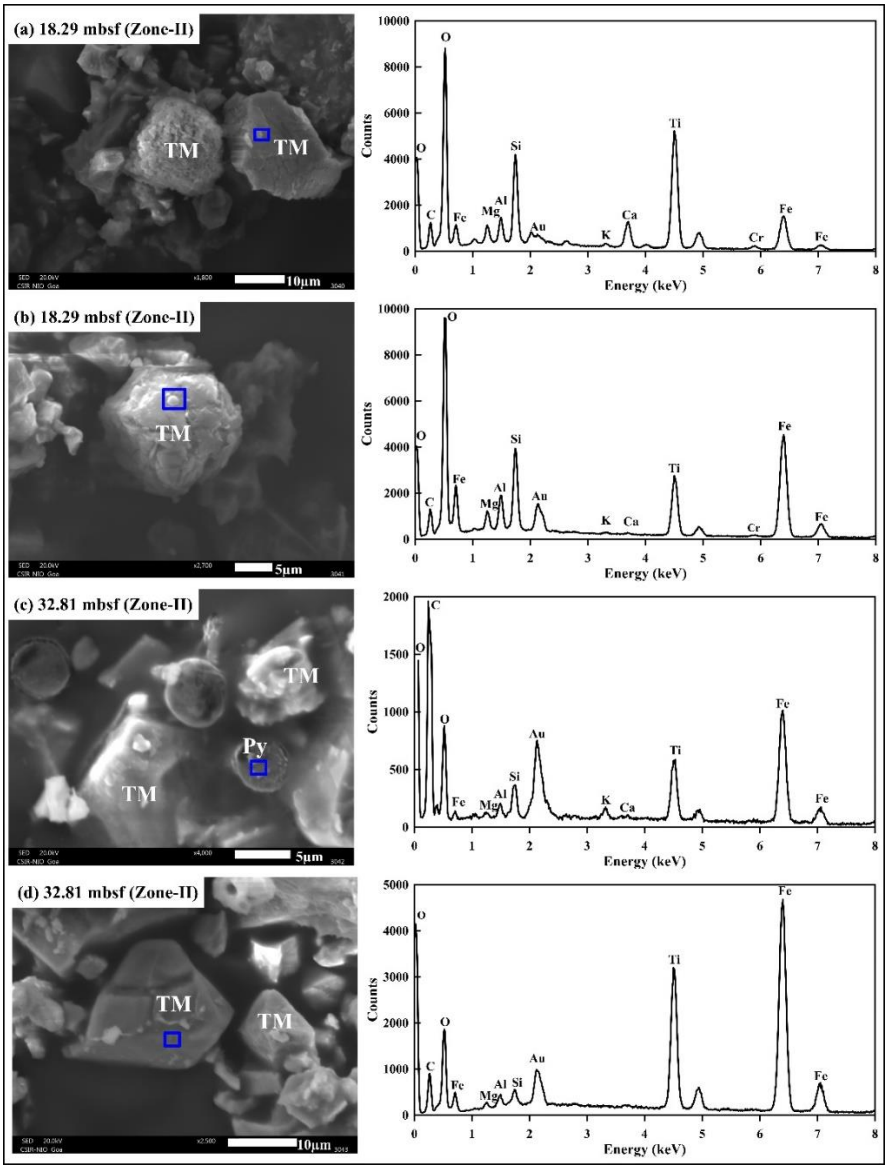

Figure 3.20: ***(a–d)*** *Scanning electron microscopy (SEM) images of magnetic particles extracted from sediment magnetic zone (Z-II) of the sediment core NGHP-01-20A. (a,d) Diagenetically altered titanomagnetite (TM) grains exhibiting dissolution features. Signatures of minor low-temperature oxidation are noticed, (b) Detrital titanomagnetite (TM) grain showing partial dissolution, and (c) Diagnetically formed iron-sulphides (pyrite; Py) occur as individual fine-grained crystals on the surface of titanomagnetite (TM) grain. The blue color square represents the area selected for generation of energy dispersive X-ray spectra (EDS).*

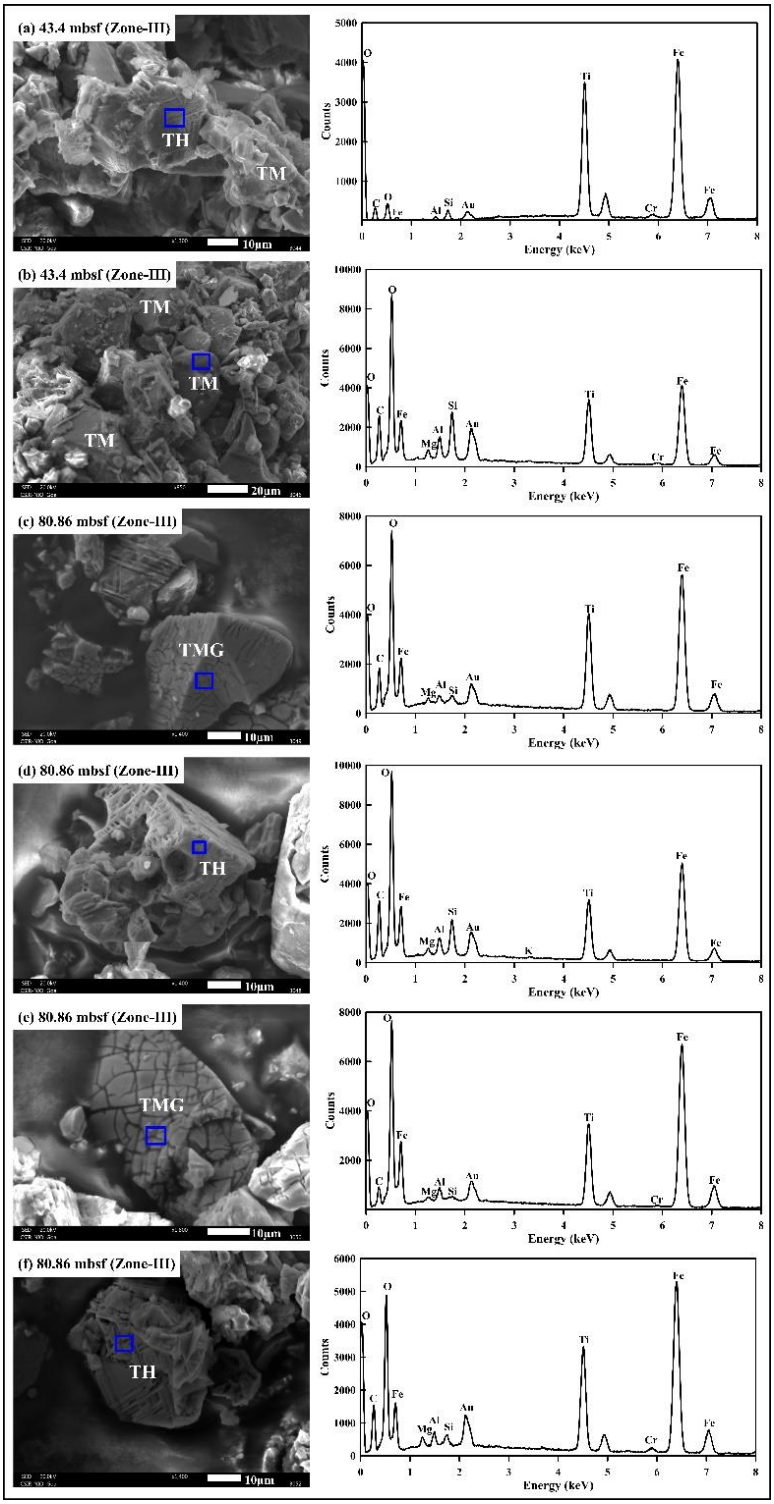

Figure 3.21: ***(a–f)*** *Scanning electron microscopy (SEM) images of magnetic particles extracted from sediment magnetic zone (Z-III) of the sediment core NGHP-01-20A. (a,d,f) Titanohematite (TH) grains exhibiting skeletal and lamellae like structure resulting from oxidation of*

titanomagnetite, (b) Well-preserved detrital titanomagnetite (TM) grains, (c,e) Titanomaghemite (TMG) grains exhibiting shrinkage cracks typical features linked with low-temperature maghemitization. The blue color square represents the area selected for generation of energy dispersive X-ray spectra (EDS).

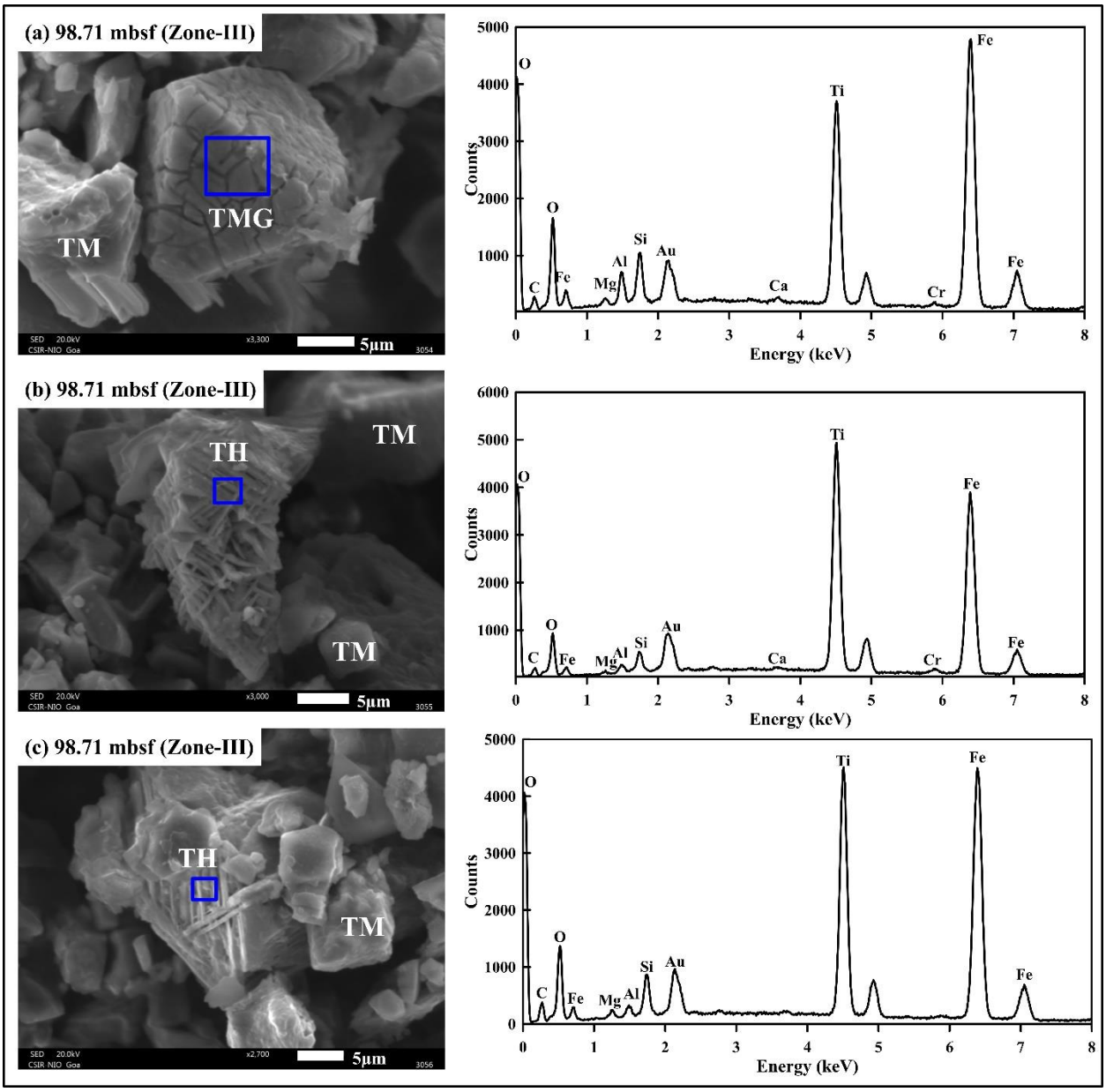

Figure 3.22: (*a–c)* *Scanning electron microscopy (SEM) images of magnetic particles extracted from sediment magnetic zone (Z-III) of the sediment core NGHP-01-20A (a) Titanomaghemite (TMG) grain characterized by shrinkage cracks formed due to low-temperature maghemitization, (b,c) Titanohematite (TH) grains exhibiting lamellae-like features reflecting*

pervasive oxidation of titanomagnetite. The blue color square represents the area selected for generation of energy dispersive X-ray spectra (EDS).

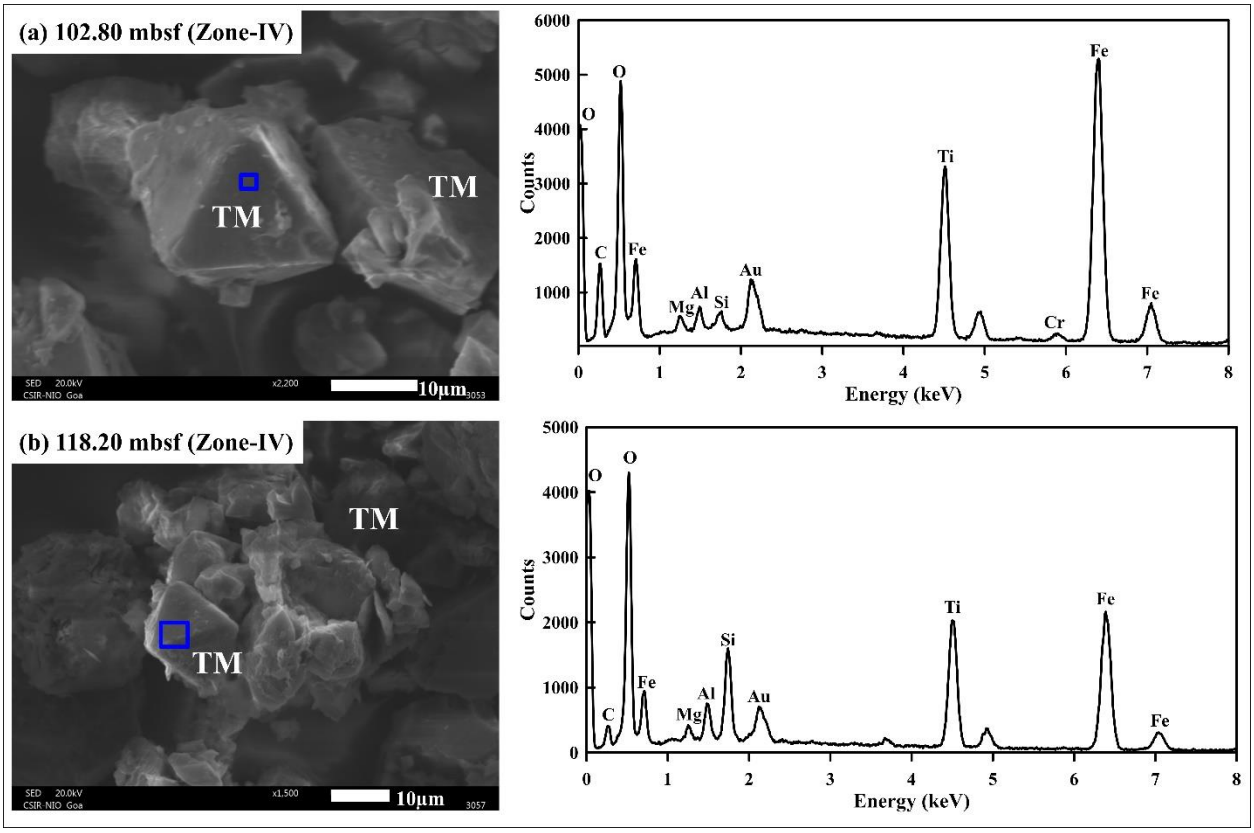

Figure 3.23: ***(a–b)*** *Scanning electron microscopy (SEM) images of magnetic particles extracted from sediment magnetic zone (Z-IV) of the sediment core NGHP-01-20A. (a,b) Well-preserved detrital titanomagnetite (TM) grains. The blue color square represents the area selected for generation of energy dispersive X-ray spectra (EDS).*

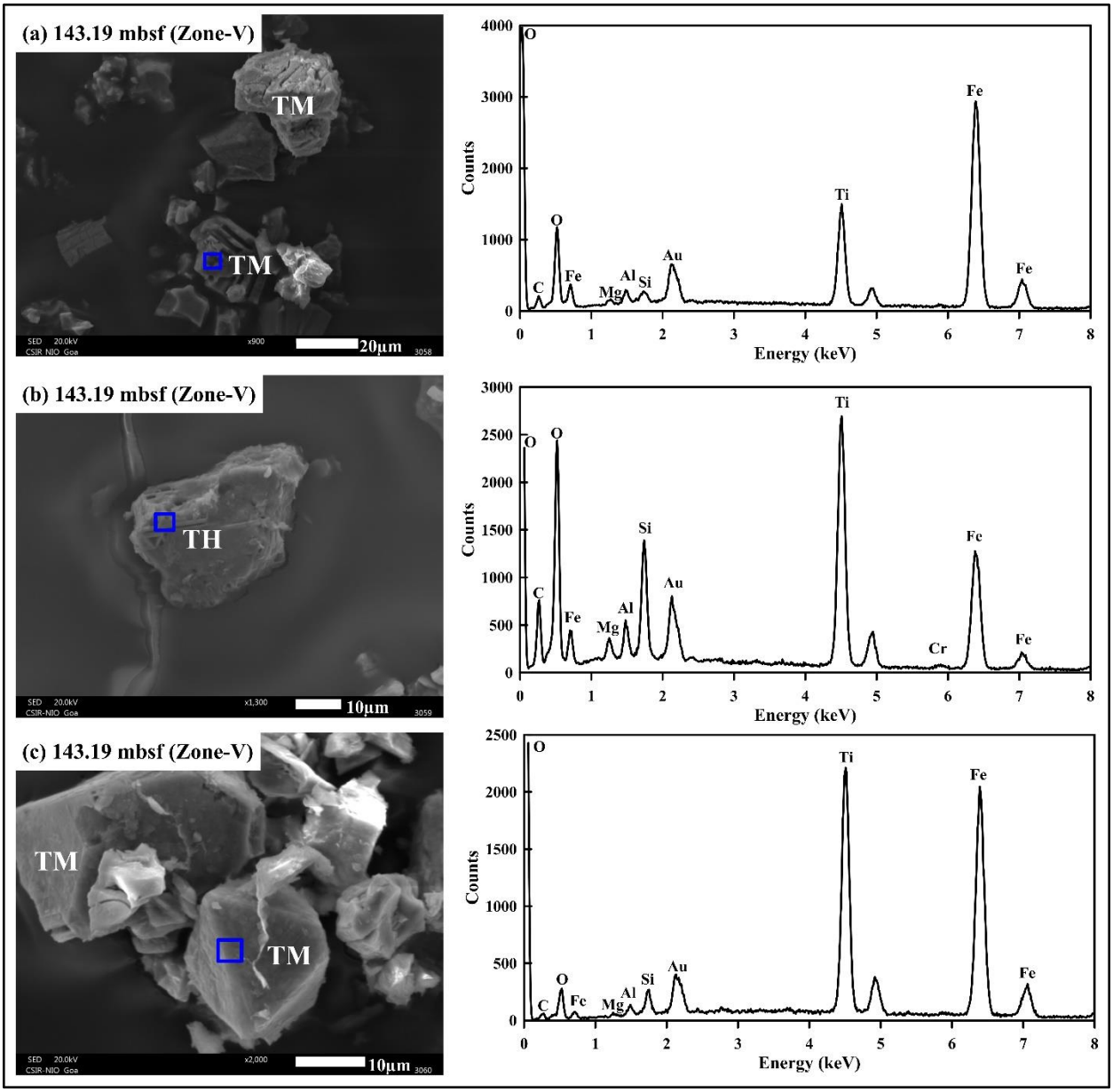

Figure 3.24: ***(a–c)*** *Scanning electron microscopy (SEM) images of magnetic particles extracted from sediment magnetic zone (Z-V) of the sediment core NGHP-01-20A. (a,b) Titanomagnetite (TM) grains of detrital origin. Few grains showed signature of low-temperature maghemitization, (b) Titanohematite (TH) grains exhibiting lamellae-like features resulting from oxidation of titanomagnetite, (c) Well-preserved detrital titanomagnetite (TM) grains. The blue color square represents the area selected for generation of energy dispersive X-ray spectra (EDS).*

3.7. Discussion

Room and high-temperature based magnetic data combined with SEM-EDS observations provided valuable insights into the magnetic mineral assemblages in core NGHP-01-20A. Data showed that the magnetic particles have encountered severe diagenetic dissolution, maghemitization, and sulphidization in the sulfidic and methanic zones. Rock magnetic record of core NGHP-01-20A helped to define five sediment magnetic zones. In this section, magnetic particle composition, grain size, and morphology-based information were evaluated to investigate how magnetic particles respond to primary (detrital) and secondary (diagenesis, authigenesis) processes in marine gas-hydrate-bearing sedimentary systems of the K-G basin, Bay of Bengal.

3.7.1. Rock magnetism of Sediment Core NGHP-01-20A

Rock magnetism of core NGHP-01-20A representing deep-seated gas-hydrate system was carried by complicated magnetic mineral assemblages comprised of detrital (titanomagnetite, silicate-hosted magnetic inclusions), altered (titanomaghemite, titanohematite), diagenetic (pyrite), and authigenic (magnetite, greigite) as confirmed through rock magnetic, SEM-EDS and optical microscopy (Figures 3.16, 3.17, 3.19-3.24, 3.26). Microbial iron-reduction in anoxic sediments is driven by (a) dissimilatory iron-reducing bacteria (DIRB) (Moskowitz, 1995; Roberts, 2015), (b) methanogens which favoured methanogenesis to iron-reduction (Sivan et al., 2016), and (c) iron-reduction coupled to AOM (Egger et al., 2014). Magnetic grain size diagnostic (ARM/SIRM) proxy has been successfully used to detect the presence of fine-grained authigenic magnetite (Figure 3.16c; Dillon and Bleil, 2006; Lin et al., 2021) in methanic sediments. A recent study by Lin et al (2021) reported a novel authigenic nanoscale magnetite source in methane seep sediments from South China Sea. They attributed the increase in ARM/SIRM in methanic zone to the presence of authigenic magnetite formed as a result of microbial iron-reduction process which permitted the newly formed magnetite to survive the sulfidic dissolution and favored preservation. Initial decrease of ARM/SIRM values in core NGHP-01-20A was linked with the preferential dissolution of fine-grained magnetic particles in the uppermost sulfidic zone (Z-I). Downcore increase of ARM/SIRM in Z-II (vicinity of present-day SMTZ) and methanic zones (Z-III: 43.4 to 72.53 mbsf, Z-IV: 98.71 to 102.8 mbsf; Z-V: 133.87 to 143.19 mbsf) was attributed to the magnetite authigenesis linked with the

microbial iron-reduction process which probably permitted the preservation of newly formed authigenic magnetite (Figure 3.16c; Dillon and Bleil, 2006; Roberts, 2015; Chang et al., 2016; Rodelli et al., 2019; Gaikwad et al., 2021; Lin et al., 2021). As highlighted by Lin et al., 2021, χ_{lf} fluctuations in methanic zones (Z-III to Z-V) indicated vertical migration of SMTZ in core NGHP-01-20A controlled by varying methane fluxes (Figure 3.16h), which is common in gas-hydrate-bearing sites for example in continental margin offshore of Argentina and Uruguay (Riedinger et al., 2005), southwestern Taiwan (Horng and Chen, 2006), and Nankai Margin, southwestern Japan (Kars and Kodama, 2015a; Shi et al., 2017). It is highly likely that higher sulphide concentration produced during intense AOM driven by enhanced methane seepage events in the past might have promoted pyrite formation at paleo-SMTZ intervals in Z-III to Z-V.

During low methane seepage, downward diffusing seawater sulfate might have enhanced the oxidation of previously formed iron sulphides at the paleo-SMTZ position resulting in the production of secondary iron (oxyhydr)oxides which acted as a potential reactive iron source for magnetite authigenesis (Lin et al., 2021). Therefore, it was proposed that the authigenic formation of fine-grained magnetite in the anoxic (methanic) environment of Z-II (8.5 to 18.29 mbsf), Z-III (43.4 to 72.53 mbsf), Z-IV (98.71 to 118.2 mbsf), and Z-V (122.9 to 143.19 mbsf) of core NGHP-01-20A was most likely driven by magnetite authigenesis coupled microbial iron-reduction processes. Biogenic (magnetite, greigite) minerals formed by biomineralization are widespread in marine sediments (Karlin and Levi, 1983; Mann et al., 1990; Moskowitz et al., 1993; Tarduno and Wilkison, 1996; Chang et al., 2013, 2014; Roberts, 2015; Rodelli et al., 2019). As confirmed through SEM-EDS, the magnetic particles were mainly dominated by detrital titanomagnetites. The presence of biogenic minerals was expected, but was not detect in the analyzed samples probably due to the limitation of our detection (microscopy, rock magnetic) techniques. However, TEM and FORC may provide confirmation on its presence.

Magnetic iron sulphide diagnostic proxy (SIRM/χ_{lf}) revealed two distinct trends (Figure 3.16d; Snowball and Thompson, 1990; Maher and Thompson, 1999; Peters and Dekkers, 2003). Initial lower values of SIRM/χ_{lf} values in Z-I suggested the presence of coarse-grained magnetic particles (Figure 3.16d). Relatively higher values and a consistent trend of SIRM/χ_{lf} from Z-II to Z-V points on the plausible presence of fine-grained authigenic greigite in these zones (Figure 3.16d; Larrasoaña et al., 2007; Kars et al., 2015; Amiel et al., 2020). The dominance of greigite

in these zones suggested that the in situ geochemical conditions probably supported the authigenic formation of greigite by inhibiting the pyritization process in the past. High sedimentation interval generated by intense monsoon-driven weathering and erosional processes might have resulted in a weaker and short-lived AOM which produced a low concentration of dissolved hydrogen sulphide and preferentially affected the completion of the pyritization process and rather favoured the greigite formation (Figure 3.16d; Housen and Musgrave, 1996; Larrasoaña et al., 2007; Kars and Kodama, 2015; Dewangan et al., 2013; Badesab et al., 2019). Lack of presence of greigite in our SEM-EDS records was explained based on the fact that previously formed unstable ferrimagnetic greigite might have got transformed into more stable pyrite (Kao et al., 2004; Larrasoaña et al. 2007; Kars and Kodama, 2015). The presence of pyrite (Figures 3.20, 3.21, 3.24) within magnetically enhanced intervals (Z-II, Z-III, Z-V) provided support for the above interpretation. The overall contribution of paramagnetic (pyrite) minerals transformed from the ferrimagnetic (greigite) mineral phase was negligible, compared to the bulk magnetic signal exhibited by Fe-Ti particles of varying size and concentration. Hence, the bulk magnetic susceptibility values in this core remained high even after the significant conversion of ferrimagnetic (greigite) to paramagnetic (pyrite) iron sulphide.

3.7.2. Lines of evidence of diagenetic dissolution, maghemitization, and oxidation of titanomagnetite in a rapidly deposited methane-bearing sediments from the Bay of Bengal.

Precise identification of magnetic minerals in methanic sediments is a prerequisite to constrain the information related to primary (provenance) and post-depositional (diagenetic/authigenic) processes from the magnetic proxies. In the present study, SEM-EDS observations (Figures 3.19-3.24) on magnetic particles from sulfidic and methanic sedimentary zones yielded direct evidence to help understand the impact of detrital sedimentation, diagenetic and authigenic processes on the rock magnetism of a sediment core NGHP-01-20A. SEM observations combined with EDS analyses provided information on the overall composition, grains size, morphology, state of preservation, and genesis of sedimentary (detrital and diagenetic) magnetic minerals (Figures 3.19-3.24). Based on the comprehensive documentation, six different types of magnetic mineral assemblages were identified (Figures 3.19-3.24). Detrital titanomagnetite, with angular, irregular, spherical and well-defined octahedral with micron and submicron-sized particles mainly related to DVP constituted the type-1 particles (Figure 3.19a, b,

Figure 3.20a-d, Figure 3.21b, Figure 3.23a, b, Figure 3.24a-c). Titanomaghemites represented type – 2 particles and are characterized by shrinkage cracks formed as a result of low-temperature maghemitization process after initial deposition (Figure 3.21c, e, Figure 3.22a, Figure 3.24a). Titanohematites exhibiting lamellae like features resulting from oxidation of titanomagnetite represented type-3 particles (Figure 3.21a, c, d, Figure 3.22b, c, Figure 3.24b). Diagenetically altered titanomagnetites constituted type-4 particles and showed dissolution features including severe etching, pits, and skeleton lamellar-like structures (Figure 3.20a, d, Figure 3.21a, d, Figure 3.24b). Fine-grained diagenetically formed iron sulphides (pyrite,) occurring on Fe-Ti grains represented type – 5 particles (Figure 3.19a, Figure 3.20c, Figure 3.21,c, d, Figure 3.24a). Silicate-hosted magnetic grains formed from exsolution within host silicates constituted type – 6 assemblages (Figure 3.26). The optical microscopy showed pyrite nodules exhibiting partial, intermediate, and full oxidation stages of magnetic particles (Figure 3.25).

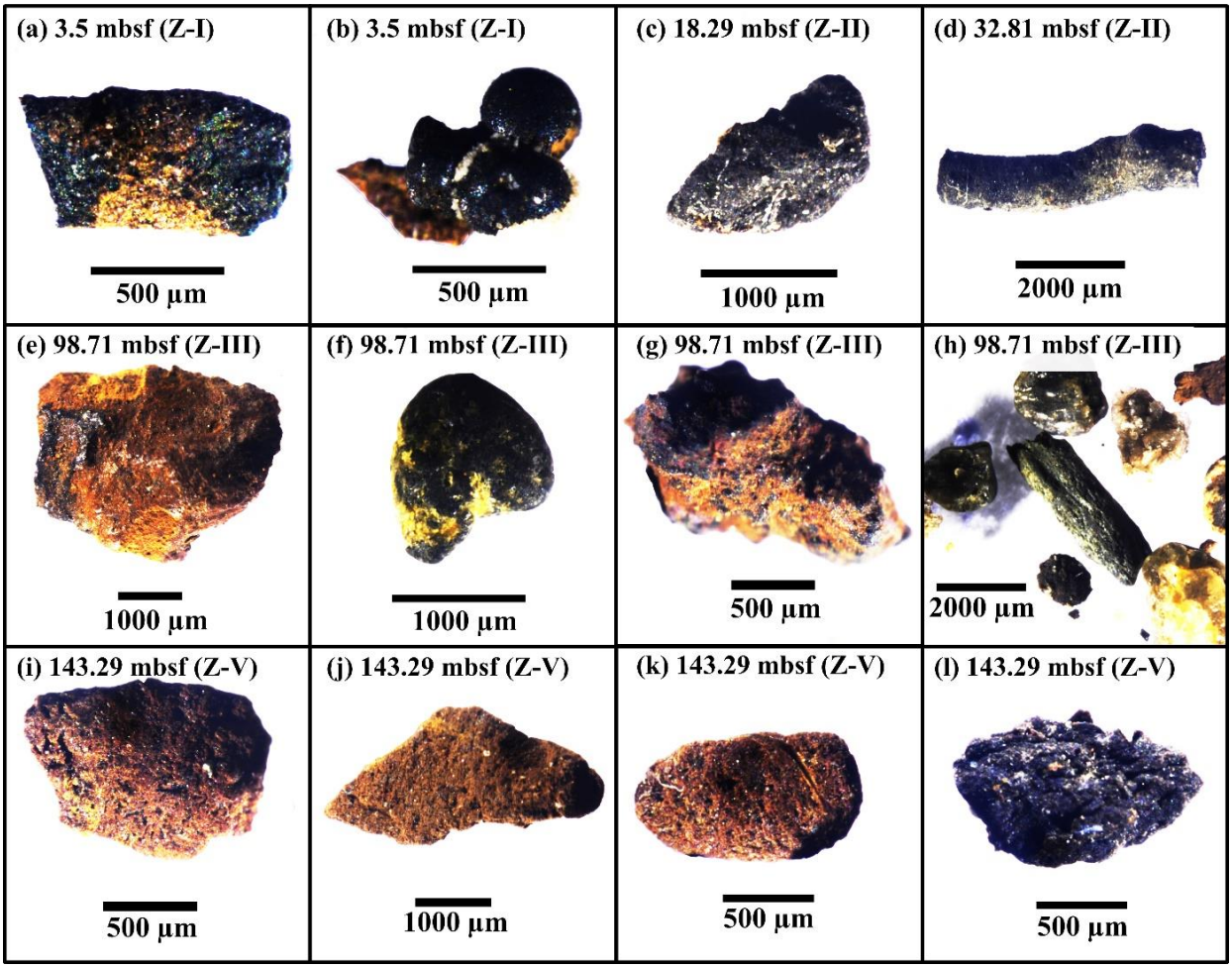

Figure 3.25: ***(a – l)*** *Optical microscopic images of the pyrite nodules separated from the sediment core NGHP-01-20A. The overgrowth (orange-reddish color) of pyrite on the magnetite grains is highlighted using arrows (white color).*

3.7.2.1. Detrital sedimentation

The Deccan basalts of DVP are the principal source of the continental slope sediment off the K-G basin (Sangode et al., 2001; Dewangan et al., 2013; Usapkar et al., 2014). The dominance of well-preserved coarse-grained (Figures 3.19-3.24) titanomagnetite grains throughout the core suggests that the detrital magnetic particles are mainly sourced from Deccan basalts and were delivered to the Bay of Bengal by the Krishna and Godavari River systems. Detrital titanomagnetites grains from all sediment magnetic zones showed high variability in shape, size, composition, and state of alteration and preservation (Figures 3.19-3.24). The majority of the particles were well-preserved and idiomorphic in shape. In general, titanomagnetite grains throughout the core exhibited well-preserved structure as well as skeleton and ilmenite-lamellae which were mainly evolved by the low-temperature exsolution of titanomagnetite (Figures 3.19-3.24; Garming et al., 2007; Dillon and Franke, 2009; Nowaczyk, 2011). Few magnetic grains showed numerous shrinkage cracks and lamellar structures which provided evidence for the maghemitization of Fe-Ti particles (Figures 3.21, 3.22, 3.24; Özdemir and Dunlop, 2010; Chang et al., 2013; Roberts, 2015; Qian et al., 2021). In Z-III, titanomagnetite particles showed clear etching on the surface indicative action of etching acids which created a wooden bark-like texture is noticed (Figures 3.21-3.22). The titanomagnetite and titanomaghemite grains were characterized by shrinkage cracks and skeleton lamellae wherein lattice in the crystals have been disturbed due to diagenetic dissolution and low-temperature exsolution from the titanomagnetite which probably led to the creation of such structures in the titanomagnetite grains (Garming et al., 2005, 2007; Nowaczyk, 2011; Just et al., 2012; Gaikwad et al., 2021).

3.7.2.2. Diagenetic dissolution and maghemitization of Fe-Ti particles

Diagenetic dissolution of titanomagnetite and preservation of titanohematite is characteristic of a strongly reducing environment (Garming et al., 2007; Canfield and Thamdrup, 2009; Roberts, 2015). The oxidized individual magnetic grains showed moderate to a high

degree of dissolution of the low Ti-bearing titanomagnetite particles thereby leaving the high Ti-rich titanohematite lamellae intact. Such magnetic particles were commonly noticed in Z-II and Z-III (Figures 3.20-3.22). Previously Garming et al. (2005) highlighted that preferential diffusion of Fe^{2+} out of titanomagnetite grains during diagenesis is much easier compared to hematite and titanohematite particles which are highly stable and exhibit strong resistance against dissolution. The presence of abundant titanohematite grains in the same magnetic zones (Z-II and Z-III) provided evidence of the stability of the Ti-rich magnetic particles which offered more resistance to diagenetic dissolutions compared to titanomagnetite (Hounslow et al., 1995; Poulton et al., 2004; Garming et al., 2005; Franke et al., 2007; Nowaczyk, 2011; Roberts, 2015 João et al., 2021).

In marine sediments, partial magnetite oxidation (maghemitization) is a common process and can significantly influence the room as well as temperature-dependent rock magnetic parameters (Karlin, 1990; Özdemir and Dunlop, 2010; Yamazaki and Solheid, 2011; Roberts, 2015). The maghemitization process mainly involves preferential leaching of Fe^{2+} out of titanomagnetite, since it gets quickly detached from the mineral structure as compared to Fe^{3+} and creates lattice vacancies (Cornell and Schwertmann, 1996; Smirnov and Tarduno, 2000; Garming et al., 2005; Roberts, 2015). Irregular, curved shrinkage cracks on the surface of magnetic particles resulting from the internal stress caused by surficial oxidation are the characteristics of maghemitization (Figures 3.21-3.22; Petersen and Vali, 1987; Nowaczyk, 2011; Höfken et al., 2021). A recent rock magnetic and electron microscopy-based studies on the magnetic particles from eastern Mediterranean sediments (Qian et al., 2021) and ridge flank sediments of the East Pacific Rise (Höfken et al., 2021) provided useful insights into the step-wise maghemitization process wherein the surfaces of magnetite particles get maghemitized at oxidation fronts. The SEM-EDS data of core NGHP-01-20A provided evidence for the dominance of the maghemitization process as indicated by the irregular surface cracks and fragmentation on the titanomagnetite particles especially in Z-II and Z-III (Figures 3.21-3.22). Similar signatures of minor low-temperature oxidation were also noticed in Z-II (Figure 3.20a, d) and Z-V (Figure 3.24a). These observations suggested that maghemitization was a significant process in both sulfidic (Z-I) and methanic (Z-II to Z-V) environments.

3.7.2.3. Sulphidization

Diagenetically formed pyrite (yellowish-dark brown-orange) nodules were noticed in all sediment magnetic zones except Z-IV (Figure 3.25). Few pyrite nodules revealed thick layering and showed a strong affinity to the magnet during the separation process (Figure 3.25). Past studies reported similar growth of pyrite rim over the ferrimagnetic (magnetite and greigite) core for example, in the Dead Sea basin (Ebert et al., 2018), South Island, New Zealand (Roberts and Turner 1993; Rowan and Roberts, 2006), and the K-G basin, Bay of Bengal (Badesab et al., 2020a). As highlighted by Larrasoaña et al. (2007), the pyrite growth over magnetic particles in the studied core (NGHP-01-20A) indicated diagenetic transformation wherein dissolved sulphide most likely interacted with highly reactive iron available on the surface of ferrimagnetic iron-bearing oxide minerals and proceeded further towards pyritization. Moreover, Ebert et al (2018) explained that during sulphidization, the reactive iron is selectively leached out from the residual titanomagnetites and gets directly transformed into the pyrite layer which grows over the magnetite core. In the analyzed samples, the growth of pyrite over the magnetite core (Figure 3.25) suggested that the reactive iron required for pyritization was most likely made available through the surficial leaching of iron from abundant Fe-Ti particles. Non-uniform (yellowish-dark brown-orange colored) layering on the magnetite grains revealed the signature of different stages of pyritization of magnetic particles (Figure 3.25). The interpretation of the present study was consistent with the observations of Rowan and Roberts (2006), Rowan et al (2009), and Ebert et al (2018) which reported similar growth of iron sulphide i.e., pyrite rim over the titanomagnetite grains and further highlighted that the magnetism exhibited by the titanomagnetite core is strong and would therefore showed affinity towards magnetic probes as noticed during the separation of magnetic particles.

Preservation of organic carbon in a rapidly depositing marine sediments is controlled by the sedimentation rates, composition of organic matter, oxygen availability, sediment texture, temperature, and rates of oxic and suboxic processes (Burdige, 2007; Galy et al., 2007; Zonneveld et al., 2010). A good covariation between increased χ_{lf} and TOC content in the magnetically enhanced zones (Z-II, Z-III, Z-V) of core NGHP-01-20A was noticed (Figure 3.16a, f). Rigorous sediment mixing and reworking in a rapidly depositing marine sedimentary system can significantly affect the oxidation of labile organic matter and enhance its preservation

(Joao et al., 2021). Elevated TOC content in magnetite-rich zones (Z-II, Z-III, Z-V) was reconciled with the efficient preservation of labile organic matter due to increased sediment deposition. Higher TOC content (Figure 3.16a, f) in Z-II, Z-III, and Z-V was attributed to the changes in the burial and degradation of organic matter due to non-steady sedimentation which might have affected the remineralization rate and consequently constrained the methane-induced diagenetic reactions (Rey et al., 2005; Joao et al., 2021). Fluctuation in χ_{lf}, SIRM, and TOC content within these zones (Z-II, Z-III, Z-V) indicated continuous shifting of the diagenetic fronts at this site (Figure 3.16a, b, f). Such phenomena is well-reported from a rapidly depositing sediments from continental margins offshore of Argentina and Uruguay (Riedinger et al., 2005), offshore of North Island, New Zealand (Rowan and Roberts, 2006), K-G basin, Bay of Bengal (Joao et al., 2021; Mazumdar et al., 2012), and Nankai Margin, southwestern Japan (Kars and Kodama, 2015b). Methane-derived authigenic carbonates (MDAC) are distributed throughout the core NGHP-01-20A and indicated paleo-SMTZ positions. The mineralogy of MDAC comprised of iron-rich carbonate and low-magnesium calcite (LMC) (Teichert et al., 2014). The LMC was present in sediment magnetic zones exhibiting low χ_{lf} (Z-I: 9.6 mbsf, Z-III: 33.1 mbsf, Z-IV: 121.5 mbsf, 124.8 mbsf) (Figure 3.16a) and depleted $\delta^{13}C$ (−27.45 to −15.26 ‰ VPDB; Teichert et al., 2014) values suggesting a major role of AOM in these magnetically altered sediment intervals. Concurrently, the presence of siderite especially in magnetically enhanced zones (Z-III: 106.5 mbsf and Z-V: 133.6 mbsf, Teichert et al., 2014) suggested that the formation of enriched carbonates were mainly linked with silicate weathering reactions coupled to microbial methanogenesis which did not altered χ_{lf} (Solomon et al., 2014; Torres et al., 2020).

3.7.2.4. Silicate-hosted magnetic mineral inclusion

Magnetic mineral inclusions within silicate grains are ubiquitously distributed in marine sediments, and their size varies between a few nanometers to several micrometers with different morphologies (Hounslow, 1996; Hounslow and Morton, 2004; Roberts, 2015; Chang et al., 2016; 2021). The occurrence of titanomagnetite as well as diagenetically formed iron sulphides (greigite) nanoparticles as inclusions within silicate minerals were reported from hemipelagic marine sediments offshore, Japan (Chang et al., 2016), Okhotsk Sea (Jiang et al., 2021), North Pacific Ocean (Hong et al., 2019), and gas-hydrate-bearing sediments from the Bay of Bengal (Badesab et al., 2020; Gaikwad et al., 2021). A recent study focusing on magnetic mineral

diagenesis in methanic sediments from the Bay of Bengal proposed that silicate weathering and silica diagenesis triggered by past methane seepage events played a crucial role in the preservation of greigite as inclusions within silicate matrix (Badesab et al., 2020a). Optical microscopy analyses on the separated quartz grains (+ 63 µm) of core NGHP-01-20A revealed the presence of nanometer-sized magnetic particles hosted within silicates in addition to fine magnetic crystals occurring as a surface coating (Figure 3.26; Nowaczyk, 2011; Ebert et al., 2018). The data analyses revealed that the silicate-hosted magnetic inclusions protected the ferrimagnetic (titanomagnetite, magnetite, greigite) particles within the silicate matrix against the surrounding diagenetic fronts through geologic times and prevented its further conversion. However, TEM-EDS analyses on the quartz grains is further warranted to confirm the mineralogy of the fine-grained magnetic particles occurring as inclusions within silicate grains and can be taken up as a dedicated independent study in the future.

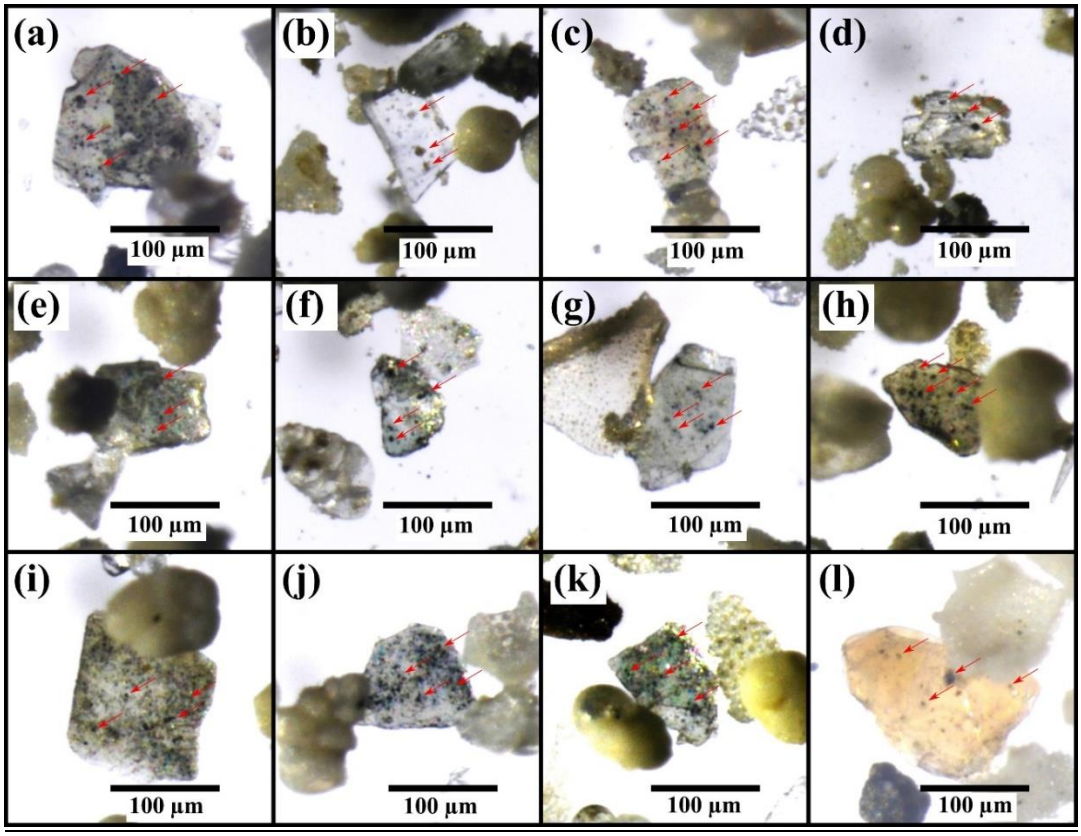

Figure 3.26: ***(a–l)*** *Optical microscopic images of the representative coarse fractions (>63 µm) from the different magnetic zones of sediment core NGHP-01-20A are presented. Fine-grained magnetic inclusion within host silicate minerals (>63 µm) fractions are marked (see red arrows).*

3.7.3. Control of rapid sedimentation events on the rock magnetism (*detrital vs diagenetic processes*)

The occurrence of high sedimentation rate events in the K-G basin is well-recorded from the seismic and multibeam bathymetry data, age, and sediment physical property data (Ramana et al., 2007; Ramprasad et al., 2011; Yamamoto et al., 2018). Large detrital magnetite grains with variable Ti-contents were found to be highly concentrated in a few magnetically enhanced sediment zones (Z-II, Z-III, Z-V) (Figures 3.16a, 3.20, 3.21, 3.22, 3.24). The presence of fine-grained SD magnetite was attributed to the authigenic magnetite formation via microbial iron-reduction as reflected in the downcore rise in ARM/SIRM (Figure 3.16c; Rodelli et al., 2019; Lin et al., 2021), or from smectite-derived iron during progressive diagenetic illitization (McCabe et al., 1989; Kars et al., 2021). The electron microscopy in combination with EDS analyses on the magnetic extracts confirmed the presence of abundant unaltered coarser magnetic grains primarily of detrital origin in each zone (Figures 3.19-3.24). This observation suggests that the higher sedimentation rates facilitated the rapid burial and preservation of the detrital magnetic particles soon after deposition which resulted in the formation of three distinct magnetite-rich bands in Z-II, Z-III, and Z-V (Figure 3.16, Figure 3.27). Few magnetic particles close to SMTZ depth showed the presence of partly dissolved titanomagnetite (Figure 3.20), suggesting the partial dissolution of the detrital titanomagnetite particles close to the SMTZ. It is most likely that, a significant portion of the detrital ferromagnetic particles survived the reductive diagenetic dissolution at SMTZ predominantly due to the increased sedimentation rate (Riedinger et al., 2005, 2014; Egger et al., 2017; Badesab et al., 2019; Johnson et al., 2021; Joao et al., 2021) or due to elevated episodic pulses of rising methane in Z-II to Z-V that led to quick migration of SMTZ fronts (Figure 3.16h; Sivan et al., 2007). The abundant occurrence of titanomagnetite coupled with high χ_{lf} in the deeper part (Z-V; Figure 3.16, Figure 3.24) of the core NGHP-01-20A also suggested that rapid sedimentation events favored the preservation of magnetic particles and inhibited the pyritization reactions by altering the AOM process which caused a decline in the production of sufficient hydrogen sulphide concentration required to trigger intense diagenesis.

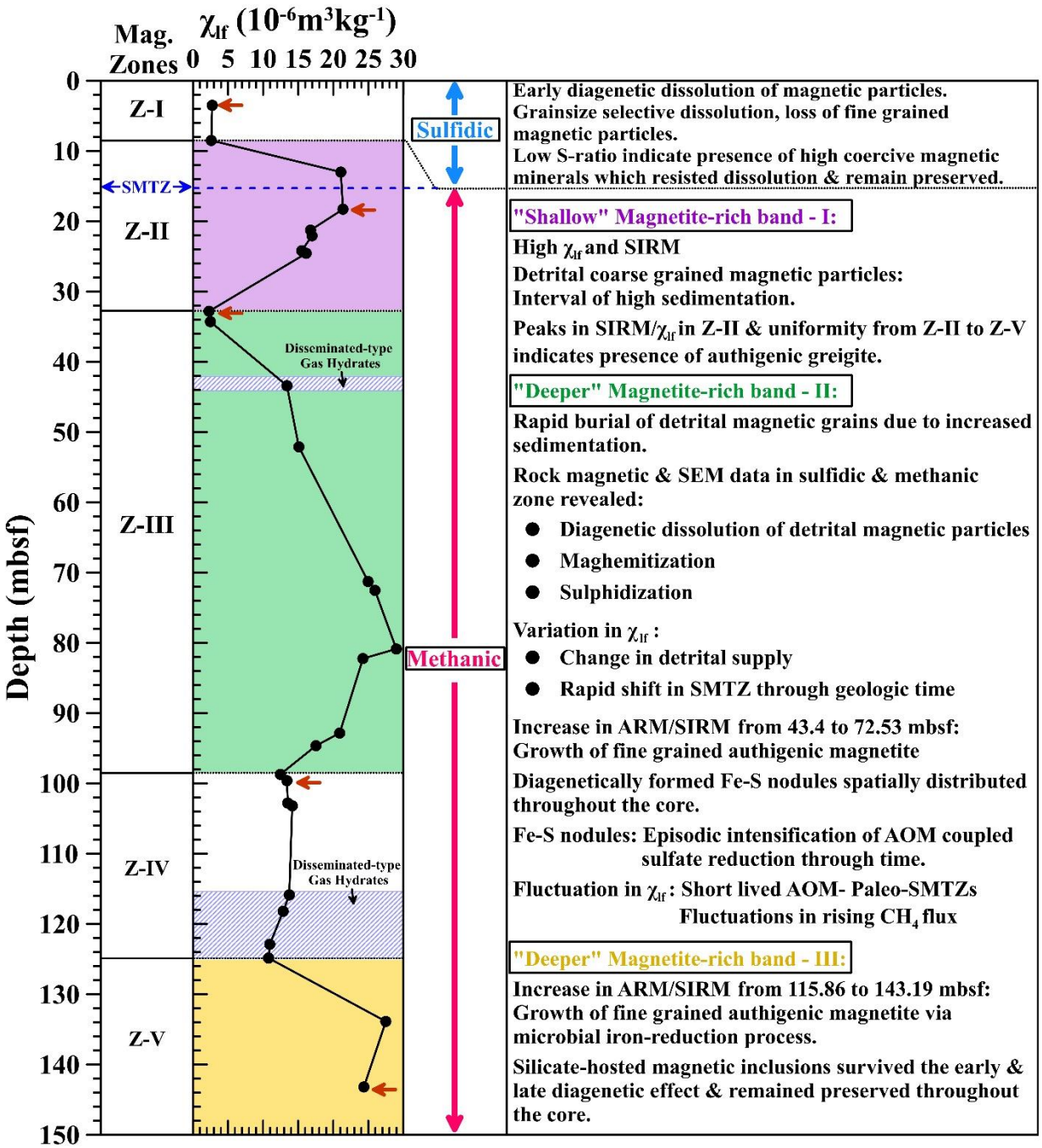

Figure 3.27: *Conceptual model explaining the constraints of detrital, diagenetic, authigenic, maghemitization and sulphidization processes on the evolution of magnetic mineralogies at Site NGHP-01-20. The arrows (red color) on the magnetic susceptibility profile of core NGHP-01-20A represent the carbonate occurrence depths.*

3.8. Conclusions

A set of rock magnetic, mineralogical, and sedimentological records of the sediment cores were utilized to (a) characterize the changes in the magnetic concentration, grain size, and mineralogy (b) to unravel the effect of a range of diagenetic processes on the magnetic minerals in the sulfidic and methanic sediments from the newly discovered active (Stn-4/SPC-01 to SPC-06) and relict (Stn-11/GC-02) cold seepand formerly identified deep-seated gas hydrate (NGHP-01-20A) system in the K-G basin, Bay of Bengal. The findings have been summarized below:

i. Sediment magnetism is mainly carried by complex magnetic mineral assemblages of detrital (titanomagnetite, titanohematite) and authigenic (magnetite, greigite) minerals. The topmost sulfidic sediment magnetic zone (Z-I) is marked by a higher concentration of magnetic minerals as evident in rock magnetic parameters. A systematic downcore decrease in χ_{lf} and IRM_{1T} in this zone was due to the progressive diagenetic dissolution of iron oxide followed by subsequent precipitation of iron sulphides.

ii. Magnetogranulometric proxy (ARM/IRM_{1T}) provided valuable insights on the preferential dissolution of fine-grained magnetite in the sulfidic zone (Z-I), and authigenic formation of magnetite in the methanic zone (Z-II) of all studied cores. At the relict site, elevated concentrations of highly coercive magnetic (titanohematite) grains relative to soft minerals (as seen through lower S-ratio and χ_{lf}) which survived diagenesis are found in the methanic zone. A strong linkage between the occurrence of authigenic carbonates and greigite formation and preservation is noticed.

iii. Electron microscopy (SEM, TEM, Optical) based observations were consistent with the bulk magnetic properties. The present study successfully demonstrated that a focussed approach based on SEM-EDS analyses of magnetic particles from sulfidic and methanic zones provided valuable insights into the mineralogy, genesis, and their state of preservation and also enhances the interpretative value of rock magnetic proxies.

iv. Important findings of this study are summarized in a conceptual models (Figure 3.12 , Figure 3.27) which provided (a) vital insights on the evolution of different magnetic mineralogies constrained by variable diagenetic processes at active and relict seep sites and (b) clearly explained the selective response of magnetic minerals to varying stages of diagenesis (reductive dissolution, maghemitization, sulphidization) constrained by the combined influence of methane-induced geochemical processes and high sedimentation rates in the marine gas-hydrate system.

Table 3.1: *Rock magnetic data of sediment core SSD-045/Stan-04/SPC-01 to SPC-06 and SSD-045/Stan-11/GC-02*

Core ID	Depth (cmbsf)	χ_{lf} ($10^{-6}m^3kg^{-1}$)	SIRM ($10^{-5}Am^2kg^{-1}$)	ARM / SIRM	SIRM/χ_{lf} (A/m)	S-ratio	χfd (%)
SSD-45/ Stn-4/ SPC-01	1	7.7091	1.9264	0.0232	0.2499	0.9605	4.9645
	3	7.9014	1.9477	0.0217	0.2465	0.9558	5.6511
	5	6.7094	1.7899	0.0213	0.2668	0.9570	3.1293
	7	4.5068	1.3414	0.0171	0.2976	0.9688	3.1315
	9	4.5360	1.2124	0.0149	0.2673	0.9497	3.6364
	11	3.5995	0.9435	0.0156	0.2621	0.9293	2.4450
	13	2.8169	0.7237	0.0159	0.2569	0.9064	1.8927
	15	2.6841	0.6865	0.0154	0.2558	0.9009	2.3333
	17	2.0480	0.4956	0.0159	0.2420	0.9138	0.9259
	19	1.5792	0.3644	0.0174	0.2307	0.8394	0.5952
	21	1.4707	0.3579	0.0184	0.2433	0.8470	1.8072
	23	1.5636	0.3090	0.0171	0.1976	0.8350	0.5917
	25	1.1428	0.2769	0.0171	0.2423	0.8247	2.4390
	27	1.1251	0.2616	0.0174	0.2325	0.8387	3.2258
	29	0.8381	0.1580	0.0177	0.1885	0.8297	1.0309
SSD-45/ Stn-4/ SPC-02	1	8.9693	2.1403	0.0236	0.2386	0.9457	4.4761
	3	7.9061	1.8894	0.0276	0.2390	0.9608	3.7569
	5	8.1817	1.9853	0.0249	0.2427	0.9795	4.1045
	7	8.6376	2.1187	0.0264	0.2453	0.9624	3.1472
	9	7.3421	1.9002	0.0274	0.2588	0.9568	2.3337
	11	5.3145	1.4447	0.0297	0.2718	0.9602	2.0408
	13	5.4419	1.3774	0.0332	0.2531	0.9477	2.4523
	15	4.4646	1.2668	0.0271	0.2837	0.9542	3.2258
	17	3.9795	1.1207	0.0205	0.2816	0.9525	3.3175
	19	3.6335	0.9835	0.0192	0.2707	0.9419	0.5464
	21	3.1651	0.8321	0.0182	0.2629	0.9568	0.5917
	23	3.2489	0.8719	0.0188	0.2684	0.9249	0.8547
	25	2.9482	0.7416	0.0156	0.2515	0.9210	1.2658
	27	3.0177	0.7581	0.0179	0.2512	0.9144	2.0896
	29	3.0830	0.7535	0.0176	0.2444	0.9369	1.1869
	31	3.0627	0.6930	0.0178	0.2263	0.8979	1.4493
	33	3.0058	0.6945	0.0177	0.2310	0.9146	1.8182

	35	2.9444	0.6534	0.0172	0.2219	0.9091	1.8868
	37	2.6851	0.5873	0.0175	0.2187	0.8936	1.6077
	39	2.5414	0.5050	0.0189	0.1987	0.8757	1.7483
	41	2.3174	0.4908	0.0180	0.2118	0.8767	1.2195
	43	2.0558	0.3965	0.0193	0.1929	0.8614	1.2876
SSD-45/ Stn-4/ SPC-03	1	8.7455	2.0186	0.0280	0.2308	0.9575	5.4490
	3	8.4254	1.9432	0.0293	0.2306	0.9666	3.8144
	5	8.2472	1.9197	0.0289	0.2328	0.9723	4.4133
	7	7.9529	1.9200	0.0270	0.2414	0.9529	4.7841
	9	8.3951	2.1170	0.0256	0.2522	0.9451	3.7330
	11	7.9278	1.9444	0.0273	0.2453	0.9683	2.0642
	13	7.4386	1.7818	0.0300	0.2395	0.9502	3.2413
	15	6.5766	1.5501	0.0343	0.2357	0.9737	1.9337
	17	6.5109	1.4960	0.0302	0.2298	0.9916	2.2321
	19	6.7555	1.5445	0.0339	0.2286	0.9633	2.0298
	21	6.9253	1.6087	0.0319	0.2323	0.9666	1.8006
	23	6.5324	1.5125	0.0344	0.2315	0.9398	2.0833
	25	6.5016	1.4873	0.0343	0.2288	0.9803	1.5449
	27	6.3350	1.4104	0.0343	0.2226	0.9836	1.5737
	29	6.5013	1.4918	0.0347	0.2295	0.9579	2.1337
	31	6.1756	1.3643	0.0355	0.2209	0.9252	2.3810
	33	6.3973	1.4333	0.0316	0.2241	0.9372	1.0802
	35	6.4883	1.4767	0.0371	0.2276	0.9686	1.8868
	37	6.5811	1.4961	0.0341	0.2273	0.9617	1.7833
	39	6.5530	1.4918	0.0361	0.2277	0.9432	1.4765
SSD-45/ Stn-4/ SPC-04	1	3.2244	0.8061	0.0204	0.2500	0.9090	3.4483
	3	2.6851	0.6680	0.0200	0.2488	0.8830	3.4965
	5	2.4630	0.6039	0.0189	0.2452	0.8825	2.9412
	7	2.3036	0.5298	0.0149	0.2300	0.9001	3.1746
	9	2.0280	0.4736	0.0146	0.2335	0.8868	3.6364
	11	1.8807	0.4422	0.0152	0.2351	0.8413	1.0309
	13	1.8971	0.4448	0.0152	0.2345	0.8481	1.3953
	15	1.8481	0.4147	0.0154	0.2244	0.8464	0.9709
	17	1.8555	0.3821	0.0159	0.2059	0.8624	0.9804
	19	1.5586	0.3367	0.0173	0.2160	0.8859	0.5618
	21	1.5026	0.3163	0.0170	0.2105	0.8956	0.5618
	23	1.6710	0.3581	0.0161	0.2143	0.8697	1.0471
	25	1.4671	0.3498	0.0160	0.2385	0.8425	1.7964
SSD-45/ Stn-4/ SPC-05	1	3.8619	0.9359	0.0228	0.2423	0.9185	3.8095
	3	2.7218	0.6631	0.0191	0.2436	0.9002	3.0000
	5	2.1275	0.5360	0.0173	0.2519	0.8852	2.1322
	7	2.2341	0.5479	0.0163	0.2453	0.8714	2.2308
	9	2.0679	0.5016	0.0159	0.2425	0.8829	1.2766
	11	2.0613	0.4895	0.0160	0.2375	0.8885	1.2641
	13	2.0256	0.4866	0.0152	0.2402	0.8765	1.3043
	15	1.9384	0.4775	0.0155	0.2464	0.8856	0.8811
	17	1.8012	0.4243	0.0153	0.2355	0.8670	1.4778
	19	1.9670	0.5233	0.0201	0.2661	0.8713	0.9050
SSD-45/ Stn-4/ SPC-06	1	1.6517	0.4867	0.0103	0.2946	0.9052	4.4199
	3	1.6350	0.3912	0.0096	0.2393	0.8962	3.7975
	5	1.5941	0.3375	0.0090	0.2117	0.9127	2.7027
	7	1.4269	0.2648	0.0082	0.1856	0.9319	3.1008
	9	1.4284	0.3036	0.0125	0.2125	0.9158	2.5641

	11	1.5601	0.3401	0.0123	0.2180	0.9056	1.7544
	13	1.2053	0.2316	0.0132	0.1921	0.9067	2.2901
	15	1.1732	0.2268	0.0132	0.1934	0.9100	2.2901
	17	1.1255	0.1873	0.0132	0.1664	0.8933	2.4390
	19	1.2326	0.2456	0.0129	0.1993	0.9127	2.1739
	21	0.9617	0.1245	0.0149	0.1294	0.8927	0.9259
	23	0.7666	0.0991	0.0168	0.1293	0.8982	3.5294
	25	0.7909	0.0847	0.0175	0.1071	0.8952	3.4091
SSD-45/ Stn-11/ GC-02	1	10.8617	3.1591	0.0139	0.2908	0.4965	1.8349
	3	10.6656	3.0108	0.0146	0.2823	0.4505	3.0120
	5	10.9084	3.1408	0.0173	0.2879	0.3876	1.1324
	7	10.5713	3.1330	0.0169	0.2964	0.3846	3.2062
	9	10.0072	3.1518	0.0156	0.3149	0.4360	2.3508
	11	13.4816	4.5605	0.0111	0.3383	0.3432	1.3089
	13	11.2642	3.6815	0.0103	0.3268	0.5193	2.5583
	15	13.0781	4.4153	0.0084	0.3376	0.5591	1.1159
	17	8.1944	2.7145	0.0093	0.3313	0.3796	2.4819
	19	7.5885	2.3005	0.0086	0.3032	0.4962	1.0846
	21	7.1915	2.1148	0.0088	0.2941	0.5873	3.9264
	23	5.2297	1.5325	0.0092	0.2930	0.4793	2.2375
	25	4.3561	1.2218	0.0094	0.2805	0.3657	2.4845
	27	4.2749	1.1924	0.0098	0.2789	0.4124	6.6946
	29	4.1977	1.1675	0.0095	0.2781	0.1165	1.6432
	31	4.7771	1.4055	0.0092	0.2942	0.2266	4.0568
	33	4.0133	1.2451	0.0094	0.3102	0.3726	2.9748
	35	3.8762	1.1366	0.0096	0.2932	0.3798	7.0905
	37	2.5874	0.7573	0.0106	0.2927	0.2954	6.4516
	39	1.2467	0.3390	0.0128	0.2719	0.4008	12.1622
	41	1.4620	0.3971	0.0136	0.2716	0.4032	9.3333
	43	0.9929	0.2917	0.0144	0.2937	0.2441	6.8376
	45	1.7412	0.4323	0.0132	0.2483	0.5516	8.8083
	47	1.2794	0.3601	0.0134	0.2815	0.2791	10.7914
	49	1.0720	0.2709	0.0142	0.2527	0.2530	7.3770
	51	1.4674	0.4020	0.0127	0.2740	0.4930	3.5294
	53	1.0350	0.2997	0.0134	0.2896	0.3142	10.3448
	55	1.8399	0.5445	0.0115	0.2959	0.5230	9.8958
	57	2.6172	0.7697	0.0101	0.2941	0.4863	6.7138
	59	2.1051	0.5850	0.0112	0.2779	0.4419	3.7209
	61	2.4515	0.7258	0.0103	0.2961	0.3471	5.1471
	63	2.2309	0.6173	0.0111	0.2767	0.2920	7.9646

Table 3.2: *Rock magnetic data of sediment core NGHP-01-20A*

Depth (mbsf)	χ_{lf} ($10^{-6}m^3kg^{-1}$)	SIRM ($10^{-5}Am^2kg^{-1}$)	ARM / SIRM	SIRM/χ_{lf} (A/m)	S-ratio	TOC (wt.%)	CaCO3 (wt.%)
3.5	2.7496	0.4552	0.0133	0.1656	0.6519	1.9100	2.9500
8.5	2.6178	0.4262	0.0147	0.1628	0.5989	1.2700	3.7600
13	21.0648	6.1256	0.0160	0.2908	0.9583		
18.29	21.3761	6.2726	0.0173	0.2934	0.9548	0.9600	12.6200
21.26	16.7585	4.9828	0.0146	0.2973	0.9723		
22.06	16.9697	5.1932	0.0140	0.3060	0.9577		
24.2	15.4863	4.5827	0.0127	0.2959	0.9299	1.8700	0.2700
24.57	16.1320	4.6948	0.0118	0.2910	0.9278		
32.81	2.2917	0.5924	0.0095	0.2585	0.9290	1.5600	4.5600
34.29	2.4792	1.8141	0.0093	0.7317	0.9373		
43.4	13.3892	3.6553	0.0088	0.2730	0.9873	2.2000	3.4900
52.1	15.0895	3.8779	0.0095	0.2570	0.9841		
71.27	24.9612	7.7311	0.0118	0.3097	0.9431	1.5300	4.8300
72.53	25.9312	7.6206	0.0126	0.2939	0.9551		
80.86	28.9709	8.1328	0.0068	0.2807	0.9685		
82.23	24.2199	6.9610	0.0077	0.2874	0.9533	1.9900	5.1000
92.84	20.9019	5.4996	0.0065	0.2631	0.9214		
94.63	17.5327	4.2984	0.0067	0.2452	0.9672	2.1500	10.7400
98.71	12.4493	3.4372	0.0098	0.2761	0.9770		
99.62	13.3954	3.6158	0.0079	0.2699	0.9232	1.6500	3.4900
102.8	13.5181	3.8618	0.0081	0.2857	0.9261	1.1900	6.4400
103.2	14.1447	4.1244	0.0070	0.2916	0.9421	1.2900	6.7100
115.86	13.7235	3.9953	0.0087	0.2911	0.9713	1.6100	4.0300
118.2	12.8585	3.7571	0.0091	0.2922	0.9678		
122.9	10.9516	2.8155	0.0120	0.2571	0.9449	0.6500	8.0500
124.86	10.7782	2.8480	0.0119	0.2642	0.9262	1.6500	4.0300
133.87	27.4809	8.7435	0.0117	0.3182	0.9686	1.7100	6.0400
143.19	24.3597	8.0042	0.0120	0.3286	0.9514	1.6500	3.7600

Chapter 4:
Comparative diagenetic analysis of shallow and deep-seated marine gas systems from the Bay of Bengal

4.1. Introduction

Marine sediments across large parts of the Krishna-Godavari (K-G) basin offshore, India contain abundant methane and gas-hydrates. The K-G basin represents an ideal natural laboratory with its unique presence of shallow (active cold seep; SSD-45/Stn-4/GC-01; Mazumdar et al., 2019) and deep-seated (NGHP-01-15A; Collett et al., 2008; Kumar et al., 2014) gas-hydrate systems to obtain a comprehensive view of the methane-related diagenetic and authigenic processes in the two different marine gas hydrate systems (Figure 4.1). Magnetic minerals at active, paleo, and relict methane seep sites and in sediments influenced by past anaerobic oxidation of methane (AOM) processes are the potential archive of past fluid sequences and provide an important constraint on the methane-related diagenetic and authigenic processes (Dewangan et al., 2013; Musgrave et al., 2019; Greve et al., 2021; Gaikwad et al., 2021; Kars et al., 2021). Geochemical processes linked with fluid migration, gas hydrate formation/dissociation favour the growth of iron sulphides which induce a magnetic signature in the host sediments (Esteban et al., 2008). For example, sulfate-reduction driven by AOM generates hydrogen sulfide in the pore water via bacterial activities (Canfield and Berner 1987). The linkage between rock magnetism, pore-water geochemistry, methane-related magnetic mineral diagenesis, and authigenesis has been well-explored (Roberts, 2015). Authigenic formation of ferrimagnetic (greigite, magnetite) and non-magnetic (pyrite) iron sulfides in methanic sediments are influenced by the history of fluid sequence and gas-hydrate dynamics (formation/dissociation) (Dewangan et al., 2013; Kars and Kodama, 2015; Roberts, 2015). Previous rock magnetic studies dealing with magnetic mineral diagenesis in methanic and gas-hydrate-bearing sediments has established the linkage between methane-related geochemical and microbial processes and sediment magnetism. For example, in Mackenzie Delta, Canada (Enki et al., 2007), Mediterranean continental shelf (Amyl et al., 2020), North-western Weddell Sea (Reilly et al., 2020), South China Sea (Lin et al., 2021), Hikurangi Margin, New Zealand (Grove et al., 2021; Kars et al., 2021), Izu-Bonin rear arc (Musgrave et al., 2019), Nankai Trough (Kars and Kodama, 2015; Shi et al., 2017) and offshore Shimokita Peninsula (Phillips et al., 2017) Japan, Bay of Bengal (Dewangan et al., 2013; Badesab et al., 2019; Gaikwad et al., 2021; Johnson et al., 2021), offshore Taiwan (Horng, 2018), Cascadia Margin (Musgrave et al., 2006; Larrasoaña et al., 2007), Arctic Vestnesa Ridge, offshore western Svalbard (Johnson et al., 2014), West Siberian Sea (Rudmin et al., 2018), and offshore Taiwan (Horng, 2018).

Detrital magnetic particles undergo a reduction process manifested by progressive diagenetic dissolution and subsequent transformation into intermediate ferrimagnetic iron sulfide (greigite) or stable non-magnetic (pyrite) minerals (Roberts, 2015). Magnetic methods bear the potential to rapidly characterize the detrital, diagenetic, and authigenic magnetic minerals in terms of their concentration, grain size, and mineralogy (Esteban et al., 2008). Previous rock magnetic studies dealing with magnetic mineral diagenesis in the K-G basin mainly focussed on elucidating the controls of structural and diagenetic (early vs. late) processes on the sediment magnetism in an active and relict seep sites (Gaikwad et al., 2021), unravelling the linkage between greigite magnetism, methane seepage dynamics, and evolution of active cold seep site associated with shallow gas-hydrate system (Badesab et al., 2020a), developing a novel magnetic-based approach for the exploration of gas-hydrates (Badesab et al., 2019), magnetic mineral diagenesis in a paleo-cold seep site (Dewangan et al., 2013), constraining the formation and preservation of greigite in methanic sediments (Badesab et al., 2020b; Gaikwad et al., 2021), isolating detrital and diagenetic signals in methane-bearing marine sediments (Johnson et al., 2021), influence of high-energy depositional environment on the magnetic mineral diagenesis, and formation of gas-hydrates (Badesab et al., 2020b). However, a focused rock magnetic study directly dealing with the diagenetic analysis of two different (shallow *versus* deep-seated) marine gas-hydrate systems in the K-G basin is still lacking.

Sediment cores retrieved during the Council of Scientific and Industrial Research (CSIR)-National Institute of Oceanography (NIO) gas hydrate discovery cruise (SSD-045 onboard R/V Sindhu Sadhana) and the first Indian National Gas-hydrate Drilling Expedition (NGHP-Exp-01) provided an excellent opportunity to illuminate the multiple methane-influenced geochemical processes that impact sediment magnetization of the continental margin hydrate system (Collett et al., 2008; Kumar et al., 2014). In this study, a comprehensive rock magnetic investigations complemented by mineralogical and petrological observations was conducted on the sediment cores representing shallow (active cold seep) and deep-seated gas-hydrate systems to examine (1) how magnetic minerals respond to the geochemical environment at two different diagenetic (shallow versus deep gas-hydrate system) settings experiencing variable fluid sequence, and (2) elucidate the control on the magnetic mineral authigenesis in methanic sediments.

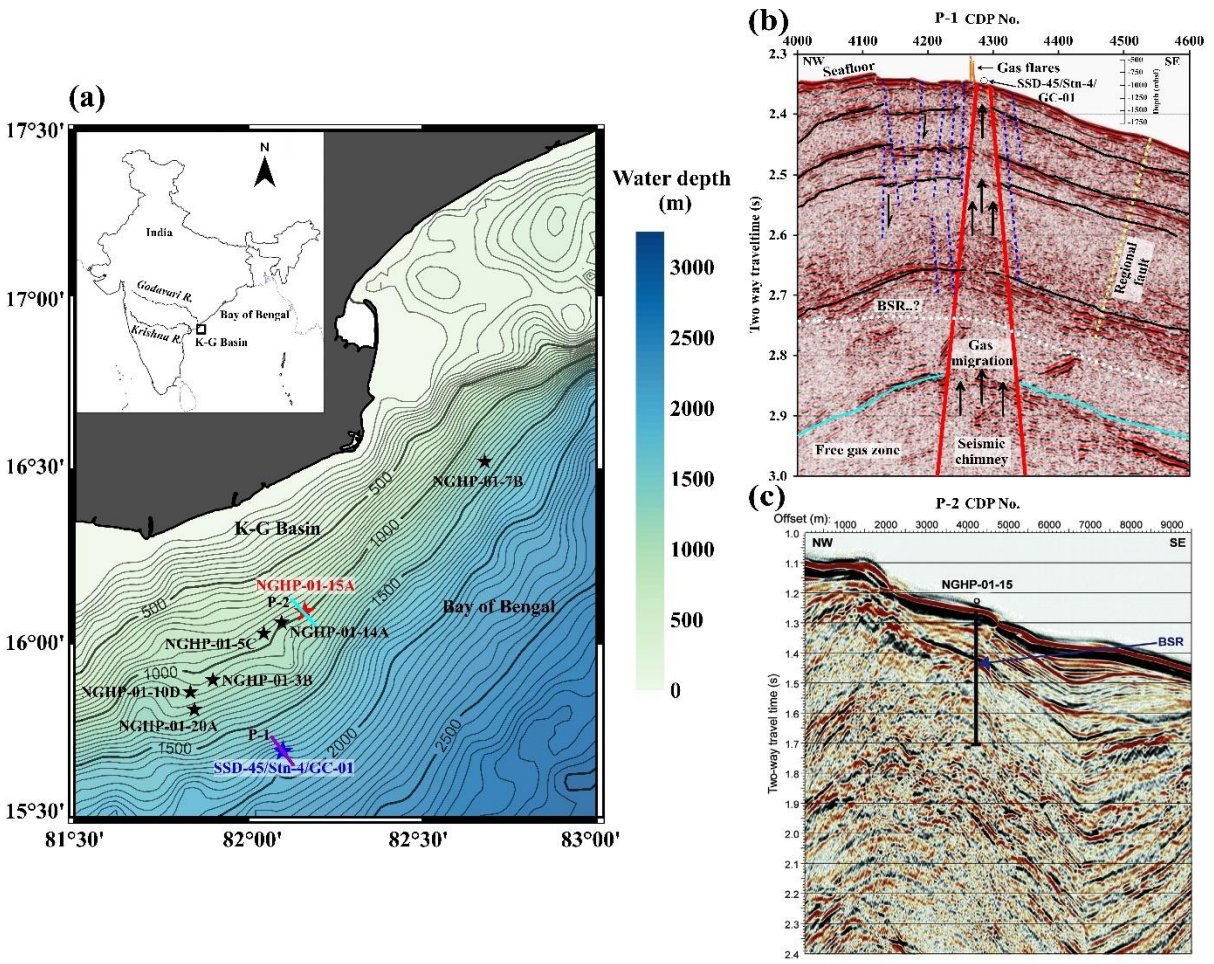

Figure 4.1: *(a) Map showing the sediment core location of shallow (active seep, Core ID: SSD-45/Stn-4/GC-01, marked by red star) and deep-seated (Core ID: NGHP-01-15A, marked by blue star) gas-hydrate site. The location of proximal and distal sediment cores (NGHP-01-20A, NGHP-01-10D, NGHP-01-3B, NGHP-01-5C, NGHP-01-14A, NGHP-01-15A, and NGHP-01-7B) collected during National Gas hydrate Expedition -01 (modified from Collett et al., 2014) from the Krishna-Godavari (K-G) basin, Bay of Bengal are shown. High-resolution seismic profile of the active seep site (SSD-45/Stn-4/GC-01) (P-1) is highlighted in purple color and the deep-seated gas-hydrate site (NGHP-01-15A) (P-2) is highlighted in light blue color (b) High-resolution seismic profile highlighting the normal faults (green dashed lines), subsurface chimney-like feature (solid blue lines) and gas flares (purple). Regional toe-thrust fault (yellow dashed line), feasible BSR (white dashed line), and subsurface horizons (solid black lines) are marked on the seismic section from the active cold seep location (Core ID: SSD-45/Stn-4/GC-01) (modified from Dewangan et al., 2021) (c) High-resolution seismic profile of site NGHP-01-15 highlighting the sediment core location and bottom simulating reflector (BSR) with the blue color arrow (modified from Kumar et al. 2014).*

4.2. Results

4.2.1. Rock magnetic record of sediment cores from shallow and deep-seated gas hydrate system

Rock magnetic profile of sediment cores from active methane seep site associated with shallow (SSD-45/Stn-4/GC-01) and deep-seated gas-hydrate (NGHP-01-15A) systems are presented in Figure 4.2. A magnetically enhanced and laterally extensive band (Figure 4.3) is clearly evident in the sediment magnetic record of seven long drilled cores from the K-G basin (Badesab et al., 2019). Such band represents several events of rapid sediment deposition that eventually led to the quick burial and formation of a distinct magnetite-rich sediment interval in the NGHP drilled sediment cores (Figure 4.3; Shanmugam et al., 2009; Shankar and Riedel, 2010; Dewangan et al., 2011; Ramprasad et al., 2011; Krishna et al., 2016; Badesab et al., 2019; Badesab et al., 2022). Based on the down-core magnetic susceptibility (χ_{lf}) trends, the entire magnetic profile of core SSD-45/Stn-4/GC-01from active seep (AS) site was demarcated into two distinct sediment magnetic zones (Z-I, Z-II, Figure 4.2). The uppermost zone of core SSD-45/Stn-4/GC-01 (Z-I: 0.01to 1.6 mbsf) showed a general downcore decline in χ_{lf}, ARM, and SIRM indicating reduction in the magnetic mineral concentration (Figure 4.2a-c). A magnetic (SIRM/χ_{lf}; Snowball and Thompson, 1990; Maher and Thompson, 1999; Peters and Dekkers, 2003) proxy for iron sulfides showed a systematic downcore decrease suggesting the loss of fine and subsequent increase in coarse-grained magnetic particles except few intervals in Z-I and Z-II (Figure 4.2e). Anomalous drop in S-ratio (0.61 – 0.96) from 0.31 to 1.09 mbsf suggest the presence of ferrimagnetic iron sulfides (greigite, hexagonal pyrrhotite) (Figure 4.2f; Peters and Dekkers, 2003; Roberts et al., 2011; Kars and Kodama, 2015; Horng, 2018). The bottom most zone (Z-II: 1.61to 2.23 mbsf) showed marked decrease in $\chi_{lf,}$ ARM, SIRM values suggesting drop in magnetite concentration (Figure 4.2a-c). Three peaks of increase in SIRM/χ_{lf} and χ_{lf} in the gas-hydrate bearing sediment intervals in Z-II suggested the presence of SP size ferrimagnetic iron sulfides (greigite, hexagonal pyrrhotite) (Figure 4.2a,e; Snowball, 1991; Tarduno, 1995; Larrasoaña et al., 2007; Rowan et al. 2009). S-ratio profile showed two trends in Z-II (Figure 4.2f). The beginning of Z-II was marked by higher values of S-ratio indicating the dominance of ferrimagnetic iron oxides. The lower most interval (1.83 to 2.23 mbsf) showed significant drop indicating the presence of high coercivity minerals or ferrimagnetic iron sulfides.

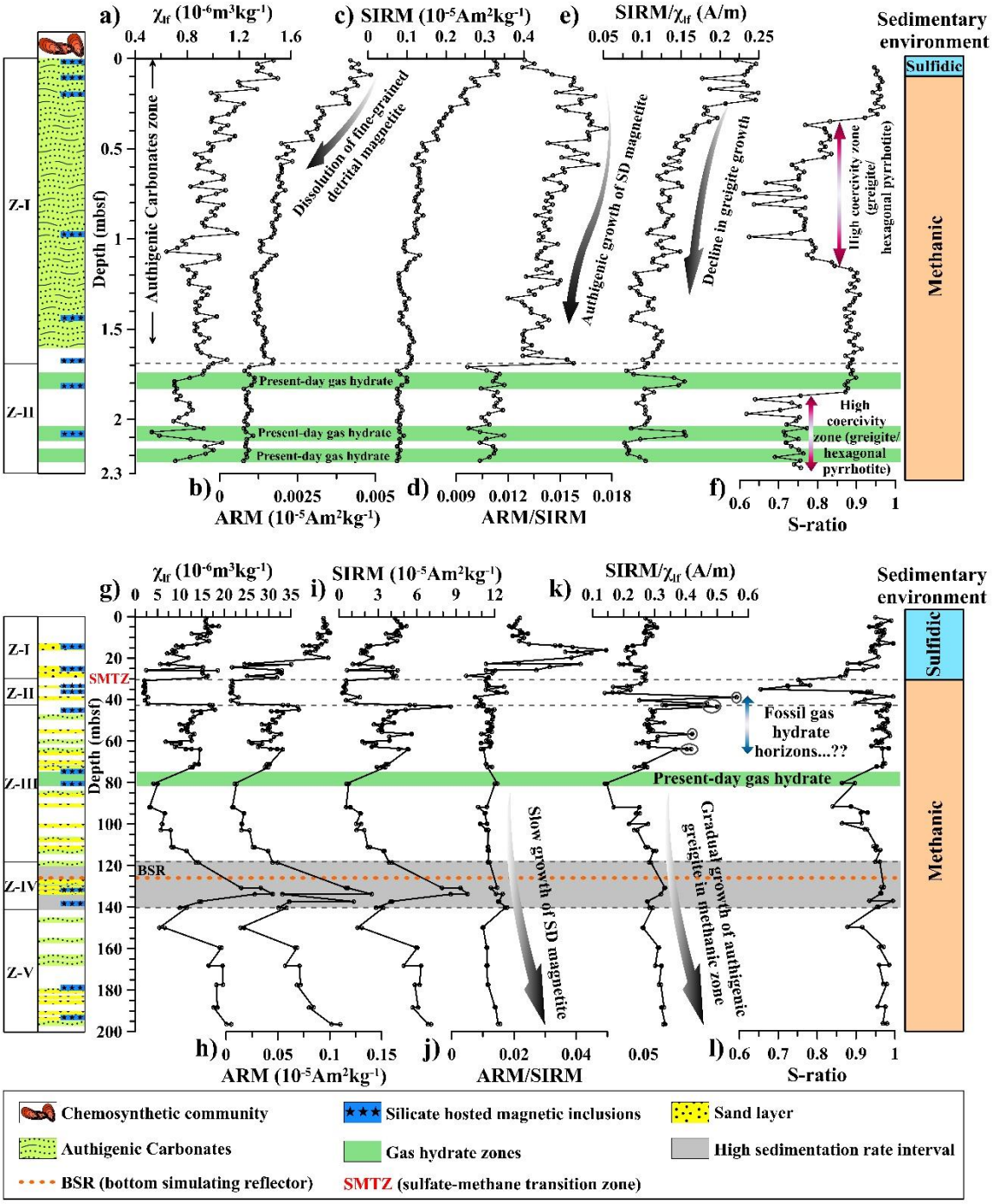

Figure 4.2: *Depth variations of selected rock magnetic data for sediment cores (a–f) shallow (active cold seep, Core ID: SSD-45/Stn-4/GC-01), and (g–l) deep-seated (Core ID: NGHP-01-15A) gas-hydrate site. Based on the variation in magnetic susceptibility (χ_{lf}), two sediment magnetic zones (Z-I, Z-II) of shallow (active cold seep) and five sediment magnetic zones (Z-I, Z-II, Z-III, Z-IV, Z-V) of deep-seated gas-hydrate site in the Krishna-Godavari (K-G) basin, Bay of Bengal are marked. (Please note that χ_{lf} = low frequency magnetic susceptibility; ARM = anhysteretic remanent magnetization; and SIRM = isothermal remanent magnetization).*

Rock magnetic profile of a deep-seated gas-hydrate core (NGHP-01-15A) was classified into five distinct sediment magnetic zones (Z-I, Z-II, Z-III, Z-IV and Z-V). A systematic downcore reduction in $\chi_{lf,}$ ARM and SIRM in Z-I (0.74 to 17.76 mbsf) indicated decline in concentration of magnetic particles (Figure 4.2g-i). The lower part (14.02 to 25.86 mbsf) of Z-I was marked by higher values of ARM/SIRM suggesting the dominance of fine-grained detrital magnetic particles in this zone (Figure 4.2j; Peters and Dekkers, 2003; Liu et al., 2012). A distinct minima in $\chi_{lf,}$ ARM and SIRM and drop in S-ratio close SMTZ (Figure 4.2, Figure 4.16) indicated the presence of paramagnetic (pyrite) and high coercivity minerals is Z-II (30.86 to 41.91 mbsf) (Figure 4.2g-i, l). The Z-III (42.57 to 72.57 mbsf) was characterized by higher $\chi_{lf,}$ ARM, SIRM and SIRM/χ_{lf} values reflecting the presence of fine-grained ferrimagnetic iron sulfides of diagenetic or authigenic origin (Figure 4.2g-i,k; Rowan et al., 2009; Roberts et al., 2018). A magnetic enhancement manifested by increase in $\chi_{lf,}$ ARM, SIRM, S-ratio and relatively low ARM/SIRM indicated the presence of coarse-grained magnetic particles in Z-IV (112.85 to 140.35 mbsf) close to the present BSR depth (Figure 4.2g-j,l). The Z-V (149.9to 196.45 mbsf) was marked by a downcore rise in $\chi_{lf,}$ ARM, SIRM and high S-ratio suggesting the period of increased supply of magnetic minerals (Figure 4.2g-i, l). A minor downcore rise in ARM/SIRM from end of Z-II to Z-V suggested gradual increase in the proportion of fine-grained authigenic magnetic particles (Figure 4.2j; Dillon and Bleil, 2006). Similarly, a trend of noticeable increase in SIRM/χ_{lf} from Z-III i.e., below the gas-hydrate occurrence zone till the bottom of the core (NGHP-01-15A) was attributed to the increase in the growth of fine-grained ferrimagnetic iron sulfide (greigite) particles (Figure 4.2k; Snowball, 1991; Larrasoaña et al., 2007; Rowan et al., 2009).

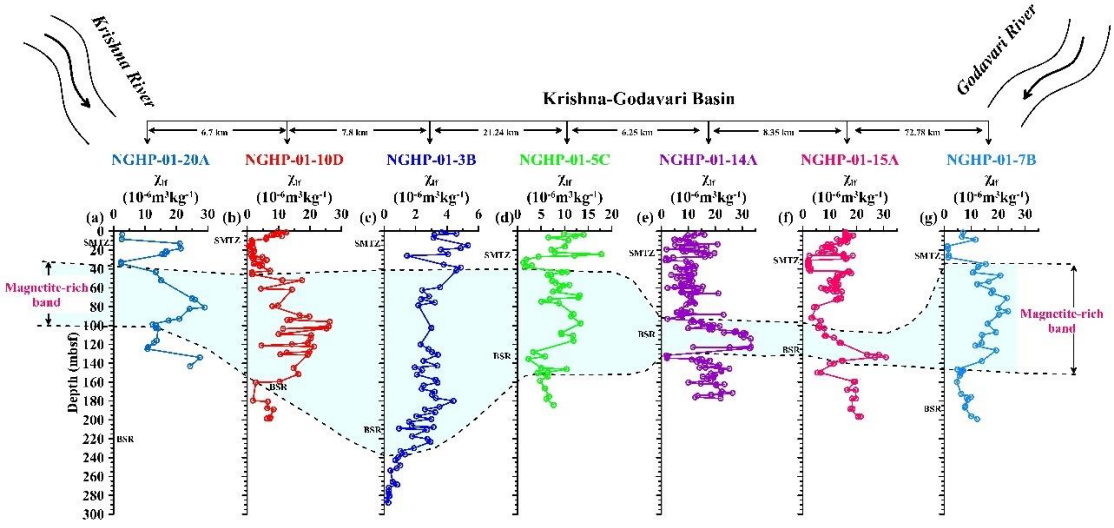

Figure 4.3: *(a-g) Downcore variations of magnetic susceptibility (χ_{lf}) in the sediment cores (NGHP-01-20A, NGHP-01-10D, NGHP-01-03B, NGHP-01-05C, NGHP-01-14A, NGHP-01-*

15A, and NGHP-01-07B) from the Krishna-Godavari (K-G) basin, Bay of Bengal. Enhanced χ_{lf} is highlighted by a color (light blue) band. The distance between the core locations, depth of the bottom simulating reflector (BSR) and the position of the sulfate-methane transition zone (SMTZ) are also marked. (Magnetic susceptibility plots of core NGHP-01-20A is modified from Badesab et al., 2022, NGHP-01-10D is modified from Badesab et al., 2017, NGHP-01-3B, NGHP-01-5C and NGHP-01-7B are modified from Badesab et al., 2019, and NGHP-01-14A is modified from Badesab et al., 2020b).

4.2.2. Temperature dependant magnetic Susceptibility

The thermomagnetic curves (χ-*T*) of all six analyzed samples from a shallow gas-hydrate core (SSD-45/Stn-4/GC-01) showed very similar pattern (Figure 4.4a). A noticeable drop in χ values between 522°C and 632°C in majority of the samples suggested that the bulk magnetic mineralogy was dominated by magnetite and titanomagnetite (Dunlop et al., 1997). A minor rise in χ between 352°C to 452°C for most of the samples was attributed to the presence of titanomagnetite exhibiting wide range of Ti-contents (Lattard et al., 2006) or due to transformation of paramagnetic minerals into magnetite during heating process (Figure 4.4a; Hirt and Gehring, 1991; Hirt et al., 1993; Passier et al., 2001; Philips, 2018).

In a deep-seated gas-hydrate core (NGHP-01-15A), χ-*T* curves (Figure 4.4b) showed a gentle decline in magnetization from room temperature up to ~ 340.5 $^{\circ}$C (average) and increased further suddenly to values close to the initial magnetization value. The noticeable increase at ~ 373.51 $^{\circ}$C (average) was consistent with high-temperature oxidation of non-magnetic iron phases into magnetic phases (Passier et al., 2001). Increase in magnetization maintains a broad peak between ~ 403.5 $^{\circ}$C and 520.8 $^{\circ}$C (average) that ends with a sharp drop between ~ 572.0 $^{\circ}$C and 635.3 $^{\circ}$C (average) indicating that the bulk magnetic mineralogy in core NGHP-01-15A was dominated by magnetite and titanomagnetite (Figure 4.4b; Dunlop et al., 1997).

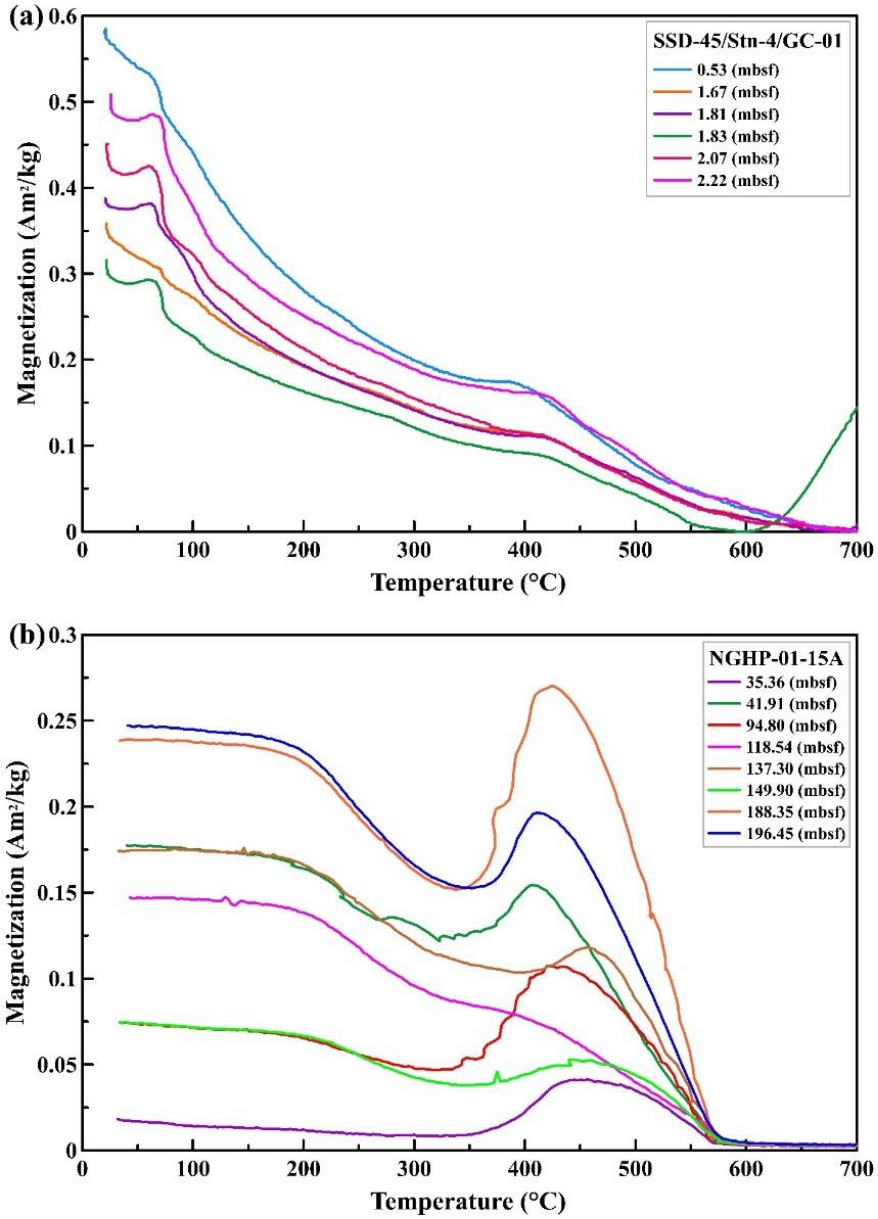

Figure 4.4: *Thermomagnetic heating curves (χ-T) for selected samples from sediment cores (a) shallow (active cold seep, Core ID: SSD-45/Stn-4/GC-01) and (b) deep-seated (Core ID: NGHP-01-15A) gas-hydrate site in the Krishna-Godavari (K-G) basin, Bay of Bengal.*

4.2.3. Low-temperature magnetometry

Results of low-temperature magnetic measurements of selective samples from core SSD-45/Stn-4/GC-01 displayed similar magnetic signatures and lacks a Verwey transition (Figure 4.5; Verwey, 1939). The curves reflect the dominance of paramagnetic signal which hindered the minor changes in the magnetization. The first derivative magnetization curves are shown in Figure 4.5b, d, f. A minor peak in the derivative curve near Verwey transition temperature was observed only in sample from Z-II (1.80 mbsf), indicative for the presence of stoichiometric magnetite in low concentration (Figure 4.5d). Rapid decrease in LT-SIRM

from 5 to 30 K and nearly 55 – 60 % loss of the applied remanence was noticed (Figure 4.5a, c, e). This indicated the presence of superparamagnetic (SP) magnetic (rapidly unblocked) particles in these samples (Tarduno, 1995; Passier and Dekkers, 2002). The Besnus transition typical indicator for pyrrhotite (Besnus and Meyer, 1964; Dekkers, 1989; Larrasoaña et al., 2007) was not observed in the analyzed samples.

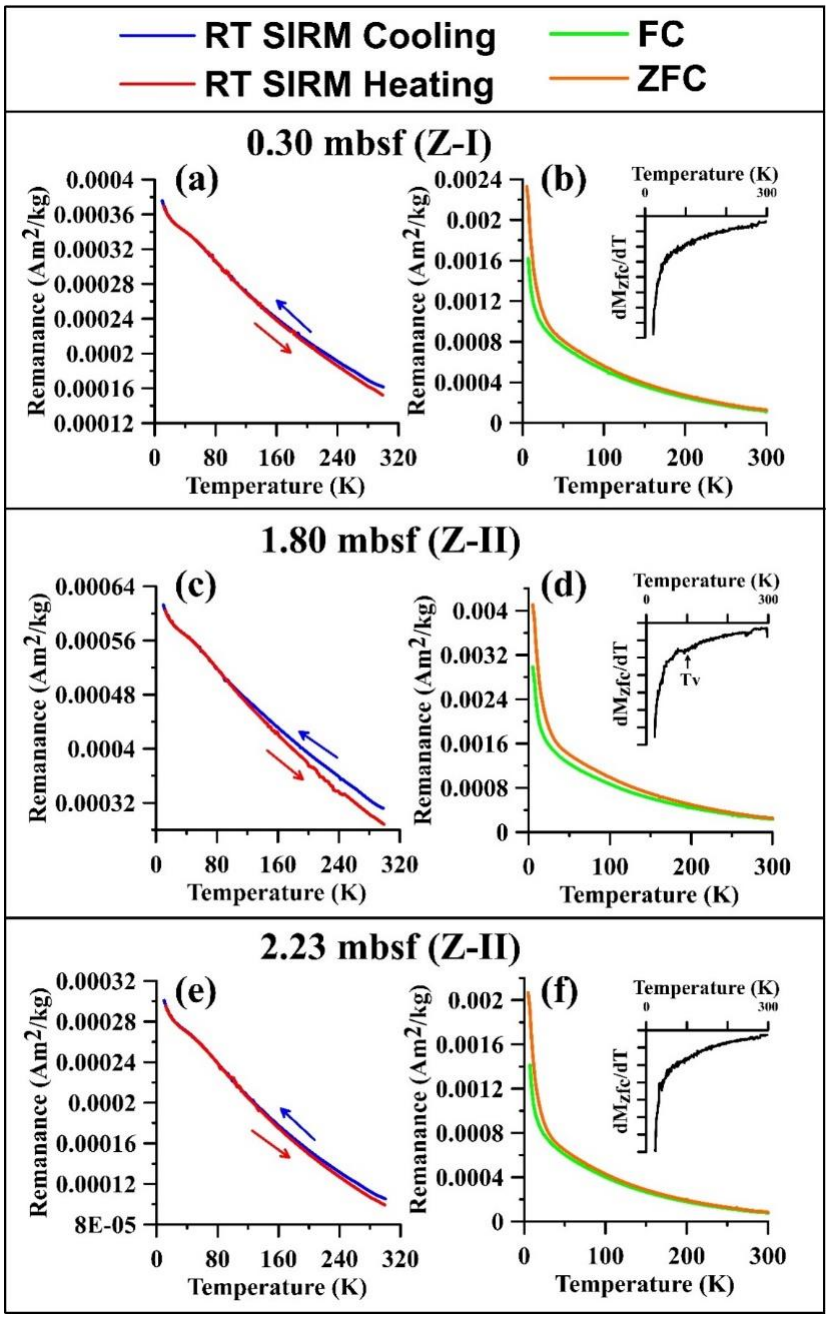

Figure 4.5: *Low-temperature (<300 K) magnetization curves (a–f) for representative samples from the two sedimentary magnetic zones identified in the shallow (active cold seep) gas-hydrate core (Core ID: SSD-45/Stn-4/GC-01) in the Krishna-Godavari (K-G) basin, Bay of Bengal (Please note that, FC = field-cooled; RTSIRM = saturation isothermal remanent magnetization at room temperature; ZFC = zero field-cooled).*

4.2.4. FORC diagrams

FORC diagrams provided important constraints on the domain states and type of magnetic minerals (Figure 4.6; Roberts et al., 2000). Closed contours in all plots indicated that the magnetic particles in the analyzed samples displayed vortex state to multidomain (MD) type behavior (Figure 4.6a-i; Roberts et al., 2000; Roberts et al., 2017; Roberts et al., 2018; Lascu et al., 2018). FORC's distribution in Figure 4.6a-i also provided clues on the magnetic mineralogy which appeared to be dominated by the ferrimagnetic iron oxides (vortex state-MD type magnetite) and sulfides (SP greigite) (Muxworthy and Dunlop, 2002).

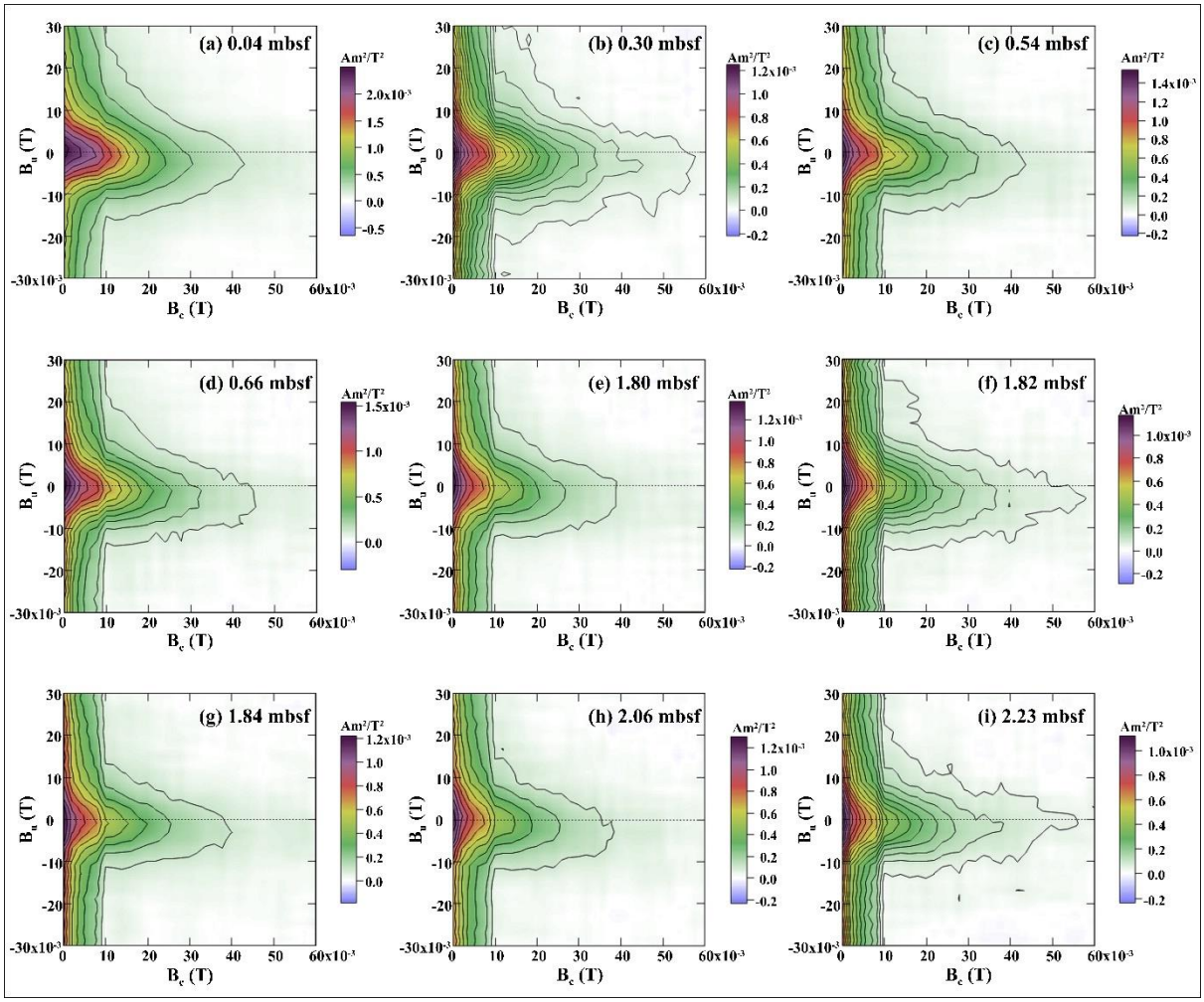

Figure 4.6: *First-order reversal curve (FORC) diagrams (a–i) for selected representative samples from the sediment core (Core ID: SSD-45/Stn-4/GC-01) from shallow (active cold seep) gas-hydrate site in the Krishna-Godavari (K-G) basin, Bay of Bengal.*

4.2.5. Identification of magnetic mineralogy using SEM-EDS, TEM-EDS, and XRD analyses

SEM-EDS data of magnetic particles representing different sediment intervals of core SSD-45/Stn-04/GC-01confirmed that titanomagnetite was the major magnetic mineral in the studied cores (Figure 4.7a-f, Figure 4.8a-f). Several ferrimagnetic iron oxides (detrital) and sulfides (diagenetic) of different sizes are noticed in both sediment magnetic zones (Z-I, Z-II). Well-preserved as well diagenetically influenced detrital titanomagnetite grains were found to be present throughout the core (Figure 4.7a-f, Figure 4.8a-f). EDS data for these grains indicated the presence of titanium, iron, and oxygen with minor amount of silicon, aluminium, calcium, manganese, chromium, and magnesium. Numerous diagenetically formed iron sulfides (pyrite) occurred as framboid (Figure 4.7b, Figure 4.8b) as well as tiny individual (Figure 4.7d-e, Figure 4.8d-e) grains were observed. Authigenically formed greigite particles were observed in association with larger titanomagnetite grains in Z-II (Figure 4.7f, Figure 4.8f). In sediment core (NGHP-01-15A) from deep-seated gas-hydrates, fine as well as coarse-grained detrital titanomagnetites were found to occur throughout all sediment magnetic zones (Z-I to Z-V) (Figure 4.7g-m, Figure 4.8g-m). Iron sulfides were found to occur as tiny particles growing on a larger titanomagnetite grains in a magnetically reduced zone (Z-II) proximal to present-day SMTZ (Figure 4.7h, Figure 4.8h). High sedimentation rate interval (Z-IV) was marked by abundant coarse-grained detrital titanomagnetites (Figure 4.7k-l, Figure 4.8k-l).

TEM analyses of magnetic particles from sediment cores representing shallow (SSD-045/Stn-4/GC-01) and deep-seated (NGHP-01-15A) gas hydrates revealed the occurrence of nanosized magnetic grains exhibiting diverse morphology. The grain size of the magnetic particles ranged between 10 nm to 50 nm. Most of the particles were found in a clustered configuration, with the occasional occurrence of isolated grains (Figure 4.9a-d). The shapes of these particles varied from equidimensional to highly irregular, including circular, ellipsoidal, hexagonal, and elongated (Figure 4.9). EDS data of selected samples confirmed the presence of fine-grained nanosized particles of magnetite (Figure 4.9 e-f).

XRD analyses on magnetic particles from all sediment magnetic zones in cores SSD-45/Stn-04/GC-01 and NGHP-01-15A confirmed that magnetic mineralogy is governed by titanomagnetite, greigite, and pyrite grains occurring in varying proportion (Figure 4.10a-l). Dominant peaks of quartz were also noticed in all samples (Figure 4.10a-l). In core SSD-

45/Stn-04/GC-01, titanomagnetite, greigite, and pyrite grains were found to occur together (Figure 4.10a-f). Samples from Z-II exhibiting high χ_{lf} and SIRM/χ_{lf} in cores SSD-45/Stn-4/GC-01 (Figure 4.2a,e, Figure 4.10e-f) showed the presence of titanomagnetite, greigite, and pyrite. In core NGHP-01-15A, titanomagnetite and quartz were two dominant minerals noticed throughout the core (Figure 4.10g-l). Few minor peaks of pyrite were seen in Z-II (Figure 4.10h), Z-IV (Figure 4.10k), and Z-V (Figure 4.10l).

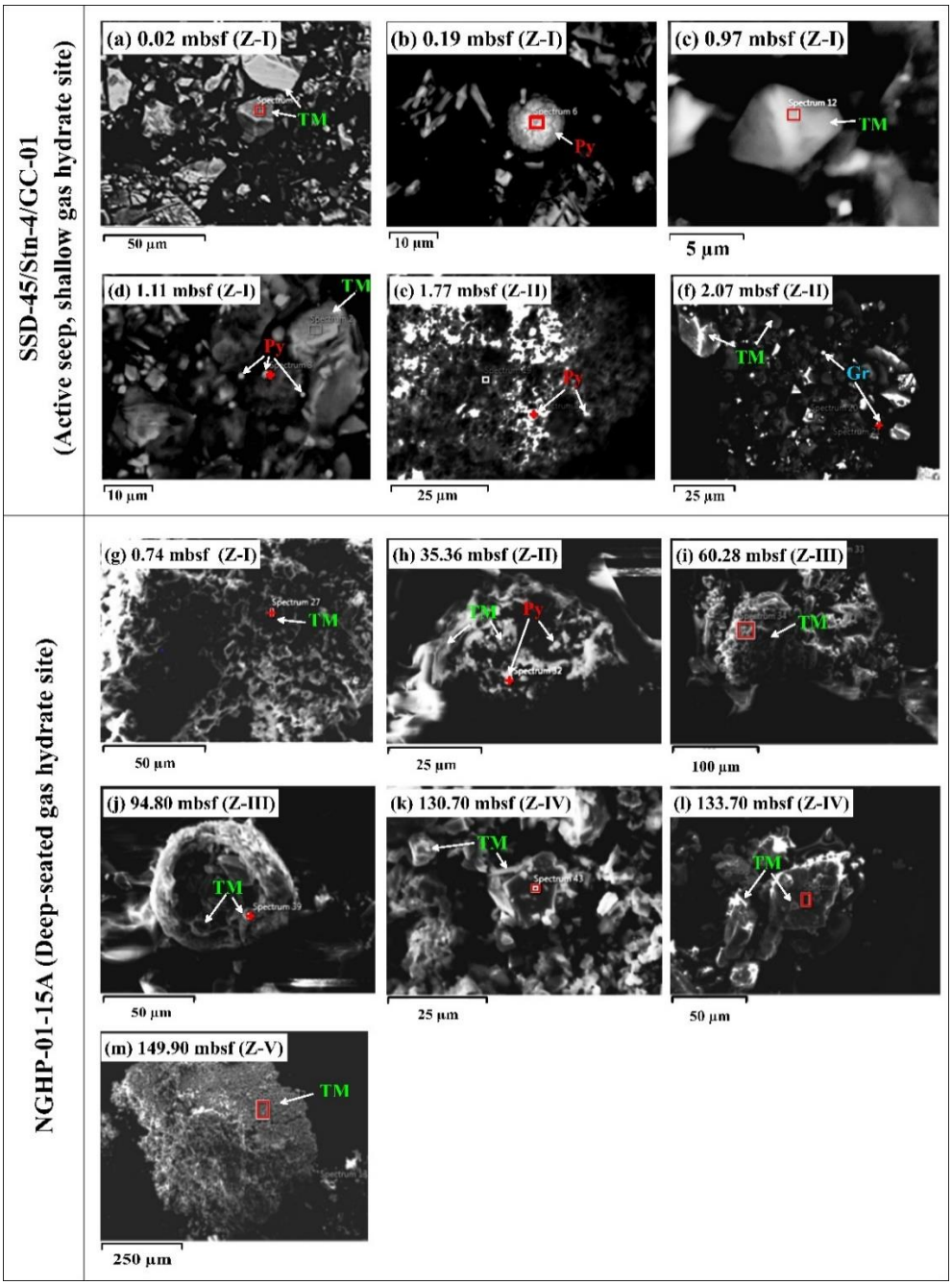

Figure 4.7: *Scanning electron microscope (SEM) images on magnetic extracts from different sediment magnetic zones of cores (a–f) from shallow (active cold seep, Core ID: SSD-45/Stn-4/GC-01) and (g–m) deep-seated (Core ID: NGHP-01-15A) gas-hydrate site in the Krishna-*

Godavari (K-G) basin, Bay of Bengal. Energy dispersive X-ray spectroscopy (EDS) spectra of the respective images presented in the Figure 4.8. Iron (Fe), titanium (Ti), sulfur (S), oxygen (O), calcium (Ca), silicon (Si), carbon (C), aluminium (Al), magnesium (Mg), potassium (K), and vanadium (V) peaks are indicated.

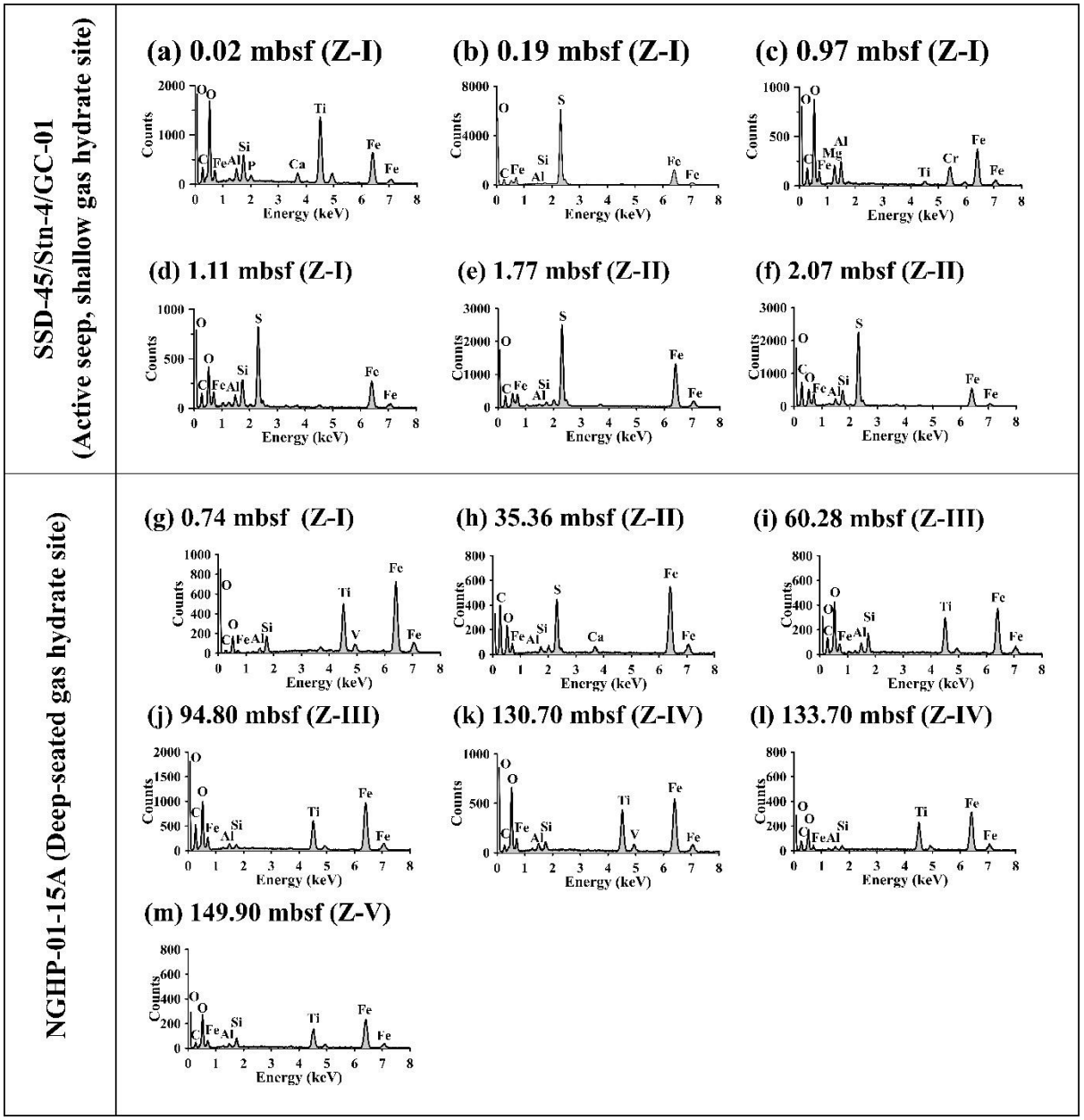

Figure 4.8*: (a-f) Energy dispersive spectroscopy (EDS) data of respective scanning electron microscopy (SEM) images of the sediment core SSD-45/Stn-4/GC-01 (active seep , shallow gas-hydrate site), and (g-m) NGHP-01-15A (deep-seated gas-hydrate site) presented in Figure 4.7.*

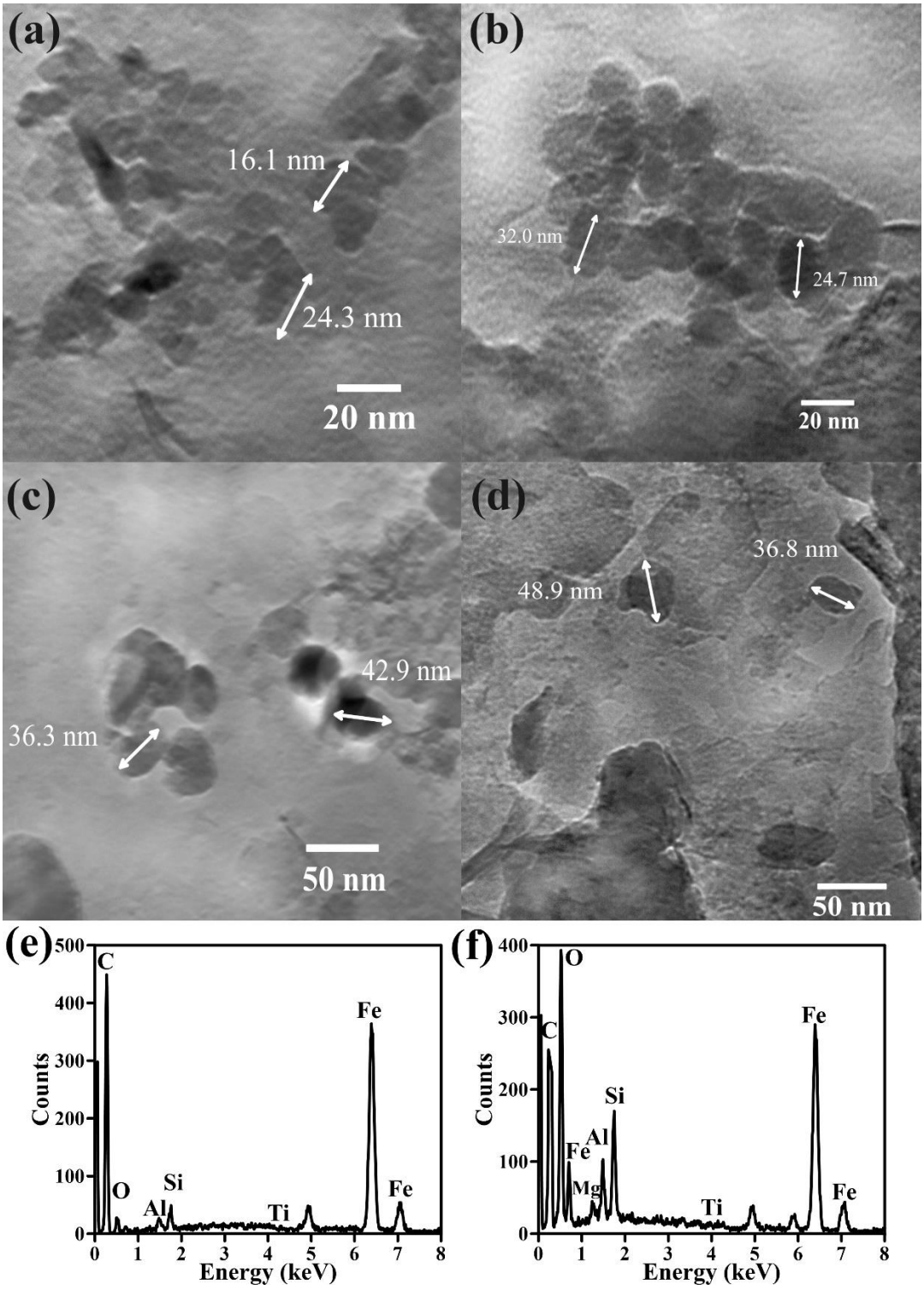

Figure 4.9: *Transmission electron microscope (TEM) images of magnetic particles representing different sediment magnetic zones of cores (a–b) from shallow (active cold seep, Core ID: SSD-45/Stn-4/GC-01) and (c–d) deep-seated (Core ID: NGHP-01-15A) gas-hydrate site in the Krishna-Godavari (K-G) basin, Bay of Bengal. Energy dispersive X-ray spectroscopy (EDS) spectra of image a and c presented in e-f respectively. Iron (Fe), oxygen*

(O), titanium (Ti), silicon (Si), carbon (C), aluminium (Al), and magnesium (Mg) peaks are indicated.

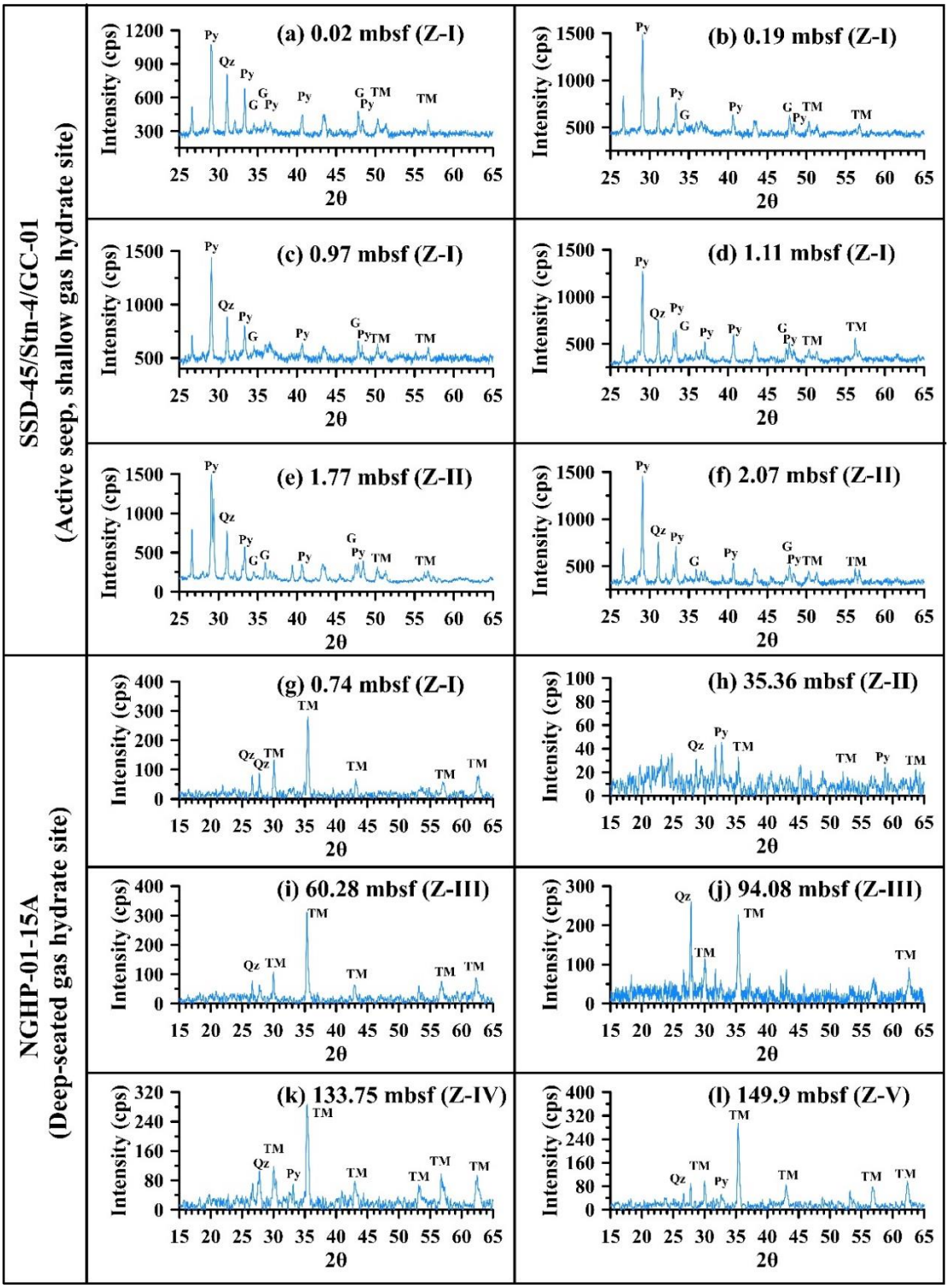

Figure 4.10: *X-ray diffraction spectra for extracted minerals from different sediment zones of cores (a–f) from shallow (active cold seep, Core ID: SSD-45/Stn-4/GC-01) and (g–l) deep-seated (Core ID: NGHP-01-15A) gas-hydrate site in the Krishna-Godavari (K-G) basin, Bay of Bengal. TM = titanomagnetite, G = greigite, Py = pyrite, Qz = quartz.*

4.2.6. Petrography of authigenic carbonates, chemosynthetic community, and sand layers

Abundant yellowish-brown color authigenic carbonates of different morphologies and sizes were found only in Z-I (upto 1.57 mbsf) of core SSD-45/Stn-4/GC-01 (Figure 4.11a-g). Living chemosynthetic communities including *Bathymodiolus* sp., (Figure 4.11h), *Calyptogena* sp. (Figure 4.11i), *Acharax* sp. shell (Figure 4.11j) and Decapod crustaceans (squat lobsters; Figure 4.11k) were noticed at the active methane seep site (SSD-45/Stn-4/GC-01).

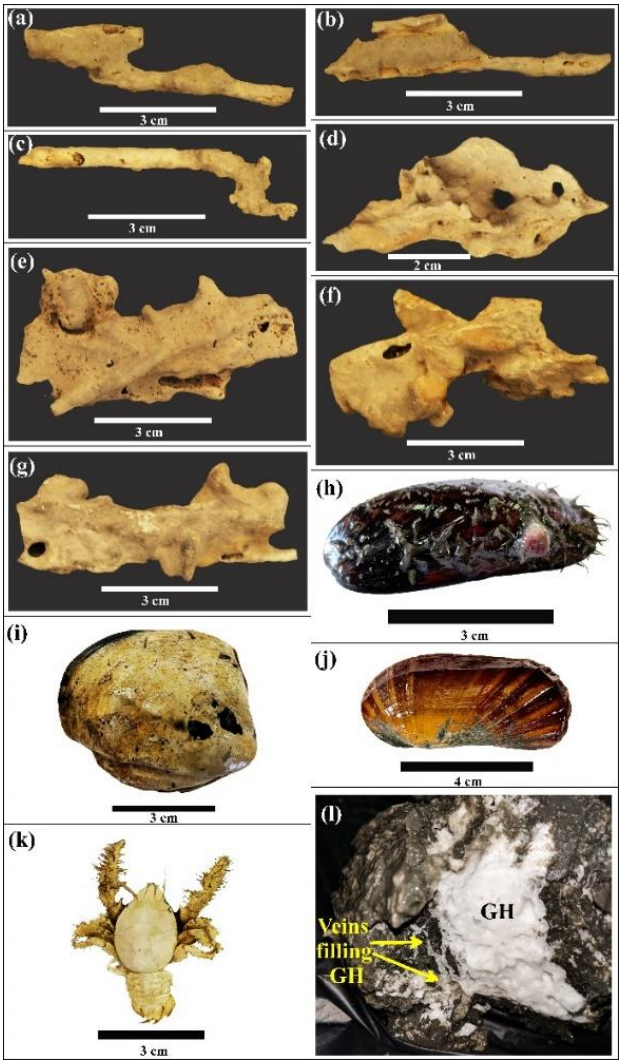

Figure 4.11: *Photographs showing methane-derived authigenic carbonates from different depth intervals of shallow (active cold seep, Core ID: SSD45/Stn-4/GC-01) gas-hydrate core: Z-I (a) 0.02 mbsf, (b) 0.18 mbsf, (c) 0.25 mbsf, (d) 0.77 mbsf, (e) 1.01 mbsf, (f) 1.25 mbsf, (g) 1.57 mbsf, chemosynthetic communities from sea floor (h) Bathymodiolus Sp., (i)*

Calyptogena Sp., (j) Acharax Sp., (k) Decapod crustaceans (Squat lobster), and (l) fracture (vein) filled gas-hydrates (2.23 mbsf) recovered from active cold seep site in the Krishna-Godavari (K-G) basin, Bay of Bengal.

Petrographic thin section analysis of methane-derived authigenic carbonates from shallow gas-hydrate (active cold seep) bearing core (SSD-45/Stn-4/GC-01) showed dissolution structure with dominant mineralogy of micritic aragonite, calcite and magnesium calcite (Figure 4.12a-b). Bryozoans of circular type structure and its preserved fossils were observed at 1.01 mbsf (Figure 4.12c). Foraminiferal tests of different size and shape cast were found in the micritic aragonite (Figure 4.12d). Several layers of fine-medium sand were observed in all sediment magnetic zones in core NGHP-01-15A (Figure 4.17a-d).

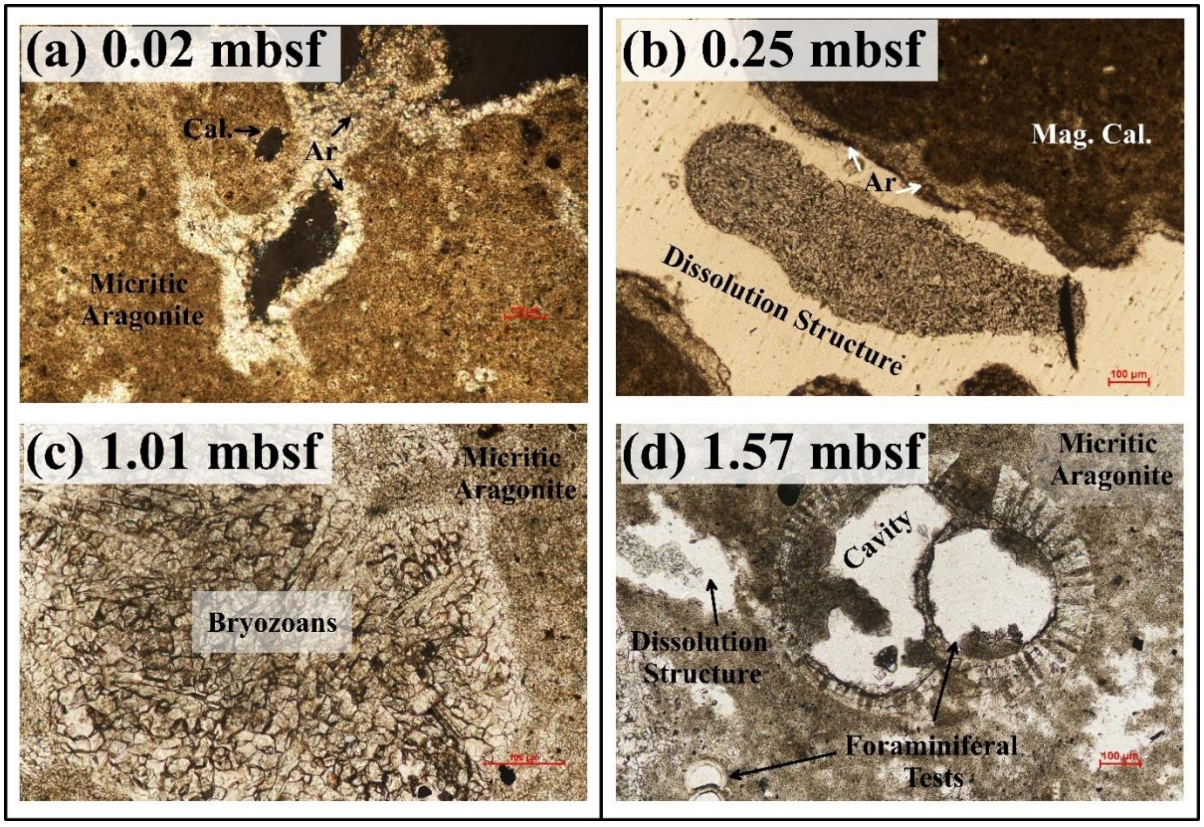

Figure 4.12 *(a–d) Petrographic thin sections of methane-derived authigenic carbonates from shallow (active cold seep, Core ID: SSD-45/Stn-4/GC-01) gas-hydrate site in the Krishna-Godavari (K-G) basin, Bay of Bengal. The thin sections were observed under plane-polarized light (Please note that arrow used to highlight the structures and mineral types).*

4.2.7. Rock magnetic properties of shallow (active cold seep) and deep-seated gas-hydrate system

Based on the rock magnetic properties, the samples were broadly classified into three distinct groupings (Figure 4.13a-c). Majority of the samples from shallow hydrate core (SSD-45/Stn-4/GC-01) exhibited both low and intermediate values of χ_{lf}, SIRM and SIRM/χ_{lf} and showed close groupings (Figure 4.13a-b). Samples possessing higher values of SIRM/χ_{lf} and comparatively low values of χ_{lf} was attributed to the presence of fine-grained ferri-and paramagnetic iron sulfides (Figure 4.13b). Contrastingly, samples from core NGHP-01-15A showed relatively high and intermediate values of χ_{lf}, SIRM and SIRM/χ_{lf} values indicating the dominance of mixed-type (iron oxides, iron sulfides) mineral assemblages (Figure 4.13a-b). A good covariation between concentration dependent (χ_{lf}) and mineralogy diagnostic (S-ratio) was noticed (Figure 4.13c). Higher values of χ_{lf} coupled with the S-ratio > 0.9 in both the sediment cores was attributed to the presence of ferrimagnetic (magnetite) particles. Samples from core SSD-45/Stn-4/GC-01 exhibiting low S-ratio showed narrow range in χ_{lf} indicating the presence of high coercive ferrimagnetic magnetic minerals (hematite, goethite) or ferrimagnetic iron sulfides (greigite, hexagonal pyrrhotite) (Figure 4.13c; Peters and Dekkers, 2003; Roberts et al., 2011; Kars and Kodama, 2015; Horng, 2018). While samples from core NGHP-01-15A which showed low S-ratio exhibited wide range in χ_{lf} (Figure 4.13c). The day plot showed that all the analyzed samples from shallow and deep-seated gas-hydrate sediment cores lie in the vortex state (Figure 4.13d; Day et al., 1977).

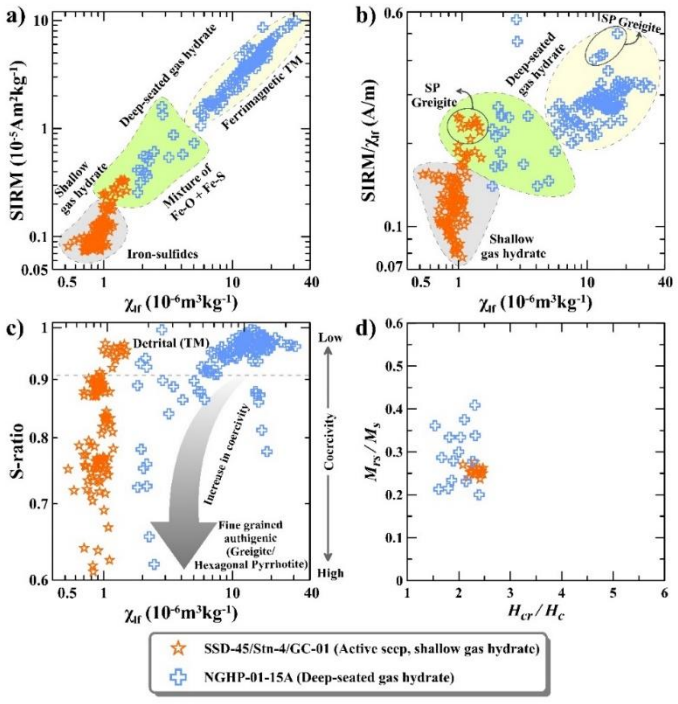

Figure 4.13: *(a–c) Bivariate scatter plots of magnetic parameters: magnetic susceptibility (χ_{lf}), saturation isothermal remanent magnetization (SIRM), SIRM/χ_{lf}, S-ratio, and (d) Day plot for samples from shallow (active cold seep, Core ID: SSD-45/Stn-4/GC-01) and deep-seated gas (Core ID: NGHP-01-15A) hydrate site in the Krishna-Godavari (K-G) basin, Bay of Bengal. (Please note that the gray arrow is used in plot (c) to highlight the trend).*

4.3. Discussion

4.3.1. Origin of magnetic minerals and its fate in sulfidic and methanic environments

Rock magnetic and mineralogical methods provided suitable means to characterize magnetic assemblages in a complex active cold seep and methane-hydrate-bearing marine sedimentary system with different sources (detrital, diagenetic, authigenic) of the magnetic particles. It is pre-requisite to evaluate the factors contributing and affecting the magnetic signals for better interpretation of sediment magnetic record in context with primary (detrital) and secondary (diagenetic/authigenic) depositional processes (Housen and Musgrave, 1996; Roberts, 2015). The sediment magnetism at sites representing shallow (SSD-45/Stn-4/GC-01) and deep-seated (NGHP-01-15A) gas-hydrate system was carried by a complicated magnetic mineral assemblages comprised of detrital (titanomagnetite, magnetite, silicate-hosted magnetic inclusions) diagenetic (pyrite), authigenic (magnetite, greigite), and biogenic (extracellular) origin as confirmed by rock magnetic, XRD, SEM-EDS, TEM-EDS, and optical microscopy (Figure 4.2-4.10, Figure 4.13-4.15). In the studied sediment cores, the degree of influence of each magnetic mineral phase varied within sulfidic and methanic sedimentary zones as clearly evident in rock magnetic (Figure 4.2) and mineralogical records (Figure 4.7-4.10). Detrital magnetic particles occurred as discrete vortex state-MD type magnetite (as confirmed through FORC and SEM-EDS; Figure 4.6; Figure 4.7, Figure 4.8) as well as silicate-hosted magnetic inclusions (Figure 4.14, Figure 4.15) in the both sediment cores. Higher values of χ_{lf} in Z-I of both cores can be attributed to the presence of fine and coarse-grained detrital titanomagnetite mainly sourced from Deccan trap basalts (Figure 4.2, Figure 4.7-4.10; Ramesh and Subramanian, 1988; Sangode et al., 2001; Badesab et al., 2019). Thermomagnetic curves (χ-T) confirmed that the bulk magnetic mineralogy was dominated by titanomagnetite including magnetite (Dunlop et al., 1997). The data also showed the dominance of non-magnetic iron phase in samples from both sediment cores (Figure 4.4a-b). The thermal transformation at 352°C (SSD-45/Stn-4/GC-01) and 373.5°C (NGHP-01-15A) was consistent with the high temperature oxidation of a non-magnetic iron phase into a magnetic phase (Figure 4.4a-b; Passier et al., 2001). The broadness of the oxidation peak in the NGHP-01-15A samples was attributed to the presence of two different morphologies of pyrite. Similar observations were reported from equatorial Atlantic (Itambi et al., 2010) and Mediterranean sediments (Passier et al., 2000). Mineralogy diagnostic low-temperature magnetic data of core SSD-45/Stn-4/GC-01 revealed no distinct Verwey transition in the topmost sediment interval (Figure 4.5a-b) and gas-hydrate-bearing layers (Figure 4.5c-f).

Such feature was reconciled to the masking of transition due to increase in paramagnetic contribution (Verwey, 1947). Rapid loss of LT-SIRM between 5 and 30 k in these samples was due to increased contribution from SP magnetic particles (Tarduno, 1995) or paramagnetic (e.g., silicates; Itambi et al., 2010).

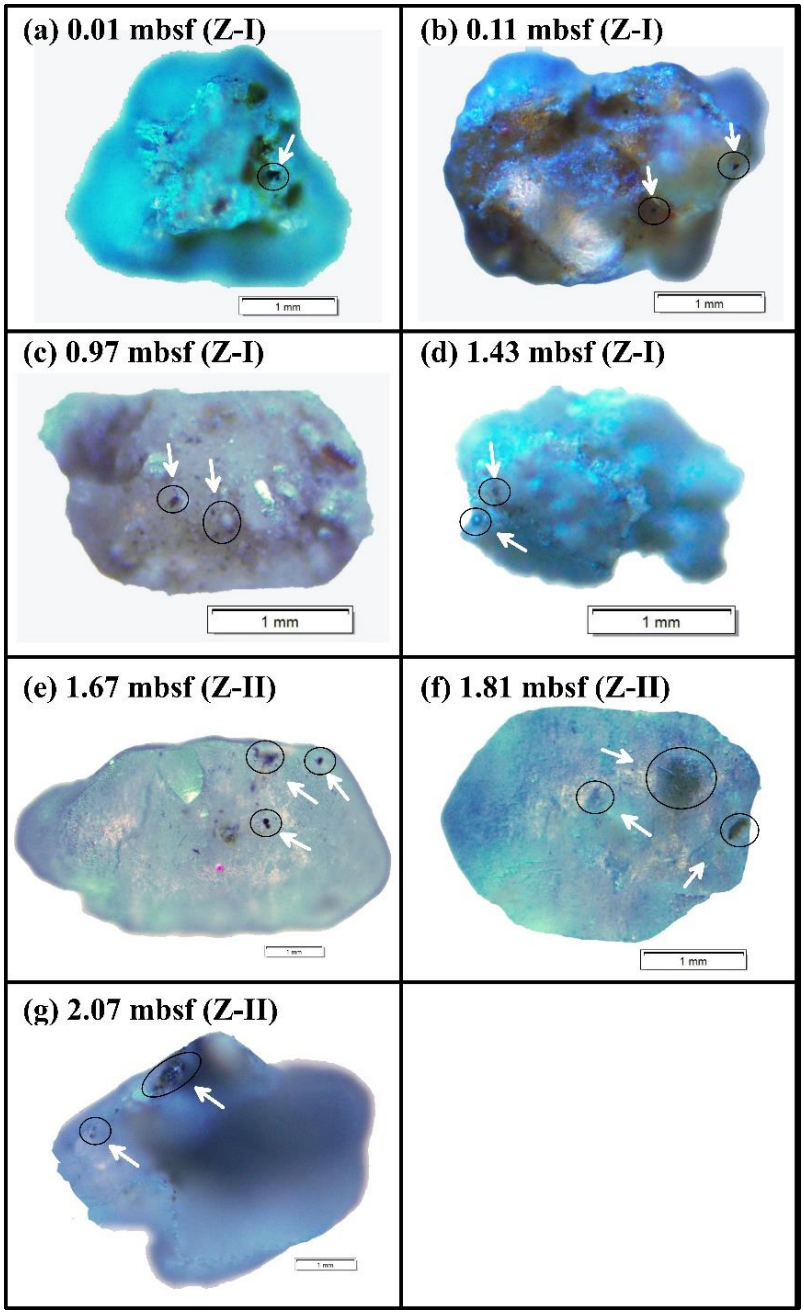

Figure 4.14: *(a–g) Optical microscopic images of the representative (>63 µm) fraction from shallow (active cold seep; Core ID: SSD-45/Stn-4/GC-01). Magnetic inclusion within host quartz (>63 µm) fractions are marked (see black circles and white arrows).*

Non-stoichiometry, cation substitution and grain size can also supress the appearance of the Verwey transition (Kakol et al., 1992; Halgedahl and Jarrard, 1995). Partial oxidation of

magnetite followed by an increase in paramagnetic contribution exhibited by diagenetically formed pyrite (Figure 4.7 b, d-f) at several sediment intervals in core SSD-45/Stn-4/GC-01 had masked the transition and provided evidence for the claim. Titanomagnetite and SP greigite (Figure 4.6; Muxworthy and Dunlop, 2002) particles were found to occur throughout in core SSD-45/Stn-4/GC-01 (Figure 4.2 a, e, Figure 4.7a-f, Figure 4.8a-f). Increase in Ti-content (Moskowitz et al., 1998) and presence of SP (Itambi et al., 2010) particles also contributed to the masking of the Verwey transition.

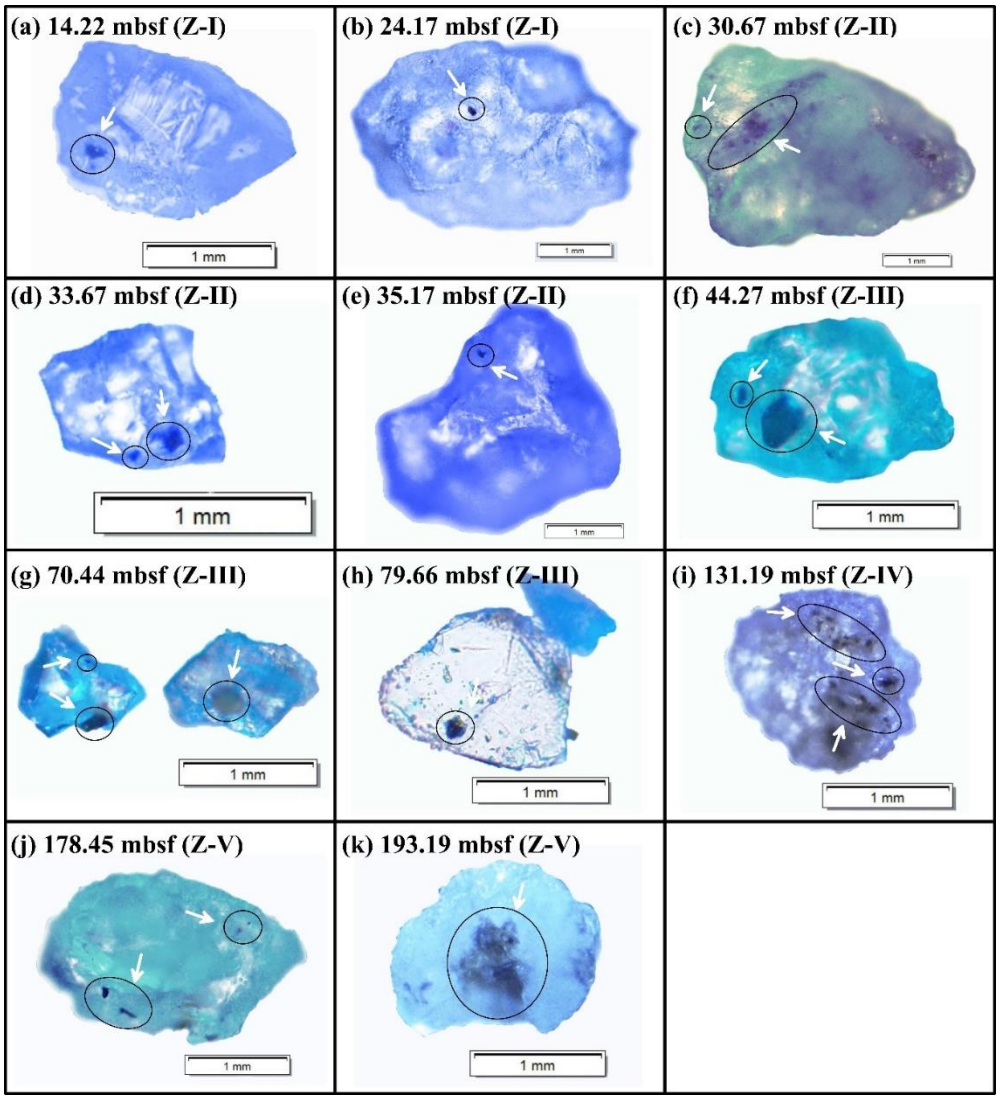

Figure 4.15: *(a–k) Optical microscopic images of the representative (>63 µm) fraction from deep-seated (Core ID: NGHP-01-15A) gas-hydrate site in the Krishna-Godavari (K-G), Bay of Bengal. Magnetic inclusion within host quartz (>63 µm) fractions are marked (see black circles and white arrows).*

Silicate hosted (fine-grained magnetic particles) inclusions were found to be spatially distributed throughout and remain survived through sulfidic, methanic, and gas-hydrate-bearing zones in both the sediment cores (Figure 4.2, Figure 4.14, Figure 4.15). Orange-brownish color coating over the surface of silicate grain indicated the overgrowth of iron-sulfide previously formed during reductive diagenesis (Figure 4.14b-c; Larrasoaña et al., 2007; Badesab et al., 2020a). It was clear that the finer magnetic particles occuring as inclusions within the silicate matrix remained protected and survived the reductive diagenetic dissolution and pyritization reactions throughout (Hounslow and Maher, 1996; Hatfield, 2014; Chang et al., 2016). Enrichment of SP particles in sulfidic and methanic environment was previously linked with the growth of fine-grained ferrimagnetic iron sulfides like greigite (Rowan et al., 2009; Kars et al., 2021). Elevated SIRM/χ_{lf} values (Figure 4.2e, k) in core SSD-45/Stn-4/GC-01 (0.01– 0.35 mbsf, 1.75 – 1.85 mbsf, 2.05 – 2.11 mbsf) and in core NGHP-01-15A (38.86 – 63.97 mbsf) indicated that the presence of authigenic SP greigite (Snowball, 1991; Larrasoaña et al., 2007; Blanchet et al., 2009; Lougheed et al., 2012). Similar observations of enhanced SIRM/ χ_{lf} linked with the presence of authigenic greigite particles were reported from Santa Barbara Basin (Blanchet et al., 2009), North Central Baltic Sea (Reinholdsson et al., 2013), and Atlantic Ocean (Oda and Torii, 2004). Magnetic grain size proxy (ARM/SIRM) has been utilized as a valuable indicator to detect fine-grained magnetic particles in methanic sediments (Dillon and Bleil, 2006; Lin et al., 2021). Higher ARM/SIRM values in both sediment cores was linked to authigenic formation of magnetite via microbial iron-reduction process (Elmore et al., 1987; Lovely et al., 1987; Phillips et al. 2017; Vigderovich et al., 2019; Lin et al., 2021). Magnetic mineralogy (S-ratio) proxy showed anomalous zones in both sediment cores. Low S-ratio intervals in shallow SSD-45/Stn-4/GC-01 (0.31 to 1.07 mbsf and 1.83 to 2.23 mbsf; Figure 4.2f) and deep-seated gas-hydrate NGHP-01-15A (22.91 to 36.77 mbsf; Figure 4.2l) bearing sediment cores was manifested by low χ_{lf} and mainly linked with the authigenic formation of ferrimagnetic iron sulfides (greigite, hexagonal pyrrhotite). Such magnetic iron sulfides were probably no longer stable and got quickly transformed into pyrite (Jiang et al., 2001; Kars and Kodama, 2015; Badesab et al., 2017). Lack of distinct peaks of SP greigite particles in mineralogical record (Figure 4.10) in both the sediment cores was explained by the fact that the presence of ample (Fe^{2+}) and (S^{2-}) in the porewater probably promoted pyrite formation without the complete preservation of intermediate ferrimagnetic iron sulfide i.e., greigite (Kao et al., 2004; Reilly et al., 2020).

4.3.2 Constraints on the formation and preservation of diagenetic and authigenic minerals in the shallow and deep-seated gas-hydrate sedimentary system

The K-G basin represented an ideal natural laboratory with its unique presence of shallow (active cold seep; SSD-45/Stn-4/GC-01; Mazumdar et al., 2019) and deep-seated (NGHP-01-15A; Collett et al., 2008) gas-hydrate systems to elucidate the constraints on the formation and preservation of diagenetic and authigenic minerals in two different diagenetic settings experiencing variable fluid sequence. Diagenetic and authigenic processes linked with methane seepage and hydrate formation/dissociation processes enhances the growth of iron sulfides which induce a detectable magnetic signature in the host sediments (Esteban et al., 2008; Greve et al., 2021). Detailed rock magnetic and mineralogical analyses on the sediment cores complemented by the petrological observations on the authigenic carbonates helped in examining the diagenetic and authigenic processes in the studied cores. This section briefly discussed how magnetic minerals respond to such processes prevailing in two different diagenetic settings. At active seeps, sudden shifting of SMTZ fronts due to changing methane flux and rates of sulfate reduction triggered the non-steady state diagenesis involving magnetite dissolution and authigenic formation of ferrimagnetic magnetite and iron sulfide (greigite, hexagonal pyrrhotite) (Larrasoaña et al., 2003; Phillips et al., 2017; Roberts, 2015; Lin et al., 2021; Reilly et al., 2020). At active site SSD-45/Stn-4/GC-01, gas-hydrates occur as fracture-filling and tube-type within the host sediments (Mazumdar et al., 2019). Gas plumbing system created by fractures efficiently facilitated the upward methane migration from deeper sources (Dewangan et al., 2011; Sriram et al., 2013; Badesab et al., 2020c). In contrast, constant supply of higher methane fluxes from deeper reservoir, occurrence of deep-seated disseminated-type gas-hydrates in sand horizons and well-developed SMTZ (Figure 4.16) at site NGHP-01-15, favoured the steady-state diagenesis (Collett et al., 2008). The sediment magnetic signal interms of magnetic mineral concentration, grain size and mineralogy in both type of gas-hydrate system was strongly constrained by the history of fluid sequence. Progressive loss of detrital magnetic minerals via dissolution and pyrite formation was clearly evident in the upper most parts of both the sediment cores. Within the sulfidic zone (Z-I), the lowest values of χ_{lf} were observed where iron oxides have been reduced to paramagnetic pyrite (Figure 4.2a, g). Such signature was typically observed in settings with high methane and sulphate or sulphide flux, for example at methane vents at Cascadia Margin (Esteban et al., 2008), southwestern Taiwan (Horng, 2018), Hikurangi Margin, New Zealand (Kars et al., 2021), Oman and North California margin (Rowan et al.,

2009), Argentina continental margin (Garming and Riedinger, 2005), and Rio De Plata, South Atlantic Ocean (Riedinger et al., 2005).

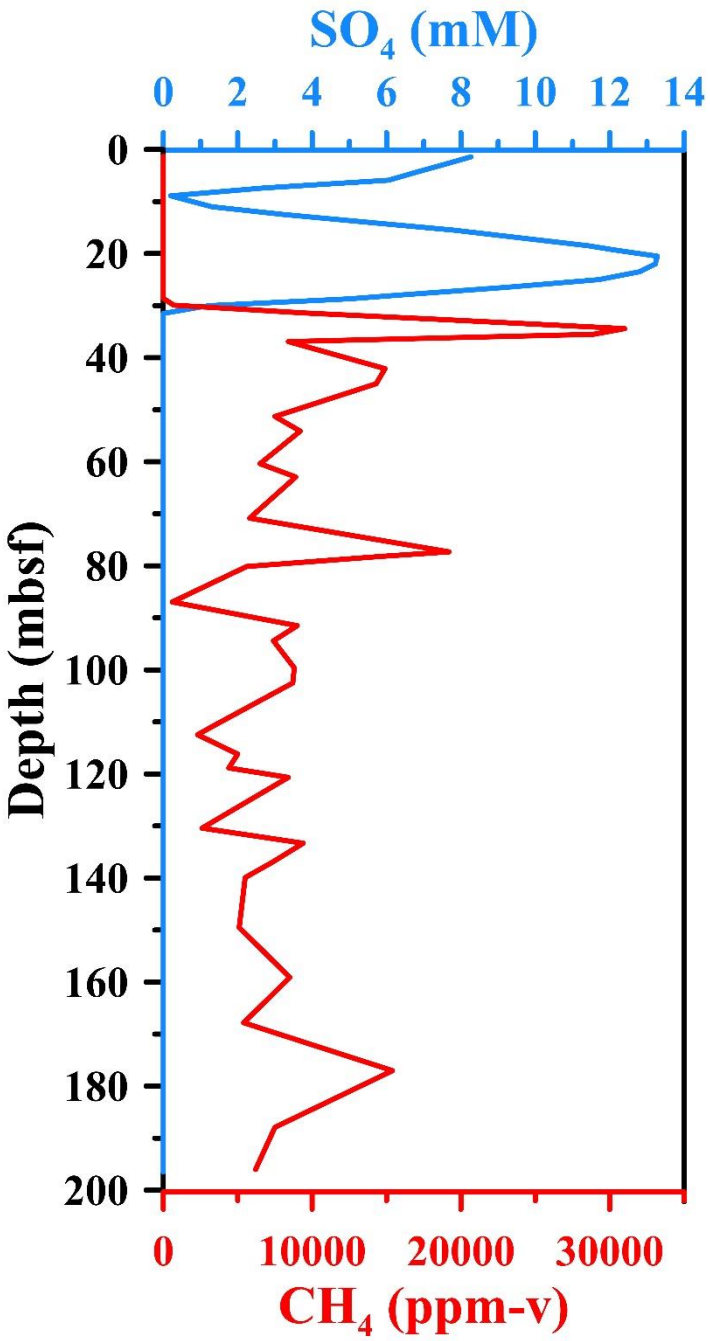

Figure 4.16: *Pore-water sulfate concentration and methane (headspace gas) profile of sediment core NGHP-01-15A (modified from Collet et al., 2008).*

Magnetic grain size diagnostic (ARM/SIRM) proxy has been effectively used to determine the presence of fine-grained authigenic magnetite in methanic sediments (Peters and Dekkers, 2003; Dillon and Bleil, 2006; Lin et al., 2021). Two distinct patterns in ARM/SIRM profile

was noticed in cores from the shallow (Figure 4.2d) as well as deep-seated (Figure 4.2j) gas-hydrate system. Initial (0.01 – 0.19 mbsf) decrease in ARM/SIRM in the uppermost sediment intervals of shallow hydrate core (SSD-45/Stn-4/GC-01) was attributed to preferential diagenetic dissolution of fine-grained detrital magnetic particles (Figure 4.2d; Peters and Dekkers, 2003). Downcore increase in ARM/SIRM from 0.21 to 1.69 mbsf within Z-I was linked with the authigenic formation of fine-grained magnetite via microbial iron reduction process (Figure 4.2d; Karlin et al., 1987; Lovely et al., 1987; Phillips et al., 2017; Vigderovich et al., 2019; Lin et al., 2021). Similar observations linking the rise in ARM/SIRM to the authigenic growth of SD magnetite in methanic were reported from the Bay of Bengal (Gaikwad et al., 2021), Niger deep-sea fan (Dillon and Bleil, 2006), South China Sea (Lin et al., 2021), and Southern Eastern Mediterranean continental shelf (Amiel et al., 2020). A marked shift of decrease of ARM/SIRM in the Z-II from 1.71 to 2.23 mbsf suggested significant reduction in the growth of authigenically formed fine-grained magnetite possibly due to decline in microbial activity coupled to iron-reduction process (Figure 4.2d; Lovely et al., 1987; Egger et al., 2015; Phillips et al., 2017; Rodelli et al., 2018; Rodelli et al., 2019; Lin et al., 2021). In deep-seated gas-hydrate core NGHP-01-15A, initial reduction in ARM/SIRM from 0.74 – 13.23 mbsf in sulfidic (Z-I) was due to magnetite reduction linked with reductive diagenesis (Figure 4.2j). A systematic gradual increase in ARM/SIRM from 14.02 to 25.86 mbsf in sulfidic (Z-I) i.e., just above SMTZ was attributed to the presence of fine-grained detrital magnetite which survived the dissolution fronts due to rapid burial in the uppermost sediment intervals. A minor downcore rise in ARM/SIRM below the present-day SMTZ (at 31.5 mbsf) followed by a slow gradual increase further till the bottom of the core (i.e., from 32.36 – 196.45 mbsf) suggested increase in growth of fine-grained authigenic magnetite (Figure 4.2j; Elmore et al., 1987; Karlin et al., 1987; Phillips et al., 2017; Lin et al., 2021). A similar steady increase of ARM/SIRM in sediment cores from methanic zone of Niger deep-sea fan (Dillon and Bleil, 2006) and Southern Eastern Mediterranean continental shelf (Amiel et al., 2020) was attributed to the gradual authigenic growth of SD-magnetite. A general trend of gradual downcore increase in greigite diagnostic SIRM/χ_{lf} (Larrasoaña et al., 2007) in the methanic zone below present-day gas-hydrate interval (i.e, from Z-II to Z-V) suggested increase in authigenic growth of fine-grained (SP) greigite particles (Figure 4.2k; Snowball, 1991). Biogenic magnetic minerals produced by magnetotactic bacteria through intracellular and extracellular mineralization proceses are ubiquitously found in marine sediments and have important implications in paleomagnetic and environmental magnetic studies (Kirschvink and Chang, 1984; Petersen et al., 1986; Dekkers, 1997; Roberts et al.,

2012). These fine-grained magnetites can be easily identified using specialized electron microscopic (TEM-EDS) techniques. The TEM-EDS (Figure. 4.9) observations made on magnetic extracts from different sediment depth intervals suggested that the magnetic particles are dominated by biogenic magnetites formed as a result of extracellular mineralization (Yan et al., 2012).

Stable SD authigenic greigite and magnetite linked with AOM has been widely documented within sediments in methanic environments (Musgrave et al., 2006; Enkin et al., 2007; Larrasoaña et al., 2007; Kars and Kodama, 2015; Phillips et al., 2017; Shi et al., 2017; Badesab et al., 2019). Rock magnetic and mineralogical records confirmed the presence of authigenic greigite and magnetite in both cores (Figure 4.2, Figure 4.7, Figure 4.10). An attempt was made in the present study to elucidate their formative mechanism and underlying controls in the sulfidic and methanic zones. Two scenarios were put forwarded to unravel the mechanism of authigenic formation of magnetite and greigite in shallow and deep-seated gas-hydrate system in the Bay of Bengal. At active seep site, sulfate-driven AOM induced by higher methane results in the formation of authigenic carbonates and iron sulfides at SMTZ (Housen and Musgrave, 1996; Suess, 2014; Liang et al., 2017). Changes in the methane flux probably created SMTZ fronts induced by multiple AOM. Subsequently, hydrogen sulfide produced at SMTZ fronts caused the dissolution of iron oxides, followed by successive precipitation of iron sulfides (Pulton et al., 2004; Riedinger et al., 2014; Kars and Kodama, 2015; Xie et al., 2019; Greve et al., 2021). Fluctuations in χ_{lf} and occurrence of authigenic carbonates throughout in Z-I provided evidence on the multiple AOM fronts at active seep site (SSD-45/Stn-4). Lin et al (2021) reported that oxidation of iron-sulfides at SMTZ was enhanced during the periods of lower methane seepage and generated secondary iron (oxyhydr) oxides. As methane seepage increased, such iron (oxyhydr) oxide served as a reactive iron source for magnetite authigenesis linked with microbial iron-reduction resulting in the authigenic formation of magnetite. Previous studies provided rock magnetic and geochemical evidence for authigenic magnetite formation via iron reduction in sediments (IODP Site C0020) offshore Shimokita Peninsula, Japan (Phillips et al., 2017) and eastern equatorial Pacific (Karlin et al., 1987). Overall, high ARM/SIRM and χ_{lf} from 0.21 to 1.69 mbsf in methanic zone (Z-I) of core SSD-45/Stn-4/GC-01 was attributed to the presence of fine-grained authigenic magnetite and provided compelling evidence on the magnetite authigenesis occurring in this zone probably due to rapid change in diffusive methane fluxes

controlled by opening/closing dynamics of underlying fault/fracture system at this site (Figure 4.2a, d).

In the methanic zone, AOM seems to be a major biogeochemical process that affected magnetic mineral assemblages in marine sediments (Roberts et al., 2018). Sulfate-reduction via AOM utilized pore water methane and sulfate to near depletion at the SMTZ and provided a secondary source of hydrogen sulfide (Niewöhner et al., 1998; Kasten and Jørgensen, 2000) that facilitated the reductive dissolution of detrital iron oxides and formation of secondary ferrimagnetic iron sulfides. A marked shift of decrease in χ_{lf} and ARM/SIRM values in methanic zone (Z-II; 1.71 to 2.23 mbsf) of core SSD-45/Stn-4/GC-01 revealed significant decline in the growth of authigenic magnetite (Figure 4.2a, d). It was quite possible that either bulk of newly formed authigenic (fine-grained) magnetite were preferentially removed by diagenetic dissolution because of intense AOM itself or decline in methane flux due to hydrate accumulation in Z-II might have not supported the authigenic formation of fine-grained magnetite. Fracture-filled gas-hydrates were recovered from Z-II of core SSD-45/Stn-4/GC-01 (Mazumdar et al., 2019). Presence of high reactive iron and limited sulfide concentration rather favoured the formation of authigenic greigite in Z-II of core SSD-45/Stn-4/GC-01. This observation suggested that greigite might have started forming only after hydrate formation in Z-II. High SIRM/χ_{lf} in the gas-hydrate bearing sediment intervals in Z-II of core SSD-45/Stn-4/GC-01 confirmed the presence of authigenic greigite (Figure 4.2e; Snowball, 1991; Blanchet et al., 2009; Lowgheed et al., 2012). SEM-EDS and XRD data confirmed the presence of detrital coarse-grained titanomagnetite (which survived dissolution), diagenetic pyrite and authigenic greigite in Z-II (Figure 4.7e-f, Figure 4.8e-f, Figure 4.10e-f). The sustenance of high methane flux in Z-II of core SSD-45/Stn-4/GC-01 probably inhibited the oxidation of previously formed diagenetic iron sulfides and constrained the production of reactive iron source needed/required for magnetite authigenesis in Z-II (Elmore et al., 1987; Karlin et al., 1987; Phillips et al., 2017; Lin et al., 2021). A noticeable drop followed by consistent lower ARM/SIRM values reflected significant reduction in the growth of fine-grained authigenic magnetite in the methanic environment (Z-II; 1.69 to 2.23 mbsf) of core SSD-45/Stn-4/GC-01 (Figure 4.2d). High SIRM/χ_{lf} (0.1 to 0.25 mbsf) in the uppermost sediment interval of Z-I suggested that the interplay between downward migrating sulfate and upward rising methane probably favoured greigite authigenesis just below the near-surface sulfidic zone (Figure 4.2e; Kars and Kodama, 2015; Larrasoaña et al., 2007). A systematic decrease of SIRM/χ_{lf} within Z-I (Figure 4.2e) was

attributed to slow conversion of ferrimagnetic greigite to pyrite in Z-I of core SSD-45/Stn-4/GC-01 (Snowball, 1991; Larrasoaña et al., 2007; Musgrave et al., 2019). Similar observations were reported from Izu-Bonin rear arc, Japan (Musgrave et al., 2019), Blake Ridge (ODP Site 997; Shipboard Scientific Party, 1996b), Nankai Margin (IODP Site C002; Shi et al., 2017). More recently, Musgrave et al. (2019) suggested that downcore decrease in SIRM/χ_{lf} was due to the shift in coercivity of the magnetic particles, as fine-grained detrital magnetite gets selectively dissolved downcore due to authigenic formation of SD/SP greigite particles which exhibited significantly low S-ratio (Peters and Dekkers, 2003; Dillon and Bleil, 2006; Larrasoaña et al., 2007; Roberts et al., 2011; Kars and Kodama, 2015; Horng, 2018). A shift in the coercivity of magnetic particles (Figure 4.2f) was seen through a broad and distinct interval exhibiting low S-ratio values in Z-I (0.31 to 1.07 mbsf) and Z-II (1.83 to 2.23 mbsf) in core SSD-45/Stn4/GC-01. This observation provided compelling evidence on the authigenic formation of SP greigite in core SSD-45/Stn-4/GC-01 (Figure 4.6; Muxworthy and Dunlop, 2002) during magnetite reduction process and validated the interpretation of Musgrave et al. (2019). A magnetic mineral diagenetic study on the sediment core from Perseverance Drift, North-western Weddell Sea by Reilly et al. (2020) made similar observations. They attributed that the high coercivity layers (marked by low S-ratio) below SMTZ in core JKC36 were formed due to porewater transition, where downward diffusing sulfate is limited, but the iron (Fe^{2+}) concentration still exist which provided favourable conditions for the growth of greigite and hexagonal 3C pyrrhotite.

Greigite is well-known to occur in methane-rich sediments, methane-hydrates or in consortium with methane diffusion (Housen and Musgrave, 1996; Musgrave et al., 2006; Larrasoaña et al., 2007; Roberts, et al., 2018; Kars et al., 2021). More recently, a high-resolution rock magnetic study on a sediment core from IODP Site U1518 at Hikurangi Margin, offshore New Zealand reported the formation of authigenic greigite linked to methane diffusion and disseminated-type methane-hydrate within sediments (Kars et al., 2021). In methanic zone (Z-II) of core SSD-45/Stn4/GC-01, enhanced microbial activity in the presence of gas-hydrates probably favoured the formation and preservation of greigite (Musgrave et al., 2006; Kars et al., 2018, 2021). High SIRM/χ_{lf} peaks within three gas-hydrate intervals in Z-II of core SSD-45/Stn4/GC-01 supported the interpretation (Figure 4.2e). Similar observations were reported from Blake Ridge (Wellsbury et al., 2010) and Hydrate Ridge (Larrasoaña et al., 2007), Santa Barbara Basin, California (Blanchet et al., 2009), Atlantic Ocean (Oda and Torii, 2004), Baltic Sea (Lowgheed et al., 2012). At active

seep site (SSD-45/Stn-4), methane seepage dynamics controlled the precipitation of authigenic carbonates (Mazumdar et al., 2019; Dewangan et al., 2021). Recently Mazumdar et al. (2019) emphasized that high flux of hydrogen sulfide across the sediment–water interface at active cold seep site (SSD-45/Stn-4) supported the existence of AOM close to the sea floor. Abundant occurrence of MDAC (almost in all samples) within Z-I (only) of SSD-45/Stn-4/GC-01 indicated that enhanced methane flux from deeper reservoir triggered multiple and strong AOM's which resulted in the formation of thick carbonate layers. Dissolution structure and cavity (Figure 4.12a,b,d) within the carbonates provided convincing evidence on the high methane seepage at this site (Aloisi et al., 2000). Lack of authigenic carbonates in the methanic environment (Z-II) of core SSD-45/Stn-4/GC-01 was either due to weak AOM caused by decline in the supply of rising methane flux from deeper reservoir, closure of underlying fractures/fault (Gaikwad et al., 2021), or due to hydrate accumulation underneath (Housen and Musgrave, 1996).

In a sediment core (NGHP-01-15A) from the deep-seated gas-hydrate system, detrital (discrete and inclusions - titanomagnetite, magnetite), diagenetic (pyrite) and authigenic (magnetite, greigite) minerals of varying concentration and grain size controlled the bulk sediment rock magnetic properties (Figure 4.2, Figure 4.4, Figure 4.7, Figure 4.8, Figure 4.10). Downcore decline in χ_{lf} from the uppermost 0.74 mbsf to 17.76 mbsf in core NGHP-01-15A was linked with preferential loss of fine-grained detrital magnetic particles due to diagenetic dissolution (Roberts, 2015). A sharp increase in χ_{lf} (19.86 – 28.07 mbsf) coupled with high ARM/SIRM just above the present-day SMTZ (Figure 4.16) in Z-I of core NGHP-01-15A was reconciled to the presence of fine-grained detrital magnetite which survived the dissolution fronts in the uppermost sediment intervals due to increase sedimentation. A trend of gradual rise in ARM/SIRM downcore from Z-II to Z-V just below present-day SMTZ in core NGHP-01-15A was reconciled with the slow growth of authigenic magnetite in these zones (Figure 4.2j, Figure 4.16; Elmore et al., 1987; Lovely et al., 1987; Karlin et al., 1987; Phillips et al., 2017; Vigderovich et al., 2019; Lin et al., 2021). The mineralogy of authigenic carbonate in core NGHP-01-15A was mainly composed of Fe-rich carbonate mineral with minor amount of low-magnesium calcite (LMC) (Teichert et al., 2014). Deep-sourced fluid and gas migration generated high gas-hydrate saturations within the sand-rich sediment interval at site NGHP-01-15 (Collet et al., 2008: Riedel et al., 2011). Similarly, several sand layers were also found to occur in different sediment intervals (15.83 mbsf to 192.48 mbsf, Figure 4.2, Figure 4.17; Table. 4.3; Collett et al., 2008) in core NGHP-01-15A.

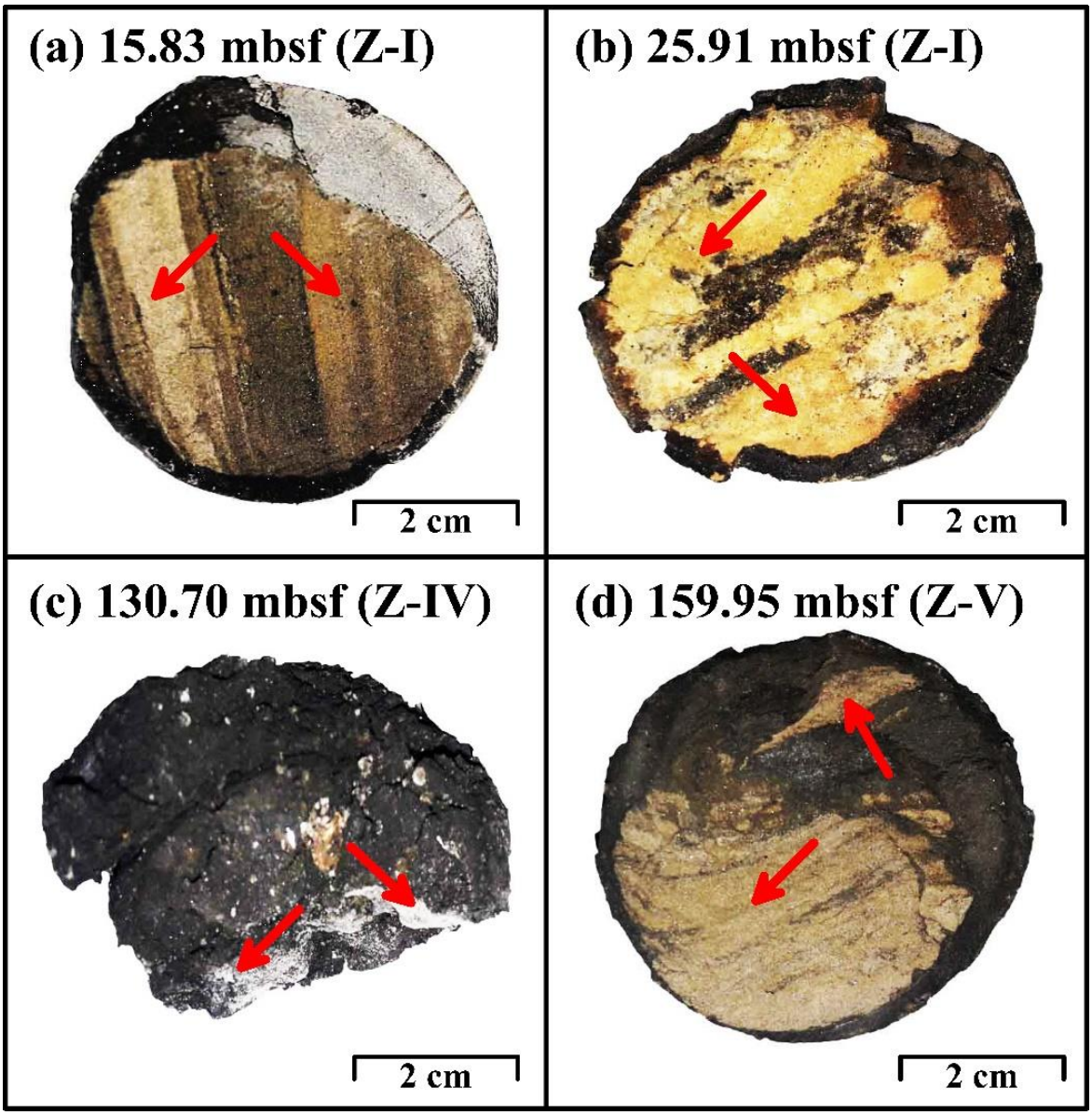

Figure 4.17: *(a-d) Photograph showing fine to medium grained sand layers from different sediment magnetic zones of a deep-seated (Core ID: NGHP-01-15A) gas-hydrate site in the Krishna-Godavari (K-G) basin, Bay of Bengal.*

A comprehensive pore-water geochemical and isotope ratio study in core NGHP-01-15A revealed that the carbon dioxide (CO_2) produced through microbial methanogenesis got effectively neutralized by silicate weathering. This process resulted in generation of excess alkalinity which got further sequestered in Ca and Fe-carbonates (Solomon et al. 2014; Teichert et al., 2014). The mineral composition of authigenic carbonates suggested that formation of Fe-rich carbonates in core NGHP-01-15A are predominantly related to the

silicate weathering reactions coupled to microbial methanogenesis (Solomon et al., 2014; Torres et al., 2020). Result could be attributed to the highly porous environment created by several layers of coarse-grained sand and discrete authigenic carbonates facilitated the efficient percolation of downward diffusing oxidizing fluids, which preferentially favoured iron sulfide oxidation. This led to the subsequent generation of secondary iron (oxyhydr) oxides required for authigenic formation of magnetite via microbial iron-reduction process in methanic zone in core NGHP-01-15A (Elmore et al., 1987; Lovely et al., 1987; Karlin et al., 1987; Phillips et al., 2017; Vigderovich et al., 2019; Lin et al., 2021). Similar to presented observations, microbial iron-reduction in the methanic zone of SE Mediterranean continental shelf (Vigderovich et al., 2019) and Bothnian Sea sediments (Egger et al., 2015) was unravelled based on the geochemical pore water profiles and isotopic records. A gradual rise in ARM/SIRM from Z-II to Z-V in core NGHP-01-15A reflected the slow growth of authigenic magnetite and provided support to hypothesis presented in this section (Figure 4.2j).

In core NGHP-01-15A, two trends of rise in SIRM/χ_{lf} from 38.86 to 63.97 mbsf (uppermost- below SMTZ) and 91.85 to 196.45 mbsf (lowermost- gas-hydrate and methanic zone) confirmed the presence of authigenic greigite in Z-III, Z-IV, and Z-V (Figure 4.2k; Snowball, 1991; Tarduno, 1995; Larrasoaña et al., 2007). Two scenarios were proposed to explain the authigenic growth of greigite below SMTZ (Figure 4.18). High concentration of hydrogen sulfide produced at the present-day SMTZ front might have been completely utilized during pyritization as seen through distinct minima in χ_{lf} just below SMTZ (Figure 4.2g, Figure 4.16). Consequently, sulfide deficient zone was created in the deeper sediment intervals below SMTZ which led to the formation and preservation of greigite (Badesab et al., 2020c). Reduction in rising methane flux due to hydrate accumulation in the underlying sediments might had constrained the sulfide production and preferentially favoured greigite formation and preservation above the present-day gas-hydrate occurrence zone (~ 75 - 91 mbsf) in this core. However, the possibility that SP greigite particles (as marked by high SIRM/χ_{lf} from 38.86 mbsf to 63.97 mbsf; Figure 4.2k) observed below the present-day

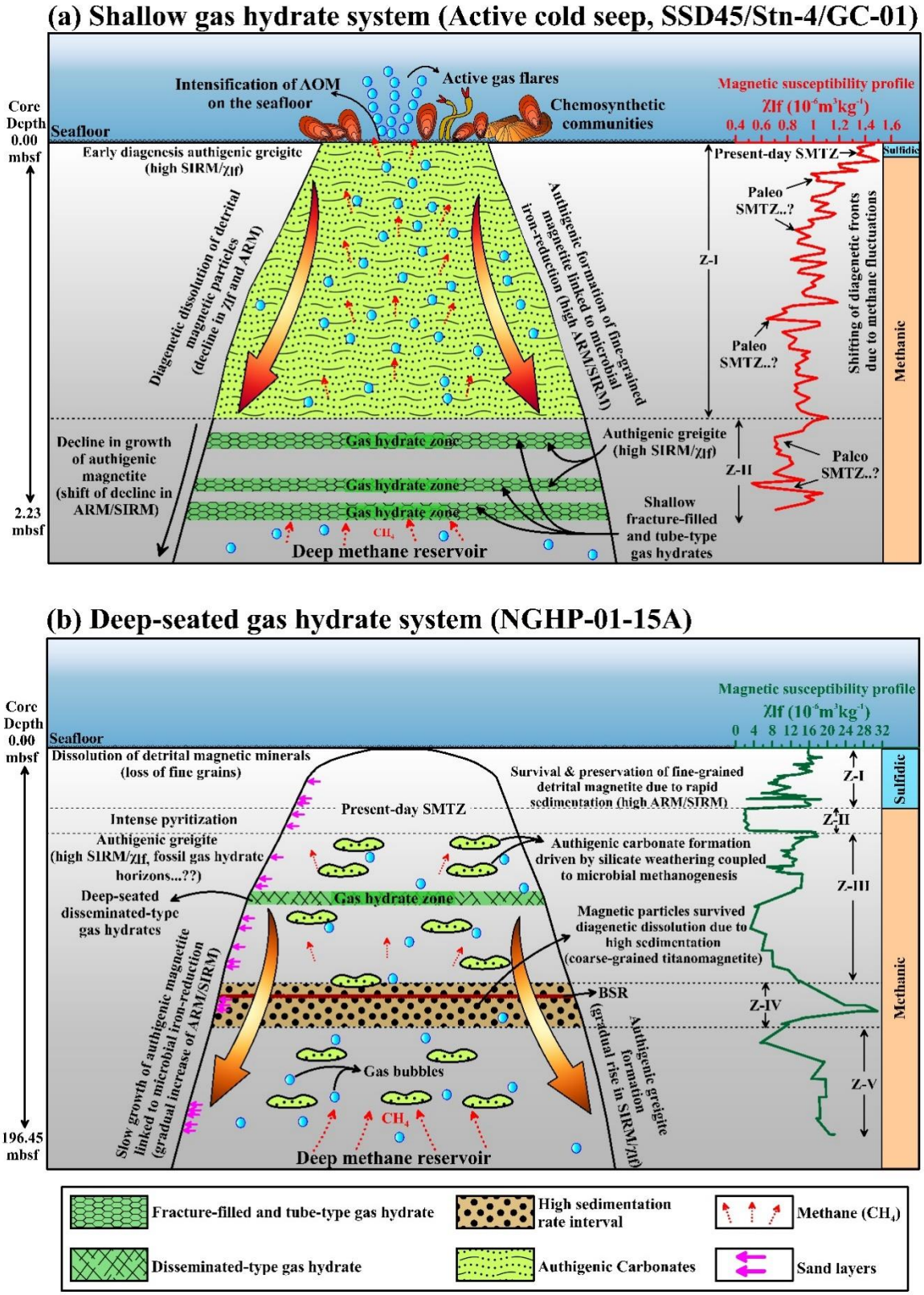

Figure 4.18: *Conceptual model explaining the diagenetic and authigenic controls on the evolution of magnetic mineralogies at (a) shallow (active cold seep, Core ID: SSD-45/Stn-4/GC-01) and (b) deep-seated (Core ID: NGHP-01-15A) in the Krishna-Godavari (K-G) basin, Bay of Bengal.*

SMTZ represented the previously formed greigite particles near the base of the paleo-SMTZ position cannot be ruled out, when the favourable porewater conditions supported their formation. Late greigite formation linked with deeper diagenetic processes such as gas-hydrate formation and AOM was reported from Neogene marine sediments from New Zealand (Rowan and Roberts, 2006, 2008), North-western Weddell Sea (Reilly et al., 2020) and Nankai Trough (Kars and Kodama, 2015). The gas-hydrate occurrence (~ 75 to 81 mbsf; Collett et al., 2008) zone in core NGHP-01-15A lies just below the upper most greigite interval (38.86 mbsf to 63.97 mbsf; Figure 4.2k). The sulfide deficient zone created by weakened AOM probably supported the greigite formation and preservation in these intervals. The weakened AOM was attributed to decline in methane flux either because of reduction in supply of rising methane flux from deeper reservoir or due to trapping during hydrate crystallization underneath (Housen and Musgrave, 1996). More recent magnetic study on sediments from Pāpaku fault, Hikurangi Subduction Margin, New Zealand reported that pyritization of authigenic greigite can produced different generations of pyrite formed during late diagenesis in methanic zone (Greve et al., 2021). Absence of greigite in SEM-EDS and XRD data of Z-II and Z-III of core NGHP-01-15A was explained considering the fact that ferrimagnetic authigenic greigite which was formed earlier probably got converted into more stable pyrite (Figure 4.7, Figure 4.8; Figure 4.10; Jiang et al., 2001; Kao et al., 2004; Larrasoaña et al., 2007; Kars and Kodama, 2015; Badesab et al., 2017).

A rock magnetic study on hydrate-bearing sediments of the Hikurangi Margin, New Zealand by Kars et al. (2021) suggested that hydrate dissociation could also result in the secondary diagenesis of previously formed greigite to pyrite. In similar lines, Badesab et al. (2020b) identified two magnetic iron sulfide bearing sediment intervals below SMTZ representing the fossil (disseminated-type) gas-hydrate zones in core NGHP-01-14A (proximal to core NGHP-01-15A; present study) from the K-G basin. They linked iron-sulfide formation to the microbially-mediated diagenetic reactions fuelled by the presence of gas-hydrates. Dedicated rock magnetic studies dealing with authigenesis of magnetic minerals in the gas-hydrate-bearing sediments in the Nankai Trough, offshore Japan (Kars and Kodama, 2015) and Cascadia Margin, offshore Oregon (Larrasoaña et al., 2007) also identified the fossil gas-hydrate horizons based on magnetic proxy (SIRM/χ_{lf}) and pore water anomalies. The high SIRM/χ_{lf} interval (38.86 to 63.97 mbsf) above the present-day gas-hydrate in core NGHP-01-15A (Figure 4.2k) represented the fossil gas-hydrate interval considering the fact that slow diffusion of methane after dissociation might have enhanced

the microbial activity and favored in situ formation of ferrimagnetic iron sulfides (greigite). Below the gas-hydrate layer, a gradual downcore rise in SIRM/χ_{lf} i.e. from Z-III to Z-V (Figure 4.2k) of core NGHP-01-15A suggested the presence of fine-grained authigenic greigite (Figure 4.2k; Snowball, 1991). It was highly possible that gas-hydrate layer above (~ 75 to 81 mbsf) restricted the flow of downward moving oxidising fluid required for the pyritization process and favoured the gradual growth of authigenic greigite in Z-III to Z-V of core NGHP-01-15A (Figure 4.2k, Figure 4.18; Kao et al., 2004; Luff et al., 2005; Badesab et al., 2020a; Lin et al., 2021; Gaikwad et al., 2021). In Z-IV, high magnetic susceptibility interval (112.85 – 140.35 mbsf) in core NGHP-01-15A was manifested by the presence of coarse-grained detrital titanomagnetite particles supplied during higher sedimentation events and subsequently survived the diagenetic dissolution fronts due to rapid deposition and burial, thereby created a magnetite-rich sediment interval (Figure 4.2g, Figure 4.3; Esteban et al., 2008; Kumar et al., 2014; Shankar et al., 2014; Badesab et al., 2019). A magnetically enhanced and laterally extensive band representing several rapid sedimentation events was clearly evident in the sediment magnetic record (Figure 4.3; Shanmugam et al., 2009; Shankar and Riedel, 2010; Dewangan et al., 2011; Ramprasad et al., 2011; Krishna et al., 2016; Badesab et al., 2019). A noticeable increase in χ_{lf} and minor rise in SIRM/χ_{lf} below the high sedimentation rate interval i.e., from 149.95 mbsf to 196.45 mbsf was indicative of presence of ferrimagnetic greigite (Figure 4.2g,k). Numerical simulation study on Nyegga pockmark field (Karsten et al., 2018) and geochemical modelling (Riedinger et al., 2005) of diagenetic processes on continental margin sediment off Argentina and Uruguay revealed that rapid changes in sedimentation can strongly impact the gas-hydrate systems by affecting fluid flow and gas seepage activity, authigenic carbonate formation and magnetic mineral diagenesis. One could imagine that increased supply of reactive iron during rapid sediment deposition events in the K-G basin had significantly altered the pyritization process and rather favoured the greigite formation and preservation (Riedinger et al., 2005; Badesab et al., 2019; João et al., 2021). Authigenic carbonate were mostly found to occur below the present-day SMTZ i.e., from 47.2 to 195.2 mbsf (Figure 4.2, Figure 4.16, Table 4.2). Geochemical data indicated that the present-day SMTZ at this site (NGHP-01-15) was at 31.5 mbsf (Figure 4.16; Collet et al., 2008). Lack of authigenic carbonates above SMTZ at this site was attributed to decline in alkalinity production (Z-I; Solomon et al., 2014) either due to reduction in silicate weathering process driven by microbial methanogenesis (Aloisi et al., 2004; Wallmann et al., 2008; Torres et al., 2020) or weakened AOM constrained by decline in methane flux rising from deeper sources and/or hydrate accumulation underneath.

4.4. Conclusions

Sediment cores SSD-45/Stn-4/GC-01 and NGHP-01-15A provided records of magnetic mineral diagenesis and authigenesis in a shallow (active cold seep) and deep-seated gas-hydrate system from the Bay of Bengal. The findings are summarized below:

(i) Detailed rock magnetic measurements complemented by mineralogical, microscopy, and petrological observation on sediment samples revealed that titanomagnetite (detrital) was the dominant magnetic mineral along with diagenetic (pyrite), authigenic (magnetite, greigite), and biogenic (magnetite) minerals in both sediment cores. Coarse-grained detrital titanomagnetite particles survived diagenetic dissolution along with silicate- hosted fine-grained magnetic inclusions that protected the magnetic particles from sulfidic pore fluids.

(ii) Magnetogranulometric proxies (ARM/SIRM and SIRM/χ_{lf}) provided useful insights on the diagenetic dissolution and authigenic formation of magnetic minerals in the sulfidic, methanic and gas-hydrate bearing zones. Rock magnetic data revealed that authigenic magnetite formation within methanic zones of both the cores was linked with microbial iron-reduction process.

(iii) A close linkage between presence of authigenic greigite and fracture-filled gas-hydrates in Z-II of shallow hydrate core (SSD-45/Stn-4/GC-01) demonstrated that the greigite formation was governed by the microbially-mediated diagenetic reactions fuelled by the presence of gas-hydrates in this zone. In deep-seated gas-hydrate core (NGHP-01-15A), greigite bearing sediment intervals (marked by high SIRM/χ_{lf} and χ_{lf}) just below the present-day gas-hydrate occurrence zone probably reflected the fossil gas-hydrate (disseminated-type) horizons at this site. Multiple occurrences of discrete authigenic carbonate throughout the sulfidic and methanic zones provided evidence on the episodic intensification of AOM at active seep and silicate weathering coupled to microbial methanogenesis at deep-seated gas-hydrate site respectively.

(iv) Present work is the first systematic rock magnetic study which made new observation on how magnetic minerals responded to the geochemical environment at two different diagenetic settings experiencing variable fluid sequence controlled by shale-tectonism in the Bay of Bengal.

(v) The findings of the study were summarized into a conceptual model (Figure 4.18) which explained the constraints on the formation and preservation of diagenetic and authigenic minerals in two different diagenetic systems from the Bay of Bengal.

Table 4.1: *Depth-wise distribution of authigenic carbonates in a sediment core from shallow (active cold seep; Core ID: SSD-45/Stn-4/GC-01) gas-hydrate site in the Krishna-Godavari (K-G) basin, Bay of Bengal.*

Depth (mbsf)	No. of Carbonate Pieces	Carbonate Size	Depth (mbsf)	No. of Carbonate Pieces	Carbonate Size
0.01	4-5 Pieces	Small + Medium Pieces	0.63	3 Pieces	Medium to Large
0.03	4-5 Pieces	Small Pieces	0.65	1 Piece	Large
0.05	3-4 Pieces	Small Pieces	0.67	2 Pieces	Medium to Large
0.07	3-4 Pieces	Small Pieces	0.69	2 Pieces	Medium to Large
0.09	3-4 Pieces	Small+ Medium Pieces	0.71	4 Pieces	Medium to Large
0.11	4 Pieces	Small Pieces	0.73	3 Pieces	Medium to Large
0.13	4 Pieces	Small Pieces	0.75	4 Pieces	Medium to Large
0.15	3 Pieces	Small Pieces	0.77	6 Pieces	Medium to Large
0.17	3 Pieces	Small Pieces	0.79	4 Pieces	Medium to Large
0.18	4 Pieces	Medium to Large	0.81	5 Pieces	Medium to Large
0.21	3 Pieces	Medium to Large	0.83	3 Pieces	Medium to Large
0.23	2 Pieces	Medium to Large	0.85	2 Pieces	Medium to Large
0.25	4 Pieces	Medium to Large	0.87	2 Pieces	Medium to Large
0.27	3 Pieces	Medium to Large	0.89	3 Pieces	Medium to Large
0.29	5 Pieces	Medium to Large	0.91	3 Pieces	Medium to Large
0.31	3 Pieces	Medium to Large	0.93	4 Pieces	Medium to Large
0.33	4 Pieces	Medium to Large	0.95	3 Pieces	Medium to Large
0.35	5 Pieces	Medium to Large	0.97	3 Pieces	Medium to Large
0.37	5 Pieces	Medium to Large	0.99	3 Pieces	Medium to Large
0.39	5 Pieces	Medium to Large	1.01	More than 10 Pieces	Medium to Large
0.41	3 Pieces	Medium to Large	1.03	4 Pieces	Medium to Large
0.43	5 Pieces	Medium to Large	1.05	--	--
0.45	4 Pieces	Medium to Large	1.07	3 Pieces	Medium to Large
0.46	6 Pieces	Medium to Large	1.09	3 Pieces	Medium to Large
0.49	4 Pieces	Medium to Large	1.11	4 Pieces	Medium to Large
0.51	3 Pieces	Medium to Large	1.13	2 Pieces	Medium to Large
0.53	4 Pieces	Medium to Large	1.14	2 Pieces	Medium to Large
0.55	2 Pieces	Medium to Large	1.17	2 Pieces	Small Pieces
0.57	2 Pieces	Medium to Large	1.19	1 Piece	Small to Medium
0.59	3 Pieces	Medium to Large	1.21	1 Piece	Small to Medium
0.61	3 Pieces	Medium to Large	1.23	1 Piece	Small to Medium

1.25	3 Pieces	Small to Medium	2.13	--	--
1.27	2 Pieces	Small to Medium	2.15	--	--
1.29	3 Pieces	Small to Medium	2.17	--	--
1.31	1 Piece	Small to Medium	2.19	--	--
1.33	2 Pieces	Small to Medium	2.21	--	--
1.35	--	--	2.23	--	--
1.37	3 Pieces	Small to Medium			
1.39	1 Piece	Small to Medium			
1.41	--	--			
1.43	1 Piece	Small to Medium			
1.45	1 Piece	Small to Medium			
1.47	1 Piece	Small to Medium			
1.49	1 Piece	Small to Medium			
1.51	--	--			
1.53	1 Piece	Small to Medium			
1.55	-	-			
1.57	4 Pieces	Small to Medium			
1.59	--	--			
1.61	--	--			
1.63	--	--			
1.65	--	--			
1.67	--	--			
1.69	--	--			
1.71	--	--			
1.73	--	--			
1.75	--	--			
1.77	--	--			
1.79	--	--			
1.81	--	--			
1.83	--	--			
1.85	--	--			
1.87	--	--			
1.89	--	--			
1.91	--	--			
1.93	--	--			
1.95	--	--			
1.97	--	--			
1.99	--	--			
2.01	--	--			
2.03	--	--			
2.05	--	--			
2.07	--	--			
2.09	--	--			
2.11	--	--			

Table 4.2: *Depth-wise distribution of authigenic carbonates in a sediment core from deep-seated (Core ID: NGHP-01-15A) gas-hydrate site in the Krishna-Godavari (K-G) basin, Bay of Bengal (modified after Teichert et al. 2014).*

Depth(mbsf)	Lithology	Carbonate composition
47.2	Nodule	Fe-rich-carbonate
47.8	Nodule	Fe-rich-carbonate
55.9	Nodule	Fe-rich-carbonate
58.4	Nodule	Fe-rich-carbonate
60.2	Nodule	Fe-rich-carbonate
62	Nodule	Fe-rich-carbonate
63.9	Nodule	Fe-rich-carbonate
64.1	Nodule	Fe-rich-carbonate
72.9	Nodule	Fe-rich-carbonate
73	Nodule	Fe-rich-carbonate
73.1	Nodule	Fe-rich-carbonate
87.2	Nodule	Fe-rich-carbonate
108.5	Nodule	Fe-rich-carbonate
111.1	Nodule	LMC
113.6	Nodule	LMC
116.6	Nodule	Fe-rich-carbonate
117.4	Nodule	Fe-rich-carbonate
119.3	Nodule	Fe-rich-carbonate
128.5	Nodule	Fe-rich-carbonate
128.6	Nodule	Fe-rich-carbonate
129.4	Nodule	Fe-rich-carbonate
130.3	Nodule	Fe-rich-carbonate
146.8	Nodule	Ca-rich dolomite/ankerite
157.3	Nodule	HMC
157.3	Nodule	Fe-rich-carbonate
158.3	Nodule	LMC
163.7	Nodule	LMC
167.4	Nodule	Fe-rich-carbonate
167.7	Nodule	Fe-rich-carbonate
179	Nodule	low calcium-carbonate
195.3	Nodule	Fe-rich-carbonate

Table 4.3: *Depth-wise distribution of sand layers in sediment core from deep-seated (Core ID: NGHP-01-15A) gas-hydrate site in the Krishna-Godavari (K-G) basin, Bay of Bengal (modified after Collett et al., 2008).*

Depth (mbsf)	Type of occurrence	Depth (mbsf)	Type of occurrence	Depth (mbsf)	Type of occurrence
15.83	sand bed	31.42	sand bed	92.61	sand laminae
15.84	sand bed	35.34	sand bed	92.7	sand laminae
25.95	sand bed	35.54	sand bed	92.83	sand laminae
25.98	sand bed	36.27	sand bed	92.86	sand laminae
27.27	sand bed	36.46	sand bed	90.4	sand pocket
27.3	sand bed	36.485	sand bed	90.45	sand pocket
27.81	sand bed	36.555	sand bed	100.33	sand bed
28.44	sand bed	36.805	sand bed	100.4	sand bed
35.31	sand bed	36.82	sand bed	110.63	sand burrow fill
31.63	sand bed	39.28	sand bed	109.08	sand laminae
34.42	sand bed	38.13	sand bed	132.47	multiple silt/sand laminae
31.29	sand bed	39.08	sand bed	132.17	multiple silt/sand laminae
36.32	sand bed	56.21	sand bed	131.43	multiple silt/sand laminae
36.4	sand bed	56.25	sand bed	130.47	sand bed
30.75	sand bed	56.3	sand bed	178.12	sand bed
30.97	sand bed	56.35	sand bed	179.42	sand bed
31.2	sand bed	67.61	sand bed	181.7	sand bed
31.23	sand bed	67.5	sand bed	178.18	sand bed
34.73	sand bed	70.57	sand bed	178.23	sand bed
36.35	sand bed	70.67	sand bed	178.315	sand bed
29.09	sand bed	70.84	sand bed	179.11	sand bed
29.23	sand bed	71.56	sand bed	183.36	sand bed
29.27	sand bed	72.09	sand bed	186.83	sand bed
29.8	sand bed	73.01	sand bed	191.95	sand bed
29.9	sand bed	77.4	sand bed	191.99	sand bed
30.14	sand bed	78.17	multiple Sand bed	192.12	sand bed
30.16	sand bed	77.24	multiple Sand bed	192.17	sand bed
30.19	sand bed	76.9	multiple Sand bed	192.23	sand bed
30.21	sand bed	79.63	multiple Sand bed	192.28	sand bed
30.23	sand bed	79.88	multiple Sand bed	192.45	sand bed
30.28	sand bed	77.37	multiple Sand bed	192.48	sand bed
30.65	sand bed	76.15	multiple Sand bed		
30.67	sand bed	79.98	multiple Sand bed		
30.71	sand bed	80.06	multiple Sand bed		
30.91	sand bed	78.23	sand bed		
31.16	sand bed	78.3	sand bed		

Table 4.4*: Rock magnetic data of sediment core SSD-045/Stn-4/GC-01*

Depth (mbsf)	χlf (10-6m3kg-1)	ARM (10-5Am2kg-1)	SIRM (10-5Am2kg-1)	ARM / SIRM	SIRM/χlf (A/m)	S-ratio
0.01	1.4663	0.0042	0.3240	0.0130	0.2209	0.9459
0.03	1.3410	0.0045	0.3303	0.0135	0.2463	0.9532
0.05	1.3801	0.0042	0.3304	0.0128	0.2394	0.9504
0.07	1.3386	0.0045	0.3150	0.0142	0.2353	0.9610
0.09	1.4412	0.0049	0.3336	0.0145	0.2315	0.9662
0.11	1.4982	0.0042	0.2656	0.0158	0.1773	0.9549
0.13	1.1938	0.0043	0.2746	0.0158	0.2301	0.9599
0.15	1.2068	0.0044	0.2837	0.0156	0.2351	0.9418
0.17	1.3384	0.0041	0.2502	0.0162	0.1869	0.9629
0.19	0.9845	0.0036	0.2453	0.0148	0.2492	0.9559
0.21	1.0429	0.0040	0.2377	0.0170	0.2280	0.9482
0.23	1.0243	0.0041	0.2517	0.0161	0.2458	0.9684
0.25	1.2358	0.0041	0.2559	0.0162	0.2071	0.9361
0.27	1.1732	0.0032	0.2117	0.0149	0.1804	0.9540
0.29	1.1633	0.0033	0.2144	0.0154	0.1843	0.9215
0.31	1.1180	0.0033	0.2004	0.0167	0.1793	0.8321
0.33	0.9932	0.0032	0.1951	0.0166	0.1964	0.7685
0.35	0.9850	0.0031	0.1832	0.0169	0.1860	0.8179
0.37	1.1141	0.0032	0.1895	0.0167	0.1701	0.8213
0.39	1.0570	0.0031	0.1767	0.0177	0.1671	0.8314
0.41	1.0146	0.0028	0.1686	0.0166	0.1661	0.8322
0.43	1.1685	0.0029	0.1765	0.0167	0.1510	0.8092
0.45	1.1255	0.0030	0.1792	0.0167	0.1593	0.8202
0.47	0.9626	0.0020	0.1386	0.0143	0.1440	0.8062
0.49	0.9999	0.0022	0.1423	0.0154	0.1423	0.8349
0.51	0.9811	0.0024	0.1498	0.0158	0.1527	0.8174
0.53	0.8608	0.0021	0.1290	0.0166	0.1498	0.7627
0.55	0.9150	0.0019	0.1230	0.0151	0.1345	0.7343
0.57	0.9730	0.0023	0.1436	0.0162	0.1476	0.7455
0.59	0.8902	0.0020	0.1140	0.0172	0.1280	0.7652
0.61	0.8791	0.0020	0.1314	0.0152	0.1495	0.7523
0.63	0.9970	0.0020	0.1308	0.0153	0.1312	0.7521
0.65	1.0832	0.0019	0.1297	0.0146	0.1198	0.6672
0.67	1.0786	0.0019	0.1333	0.0141	0.1236	0.7415
0.69	0.9138	0.0020	0.1336	0.0150	0.1462	0.7515
0.71	0.8265	0.0019	0.1249	0.0154	0.1511	0.6100
0.73	1.0957	0.0021	0.1382	0.0152	0.1261	0.7686
0.75	1.0244	0.0018	0.1289	0.0143	0.1258	0.7148
0.77	0.9005	0.0018	0.1222	0.0145	0.1357	0.6367

0.79	0.8832	0.0017	0.1190	0.0142	0.1348	0.7678
0.81	1.0776	0.0019	0.1305	0.0146	0.1211	0.7420
0.83	1.0273	0.0018	0.1271	0.0141	0.1238	0.7564
0.85	0.9849	0.0018	0.1238	0.0144	0.1257	0.7692
0.87	1.0149	0.0019	0.1416	0.0136	0.1395	0.7669
0.89	0.9488	0.0018	0.1264	0.0145	0.1332	0.7651
0.91	0.9153	0.0017	0.1199	0.0141	0.1310	0.7662
0.93	0.9367	0.0017	0.1203	0.0141	0.1284	0.7315
0.95	1.1071	0.0018	0.1231	0.0144	0.1112	0.6244
0.97	1.1836	0.0017	0.1265	0.0138	0.1069	0.7825
0.99	0.8446	0.0017	0.1185	0.0140	0.1403	0.7860
1.01	0.7632	0.0013	0.0945	0.0138	0.1239	0.7950
1.03	0.7914	0.0014	0.0937	0.0149	0.1185	0.7883
1.05	0.7250	0.0013	0.0913	0.0141	0.1259	0.7728
1.07	0.6412	0.0013	0.0953	0.0139	0.1487	0.7873
1.09	1.0429	0.0018	0.1326	0.0137	0.1271	0.8361
1.11	1.0467	0.0016	0.1197	0.0137	0.1144	0.8439
1.13	0.9391	0.0015	0.1063	0.0145	0.1132	0.8850
1.15	0.7625	0.0014	0.1005	0.0142	0.1318	0.9014
1.17	0.8073	0.0013	0.0984	0.0137	0.1219	0.8931
1.19	0.8669	0.0011	0.0783	0.0145	0.0904	0.9041
1.21	0.8517	0.0010	0.0796	0.0130	0.0935	0.8848
1.23	0.8147	0.0012	0.0788	0.0150	0.0967	0.8954
1.25	0.8149	0.0012	0.0802	0.0149	0.0985	0.8767
1.27	0.9703	0.0011	0.0821	0.0139	0.0846	0.9085
1.29	0.9117	0.0011	0.0857	0.0132	0.0940	0.8961
1.31	0.9556	0.0013	0.0927	0.0135	0.0970	0.8913
1.33	0.9113	0.0013	0.1051	0.0120	0.1153	0.8826
1.35	0.8647	0.0012	0.0936	0.0128	0.1083	0.8701
1.37	0.8924	0.0012	0.0960	0.0130	0.1076	0.8940
1.39	0.8639	0.0013	0.0988	0.0133	0.1143	0.8716
1.41	0.8752	0.0011	0.0826	0.0133	0.0944	0.8854
1.43	1.0274	0.0013	0.0890	0.0141	0.0866	0.8766
1.45	0.9372	0.0012	0.0803	0.0143	0.0856	0.8845
1.47	0.8578	0.0012	0.0890	0.0137	0.1038	0.8729
1.49	0.8763	0.0014	0.1024	0.0140	0.1169	0.9046
1.51	0.8576	0.0014	0.1072	0.0130	0.1250	0.8958
1.53	0.9011	0.0014	0.1074	0.0128	0.1192	0.8820
1.55	0.9683	0.0015	0.1126	0.0129	0.1163	0.8936
1.57	0.9292	0.0015	0.1171	0.0129	0.1261	0.9130
1.59	0.8706	0.0014	0.1061	0.0134	0.1218	0.8932
1.61	0.8810	0.0014	0.1053	0.0129	0.1195	0.8715
1.63	0.9066	0.0014	0.1032	0.0139	0.1138	0.8897

1.65	0.9751	0.0014	0.1115	0.0128	0.1144	0.8839
1.67	1.1068	0.0017	0.1117	0.0154	0.1009	0.8778
1.69	1.0004	0.0017	0.1073	0.0158	0.1073	0.8903
1.71	0.9633	0.0010	0.0993	0.0097	0.1031	0.8860
1.73	0.9319	0.0008	0.0744	0.0108	0.0798	0.8984
1.75	0.9201	0.0009	0.0821	0.0115	0.0892	0.8784
1.77	0.8194	0.0011	0.0992	0.0113	0.1411	0.8701
1.79	0.7020	0.0011	0.0998	0.0111	0.1544	0.8782
1.81	0.7025	0.0010	0.0868	0.0118	0.1469	0.8714
1.83	0.7217	0.0008	0.0746	0.0104	0.1034	0.7564
1.85	0.7029	0.0009	0.0808	0.0114	0.1150	0.6399
1.87	0.7478	0.0008	0.0758	0.0112	0.1014	0.7336
1.89	0.7196	0.0009	0.0738	0.0115	0.1025	0.7545
1.91	0.8177	0.0009	0.0759	0.0113	0.0928	0.7040
1.93	0.8199	0.0010	0.0852	0.0112	0.1039	0.6175
1.95	0.8424	0.0010	0.0878	0.0117	0.1042	0.7534
1.97	0.7976	0.0009	0.0828	0.0109	0.1038	0.7450
1.99	0.7389	0.0008	0.0807	0.0105	0.1093	0.7206
2.01	0.6950	0.0008	0.0742	0.0107	0.1068	0.7724
2.03	0.7941	0.0009	0.0822	0.0109	0.1035	0.7132
2.05	0.9256	0.0008	0.0796	0.0097	0.0860	0.7171
2.07	0.5274	0.0008	0.0812	0.0104	0.1540	0.7507
2.09	0.5856	0.0011	0.0913	0.0118	0.1559	0.7188
2.11	0.8270	0.0009	0.0808	0.0107	0.0976	0.7321
2.13	1.0695	0.0009	0.0827	0.0104	0.0773	0.7515
2.15	0.9366	0.0008	0.0747	0.0111	0.0797	0.7633
2.17	1.0016	0.0009	0.0832	0.0113	0.0831	0.6908
2.19	0.9414	0.0009	0.0765	0.0112	0.0813	0.7554
2.21	0.8221	0.0009	0.0795	0.0109	0.0967	0.7396
2.23	0.7095	0.0008	0.0740	0.0104	0.1044	0.7568

Table 4.4: *Rock magnetic data of sediment core NGHP-01-15A*

Depth (mbsf)	χlf (10-6m3kg-1)	ARM (10-5Am2kg-1)	SIRM (10-5Am2kg-1)	ARM / SIRM	SIRM/χlf (A/m)	S-ratio
0.74	15.8928	0.0940	4.3017	0.0219	0.2707	0.9498
2.26	15.8104	0.0943	4.5006	0.0209	0.2847	0.9903
3.74	15.9216	0.0970	4.7423	0.0204	0.2979	0.9647
4.6	17.3362	0.0948	4.7426	0.0200	0.2736	0.9590
4.65	18.7589	0.0957	5.1869	0.0185	0.2765	0.9547
5.26	15.7509	0.0935	4.8345	0.0193	0.3069	0.9339
6.77	16.5410	0.0982	4.4821	0.0219	0.2710	0.9726
7.73	16.3638	0.0981	4.3535	0.0225	0.2660	0.9597
7.78	16.9007	0.1001	4.5673	0.0219	0.2702	0.9524
8.26	12.6797	0.0885	3.6201	0.0244	0.2855	0.9717
9.36	16.0227	0.0920	4.6981	0.0196	0.2932	0.9685
10.26	13.9906	0.0890	3.8405	0.0232	0.2745	0.9617
11.76	16.5462	0.0968	4.4701	0.0216	0.2702	0.9574
13.26	13.8271	0.0919	3.7086	0.0248	0.2682	0.9955
14.02	10.5739	0.0805	2.4250	0.0332	0.2293	0.9595
14.07	9.2017	0.0743	2.1308	0.0349	0.2316	0.9489
14.76	10.7021	0.0884	2.2781	0.0388	0.2129	0.9395
16.26	8.3794	0.0861	1.7369	0.0496	0.2073	0.9440
17.02	8.6355	0.0809	2.0079	0.0403	0.2325	0.9494
17.07	9.1203	0.0773	2.1196	0.0365	0.2324	0.9367
17.76	7.1888	0.0762	1.6995	0.0448	0.2364	0.9486
19.86	11.8930	0.0984	2.5606	0.0384	0.2153	0.9576
22.86	7.2958	0.0179	1.6223	0.0110	0.2224	0.9095
22.91	5.6632	0.0228	1.0592	0.0215	0.1870	0.8784
22.96	7.5780	0.0627	1.5164	0.0414	0.2001	0.9094
24.36	15.1921	0.0059	4.1057	0.0314	0.2703	0.9541
25.86	2.4628	0.0538	0.6123	0.0272	0.2486	0.9193
25.91	18.5399	0.0496	4.5046	0.0110	0.2430	0.8778
25.96	15.0973	0.0500	3.5776	0.0140	0.2370	0.8784
27.36	15.1300	0.0535	4.0949	0.0131	0.2706	0.8743
28.63	16.3055	0.0205	4.3882	0.0047	0.2691	0.8726
29.36	15.9344	0.0491	4.1538	0.0118	0.2607	0.8596
30.86	2.0375	0.0060	0.5528	0.0109	0.2713	0.7519
32.36	2.1528	0.0062	0.5471	0.0113	0.2541	0.7585
33.47	1.9493	0.0049	0.4118	0.0118	0.2112	0.7814
33.52	1.8338	0.0047	0.4132	0.0113	0.2253	0.7237
33.86	2.1560	0.0060	0.3593	0.0168	0.1666	0.7253
35.36	2.2543	0.0055	0.4993	0.0110	0.2215	0.6549
36.47	2.1082	0.0056	0.3929	0.0143	0.1863	0.9395

36.52	1.9198	0.0046	0.3163	0.0147	0.1648	0.9296
36.77	1.8333	0.0045	0.2564	0.0176	0.1398	0.8890
38.86	2.8274	0.0119	1.5920	0.0075	0.5631	0.9949
40.36	2.1521	0.0050	0.5397	0.0093	0.2508	0.9229
41.91	2.8606	0.0119	1.3390	0.0089	0.4681	0.8981
42.57	16.7463	0.0550	5.4474	0.0101	0.3253	0.9780
42.62	17.3883	0.0600	5.8502	0.0103	0.3364	0.9850
43.36	17.1882	0.0690	8.5952	0.0080	0.5001	0.9847
44.86	17.9050	0.0701	5.1327	0.0137	0.2867	0.9731
45.57	12.9454	0.0436	3.7974	0.0115	0.2933	0.9789
45.62	14.6836	0.0493	4.4128	0.0112	0.3005	0.9666
46.36	14.7679	0.0549	4.3300	0.0127	0.2932	0.9527
48.35	13.1412	0.0512	3.8674	0.0132	0.2943	0.9618
49.64	12.4191	0.0449	3.4354	0.0131	0.2766	0.9794
51.12	12.8036	0.0479	4.2308	0.0113	0.3304	0.9813
51.88	11.8941	0.0416	3.3551	0.0124	0.2821	0.9689
51.93	9.9982	0.0346	2.6887	0.0129	0.2689	0.9750
53.22	11.7075	0.0421	3.2538	0.0130	0.2779	0.9591
53.78	11.3347	0.0406	3.2328	0.0126	0.2852	0.9734
54.79	10.3713	0.0354	3.0474	0.0116	0.2938	0.9425
54.84	11.6548	0.0404	3.3052	0.0122	0.2836	0.9703
55.63	11.7509	0.0424	3.3003	0.0129	0.2809	0.9769
56.56	13.2823	0.0530	5.5846	0.0095	0.4205	0.9846
57.86	12.4513	0.0463	3.8646	0.0120	0.3104	0.9866
59.77	12.6353	0.0431	3.8877	0.0111	0.3077	0.9659
60.28	6.8488	0.0223	1.7996	0.0124	0.2628	0.9512
61.03	8.2378	0.0252	1.9830	0.0127	0.2407	0.9613
61.08	10.2077	0.0248	2.6411	0.0094	0.2587	0.9659
61.26	10.1477	0.0350	2.8422	0.0123	0.2801	0.9565
62.74	8.9493	0.0309	2.5137	0.0123	0.2809	0.9396
63.82	12.6735	0.0494	5.2869	0.0093	0.4172	0.9825
63.87	11.3613	0.0430	4.5826	0.0094	0.4033	0.9840
63.97	14.5477	0.0546	5.3328	0.0102	0.3666	0.9674
71.13	14.2502	0.0420	3.7859	0.0111	0.2657	0.9704
71.18	13.3741	0.0394	3.5901	0.0110	0.2684	0.9745
72.52	12.3564	0.0376	2.9123	0.0129	0.2357	0.9671
72.57	12.8621	0.0407	3.5534	0.0115	0.2763	0.9527
80.52	4.1039	0.0084	0.5753	0.0146	0.1402	0.8635
80.57	5.0279	0.0102	0.7345	0.0139	0.1461	0.8972
91.8	3.2058	0.0061	0.5388	0.0113	0.1681	0.8399
91.85	3.4730	0.0074	0.8712	0.0085	0.2508	0.8870
94.8	6.6830	0.0173	1.6024	0.0108	0.2398	0.9293
94.85	6.5860	0.0175	1.6597	0.0105	0.2520	0.9123

99.9	6.0149	0.0149	1.3100	0.0113	0.2178	0.9145
99.95	6.0672	0.0155	1.6888	0.0092	0.2784	0.8640
102.9	5.7371	0.0149	1.3418	0.0111	0.2339	0.9232
102.95	7.9490	0.0227	1.9390	0.0117	0.2439	0.9285
111	8.1525	0.0258	2.2135	0.0117	0.2715	0.9528
111.05	8.5864	0.0277	2.3822	0.0116	0.2774	0.9447
112.85	11.4895	0.0408	3.4979	0.0117	0.3044	0.9514
112.9	11.5386	0.0406	3.4139	0.0119	0.2959	0.9623
118.49	13.6697	0.0449	3.8636	0.0116	0.2826	0.9496
118.54	14.1779	0.0497	4.0866	0.0122	0.2882	0.9608
130.7	23.8018	0.1156	7.9276	0.0146	0.3331	0.9710
130.75	28.2134	0.1174	9.3423	0.0126	0.3311	0.9653
133.7	30.8937	0.1405	9.8959	0.0142	0.3203	0.9622
133.75	26.8500	0.0544	8.5989	0.0163	0.3203	0.9644
137.3	14.4024	0.1231	3.9770	0.0152	0.2761	0.9341
137.35	14.7968	0.0610	4.0969	0.0149	0.2769	0.9946
140.3	10.0407	0.0507	2.8516	0.0178	0.2840	0.9577
140.35	11.5658	0.0583	3.3933	0.0172	0.2934	0.9538
149.9	5.4248	0.0141	1.4204	0.0099	0.2618	0.8780
149.95	6.6298	0.0176	1.7434	0.0101	0.2630	0.9157
159.5	18.9579	0.0665	5.9443	0.0112	0.3136	0.9707
159.55	19.3964	0.0685	6.0288	0.0114	0.3108	0.9596
168.2	16.4885	0.0570	4.9780	0.0115	0.3019	0.9852
168.25	19.6321	0.0708	6.3171	0.0112	0.3218	0.9593
177.41	19.7271	0.0718	6.1971	0.0116	0.3141	0.9702
177.46	18.2460	0.0684	5.8389	0.0117	0.3200	0.9789
188.3	18.4575	0.0845	6.0898	0.0139	0.3299	0.9554
188.35	17.6371	0.0801	5.6764	0.0141	0.3218	0.9753
196.4	20.5013	0.1017	6.8407	0.0149	0.3337	0.9691
196.45	21.5644	0.1101	7.0773	0.0156	0.3282	0.9794

Chapter 5:
Summary, conclusions, and perspectives for future research

Diagenesis and authigenesis of magnetic minerals in marine cold seep (active, relict, paleo) sites associated with the shallow and deep-seated methane hydrate systems from the Krishna-Godavari basin, Bay of Bengal were investigated in detail. Rock magnetic methods complemented by mineralogical, sedimentological, and petrological analyses were conducted on the sediment cores retrieved from the cold seep and gas hydrate-bearing sites to understand the diagenetic and authigenic processes. Multiproxy datasets generated on the studied sediment cores helped to develop the inventory of magnetic minerals in methanic and sulfidic environments, unravel the controls on detrital sedimentation events and shale-tectonism on diagenesis and authigenesis of magnetic minerals in marine cold seep systems from the Bay of Bengal. Key conclusions drawn from this study are listed below:

- Present work is the first systematic rock magnetic study which provided a new observation on how magnetic minerals selectively respond to the geochemical environment at different diagenetic (active, relict, paleo-seep) systems experiencing variable fluid sequence controlled by shale-tectonism and rapid sedimentation events in the Bay of Bengal.

- A set of rock magnetic, mineralogical, and sedimentological records of the sediment cores from the K-G basin helped to characterize the changes in the magnetic concentration, grain size, and mineralogy induced by diagenetic and authigenic processes. Bulk sediment magnetism was governed by the presence of complex magnetic mineral assemblages of detrital (titanomagnetite, titanohematite), authigenic (magnetite, greigite), and biogenic (magnetite) minerals.

- Magnetogranulometric proxies complemented by microscopic (SEM, TEM) analyses provided valuable insights on the mechanism constraining the diagenetic dissolution, preservation, authigenic, and biogenic formations of magnetic minerals in the sulphidic and methanic environments of all studied cores.

- A mechanism controlling the authigenic magnetite formation within methanic zones via microbial iron-reduction process was unravelled. A close linkage between the presence of

authigenic greigite and fracture-filled gas-hydrates was reported. Multiple occurrences of discrete authigenic carbonate throughout the sulfidic and methanic zones provided evidence on the episodic intensification of AOM at active cold seep and silicate weathering coupled to microbial methanogenesis at deep-seated gas-hydrate site.

- A conceptual model (Figure 3.12, Figure 3.27 and Figure 4.18) summarizing the findings were developed during this study. This model provided important insights into the evolution of different magnetic mineralogies constrained by variable diagenetic (reductive dissolution, maghemitization, subsidization) processes at active and relict seep sites in the K-G basin, Bay of Bengal. Furthermore, the present study provided valuable information on the magnetic mineralogy, genesis, and their state of preservation and also enhanced the interpretative value of rock magnetic proxies.

Future perspectives:

- Rock magnetic approach for the exploration of the cold seep and associated methane hydrate developed in this study has a wider scope and can be applied to other marine gas hydrate sedimentary systems. However, additional geochemical and microbiological data of the studied sites are warranted to strengthen the interpretation on diagenesis, authigenesis, and biogenesis of magnetic minerals and can be taken up as a dedicated independent study in future. Future work on this aspect is also required to establish the importance of the diagenetic, authigenic, and biogenic processes in the dissolution, transformation, and preservation of the magnetic minerals in the geological record.

- The present sample-based multi-proxy study on the sediments from the K-G basin, Bay of Bengal has deepened our fundamental understanding the controls on evolution of magnetic mineralogies at cold seep and methane hydrate systems, which is also a prerequisite for future high-resolution mapping and modeling of sub-surface gas hydrates. The outcome of this study has set the basis for developing a new geophysical (rock magnetic based tool) method in future for detecting and mapping the gas hydrate deposits.

- A comprehensive ROV-based survey together with detailed sea-floor sediment and authigenic carbonate sampling at active seep sites in the K-G basin, Bay of Bengal can be organized in future to understand the linkage between cold seep processes, magnetite and greigite authigenesis, biogenic mineralization processes, and authigenic carbonate formation.

References

Abubakar, R., Muxworthy, A. R., Sephton, M. A., Southern, P., Watson, J. S., Fraser, A. J., Almeida, T. P. (2015). Formation of magnetic minerals at hydrocarbon-generation conditions. Marine and Petroleum Geology, 68, 509-519. https://doi.org/10.1016/j.marpetgeo.2015.10.003

Aloisi, G., Pierre, C., Rouchy, J.M., Foucher, J.P., Woodside, J. (2000). Methane-related authigenic carbonates of eastern Mediterranean Sea mud volcanoes and their possible relation to gas hydrate destabilization. Earth Planet. Sci. Lett. 184(1), pp.321-338. https://doi.org/10.1016/S0012-821X(00)00322-8

Alpar, B. (1999). Underwater signatures of the Kocaeli earthquake (August 17th 1999). Journal of Black Sea/Mediterranean Environment, 5(3).

Amiel, N., Shaar, R., Sivan, O. (2020). The Effect of Early Diagenesis in Methanic Sediments on Sedimentary Magnetic Properties: Case Study From the SE Mediterranean Continental Shelf. Front. Earth Sci. 8:283. https://doi.org/10.3389/feart.2020.00283

Anitha, G., Ramana, M. V., Ramprasad, T., Dewangan, P., Anuradha, M. (2014). Shallow geological environment of Krishna–Godavari offshore, eastern continental margin of India as inferred from the interpretation of high resolution sparker data. Journal of Earth System Science, 123(2), 329-342. https://doi.org/10.1007/s12040-013-0399-3

Ao, H., Deng, C., Dekkers, M. J., Liu, Q. (2010). Magnetic mineral dissolution in Pleistocene fluvio-lacustrine sediments, Nihewan Basin (North China). Earth and Planetary Science Letters, 292(1-2), 191-200. https://doi.org/10.1016/j.epsl.2010.01.035

Aubourg, C., Pozzi, J. P. (2010). Toward a new< 250 C pyrrhotite–magnetite geothermometer for claystones. Earth and Planetary Science Letters, 294(1-2), 47-57. https://doi.org/10.1016/j.epsl.2010.02.045

Badesab F, Dewangan P, Gaikwad V, Kars M, Kocherla M, Krishna KS, Sangode SJ, Deenadayalan K, Kumar P, Naikgaonkar O, Ismaiel M. (2019). Magnetic mineralogical

approach for the exploration of gas hydrates in the Bay of Bengal. Journal of Geophysical Research: Solid Earth. https://doi.org/10.1029/2019JB017466

Badesab, F., Gaikwad, V., Dewangan, P. (2020a). Controls on greigite preservation in a gas hydrate system of the Krishna-Godavari basin, Bay of Bengal. Geo-Mar. Lett., 40(4), 439-452. https://doi.org/10.1007/s00367-019-00604-z

Badesab, F., Dewangan, P., Gaikwad, V., Sebastian, J. G., Venkateshwarlu, M. (2020b). A rock magnetic perspective of gas hydrate occurrences in a high-energy depositional system in the Krishna-Godavari basin, Bay of Bengal. Geo-Mar. Lett. 1-15. https://doi.org/10.1007/s00367-020-00646-8

Badesab, F., Dewangan, P., Gaikwad, V. (2020c). Magnetic mineral diagenesis in a newly discovered active cold seep site in the Bay of Bengal. Front. Earth Sci. https://doi.org/10.3389/feart.2020.592557

Badesab, F., Dewangan, P., Usapkar, A., Kocherla, M., Peketi, A., Mohite, K., et al., (2017). Controls on evolution of gas-hydrate system in the Krishna-Godavari basin, offshore India. Geochem., Geophys., Geosys. 18(1), 52–74. https://doi.org/10.1002/2016GC006606

Badesab, F., Gaikwad, V., Venkateshwarlu, M., Kadam, N., João, H.M., (2022). Diagenetic dissolution, maghemitization and sulphidization of magnetic minerals in rapidly deposited gas hydrate bearing sediments from the Bay of Bengal. Marine and Petroleum Geology, p.105585. https://doi.org/10.1016/j.marpetgeo.2022.105585

Badesab, F., Gaikwad, V., Nath, B.N., Venkateshwarlu, M., Aiswarya, P.V., Tyagi, A., Salunke, K., Fernandes, W., Kadam, N., Sangode, S.J. and Sardar, A., (2021). Controls of contrasting provenance and fractionation on the sediment magnetic records from the Bay of Bengal. Marine Geology, 437, p.106515 https://doi.org/10.1016/j.margeo.2021.106515

Banerjee, S. K., Hunt, C. P., Liu, X. M. (1993). Separation of local signals from the regional paleomonsoon record of the Chinese Loess Plateau: A rock-magnetic approach. Geophys. Res. Lett., 20(9), 843-846. https://doi.org/10.1029/93GL00908

Bastia, R. (2007). Geologic settings and petroleum systems of India's east coast offshore basins: Concepts and applications. Bangalore, India:Technology Publications.

Bayrakci, G., Scalabrin, C., Dupr´e, S., Leblond, I., Tary, J.-B., Lanteri, N., Augustin, J.-M., Berger, L., Cros, E., Ogor, A., Tsabaris, C., Lescanne, M., G´eli, L. (2014). Acoustic monitoring of gas emissions from the seafloor. Part II: a case study from the Sea of Marmara. Mar. Geophys. Res. 35, 211–229.

Beal, E. J., House, C. H., Orphan, V. J. (2009). Manganese-and iron-dependent marine methane oxidation. Science, 325(5937), 184-187. https://doi.org/10.1126/science.1169984

Berndt, C. (2005). Focused fluid flow in passive continental margins. Philosophical Transactions of the Royal Society A: Mathematical, Physical and Engineering Sciences, 363(1837), 2855-2871.

Berndt, C., Feseker, T., Treude, T., Krastel, S., Liebetrau, V., Niemann, H., et al. (2014). Temporal constraints on hydrate-controlled methane seepage off Svalbard. Science, 343(6168), 284–287. https://doi.org/10.1126/science.1246298

Berner, R. A. (1970). Sedimentary pyrite formation. American Journal of Science, 268(1), 1–23.

Berner, R. (1981). Authigenic mineral formation resulting from organic matter decomposition in modern sediments.

Berner, R. A. (1984). Sedimentary pyrite formation: An update. Geochimica et Cosmochimica Acta, 48(4), 605–615. https://doi.org/10.1016/ 0016-7037(84)90089-9

Besnus, M. J., Meyer, A. J. (1964). Nouvelles données expérimentales sur le magnétisme de la pyrrhotine naturelle. In Proc. Int. Conf. Mag (Vol. 20, pp. 507-511).

Biksham, G., Subramanian, V. (1988). Sediment transport of the Godavari River basin and its controlling factors. J. Hydrol., 101(1-4), 275-290. https://doi.org/10.1016/0022-1694(88)90040-6

Blanchet, C. L., Thouveny, N., Vidal, L. (2009). Formation and preservation of greigite (Fe3S4) in sediments from the Santa Barbara Basin: Implications for paleoenvironmental changes during the past 35 ka. Paleoceanography 24(2). https://doi.org/10.1029/2008PA001719

Bloemendal, J., King, J.W., Hall, F.R., Doh, S.J. (1992). Rock magnetism of late Neogene and Pleistocene deep-sea sediments: relationship to sediment source, diagenetic processes, and sediment lithology. J. Geophys. Res. Solid Earth, 96: 4361–4375 https://doi.org/10.1029/91JB03068

Boetius, A., Ravenschlag, K., Schubert, C.J., Rickert, D., Widdel, F., Gieseke, A., et al. (2000). A marine microbial consortium apparently mediating anaerobic oxidation of methane: Nature, v. 407, p. 623–626, https://doi.org/10.1038/35036572.

Bohrmann, G., Greinert, J., Suess, E., & Torres, M. (1998). Authigenic carbonates from the Cascadia subduction zone and their relation to gas hydrate stability. Geology, 26(7), 647-650.

Bohrmann, G., Ivanov, M., Foucher, J. P., Spiess, V., Bialas, J., Greinert, J., et al. (2003). Mud volcanoes and gas hydrates in the Black Sea: new data from Dvurechenskii and Odessa mud volcanoes. Geo-Mar. Lett., 23(3-4), 239-249. https://doi.org/10.1007/s00367-003-0157-7

Borowski, W. S., Paull, C. K., Ussler, W. III (1996). Marine pore-water sulfate profiles indicate in situ methane flux from underlying gas hydrate. Geology, 24(7), 655–658. https://doi.org/10.1130/0091-7613(1996)024<0655:MPWSPI>2.3.CO;2

Boswell, R., Collett, T. S. (2011). Current perspectives on gas hydrate resources. Energy & environmental science, 4(4), 1206-1215.

Boswell, R., Yamamoto, K., Lee, S. R., Collett, T., Kumar, P., Dallimore, S. (2014). Methane hydrates. In Future energy (pp. 159-178). Elsevier. https://doi.org/10.1016/B978-0-08-099424-6.00008-9

Bünz, S., Polyanov, S., Vadakkepuliyambatta, S., Consolaro, C., Mienert, J. (2012). Active gas venting through hydrate-bearing sedimentson the Vestnesa Ridge, offshore W-Svalbard. Mar. Geol., 332–334, 189–197. https://doi.org/10.1016/j.margeo.2012.09.012

Burdige, D.J. (2007) Preservation of organic matter in marine sediments: controls, mechanisms, and an imbalance in sediment organic carbon budgets? Chem Rev. 2007 Feb; 107(2):467-85. https://doi.org/10.1021/cr050347q

Canfield, D. E. (1989). Reactive iron in marine sediments. Geochimica et cosmochimica acta, 53(3), 619-632. https://doi.org/10.1016/0016-7037(89)90005-7

Canfield, D. E., Thamdrup, B. O. (2009). Towards a consistent classification scheme for geochemical environments, or, why we wish the term 'suboxic' would go away. Geobiology 7, 385–392. https://doi.org/10.1111/j.1472-4669.2009.00214.x

Canfield, D. E., Berner, R. A. (1987). Dissolution and pyritization of magnetite in anoxic marine sediments. Geochim. Cosmochim. Acta. 51(3), 645–659. https://doi.org/10.1016/0016-7037(87)90076-7

Chang, L., Roberts, A.P., Heslop, D., Hayashida, A., Li, J., Zhao, X. et al. (2016a). Widespread occurrence of silicate-hosted magnetic mineral inclusions in marine sediments and their contribution to paleomagnetic recording. J. Geophys. Res. Solid Earth, 121(12):8415–8431. https://doi.org/10.1002/2016JB013109

Chang, L., Heslop, D., Roberts, A. P., Rey, D., Mohamed, K. J. (2016b). Discrimination of biogenic and detrital magnetite through a double Verwey transition temperature. Journal of Geophysical Research: Solid Earth, 121(1), 3-14. https://doi.org/10.1002/2015JB012485

Chang, L., Hong, H., Bai, F., Wang, S., Pei, Z., Paterson, G. A., Heslop, D., Roberts, A.P., Huang, B., Tauxe, L., Muxworthy, A.R. (2021). Detrital remanent magnetization of single-crystal silicates with magnetic inclusions: constraints from deposition experiments. Geophysical Journal International, 224(3), 2001-2015. https://doi.org/10.1093/gji/ggaa559

Chang, L., Roberts, A. P., Rowan, C. J., Tang, Y., Pruner, P., Chen, Q., et al. (2009) Low-temperature magnetic properties of greigite (Fe3S4). Geochem., Geophy. Geosy., 10, Q01Y04. https://doi.org/10.1029/2008GC002276

Chang, L., Roberts, A.P., Winklhofer, M., Heslop, D., Dekkers, M.J., Krijgsman, W., et al. (2014). Magnetic detection and characterization of biogenic magnetic minerals: a comparison of ferromagneticresonance and first-order reversal curve diagrams. J. Geophys. Res. Solid Earth,119(8):6136–6158. https://doi.org/10.1002/2014JB011213

Chang, L., Winklhofer, M., Roberts, A. P., Heslop, D., Florindo, F., Dekkers, M. J., et al. (2013). Low-temperature magnetic properties of pelagic carbonates: Oxidation of biogenic magnetite and identification of magnetosome chains. J. Geophys. Res. Solid Earth, 118(12), 6049-6065. https://doi.org/10.1002/2013JB010381

Chang, S. B. R., Kirschvink, J. L., Stolz, J. F. (1987). Biogenic magnetite as a primary remanence carrier in limestone deposits. Phys. Earth Planet. Inter. 46, 289–303. https://doi.org/10.1016/0031-9201(87)90191-9

Channell, J. E. T., Stoner, J. S. (2002). Plio-Pleistocene magnetic polarity stratigraphies and diagenetic magnetite dissolution at ODP Leg 177 Sites (1089, 1091, 1093 and 1094). Marine Micropaleontology, 45(3-4), 269-290. https://doi.org/10.1016/S0377-8398(02)00032-4

Channell, J. E. T., Hawthorne, T. (1990). Progressive dissolution of titanomagnetites at ODP Site 653 (Tyrrhenian Sea). Earth Planet. Sci. Lett, 96(3-4), 469–480. https://doi.org/10.1016/0012-821X(90)90021-O

Choudhuri, M., Guha, D., Dutta, A., Sinha, S., Sinha, N. (2010). Spatio-temporal variations and kinematics of shale mobility in the Krishna-Godavari basin, India. In: AAPG Hedberg Conference, Port of Spain, Port of Spain, Trinidad and Tobago, 5–7 June 2006.

Collett, T. S., Boswell, R., Cochran, J. R., Kumar, P., Lall, M., Mazumdar, A., et al. (2014). Geologic implications of gas hydrates in the offshore of India: Results of the National Gas Hydrate Program Expedition 01. Mar. Pet. Geol. 58, 3–28. https://doi.org/10.1016/j.marpetgeo.2014.07.021

Collett, T., Riedel, M., Cochran, J. R., Boswell, R., Presley, J., Kumar, P., et al., and the NGHP Expedition 01 Scientists (2008). Indian National Gas Hydrate Program, Expedition - 01, Initial report, Directorate General of Hydrocarbons, Ministry of Petroleum and Natural gas, India.

Collett, T.S., Kumar, P., Boswell, R. Waite, W. (2019). Preface: Marine gas hydrate reservoir systems along the eastern continental margin of India: Results of the National Gas Hydrate Program Expedition 02. Journal of Marine and Petroleum Geology, 108, pp.1-2. https://doi.org/10.1016/j.marpetgeo.2019.03.005

Cornell, R.M., Schwertmann, U. (1996). The Iron Oxides: Structure, Properties, Reactions, Occurrences, and Uses. VCH Publishers, New York (753 pp.).

Crémièrea, A., Chanda, S., Sahyc, D., Thorsnesa, T., Martmad, T., Noblec, S.R. et al. (2018). Structural controls on seepage of thermogenic and microbial methane sincethe last glacial maximum in the Harstad Basin, southwest Barents Sea. Mar. Petrol. Geol., 98 (2018) 569–58. https://doi.org/10.1016/j.marpetgeo.2018.07.010

Crutchley, G. J., Berndt, C., Geiger, S., Klaeschen, D., Papenberg, C., Klaucke, I., ... & Maier, C. (2013). Drivers of focused fluid flow and methane seepage at south Hydrate Ridge, offshore Oregon, USA. Geology, 41(5), 551-554.

Das, A., Krishnaswami, S. (2007). Elemental geochemistry of river sediments from the Deccan Traps, India: implications to sources of elements and their mobility during basalt–water interaction. Chemical Geology, 242(1-2), 232-254. https://doi.org/10.1016/j.chemgeo.2007.03.023

Day R., Fuller M., Schmidt V.A. (1977). Hysteresis properties of titanomagnetites: grain-size and compositional dependence. Phys. Earth. Planet. Inter. 13(4):260–267. https://doi.org/10.1016/0031-9201(77)90108-X

Dekkers, M. J. (1989). Magnetic properties of natural pyrrhotite. II. High- and low-temperature behavior of Jrs and TRM as function of grain size. Phys. Earth Planet. Inter. 57, 266–283. https://doi.org/10.1016/0031-9201(89)90116-7

Dewangan, P., Basavaiah N., Badesab F. K., Usapkar A., Mazumdar A., Joshi R., Ramprasad T. (2013). Diagenesis of magnetic minerals in a gas hydrate/cold seep environment off the Krishna–Godavari basin, Bay of Bengal, Marine Geology, 340, 57–70, https://doi.org/10.1016/j.margeo.2013.04.016

Dewangan, P., Ramprasad, T., Ramana, M. V., Mazumdar, A., Desa, M., Badesab, F. K. (2010). Seabed morphology and gas venting features in the continental slope region of Krishna-Godavari basin, Bay of Bengal: Implications in gas-hydrate exploration. Mar. Petrol. Geol. 27(7), 1628–1641. https://doi.org/10.1016/j.m Dupr´e arpetgeo.2010.03.015

Dewangan, P., Ramprasad, T., Ramana, M. V., Mazumdar, A., Desa, M., Badasab, F. (2008). Shale Tectonics in the Continental Slope and Rise Regions of Krishna-Godavari Basin, Bay of Bengal: Implication in Gas-Hydrate Exploration. In AGU Fall Meeting Abstracts (Vol. 2008, pp. OS33A-1313).

Dewangan, P., Sriram G., Ramprasad T., Ramana M. V., Jaiswal P. (2011). Fault system and thermal regime in the vicinity of site NGHP-01-10, Krishna–Godavari basin, Bay of Bengal. Marine and Petroleum Geology, 28, 1899–1914, https://doi/10.1016/j.marpetgeo.2011.03.009.

Dewangan, P., Sriram, G., Kumar, A., Mazumdar, A., Peketi, A., Mahale, V. et al. (2021). Widespread occurrence of methane seeps in deep-water regions of Krishna-Godavari basin, Bay of Bengal. Mar. Pet. Geol. 124 104783. https://doi.org/10.1016/j.marpetgeo.2020.104783

Delisle, G., von Rad, U., Andruleit, H., Von Daniels, C., Tabrez, A., Inam, A. (2002). Active mud volcanoes on- and offshore eastern Makran, Pakistan. Int. J. Earth Sci. 91, 93–110.

Dillon, M., Bleil, U. (2006). Rock magnetic signatures in diagenetically altered sediments from the Niger deep-sea fan. Journal of Geophysical Research: Solid Earth, 111(B3). https://doi.org/10.1029/2004JB003540

Dillon, M., Franke, C. (2009). Diagenetic alteration of natural Fe–Ti oxides identified by energy dispersive spectroscopy and low-temperature magnetic remanence and hysteresis measurements. Physics of the Earth and Planetary Interiors, 172(3-4), 141-156. https://doi.org/10.1016/j.pepi.2008.08.003

Dupré, S., Scalabrin, C., Grall, C., Augustin, J. M., Henry, P., Şengör, A. C., ... & Géli, L. (2015). Tectonic and sedimentary controls on widespread gas emissions in the Sea of Marmara: Results from systematic, shipborne multibeam echo sounder water column imaging. Journal of Geophysical Research: Solid Earth, 120(5), 2891-2912.

Dunlop, D. J., Özdemir, Ö., Schmidt, P. W. (1997). Paleomagnetism and paleothermometry of the Sydney Basin 2. Origin of anomalously high unblocking temperatures. J. Geophys. Res. 102(B12), 27, 285–295. https://doi.org/10.1029/97JB02478

Dunlop, D.J. (2002). Theory and application of the Day plot (Mrs/Ms versus Hcr/Hc) 1. Theoretical curves and tests using titanomagnetite data. J. Geophys. Res. 107, B2056. http://dx.doi.org/10.1029/2001JB000486.

Dupré, S., Scalabrin, C., Grall, C., Augustin, J.M., Henry, P., Şengör, A.C., Görür, N., Çağatay, M.N. and Géli, L. (2015). Tectonic and sedimentary controls on widespread gas emissions in the Sea of Marmara: Results from systematic, shipborne multibeam echo sounder water column imaging. Journal of Geophysical Research: Solid Earth, 120(5), pp.2891-2912.

Ebert, Y., Shaar, R., Emmanuel, S., Nowaczyk, N., Stein, M. (2018). Overwriting of sedimentary magnetism by bacterially mediated mineral alteration. Geology, 46(4), 291-294. https://doi.org/10.1130/G39706.1

Egeberg, P. K., and Dickens, G. R. (1999). Thermodynamic and pore water halogen constraints on gas hydrate distribution at ODP Site 997 (Blake Ridge). Chemical Geology, 153(1-4), 53-79.

Egger, M., Hagens, M., Sapart, C. J., Dijkstra, N., van Helmond, N. A., Mogollón, J. M., Risgaard-Petersen, N., van der Veen, C., Kasten, S., Riedinger, N., Böttcher, M.E., Thomas, R., Bo, B. J., Caroline, P.S. (2017). Iron oxide reduction in methane-rich deep Baltic Sea sediments. Geochimica et Cosmochimica Acta, 207, 256-276. https://doi.org/10.1016/j.gca.2017.03.019

Egger, M., Rasigraf, O., Sapart, C.J., Jilbert, T., Jetten, M.S., Röckmann, T., Van der Veen, C., Banda, N., Kartal, B., Ettwig, K.F., Slomp, C.P. (2015). Iron-mediated anaerobic oxidation of methane in brackish coastal sediments. Environ. Sci. Technol. 49(1), pp.277-283. https://doi.org/10.1021/es503663z

Egli, R. and Lowrie, W. (2002). Anhysteretic remanent magnetization of fine magnetic particles. Journal of Geophysical Research: Solid Earth, 107(B10), pp.EPM-2. https://doi.org/10.1029/2001JB000671

Elmore, R. D., Kelley, J., Evans, M., Lewchuk, M. T. (2001). Remagnetization and orogenic fluids: testing the hypothesis in the central Appalachians. Geophysical Journal International, 144(3), 568-576. https://doi.org/10.1046/j.0956-540X.2000.01349.x

Enkin, R. J., Baker, J., Nourgaliev, D., Iassonov, P., Hamilton, T. S. (2007). Magnetic hysteresis parameters and Day plot analysis to characterize diagenetic alteration in gas hydrate-bearing sediments. J. Geophys. Res. Solid Earth. 112, B06S90. https://doi.org/10.1029/2006JB004638

Esteban, L., Enkin, R. J., Hamilton, T. (2008). Gas hydrates and magnetism: Comparative geological settings for diagenetic analysis. Proceedings of the 6th International Conference on Gas Hydrates (pp. 1-9).

Eyre, J.K. (1997). Frequency dependence of magnetic susceptibility for populations of single-domain grains. Geophys. J. Int. 129, 209e211.

Faure, K., Greinert, J., Pecher, I.A., Graham, I.J., Massoth, G.J., De Ronde, C.E., Wright, I.C., Baker, E.T. and Olson, E.J. (2006). Methane seepage and its relation to slumping and gas hydrate at the Hikurangi margin, New Zealand. New Zealand journal of geology and geophysics, 49(4), pp.503-516.

Feinberg, J. M., Scott, G. R., Renne, P. R., Wenk, H. R. (2005). Exsolved magnetite inclusions in silicates: Features determining their remanence behavior. Geology, 33(6), 513-516. https://doi.org/10.1130/G21290.1

Feng, D., & Chen, D. (2015). Authigenic carbonates from an active cold seep of the northern South China Sea: new insights into fluid sources and past seepage activity. Deep sea research part II: topical studies in oceanography, 122, 74-83.

Florindo, F., Karner, D. B., Marra, F., Renne, P. R., Roberts, A. P., Weaver, R. (2007). Radioisotopic age constraints for Glacial Terminations IX and VII from aggradational sections of the Tiber River delta in Rome, Italy. Earth Planet. Sci. Lett., 256(1-2), 61-80. https://doi.org/10.1016/j.epsl.2007.01.014

Frank, U., Nowaczyk, N. R. (2008). Mineral magnetic properties of artificial samples systematically mixed from haematite and magnetite. Geophy. J. Inter., 175(2), 449-461. https://doi.org/10.1111/j.1365-246X.2008.03821.x

Franke, C., von Dobeneck, T., Drury, M. R., Meeldijk, J. D., Dekkers, M. J. (2007). Magnetic petrology of equatorial Atlantic sediments: Electron microscopy results and their implications for

environmental magnetic interpretation. Paleoceanography, 22(4). https://doi.org/10.1029/2007PA001442

Frederichs, T., Bleil, U., Däumler, K., von Dobeneck, T., Schmidt, A.M. (1999). The Magnetic View on the Marine Paleoenvironment: Parameters, Techniques and Potentials of Rock Magnetic Studies as a Key to Paleoclimatic and Paleoceanographic Changes, in: Use of Proxies in Paleoceanography. Springer Berlin Heidelberg, Berlin, Heidelberg, pp. 575–599. https://doi.org/10.1007/978-3-642-58646-0_24

Froelich, P.N., Klinkhammer, G.P., Bender, M.L., Luedtke, N.A., Heath, G.R., Cullen, D., Dauphin, P., Hammond, D., Hartman, B., Maynard, V. (1979). Early oxidation of organic matter in pelagic sediments of the eastern equatorial Atlantic: suboxic diagenesis. Geochim. Cosmochim. Acta 43, 1075–1090.

Foucher, J.-P., Dupr´e, S., Scalabrin, C., Feseker, T., Harmegnies, F., Nouz´e, H. (2010). Changes in seabed morphology, mud temperature and free gas venting at the Håkon Mosby mud volcano, offshore northern Norway, over the time period 2003–2006. Geo Mar. Lett. 30, 157–167.

Fu, Y., Von Dobeneck, T., Franke, C., Heslop, D., Kasten, S. (2008). Rock magnetic identification and geochemical process models of greigite formation in Quaternary marine sediments from the Gulf of Mexico (IODP Hole U1319A). Earth Planet. Sci. Lett, 275(3-4), 233-245. https://doi.org/10.1016/j.epsl.2008.07.034

Gaikwad, V. V., Badesab, F. K., Dewangan, P., Kotha, M. (2021). Diagenesis of Magnetic Minerals in Active/Relict Methane Seep: Constraints from Rock Magnetism and Mineralogical Records from Bay of Bengal. Front. Earth Sci. 9, 60. https://doi.org/ 10.3389/feart.2021.638594

Galy, V., France-Lanord, C., Beyssac, O. et al. (2007). Efficient organic carbon burial in the Bengal fan sustained by the Himalayan erosional system. Nature 450, 407–410. https://doi.org/10.1038/nature06273

Garming, J. F. L., Bleil, U., Riedinger, N. (2005). Alteration of magnetic mineralogy at the sulfate–methane transition: Analysis of sediments from the Argentine continental slope. Phys. Earth Planet. Inter. 151(3-4), 290–308. https://doi.org/10.1016/j.pepi.2005.04.001

Garming, J. F. L., Von Dobeneck, T., Franke, C., Bleil, U. (2007). Low-temperature partial magnetic self-reversal in marine sediments by magnetostatic interaction of titanomagnetite and titanohematite intergrowths. Geophysical Journal International, 170(3), 1067-1075. https://doi.org/10.1111/j.1365-246X.2007.03504.x

Geersen, J., Scholz, F., Linke, P., Schmidt, M., Lange, D., Behrmann, J.H., et al. (2016). Fault zone controlled seafloor methane seepage in the rupture area of the 2010 Maule earthquake, Central Chile. Geochem., Geophy., Geosys. 17(11), pp.4802-4813. https://doi.org/10.1002/2016GC006498

Greve, A., Kars, M., Dekkers, M. J. (2021). Fluid accumulation, migration and anaerobic oxidation of methane along a major splay fault at the Hikurangi subduction margin (New Zealand): A magnetic approach. J. Geophys. Res. Solid Earth. 126(2), e2020JB020671. https://doi.org/10.1029/2020JB020671

Greinert, J., Lewis, K.B., Bialas, J., Pecher, I.A., Rowden, A., Bowden, D.A., De Batist, M., Linke, P. (2010). Methane seepage along the Hikurangi Margin, New Zealand: overview of studies in 2006 and 2007 and new evidence from visual, bathymetric and hydroacoustic investigations. Mar. Geol. 272 (1–4), 6–25.

Gullapalli, S., Dewangan, P., Kumar, A., Dakara, G., Mishra, C. K. (2019). Seismic evidence of free gas migration through the gas hydrate stability zone (GHSZ) and active methane seep in Krishna-Godavari offshore basin. Mar. Petrol. Geol., 110, 695-705. https://doi.org/10.1016/j.marpetgeo.2019.07.052

Halgedahl, S. L., Jarrard, R. D. (1995). Low-temperature behavior of single-domain through multidomain magnetite. Earth Planet. Sci. Lett. 130(1-4), 127-139. https://doi.org/10.1016/0012-821X(94)00260-6

Harrison, R. J., Feinberg, J. M. (2008). FORCinel: An improved algorithm for calculating first order reversal curve distributions using locally weighted regression smoothing. Geochem., Geophy., Geosys. 9, Q05016. https://doi.org/10.1029/2008GC001987

Hatfield, R. G. (2014). Particle size-specific magnetic measurements as a tool for enhancing our understanding of the bulk magnetic properties of sediments. Minerals 4(4), 758-787. https://doi.org/10.3390/min4040758

Hinrichs, K. U., & Boetius, A. (2002). The anaerobic oxidation of methane: new insights in microbial ecology and biogeochemistry. Ocean margin systems, 457-477.

Henry, P., Lallemant, S., Nakamura, K. I., Tsunogai, U., Mazzotti, S., Kobayashi, K. (2002). Surface expression of fluid venting at the toe of the Nankai wedge and implications for flow paths. Mar. Geol., 187(1-2), 119-143. https://doi.org/10.1016/S0025-3227(02)00262-1

Herbozo, G., Hübscher, C., Kaul, N., Wagner, M., Pecher, I., & Kukowski, N. (2013). Influence of recent depositional and tectonic controls on marine gas hydrates in Trujillo Basin, Peru Margin. Marine Geology, 340, 30-48.

Heslop, D., Roberts, A. P., Chang, L., Davies, M., Abrajevitch, A., Deckker, P. (2013). Quantifying magnetite magnetofossil contributions to sedimentary magnetizations. Earth Planet. Sci. Lett., 382, 58-65. https://doi.org/10.1016/j.epsl.2013.09.011

Hirt, A. M., Gehring, A. U. (1991). Thermal alteration of the magnetic mineralogy in ferruginous rocks. J. Geophys. Res. Solid Earth. 96(B6), 9947–9953. https://doi.org/10.1029/91JB00573

Hirt, A. M., Lowrie, W., Clendenen, W. S., Kligfield, R. (1993). Correlation of strain and the anisotropy of magnetic susceptibility in the Onaping Formation: evidence for a near-circular origin of the Sudbury basin. Tectonophysics 225(4), 231–254. https://doi.org/10.1016/0040-1951(93)90300-9

Höfken, A. F., Dobeneck, T. V., Kuhn, T., Kasten, S. (2021). Impact of upward oxygen diffusion from the oceanic crust on the magnetostratigraphy and iron biomineralization of East Pacific ridge-flank sediments. Frontiers in Earth Science. https://doi.org/10.3389/feart.2021.689931

Hong, H., Chang, L., Hayashida, A., Roberts, A.P., Heslop, D., Paterson, G.A., Kodama, K. Tauxe, L. (2019). Paleomagnetic recording efficiency of sedimentary magnetic mineral inclusions: implications for relative paleointensity determinations. Journal of Geophysical Research: Solid Earth, 124(7), pp.6267-6279. https://doi.org/10.1029/2018JB016859

Horng, C. S. (2018). Unusual magnetic properties of sedimentary pyrrhotite in methane seepage sediments: Comparison with metamorphic pyrrhotite and sedimentary greigite. J. Geophys. Res. Solid Earth. 123(6), 4601-4617. https://doi.org/10.1002/2017JB015262

Horng, C. S., Chen, K. H. (2006). Complicated magnetic mineral assemblages in marine sediments offshore southwestern Taiwan: Possible influences of methane flux on the early diagenetic process. Terr., Atmos. Ocean. Sci., 17, 1009–1026. https://doi.org/10.3319/TAO.2006.17.4.1009(GH)

Horng, C. S., Roberts, A. P. (2018). The low-temperature Besnus magnetic transition: Signals due to monoclinic and hexagonal pyrrhotite. Geochem., Geophy., Geosys., 19, 3364–3375. https://doi.org/10.1029/2017GC007394

Hounslow, M. W., Morton, A. C. (2004). Evaluation of sediment provenance using magnetic mineral inclusions in clastic silicates: comparison with heavy mineral analysis. Sedimentary Geology, 171(1-4), 13-36. https://doi.org/10.1016/j.sedgeo.2004.05.008

Hounslow, M. W., Maher, B. A. (1996). Quantitative extraction and analysis of carriers of magnetization in sediments. Geophys. J. Int. 124(1), 57-74. https://doi.org/10.1111/j.1365-246X.1996.tb06352.x

Housen, B. A., & Musgrave, R. J. (1996). Rock-magnetic signature of gas hydrates in accretionary prism sediments. Earth and Planetary Science Letters, 139(3-4), 509-519.

Hounslow, M.W. (1996). Ferrimagnetic Cr and Mn spinels in sediments: residual magnetic minerals after diagenetic dissolution. Geophys. Res. Lett. 23, 2823–2826. https://doi.org/10.1029/96GL01327

Hounslow, M.W., Maher, B.A., Thistlewood, L. (1995). Magnetic mineralogy of sandstones from the Lunde Formation (late Triassic), northern North Sea, UK: origin of the palaeomagnetic signal. Geol. Soc. Lond. Spec. Publ. 98, 119–147. https://doi.org/10.1144/GSL.SP.1995.098.01.07

Hovland, M., & Judd, A. G. (1988). Seabed pockmarks and seepages: impact on geology, biology and the marine environment (Vol. 293). London: Graham & Trotman.

Hunt, C.P., Moskowitz, B.M., Banerjee, S.K. (1995). Magnetic properties of rocks and minerals. In: Rock Physics and Phase Relations. A Handbook of Physical Constants. AGU Reference Shelf, 3, pp. 189e204.

Itambi, A. C., Von Dobeneck, T., Dekkers, M. J., Frederichs, T. (2010). Magnetic mineral inventory of equatorial Atlantic Ocean marine sediments off Senegal—glacial and interglacial contrast. Geophys. J. Int. 183(1), 163-177. https://doi.org/10.1111/j.1365-246X.2010.04736.x

Jiang, W. T., Horng, C. S., Roberts, A. P., Peacor, D. R. (2001). Contradictory magnetic polarities in sediments and variable timing of neoformation of authigenic greigite. Earth Planet. Sci. Lett. 193(1-2), 1-12. https://doi.org/10.1016/S0012-821X(01)00497-6

Jiang, X.D., Zhao, X.Y., Zhao, X., Jiang, Z.X., Chou, Y.M., Zhang, T.W., Yang, X.Q., Liu, Q.S. (2021). Quantifying Contributions of Magnetic Inclusions Within Silicates to Marine Sediments: A Dissolution Approach to Isolating Volcanic Signals for Improved Paleoenvironmental Reconstruction. Journal of Geophysical Research: Solid Earth, 126(10), p.e2021JB022680. https://doi.org/10.1029/2021JB022680

João, H. M., Badesab, F., Gaikwad, V., Kocherla, M., Deenadayalan, K. (2021). Controls of mass transport deposit and magnetic mineral diagenesis on the sediment magnetic record from the Bay of Bengal. Mar. Petrol. Geol. 128, 104994. https://doi.org/10.1016/j.marpetgeo.2021.104994

Johnson, J.E., Phillips, S.C., Clyde, W.C., Giosan, L., Torres, M.E. (2021). Isolating detrital and diagenetic signals in magnetic susceptibility records from methane-bearing marine sediments. G-cubed 22 (9), e2021GC009867. https://doi.org/10.1029/2021GC009867.

Johnson, J.E., Phillips, S.C., Torres, M.E., Pi˜nero, E., Rose, K.K., Giosan, L. (2014). Influence of total organic carbon deposition on the inventory of gas hydrate in the Indian continental margins. Mar. Petrol. Geol. 58, 406–424. https://doi.org/10.1016/j.marpetgeo.2014.08.021.

Jordanova, N. (2016). Soil magnetism: Applications in pedology, environmental science and agriculture. Academic press.

Jørgensen, B. B., Böttcher, M. E., Lüschen, H., Neretin, L. N., Volkov, I. I. (2004). Anaerobic methane oxidation and a deep H2S sink generate isotopically heavy sulfides in Black Sea sediments. Geochim. Cosmochim. Acta, 68(9), 2095–2118. https://doi.org/10.1016/j.gca.2003.07.017

Jørgensen, B.B., Kasten, S. (2006). Sulfur cycling and methane oxidation. In: Schulz, H.D., Zabel, M. (Eds.), Marine Geochemistry, pp. 271–309.

Judd, A., Hovland, M. (2007). Seabed fluid flow: the impact on geology, biology and the marine environment. Cambridge University Press, Cambridge.

Just, J., Heslop, D., von Dobeneck, T., Bickert, T., Dekkers, M.J., Frederichs, T., Meyer, I., Zabel, M. (2012). Multiproxy characterization and budgeting of terrigenous end-members at the NW African continental margin. Geochem., Geophy., Geosys., 13(9). https://doi.org/10.1029/2012GC004148

Kakol, Z., Sabol, J., Stickler, J., Honig, J. M. (1992). Effect of low-level titanium (IV) doping on the resistivity of magnetite near the Verwey transition. Phys. Rev. B 46 (4), 1975. https://doi.org/10.1103/PhysRevB.46.1975

Kao, S. J., Horng, C. S., Roberts, A. P., Liu, K. K. (2004). Carbon–sulfur–iron relationships in sedimentary rocks from southwestern Taiwan: influence of geochemical environment on greigite and pyrrhotite formation. Chem. Geol. 203(1-2), 153-168. https://doi.org/10.1016/j.chemgeo.2003.09.007

Karlin, R. (1990). Magnetic mineral diagenesis in suboxic sediments at Bettis site W-N, NE Pacific Ocean. J. Geophys. Res. Solid Earth, 95(B4), 4421-4436. https://doi.org/10.1029/JB095iB04p04421

Karlin, R. (1990a). Magnetite diagenesis in marine sediments from the Oregon continental margin. J. Geophys. Res. Solid Earth, 95(B4), 4405-4419. https://doi.org/10.1029/JB095iB04p04405

Karlin, R., Levi, S. (1983). Diagenesis of magnetic minerals in recent haemipelagic sediments. Nature, 303(5915), 327. https://doi.org/10.1038/303327a0

Karlin, R., Lyle, M., Heath, G. R. (1987). Authigenic magnetite formation in suboxic marine sediments. Nature 326(6112), 490-493. https://doi.org/10.1038/326490a0

Kars, M. M., Kodama K. (2015a), Authigenesis of magnetic minerals in gas hydrate bearing sediments in the Nankai Trough, Offshore Japan, Geochemistry, Geophysics, Geosystems, 16, 947–961, https://doi.org/10.1002/2014GC005614.

Kars, M., Kodama, K. (2015b). Rock magnetic characterization of ferrimagnetic iron sulfides in gas hydrate-bearing marine sediments at Site C0008, Nankai Trough, Pacific Ocean, off-coast Japan. Earth, Planets and Space, 67(1), 118. https://doi.org/10.1186/s40623-015-0287-y

Kars, M., Aubourg, C., Labaume, P., Berquó, T.S., Cavailhes, T. (2014). Burial diagenesis of magnetic minerals: new insights from the Grès D'Annot transect (SE France). Minerals 4, 667–689. https://doi.org/10.3390/min4030667

Kars, M., Aubourg, C., Pozzi, J.P., Janots, D. (2012). Continuous production of nanosized magnetite through low grade burial. Geochem. Geophys. Geosyst. 13, Q08Z48. http://dx.doi.org/10.1029/2012GC004104.

Kars, M., Greve, A., Zerbst, L., (2021). Authigenic greigite as an indicator of methane diffusion in gas hydrate-bearing sediments of the Hikurangi Margin, New Zealand. Front. Earth Sci. 9, 80. https://doi.org/10.3389/feart.2021.603363

Kars, M., Musgrave, R. J., Hoshino, T., Jonas, A. S., Bauersachs, T., Inagaki, F., Kodama, K. (2018). Magnetic mineral diagenesis in a high temperature and deep methanic zone in Izu rear arc marine sediments, northwest Pacific Ocean. J. Geophys. Res. Solid Earth. 123(10), 8331-8348. https://doi.org/10.1029/2018JB015861

Karstens, J., Haflidason, H., Becker, L. W., Berndt, C., Rüpke, L., Planke, S., et al. (2018). Glacigenic sedimentation pulses triggered postglacialgas hydrate dissociation. Nat. Commun. 9(1), 635. https://doi.org/10.1038/s41467-018-03043-z

Kasten, S., Freudenthal, T., Gingele, F. X., Schulz, H. D. (1998). Simultaneous formation of iron-rich layers at different redox boundariesin sediments of the Amazon deep-sea fan. Geochim. Cosmochim. Acta, 62, 2253–2264. https://doi.org/10.1016/S0016-7037(98)00093-3

Kasten, S., Zabel, M., Heuer, V., Hensen, C. (2003). Processes and signals of nonsteady-state diagenesis in deep-sea sediments and their pore waters. In The South Atlantic in the Late Quaternary, (pp. 431–459). Berlin, Heidelberg: Springer. https://doi.org/10.1016/j.gca.2007.08.019

Katz, B., Elmore, R. D., Cogoini, M., Engel, M. H., Ferry, S. (2000). Associations between burial diagenesis of smectite, chemical remagnetization, and magnetite authigenesis in the Vocontian trough, SE France. Journal of Geophysical Research: Solid Earth, 105(B1), 851-868. https://doi.org/10.1029/1999JB900309

Kawamura, N., Oda, H., Ikehara, K., Yamazaki, T., Shioi, K., Taga, S., Hatakeyama, S., Torii, M. (2007). Diagenetic effect on magnetic properties of marine core sediments from the southern Okhotsk Sea. Earth Planets Space 59, 83–93. https://doi.org/10.1186/BF03352680

Kvenvolden, K. A., & Lorenson, T. D. (2001). The global occurrence of natural gas hydrate. Washington DC American Geophysical Union Geophysical Monograph Series, 124, 3-18.

Kvenvolden, K. A. (1995). A review of the geochemistry of methane in natural gas hydrate. Organic geochemistry, 23(11-12), 997-1008.

Kim, J., Dong, H., Yang, K., Park, H., Elliott, W.C., Spivack, A., Koo, T.H., Kim, G., Morono, Y., Henkel, S., Inagaki, F. (2019). Naturally occurring, microbially induced smectite-to-illite reaction. Geology, 47(6), pp.535-539. https://doi.org/10.1130/G46122.1

Knittel, K., Boetius, A. (2009). Anaerobic oxidation of methane: Progress with an unknown process. Ann. Rev. Microb., 63,311–334. https://doi.org/10.1038/296643a0

Kopf, A. J. (2003). Global methane emission through mud volcanoes and its past and present impact on the Earth's climate. International Journal of Earth Sciences, 92(5), 806-816.

Kopp, R. E., Kirschvink, J. L. (2008). The identification and biogeochemical interpretation of fossil magnetotactic bacteria. Earth-Sci. Rev., 86(1-4), 42-61. https://doi.org/10.1016/j.earscirev.2007.08.001

Korff, L., von Dobeneck, T., Frederichs, T., Kasten, S., Kuhn, G., Gersonde, R., Diekmann, B. (2016). Cyclic magnetite dissolution in Pleistocene sediments of the abyssal northwest Pacific

Ocean: evidence for glacial oxygen depletion and carbon trapping. Paleoceanography, 31(5), 600-624. https://doi.org/10.1002/2015PA002882

Köster, M., Kars, M., Schubotz, F., Tsang, M.Y., Maisch, M., Kappler, A., Morono, Y., Inagaki, F., Heuer, V.B., Kasten, S., Henkel, S. (2021). Evolution of (Bio-) Geochemical Processes and Diagenetic Alteration of Sediments Along the Tectonic Migration of Ocean Floor in the Shikoku Basin off Japan. Geochemistry, Geophysics, Geosystems, 22(8), p.e2020GC009585. https://doi.org/10.1029/2020GC009585

Krishna, K. S., Ismaiel, M., Srinivas, K., Gopala Rao, D., Mishra, J., Saha, D. (2016). Sediment pathways and emergence of Himalayan source material in the Bay of Bengal. Curr. Sci. 110. https://doi.org/10.18520/cs/v110/i3/363-372

Kumar, P., Collett, T. S., Boswell, R., Cochran, J. R., Lall, M., Mazumdar, A., et al. (2014). Geologic implications of gas hydrates in the offshore of India: Krishna-Godavari Basin, Mahanadi Basin, Andaman Sea, Kerala–Konkan Basin. Mar. Petrol. Geol. 58, 29–98. https://doi.org/10.1016/j.marpetgeo.2014.07.031

Kvenvolden, K.A. (1993). Gas hydrates—geological perspective and global change. Reviews of geophysics, 31(2), pp.173-187. https://doi.org/10.1029/93RG00268

Larrasoaña, J. C., Roberts, A. P., Musgrave, R. J., Gràcia, E., Piñero, E., Vega, M., et al. (2007). Diagenetic formation ofgreigite and pyrrhotite in gas hydrate marine sedimentary systems. Earth Planet. Sci. Lett. 261(3-4), 350–366. https://doi.org/10.1016/j.epsl.2007.06.032

Larrasoaña, J. C., Roberts, A. P., Stoner, J. S., Richter, C., Wehausen, R. (2003). A new proxy for bottom-water ventilation in the eastern Mediterranean based on diagenetically controlled magnetic properties of sapropel-bearing sediments. Palaeogeogr., Palaeoclimatol., Palaeoecol. 190, 221-242. https://doi.org/10.1016/S0031-0182(02)00607-7

Lascu, I., Einsle, J. F., Ball, M. R., Harrison, R. J. (2018). The vortex state in geologicmaterials: A micromagnetic perspective. J. Geophys. Res. Solid Earth. 123, 7285–7304. https://doi.org/10.1029/2018JB015909

Lattard, D., Engelmann, R., Kontny, A., Sauerzapf, U. (2006). Curie temperatures of synthetic titanomagnetites in the Fe-Ti-O system: Effects of composition, crystal chemistry, and thermomagnetic methods. J. Geophys. Res. Solid Earth. 111(B12). https://doi.org/10.1029/2006JB004591

Levin, S. A. (2005). Self-organization and the emergence of complexity in ecological systems. Bioscience, 55(12), 1075-1079. https://doi.org/10.1641/0006-3568(2005)055[1075:SATEOC]2.0.CO;2

Le Pichon, X., Iiyama, T., Boul`egue, J., Charvet, J., Faure, M., Kano, K., Lallemant, S., Okada, H., Rangin, C., Taira, A., Urabe, T., Uyeda, S. (1987). Nankai trough and zenisu ridge: a Deep-sea submersible survey. Earth Planet Sci. Lett. 83 (1–4), 285–299.

Liang, Q., Hu, Y., Feng, D., Peckmann, J., Chen, L., Yang, S., Liang, J., Tao, J. Chen, D. (2017). Authigenic carbonates from newly discovered active cold seeps on the northwestern slope of the South China Sea: Constraints on fluid sources, formation environments, and seepage dynamics. Deep Sea Res. Part I Oceanogr. Res. Pap. 124, pp.31-41. https://doi.org/10.1016/j.dsr.2017.04.015

Lin, Q., Wang, J., Algeo, T.J., Su, P., Hu, G. (2016). Formation mechanism of authigenic gypsum in marine methane hydrate settings: Evidence from the northern South China Sea. Deep-Sea Research: Part I, Oceanographic Research Papers, v. 115, p. 210–220, https://doi.org/10.1016/j.dsr.2016.06.010.

Lin, Z., Sun, X., Lu, Y., Strauss, H., Xu, L., Gong, J., et al. (2017). The enrichment of heavy iron isotopes in authigenic pyrite as a possible indicator of sulfate-driven anaerobic oxidation of methane: Insights from the South China Sea. Chem. Geol., 449, pp.15-29. https://doi.org/10.1016/j.chemgeo.2016.11.032

Lin, Z., Sun, X., Roberts, A.P., Strauss, H., Lu, Y., Yang, X., et al. (2020). A novel authigenic magnetite source for sedimentary magnetization. Geology. 49 (4), 360-365. https://doi.org/10.1130/G48069.1

Lin, Z., Sun, X., Strauss, H., Lu, Y., Böttcher, M.E., Teichert, B.M., et al. (2018). Multiple sulfur isotopic evidence for the origin of elemental sulfur in an iron-dominated gas hydrate-bearing sedimentary environment. Mar. Geol., 403, pp.271-284. https://doi.org/10.1016/j.margeo.2018.06.010.

Linke, P., S. Sommer, L. Rovelli, and D. F. McGinnis (2010), Physical limitations of dissolved methane fluxes: The role of bottom-boundary layer processes, Mar. Geol., 272(1-4), 209–222, https://doi.org/10.1016/j.margeo.2009.03.020.

Liu, Q., Deng, C., Yu, Y., Torrent, J., Jackson, M. J., Banerjee, S. K., Zhu, R. (2005). Temperature dependence of magnetic susceptibility in an argon environment: implications for pedogenesis of Chinese loess/palaeosols. Geophysical Journal International, 161(1), 102-112. https://doi.org/10.1111/j.1365-246X.2005.02564.x

Liu, Q., Jackson, M. J., Yu, Y., Chen, F., Deng, C., Zhu, R. (2004). Grain size distribution of pedogenic magnetic particles in Chinese loess/paleosols. Geophy. Res. Lett., 31(22). . https://doi.org/10.1029/2004GL021090

Liu, Q., Roberts, A. P., Larrasoana, J. C., Banerjee, S. K., Guyodo, Y., Tauxe, L., Oldfield, F. (2012). Environmental magnetism: principles and applications. Reviews of Geophysics, 50(4). https://doi.org/10.1029/2012RG000393

Loncke, L., Mascle, J., & Parties, F. S. (2004). Mud volcanoes, gas chimneys, pockmarks and mounds in the Nile deep-sea fan (Eastern Mediterranean): geophysical evidences. Marine and petroleum geology, 21(6), 669-689.

Lougheed, B. C., Snowball, I., Moros, M., Kabel, K., Muscheler, R., Virtasalo, J. J., Wacker, L. (2012). Using an independent geochronology based on palaeomagnetic secular variation (PSV) and atmospheric Pb deposition to date Baltic Sea sediments and infer 14C reservoir age. Quat. Sci. Rev. 42, 43-58. https://doi.org/10.1016/j.quascirev.2012.03.013

Lovley, D. R., Stolz, J. F., Nord, G. L., Phillips, E. J. (1987). Anaerobic production of magnetite by a dissimilatory iron-reducing microorganism. Nature 330(6145), 252-254. https://doi.org/10.1038/330252a0

Luff, R., Greinert, J., Wallmann, K., Klaucke, I., Suess, E. (2005). Simulation of long-term feedbacks from authigenic carbonate crust formation at cold vent sites. Chem. Geol. 216(1-2), 157-174. https://doi.org/10.1016/j.chemgeo.2004.11.002

Maher, B. A. (1988). Magnetic properties of some synthetic sub-micron magnetites. Geophy. J. Inter., 94(1), 83-96. https://doi.org/10.1111/j.1365-246X.1988.tb03429.x

Maher, B. A., Thompson, R. (Eds.). (1999). Quaternary climates, environments and magnetism. Cambridge University Press.

Mazumdar A., Dewangan P., Peketi A., Gullapalli S., Kalpana M. S., Naik G. P., et al. (2019). The first record of active methane (cold) seep ecosystem associated with shallow methane hydrate from the Indian EEZ. J. Earth Sys. Sci. 128:18, https://doi.org/10.1007/s12040-018-1044-y

Mazumdar, A., Dewangan, P., Joäo, H.M., Peketi, A.,Khosla, V.R., Kocherla, M., et al. (2009). Evidence of paleo–cold seep activity from theBay of Bengal, offshore India. Geochem., Geophy., Geosys., 10Q06005. https://doi.org/10.1029/2008GC002337

Mazumdar, A., Dewangan, P., Joäo, H.M., Peketi, A.,Khosla, V.R., Kocherla, M., et al. (2009). Evidence of paleo–cold seep activity from theBay of Bengal, offshore India. Geochem., Geophy., Geosys., 10Q06005. https://doi.org/10.1029/2008GC002337

Mazumdar, A., Joao, H.M., Peketi, A., Dewangan, P., Kocherla, M., Joshi, R.K., Ramprasad, T. (2012). Geochemical and geological constraints on the composition of marine sediment pore fluid: possible link to gas hydrate deposits. Mar. Petrol. Geol. 38 (1), 35–52. https://doi.org/10.1016/j.marpetgeo.2012.07.004

Mazumdar, A., Kocherla, M., Carvalho, M.A., Peketi, A., Joshi, R.K., Mahalaxmi, P. (2015). Geochemical characterization of the Krishna-Godavari and Mahanadi offshore basin (Bay of Bengal) sediments: a comparative study of provenance. Mar. Petrol. Geol., 60, 18-33. https://doi.org/10.1016/jmarpetgeo.2014.09.005

McCabe, C., Jackson, M., Saffer, B. (1989). Regional patterns of magnetite authigenesis in the Appalachian Basin: implications for themechanism of late Paleozoic remagnetization. J. Geophys. Res. 94, 10,429–10,443. https://doi.org/10.1029/JB094iB08p10429

Milkov, A. V. (2000). Worldwide distribution of submarine mud volcanoes and associated gas hydrates. Marine Geology, 167(1-2), 29-42.

Milkov, A. V., and Sassen, R. (2003). Two-dimensional modeling of gas hydrate decomposition in the northwestern Gulf of Mexico: significance to global change assessment. Global and Planetary Change, 36(1-2), 31-46.

Mohamed, K. J., Rey, D., Rubio, B., Dekkers, M. J., Roberts, A. P., Vilas, F. (2011). Onshore–offshore gradient in reductive early diagenesis in coastal marine sediments of the Ria de Vigo, Northwest Iberian Peninsula. Cont. Shelf Res., 31(5), 433-447. https://doi.org/10.1016/j.csr.2010.06.006

Moore, J.C., Orange, D., Kulm, L.D. (1990). Interrelationship of fluid venting and structural evolution: alvin observations from the frontal accretionary prism, Oregon. J. Geophys. Res. Solid Earth 95 (B6), 8795–8808.

Moore, G. F., Boston, B. B., Strasser, M., Underwood, M. B., & Ratliff, R. A. (2015). Evolution of tectono-sedimentary systems in the Kumano Basin, Nankai Trough forearc. Marine and Petroleum Geology, 67, 604-616.

Moskowitz, B. M., Frankel, R. B., and Bazylinski, D. A. (1993). Rock magnetic criteria for the detection of biogenic magnetite. Earth Planet. Sci. Lett., 120(3-4), 283–300. https://doi.org/10.1016/0012-821X(93)90245-5

Moskowitz, B. M., Jackson, M., Kissel, C. (1998). Low-temperature magnetic behavior of titanomagnetites. Earth Planet. Sci. Lett. 157(3-4), 141-149. https://doi.org/10.1016/S0012-821X(98)00033-8

Moskowitz, B. M., Jackson, M. J., Chandler, V. W. (2015). Geophysical Properties of the Near Surface Earth: Magnetic. In Treatise on geophysics (pp. 139-174). https://doi.org/10.1016/B978-0-444-53802-4.00191-3

Mountjoy, J. J., Pecher, I., Henrys, S., Crutchley, G., Barnes, P. M., Plaza-Faverola, A. (2014). Shallow methane hydrate system controls ongoing, downslope sediment transport in a low-velocity active submarine landslide complex, H ikurangi M argin, N ew Z ealand. Geochemistry, Geophysics, Geosystems, 15(11), 4137-4156. https://doi.org/10.1002/2014GC005379

Musgrave, R. J., Bangs, N. L., Larrasoaña, J. C., Gràcia, E., Hollamby, J. A., Vega, M. E. (2006). Rise of the base of the gas hydrate zone since the last glacial recorded by rock magnetism. Geology 34(2), 117–120. https://doi.org/10.1130/G22008.1

Musgrave, R. J., Kars, M., Vega, M. E. (2019). Progressive and punctuated magnetic mineral diagenesis: The rock magnetic record of multiple fluid inputs and progressive pyritization in a volcano-bounded basin, IODP Site U1437, Izu rear arc. J. Geophys. Res. Solid Earth. 124(6), 5357-5378. https://doi.org/10.1029/2018JB017277

Muxworthy, A. R., Evans, M. E. (2013). Micromagnetics and magnetomineralogy of ultrafine magnetite inclusions in the Modipe Gabbro. Geochem., Geophy., Geosys., 14(4), 921-928. https://doi.org/10.1029/2012GC004445

Muxworthy, A. R., McClelland, E. (2000). Review of the low-temperature magnetic properties of magnetite from a rock magnetic perspective. Geophy. J. Inter., 140(1), 101–114. https://doi.org/10.1046/j.1365-246x.2000.00999.x

Muxworthy, A. R., Roberts, A. P. (2007), First-order reversal curve (FORC) diagrams, In: Gubbins, D and Herrero-Bervera, E, editor, Encycl. Geomag. Paleomag., Springer, Pages: 266 – 272

Muxworthy, A. R., Dunlop, D. J. (2002). First-order reversal curve (FORC) diagrams for pseudo-single-domain magnetites at high temperature. Earth Planet. Sci. Lett. 203(1), 369-382. https://doi.org/10.1016/S0012-821X(02)00880-4

Neretin, L. N., Böttcher, M. E., Jørgensen, B. B., Volkov, I. I., Lüschen, H., Hilgenfeldt, K. (2004). Pyritization processes and greigiteformation in the advancing sulfidization front in the upper Pleistocene sediments of the Black Sea 1. Geochim. Cosmochim. Acta,68(9), 2081–2093. https://doi.org/10.1016/S0016-7037(03)00450-2

Newell, A. J. (2005). A high-precision model of first-order reversal curve (FORC) functions for single-domain ferromagnets with uniaxial anisotropy. Geochem., Geophy., Geosys., 6(5). https://doi.org/10.1029/2004GC000877

Niewöhner, C., Hensen, C., Kasten, S., Zabel, M., Schulz, H. D. (1998). Deep sulfate reduction completely mediated by anaerobic methane oxidation in sediments of the upwelling area off Namibia. Geochim. Cosmochim. Acta. 62(3), 455-464. https://doi.org/10.1016/S0016-7037(98)00055-6

Novosel, I., Spence, G. D., Hyndman R. D. (2005), Reduced magnetization produced by increased methane flux at a gas hydrate vent, Mar. Geol., 216(4), 265–274. https://doi.org/10.1016/j.margeo.2005.02.027.

Novosel, N., Galić, S., Pajić, D., Zadro, K., Babić, E. (2015). Enhancing Superconducting Properties of MgB 2 by Addition of Magnetic Particles. J. Supercond.novel magnet., 28(2), 425-430. https://doi.org/10.1007/s10948-014-2807-6

Nowaczyk, N. R. (2011). Dissolution of titanomagnetite and sulphidization in sediments from Lake Kinneret, Israel. Geophys. J. Inter., 187(1), 34-44. https://doi.org/10.1111/j.1365-246X.2011.05120.x

Nowaczyk, N. R., Arz, H. W., Frank, U., Kind, J., Plessen, B. (2012). Dynamics of the Laschamp geomagnetic excursion from Black Sea sediments. Earth Planet Sci. Lett., 351, 54-69. https://doi.org/10.1016/j.epsl.2012.06.050

Oda, H., Torii, M., (2004). Sea-level change and remagnetization of continental shelf sediments off New Jersey (ODP Leg 174A): magnetite and greigite diagenesis. Geophys. J. Int. 156(3), 443-458. https://doi.org/10.1111/j.1365-246X.2004.02162.x

Ojha, P. S., Dubey, M. (2006). Gaint hydrocarbon fields of offshore Krishna-Godavari Basin. Petroview, 1, 26-30.

Özdemir, Ö., Dunlop, D.J. (2010). Hallmarks of maghemitization in low-temperature remanence cycling of partially oxidized magnetite nanoparticles. J. Geophys. Res. 115, B02101. http://dx.doi.org/10.1029/2009JB006756.

Özdemir, Ö., Dunlop, D. J., Moskowitz, B. M. (1993). The effect of oxidation on the Verwey transition in magnetite. Geophy. Res. Lett., 20(16), 1671-1674. https://doi.org/10.1029/93GL01483

Özdemir, Ö., Dunlop, D. J., Moskowitz, B. M. (2002). Changes in remanence, coercivity and domain state at low temperature in magnetite. Earth Planet. Sci. Lett., 194(3-4), 343–358. https://doi.org/10.1016/S0012-821X(01)00562-3

Pan, Y. X., Zhu, R. X., Banerjee, S. K., Gill, J., Williams, Q. (2000). Rock magnetic properties related to thermal treatment of siderite: Behavior and interpretation. J. Geophys. Res. Solid Earth,, 105, 783–794. https://doi.org/10.1029/1999JB900358

Panieri, G., Graves, C. A., James, R. H. (2016). Paleo-methane emissions recorded in foraminifera near the landward limit of the gashydrate stability zone offshore western Svalbard. Geochem., Geophy., Geosys., 17, 521–537. https://doi.org/10.1002/2015GC006153

Party, S.S. (1996). Site 997. Proc. ODP Initial Repts. [CD-ROM], 1996, 164, pp.277-334.

Passier, H. D., De Lange, G. J., Dekkers, M. J. (2001). Magnetic properties and geochemistry of the active oxidation front and the youngestsapropel in the eastern Mediterranean Sea. Geophy. J. Inter., 145(3), 604–614. https://doi.org/10.1046/j.0956-540x.2001.01394.x

Passier, H. D., De Lange, G. J., Dekkers, M. J. (2001). Magnetic properties and geochemistry of the active oxidation front and the youngest sapropel in the eastern Mediterranean Sea. Geophys. J. Int. 145(3), 604–614. https://doi.org/10.1046/j.0956-540x.2001.01394.x

Passier, H. F., Dekkers, M. J., De Lange, G. J. (2000). Rock-magnetic properties, geochemistry and diagenesis of eastern Mediterranean surface sediments. Geol. Carpath. 51(3), 189-190.

Passier, H.F. Dekkers, M.J. (2002). Iron oxide formation in the active oxidation front above sapropel S1 in the eastern Mediterranean Sea as derived from low-temperature magnetism. Geophysical Journal International, 150(1), pp.230-240. https://doi.org/10.1046/j.1365-246X.2002.01704.x

Paull, C.K., Brewer, P.G., Ussler, W., Peltzer, E.T., Rehder, G., Clague, D. (2002). An experiment demonstrating that marine slumping is a mechanism to transfer methane from seafloor gas-hydrate deposits into the upper ocean and atmosphere. Geo Mar. Lett. 22 (4), 198–203.

Paull, C. K., Barbara Hecker, R. Commeau, R. P. Freeman-Lynde, C. Neumann, W. P. Corso, S. Golubic, J. E. Hook, E., Sikes, J. Curray (1984). "Biological communities at the Florida Escarpment resemble hydrothermal vent taxa." Science 226, no. 4677, 965-967. https://doi.org/10.1126/science.226.4677.965

Peters, C., Dekkers, M. J. (2003). Selected room temperature magnetic parameters as a function of mineralogy, concentration and grain size. Phys. Chem. Earth, Parts A/B/C 28(16-19), 659-667. https://doi.org/10.1016/S1474-7065(03)00120-7

Petersen, N., Vali, H. (1987). Observation of shrinkage cracks in ocean floor titanomagnetites. Phys. Earth Planet. Inter. 46, 197–205. https://doi.org/10.1016/0031-9201(87)90182-8

Petersen, N., Von DobeneckT., Vali H. (1986). Fossil bacterial magnetite in deep-sea sediments from the South Atlantic Ocean. Nature 320, 611–615. https://doi.org/10.1038/320611a0

Philips, S. C. (2018). Diagenetic degradation of paleoenvironmental signals in magnetic susceptibility in the northern Bay of Bengal, The IRM Quarterly, Winter 2017-2018, Vol. 27 No.4

Phillips, S. C., Johnson, J. E., Clyde, W. C., Setera, J. B., Maxbauer, D. P., Severmann, S., Riedinger, N. (2017). Rock magnetic and geochemical evidence for authigenic magnetite formation via iron reduction in coal-bearing sediments offshore Shimokita Peninsula, Japan (IODP Site C0020). Geochem.Geophys. Geosyst. 18, 2076–2098. https://doi.org/10.1002/2017GC006943

Phillips, S.C., Johnson, J.E., Underwood, M.B., Guo, J., Giosan, L., Rose, K. (2014). Longtimescale variation in bulk and clay mineral composition of Indian continental margin sediments in the Bay of Bengal, Arabian Sea, and Andaman Sea. Mar. Petrol. Geol. 58, 117–138. https://doi.org/10.1016/j.marpetgeo.2014.06.018.

Pike, C.R., Roberts, A.P., Verosub, K.L. (1999) Characterizing interactions infine magnetic particle systems using first order reversal curves. J. Appl. Phys. 85(9):6660–6667. https://doi.org/10.1063/1.370176

Plaza-Faverola, A., Bünz, S., Johnson, J.E., Chand, S., Knies, J., Mienert, J., Franek, P. (2015). Role of tectonic stress in seepage evolution along the gas hydrate-charged Vestnesa Ridge, Fram Strait. Geophys. Res. Lett. 42 (3), 733–742. https://doi.org/10.1002/2014GL062474.

Portail, M., Olu, K., Escobar-Briones, E., Caprais, J.C., Menot, L., Waeles, M., Cruaud, P., Sarradin, P.M., Godfroy, A. Sarrazin, J. (2015). Comparative study of vent and seep macrofaunal communities in the Guaymas Basin. Biogeosciences, 12(18), pp.5455-5479. https://doi.org/10.5194/bg-12-5455-2015

Poulton, S. W., Krom, M. D., Raiswell, R. (2004). A revised scheme for the reactivity of iron (oxyhydr) oxide minerals towards dissolved sulfide. Geochim. Cosmochim. Acta. 68(18), 3703-3715. https://doi.org/10.1016/j.gca.2004.03.012.

Prabhakar, K.N., Zutshi, P.L. (1993). Evolution of southern part of Indian East Coast basin. J. Geol. Soc. Ind. 41:215–230.

Prozorov, T., Mallapragada, S. K., Narasimhan, B., Wang, L., Palo, P., Nilsen-Hamilton, et al. (2007). Protein-mediated synthesis of uniform super paramagnetic magnetite nanocrystals. Advanced Functional Materials, 17(6), 951-957. https://doi.org/10.1002/adfm.200600448

Qian, Y., Heslop, D., Roberts, A. P., Hu, P., Zhao, X., Liu, Y., et al. (2021). Low-temperature magnetic properties of marine sediments—Quantifying magnetofossils, superparamagnetism, and maghemitization: Eastern Mediterranean examples. Journal of Geophysical Research: Solid Earth, 126, e2021JB021793. https://doi.org/10.1029/2021JB021793

Raiswell, R., Canfield, D.E. (2012). The iron biogeochemical cycle past and present. Geochem. Perspect. 1, 1–215.

Ramana, M. V., Ramprasad, T., Kamesh Raju, K. A., Desa, M. (2007). Occurrence of gas hydrates along the continental margins of India, particularly the Krishna-Godavari off shore basin. Int. J.Env. Stu., 64(6), 675–693. https://doi.org/10.1080/00207230701476321

Ramana, M. V., Ramprasad, T., Paropkari, A. L., Borole, D. V., Rao, B. R., Karisiddaiah, S. M., Gonsalves, M. J. (2009). Multidisciplinary investigations exploring indicators of gas hydrate occurrence in the Krishna–Godavari Basin offshore, east coast of India. Geo-Marine Letters, 29(1), 25–38. https://doi.org/10.1007/s00367-008-0121-7

Ramesh R., V. Subramanian (1988), Temporal, spatial and size variation in the sediment transport in the Krishna River basin, India, Journal of Hydrology, 98, 53–65. https://doi.org/10.1016/0022-1694(88)90205-3

Ramprasad, T., Dewangan, P., Ramana, M. V., Mazumdar, A., Karisiddaiah, S. M., Ramya, E. R., Sriram, G. (2011). Evidence of slumping/sliding in Krishna–Godavari offshore basin due to gas/fluid movements. Marine and Petroleum Geology, 28(10), 1806–1816. https://doi.org/10.1016/j.marpetgeo.2011.02.007

Rao, G. N. (2001). Sedimentation, stratigraphy, and petroleum potential of Krishna-Godavari basin, East Coast of India. AAPGB 85(9), 1623–1643. https://doi.org/10.1306/8626CCDF-173B-11D7-8645000102C1865D

Rao, V. P. (1991). Clay mineral distribution in the continental shelf sediments from Krishna to Ganges river mouth, east coast of India. Ind. J. Mar. Sci., 20, 7–12.

Reidinger, N., Pfeifer, K., Kasten, S., Garming, J. F. L., Vogt, C., Hensen C. (2005). Diagenetic alteration of magnetic signals by anaerobic oxidation of methane related to a change in sedimentation rate, Geochim. Cosmochim. Acta, 69, 4117–4126, https://doi.org/10.1016/j.gca.2005.02.004.

Reilly, B. T., McCormick, M. L., Brachfeld, S. A., Haley, B. A. (2020). Authigenic ferrimagnetic iron sulfide preservation due to non-steady state diagenesis: A perspective from Perseverance Drift, North western Weddell Sea. Geochem., Geophy., Geosys. e2020GC009380. https://doi.org/10.1029/2020GC009380

Reinholdsson, M., Snowball, I., Zillén, L., Lenz, C., Conley, D.J. (2013). Magnetic enhancement of Baltic Sea sapropels by greigite magnetofossils. Earth Planet. Sci. Lett. 366, pp.137-150.http://dx.doi.org/10.1016/j.epsl.2013.01.029

Riedel, M., Collett, T. S., Shankar, U. (2011). Documenting channel features associated with gas hydrates in the Krishna–Godavari Basin, offshore India. Mar. Geol. 279(1-4), 1–11. https://doi.org/10.1016/j.margeo.2010.10.008

Riedel, M., Goldberg, D., Guerin, G. (2014). Compressional and shear-wave velocities from gas hydrate bearing sediments: Examples from the India and Cascadia margins as well as Arctic permafrost regions. Mar. Petrol. Geol. 58, 292-320. https://doi.org/10.1016/j.marpetgeo.2014.07.028

Riedel, M., Spence, G. D., Chapman, N. R., Hyndman, R. D. (2002). Seismic investigations of a vent field associated with gas hydrates, offshore Vancouver Island. J. Geophys. Res. Solid Earth, 107(B9), EPM-5. https://doi.org/10.1029/2001JB000269

Riedinger, N., Formolo, M. J., Lyons, T. W., Henkel, S., Beck, A., Kasten, S. (2014). An inorganic geochemical argument for coupled anaerobic oxidation of methane and iron reduction in marine sediments. Geobiology 12(2), 172-181.https://doi.org/10.1111/gbi.12077

Riedinger, N., Pfeifer, K., Kasten, S., Garming, J. F. L., Vogt, C., Hensen C. (2005). Diagenetic alteration of magnetic signals by anaerobic oxidation of methane related to a change in sedimentation rate, Geochim. Cosmochim. Acta. 69, 4117–4126, https://doi.org/10.1016/j.gca.2005.02.004.

Roberts, A. P. (1995). Tectonic rotation about the termination of a major strike-slip fault, Marlborough Fault System, New Zealand. Geophy. res. lett., 22(3), 187-190. https://doi.org/10.1029/94GL02582

Roberts, A. P. (2015). Magnetic mineral diagenesis. Earth-Sci. Rev. 151, 1–47. https://doi.org/10.1016/j.earscirev.2015.09.010

Roberts, A. P., Almeida, T. P., Church, N. S., Harrison, R. J., Heslop, D., Li, Y., et al. (2017). Resolving the origin of pseudo-single domain magnetic behavior. J. Geophys. Res. Solid Earth. 122, 9534–9558. https://doi.org/10.1002/2017JB014860

Roberts, A. P., Turner, G. M. (1993). Diagenetic formation of ferrimagnetic iron sulphide minerals in rapidly deposited marine sediments, South Island, New Zealand. Earth and Planetary Science Letters, 115(1-4), 257-273. https://doi.org/10.1016/0012-821X(93)90226-Y

Roberts, A. P., Weaver, R. (2005). Multiple mechanisms of remagnetization involving sedimentary greigite (Fe3S4). Earth Planet. Sci. Lett., 231, 263–277. https://doi.org/10.1016/j.epsl.2004.11.024

Roberts, A. P., Chang, L., Rowan, C. J., Horng, C. S., Florindo, F. (2011). Magnetic properties of sedimentary greigite (Fe3S4): An update. Rev. Geophys. 49, RG1002. https://doi.org/10.1029/2010RG000336

Roberts, A. P., Jiang, W. T., Florindo, F., Horng, C. S., Laj, C. (2005). Assessing the timing of greigite formation and the reliability of the Upper Olduvai polarity transition record from the Crostolo River, Italy. Geophy. Res. Lett., 32(5). https://doi.org/10.1029/2004GL022137

Roberts, A. P., Pike, C. R., Verosub, K. L. (2000). First-order reversal curve diagrams: A new tool for characterizing the magnetic properties of natural samples. J. Geophys. Res. Solid Earth. 105(B12), 28461-28475. https://doi.org/10.1029/2000JB900326

Roberts, A. P., Zhao, X., Harrison, R. J., Heslop, D., Muxworthy, A. R., Rowan, C. J., et al. (2018). Signatures of reductive magnetic mineral diagenesis from unmixing of first order reversal curves. J. Geophys. Res. Solid Earth. 123, 4500–4522. https://doi.org/10.1029/2018JB015706

Roberts, A. P., Zhao, X., Heslop, D., Abrajevitch, A., Chen, Y. H., Hu, P., et al. (2020). Hematite (α-Fe_2O_3) quantification in sedimentary magnetism: limitations of existing proxies and ways forward. Geoscience Letters, 7(1), 1-11. https://doi.org/10.1186/s40562-020-00157-5

Roberts, A.P., Reynolds, R.L., Verosub, K.L., Adam, D.P. (1996). Environmental magnetic implications of greigite (Fe3S4) formation in a 3 million year lake sediment record from Butte Valley, Northern California. Geophys. Res. Lett. 23, 2859–2862. https://doi.org/10.1029/96GL02831

Rodelli, D., Jovane, L., Giorgioni, M., Rego, E. S., Cornaggia, F., Benites, M., et al. (2019). Diagenetic fate of biogenic soft and hard magnetite in chemically stratified sedimentary environments of Mamanguá Ría, Brazil. J. Geophys. Res. Solid Earth. 124 (3), 2313–2330. https://doi.org/10.1029/2018JB016576

Rodelli, D., Jovane, L., Roberts, A. P., Cypriano, J., Abreu, F., Lins, U. (2018). Fingerprints of partial oxidation of biogenic magnetite from cultivated and natural marine magnetotactic bacteria using synchrotron radiation. 1226 Environ. Microbiol. Rep. 10 (3), 337–343. https://doi.org/10.1111/1758-2229.12644

Römer, M., Sahling, H., Pape, T., dos Santos Ferreira, C., Wenzhöfer, F., Boetius, A., et al. (2014). Methane fluxes and carbonate deposits at a cold seep area of the Central Nile Deep Sea Fan, Eastern Mediterranean Sea. Mar. Geol., 347, 27-42. https://doi.org/10.1016/j.margeo.2013.10.011

Rowan, C. J., Roberts, A. P. (2006). Magnetite dissolution, diachronous greigite formation, and secondary magnetizations from pyrite oxidation: Unravelling complex magnetizations in Neogene marine sediments from New Zealand. Earth Planet. Sci. Lett. 241(1-2), 119–137. https://doi.org/10.1016/j.epsl.2005.10.017

Rowan, C. J., Roberts, A. P. (2008). Widespread remagnetizations and a new view of Neogene tectonic rotations within the Australia-Pacific plate boundary zone, New Zealand. J. Geophys. Res. Solid Earth. 113(B3). https://doi.org/10.1029/2006JB004594

Rowan, C. J., Roberts, A. P., Broadbent, T. (2009). Reductive diagenesis, magnetite dissolution, greigite growth and paleomagnetic smoothing in marine sediments: A new view. Earth Planet. Sci. Lett. 277(1-2), 223–235. https://doi.org/10.1016/j.epsl.2008.10.016

Rudmin, M., Roberts, A.P., Horng, C.S., Mazurov, A., Savinova, O., Ruban, A., Kashapov, R., Veklich, M. (2018). Ferrimagnetic iron sulfide formation and methane venting across the Paleocene-Eocene Thermal Maximum in shallow marine sediments, ancient West Siberian Sea. Geochem., Geophy., Geosys.19(1), pp.21-42. https://doi.org/10.1002/2017GC007208

Rudolph, M. L., & Manga, M. (2010). Mud volcano response to the 4 April 2010 El Mayor-Cucapah earthquake. Journal of Geophysical Research: Solid Earth, 115(B12).

Ruppel, C., Dickens, G.R., Castellini, D.G., Gilhooly, W., Lizarralde, D. (2005). Heat and salt inhibition of gas hydrate formation in the northern Gulf of Mexico. Geophys. Res. Lett. 32 (4), 1–4.

Sagnotti, L., Winkler, A. (1999). Rock magnetism and palaeomagnetism of greigite-bearing mudstones in the Italian peninsula. Earth Planet. Sci. Lett, 165,67–80. https://doi.org/10.1016/s0012-821x(98)00248-9

Sagnotti, L., Cascella, A., Ciaranfi, N., Macrì, P., Maiorano, P., Marino, M., et al. (2010). Rock magnetism and palaeomagnetism of the Montalbano Jonico section (Italy): evidence for late diagenetic growth of greigite and implications for magnetostratigraphy. Geophy. J. Int., 180(3), 1049-1066. https://doi.org/10.1111/j.1365-246X.2009.04480.x

Sagnotti, L., Roberts, A. P., Weaver, R., Verosub, K. L., Florindo, F., Pike, C. R., et al. (2005). Apparent magnetic polarity reversals due to remagnetization resulting from late diagenetic growth of greigite from siderite. Geophy J Int, 160(1), 89–100. https://doi.org/10.1111/j.1365-246X.2005.02485.x

Sahu, H.S., Raab, M.J., Kohn, B.P., Gleadow, A.J.W. (2013). Thermal history of the Krishna-Godavari basin, India: Constraints from apatite fission track thermochronology and organic maturity data. Journal of Asian Earth Sciences, 73, 1-20. https://doi.org/10.1016/j.jseaes.2013.04.028

Sangode, S. J., R. Sinha, B. Phartiyal, Chauhan, O. S., Mazari, R. K., Bagati, T. N., Suresh, N., Mishra, S., Kumar, R., Bhattacharjee P. (2007). Environmental magnetic studies on some quaternary sediments of varied depositional settings in the Indian sub-continent, Quat. Int., 159, 102–118, https://doi.org/10.1016/j.quaint.2006.08.015.

Sangode, S. J., Suresh, N., Bagati, T. N. (2001). Godavari source in the Bengal fan sediments: Results from magnetic susceptibility dispersal pattern. Curr. Sci., 80 (5), 660–664.

Shankar, U., Riedel, M. (2010). Seismic and heat flow constraints from the gas hydrate system in the Krishna–Godavari Basin, India. Mar. Geol. 276 (1-4), 1-13. https://doi.org/10.1016/j.margeo.2010.06.006

Shankar, U., Sain, K., Riedel, M. (2014). Assessment of gas hydrate stability zone and geothermal modeling of BSR in the Andaman Sea. J. Asian Earth Sci. 79, 358-365. https://doi.org/10.1016/j.jseaes.2013.10.021

Shanmugam, G., Shrivastava, S. K., Das, B. (2009). Sandy debrites and tidalites of Pliocene reservoir sands in upperslope canyon environments, offshore Krishna–Godavari Basin (India): implications. J. Sediment. Res. 79(9), 736–756. https://doi.org/10.2110/jsr.2009.076

Sahling, H., Römer, M., Pape, T., Bergès, B., dos Santos Fereirra, C., Boelmann, J., ... & Bohrmann, G. (2014). Gas emissions at the continental margin west of Svalbard: mapping, sampling, and quantification. Biogeosciences, 11(21), 6029-6046.

Shi, M., Wu, H., Roberts, A. P., Zhang, S., Zhao, X., Li, H., et al. (2017). Tectonic, climatic, and diagenetic control of magnetic properties of sediments from Kumano Basin, Nankai margin, southwestern Japan. Mar. Geol. 391, 1–12. https://doi.org/10.1016/j.margeo.2017.07.006

Sibuet, M., Olu, K. (1998). Biogeography, biodiversity and fluid dependence of deep-sea cold-seep communities at active and passive margins. Deep Sea Research Part II: Topical Studies in Oceanography, 45(1-3), 517-567. https://doi.org/10.1016/S0967-0645(97)00074-X

Simonetti, A., Knapp, J. H., Sleeper, K., Lutken, C. B., Macelloni, L., Knapp, C. C. (2013), Spatial distribution of gas hydrates from higher solutionseismic and core data, Woolsey Mound, Northern Gulf of Mexico, Mar. Petrol. Geol., 44, 21–33, https://doi.org/10.1016/j.marpetgeo.2013.04.004.

Singhroha, S., Bünz, S., Plaza-Faverola, A., Chand, S. (2020). Detection of Gas Hydrates in Faults Using Azimuthal Seismic Velocity Analysis, Vestnesa Ridge, W-Svalbard Margin. . J. Geophys. Res. Solid Earth, 125(2), e2019JB017949. https://doi.org/10.1029/2019JB017949

Sivan, O., Schrag, D. P., Murray, R. W. (2007). Rates of methanogenesis and methanotrophy in deep-sea sediments. Geobiology 5, 141–151. https://doi.org/10.1111/j.1472-4669.2007.00098.x

Sloan Jr, E. D., Koh, C. A. (2007). Clathrate hydrates of natural gases. CRC press. https://doi.org/10.1201/9781420008494

Sloan, E. D. (2003). Fundamental principles and applications of natural gas hydrates. Nature, 426(6964), 353-359. https://doi.org/10.1038/nature02135

Sloan Jr, E. D. (1998). Physical/chemical properties of gas hydrates and application to world margin stability and climatic change. Geological society, London, special publications, 137(1), 31-50.

Smirnov, A.V., Tarduno, J.A. (2000). Low-temperature magnetic properties of pelagic sediments (Ocean Drilling Program Site 805C): tracers of maghemitization and magnetic mineral reduction. J. Geophys. Res. 105, 16,457–16,471. https://doi.org/10.1029/2000JB900140

Snowball, I. F. (1991). Magnetic hysteresis properties of greigite (Fe3S4) and a new occurrence in Holocene sediments from Swedish Lappland. Phys. Earth Planet. Inter. 68(1-2), 32-40. https://doi.org/10.1016/0031-9201(91)90004-2

Snowball, I., Thompson, R. (1990). A stable chemical remanence in Holocene sediments. J. Geophys. Res. Solid Earth. 95(B4), 4471-4479. https://doi.org/10.1029/JB095iB04p04471

Solomon, E. A., Spivack, A. J., Kastner, M., Torres, M. E., Robertson, G. (2014). Gas hydrate distribution and carbon sequestration through coupled microbial methanogenesis and silicate weathering in the Krishna–Godavari basin, offshore India. Mar. Petrol. Geol. 58, 233-253. https://doi.org/10.1016/j.marpetgeo.2014.08.020

Sloan, E. D. (1998). Gas hydrates: review of physical/chemical properties. Energy & fuels, 12(2), 191-196.

Sriram, G., Dewangan, P., Ramprasad, T., Rama Rao, P. (2013). Anisotropic amplitude variation of the bottom-simulating reflector beneath fracture-filled gas hydrate deposit. J. Geophys. Res. Solid Earth. 118 (5), 2258–2274. https://doi.org/10.1002/jgrb.50176

Suess, E. (2014). Marine cold seeps and their manifestations: geological control, biogeochemical criteria and environmental conditions. Int. J. Earth Sci. 103(7), 1889-1916. https://doi.org/10.1007/s00531-014-1010-0

Sultan, N., Cochonat, P., Foucher, J. P., Mienert, J. (2004). Effect of gas hydrates melting on seafloor slope instability. Marine geology, 213(1-4), 379-401. https://doi.org/10.1016/j.margeo.2004.10.015

Sweeney, R.E., Kaplan, I.R. (1973). Pyrite framboid formation; laboratory synthesis and marine sediments. Economic Geology 68 (5), 618–634. https://doi.org/10.2113/gsecongeo.68.5.618

Sztybor, K., Rasmussen, T. L. (2017). Diagenetic disturbances of marine sedimentary records from methane-influenced environments in the Fram Strait as indications of variation in seep intensity during the last 35 000 years. Boreas, 46(2), 212-228. https://doi.org/10.1111/bor.12202

Tarduno, J. A. (1995). Superparamagnetism and reduction diagenesis in pelagic sediments: enhancement or depletion? Geophy. Res. Lett. 22(11), 1337-1340. https://doi.org/10.1029/95GL00888

Tarduno, J. A., Cottrell, R. D., Smirnov, A. V. (2006). The paleomagnetism of single silicate crystals: Recording geomagnetic field strength during mixed polarity intervals, super chrons, and inner core growth. Rev. Geophy., 44(1). https://doi.org/10.1029/2005RG000189

Tarduno, J.A., Wilkison, S. (1996). Non-steady state magnetic mineral reduction, chemical lock-in, and delayed remanence acquisition in pelagic sediments. Earth Planet. Sci. Lett. 144, 315–326. https://doi.org/10.1016/S0012-821X(96)00174-4

Teichert, B.M.A., Johnson, J.E., Solomon, E.A., Giosan, L., Rose, K., Kocherla, M., Connolly, E.C. Torres, M.E. (2014). Composition and origin of authigenic carbonates in the Krishna–Godavari and Mahanadi Basins, eastern continental margin of India. Mar. Petrol. Geol. 58, pp.438-460. https://doi.org/10.1016/j.marpetgeo.2014.08.023

Thompson, R., Oldfield, F. (1986). Environmental magnetism, (p. 227). London: Allen and Unwin.

Torres, M. E., J. McManus, D. E. Hammond, M. A. de Angelis, K. U. Heeschen, S. L. Colbert, M. D. Tryon, K. M. Brown, and E. Suess (2002), Fluid and chemical fluxes in and out of sediments hosting methane hydrate deposits on Hydrate Ridge, OR, I: Hydrological provinces, Earth Planet. Sci. Lett., 201(3-4), 525–540, doi:10.1016/S0012-821X(02)00733-1.

Torres, M. E., Trehu, A. M., Cespedes, N., Kastner, M., Wortmann, U. G., Kim, J. H., ... & Collett, T. (2008). Methane hydrate formation in turbidite sediments of northern Cascadia, IODP Expedition 311. Earth and Planetary Science Letters, 271(1-4), 170-180.

Torres, M.E., Hong, W.L., Solomon, E.A., Milliken, K., Kim, J.H., Sample, J.C., Teichert, B.M., Wallmann, K. (2020). Silicate weathering in anoxic marine sediment as a requirement for authigenic carbonate burial. Earth Sci. Rev. 200, 102960. https://doi.org/10.1016/j.earscirev.2019.102960.

Treude, T., Krüger, M., Boetius, A., & Jørgensen, B. B. (2005). Environmental control on anaerobic oxidation of methane in the gassy sediments of Eckernförde Bay (German Baltic). Limnology and oceanography, 50(6), 1771-1786.

Tsunogai, U., Maegawa, K., Sato, S., Komatsu, D. D., Nakagawa, F., Toki, T., & Ashi, J. (2012). Coseimic massive methane release from a submarine mud volcano. Earth and Planetary Science Letters, 341, 79-85.

Usapkar, A., Dewangan, P., Kocherla, M., Ramprasad, T., Mazumdar, A., Ramana, M. V. (2014). Enhanced methane flux event and sediment dispersal pattern in the Krishna–Godavari offshore basin: Evidences from rock magnetic techniques. Mar. Petrol. Geol., 58, 461–475 https://doi.org/10.1016/j.marpetgeo.2014.08.008

Vadakkepuliyambatta, S., Bünz, S., Mienert, J., & Chand, S. (2013). Distribution of subsurface fluid-flow systems in the SW Barents Sea. Marine and Petroleum Geology, 43, 208-221.

Valdez-Grijalva, M. A., Nagy, L., Muxworthy, A. R., Williams, W., Roberts, A. P., Heslop, D. (2020). Micromagnetic simulations of first-order reversal curve (FORC) diagrams of framboidal greigite. Geophysical Journal International, 222(2), 1126-1134. https://doi.org/10.1093/gji/ggaa241

Verwey, E. J. W. (1939). Electronic conduction of magnetite (Fe3O4) and its transition point at low temperatures. Nature 144(3642), 327. https://doi.org/10.1038/144327b0

Verwey, E. J. W. (1947). Theory of the stability of lyophobic colloids. J. Phys. Chem. 51(3), 631-636. https://doi.org/10.1021/j150453a001

Vigderovich, H., Liang, L., Herut, B., Wang, F., Wurgaft, E., Rubin-Blum, M., Sivan, O. (2019). Evidence for microbial iron reduction in the methanic sediments of the oligotrophic southeastern Mediterranean continental shelf. Biogeosciences 16(16), 3165-3181. https://doi.org/10.5194/bg-16-3165-2019

Walden, J., Oldfield, F., Smith, J. (Eds.) (1999). Environmental Magnetism. A Practical Guide. Technical Guide No 6. Quaternary Research Association, London.

Wallmann, K., Aloisi, G., Haeckel, M., Tishchenko, P., Pavlova, G., Greinert, J., Kutterolf, S. Eisenhauer, A. (2008). Silicate weathering in anoxic marine sediments. Geochimica et Cosmochimica Acta, 72(12), pp.2895-2918. https://doi.org/10.1016/j.gca.2008.03.026

Wang, X., Liu, B., Qian, J., Zhang, X., Guo, Y., Su, P. et al. (2018). Geophysical evidence for gas hydrate accumulation related to methane seepage in the Taixinan Basin, South China Sea. J.f Asian Earth Sci., 168, 27-37. https://doi.org/10.1016/j.jseaes.2017.11.011

Weinberger, J. L., and Brown, K. M. (2006). Fracture networks and hydrate distribution at Hydrate Ridge, Oregon. Earth and Planetary Science Letters, 245(1-2), 123-136.

Wenau, S., Spiess, V., Keil, H., & Fei, T. (2018). Localization and characterization of a gas bubble stream at a Congo deep water seep site using a 3D gridding approach on single-beam echosounder data. Marine and Petroleum Geology, 97, 612-623.

Wellsbury, P., Goodman, K., Cragg, B. A., Parkes, R. J. (2000). The geomicrobiology of deep marine sediments from Blake Ridge containing methane hydrate (Sites 994, 995 and 997). In Proceedings of the Ocean drilling program, Scientific results, (Vol. 164, pp. 379–391). College Station, TX: Ocean Drilling Program.

Wenau, S., Spiess, V., Pape, T., Fekete, N. (2015). Cold seeps at the salt front in the Lower Congo Basin II: The impact of spatial and temporal evolution of salt-tectonics on hydrocarbon seepage. Mar. Petrol. Geol., 67, 880-893. https://doi.org/10.1016/j.marpetgeo.2014.09.021

Whiticar, M. J. (1999). Carbon and hydrogen isotope systematics of bacterial formation and oxidation of methane. Chemical Geology, 161(1-3), 291-314. https://doi.org/10.1016/S0009-2541(99)00092-3

Worm, H.-U. (1998). On the superparamagnetic - stable single domain transition for magnetite, and frequency dependence of susceptibility. Geophys. J. Int. 133, 201e206.

Xie, R., Wu, D., Liu, J., Sun, T., Liu, L., Wu, N. (2019). Geochemical Evidence of Metal-Driven Anaerobic Oxidation of Methane in the Shenhu Area, the South China Sea. Int. J. Env. Res. Pub. He. 16(19), 3559. https://doi.org/10.3390/ijerph16193559

Yamamoto, Y., Chiyonobu, S., Kanamatsu, T., Ahagon, N., Aoike, K., Kamiya, N., Kinoshita, M. (2018). Repeated large-scale masstransport deposits and consequent rapid sedimentation in the western part of the Bay of Bengal, India. Geological Society, London, Special Publications. In G. London: Geological Society (Vol. 477SP477–12). https://doi.org/10.1144/SP477.12

Yamazaki, T., Solheid, P. (2011). Maghemite-to-magnetite reduction across the Fe-redox boundary in a sediment core from the Ontong-Java Plateau: influence on relative palaeointensity estimation and environmental magnetic application. Geophys. J. Int. 185, 1243–1254. https://doi.org/10.1111/j.1365-246X.2011.05021.x

Yamazaki, T., Abdeldayem, A. L. Ikehara, K. (2003), Rock-magnetic changes with reduction diagenesis in Japan Sea sediments and preservation of geomagnetic secular variation in inclination during the last 30,000 years, Earth Planet Space, 55, 327–340. https://doi.org/10.1186/BF03351766

Yao, H., Hong, W. L., Panieri, G., Sauer, S., Torres, M. E., Lehmann, M. F., et al. (2019). Fracture-controlled fluid transport supports microbial methane-oxidizing communities at Vestnesa Ridge. Yao, H. (2020). Reconstruction of past and present methane emission in the Arctic cold seeps using biogeochemical proxies. (Doctoral thesis).

Yan, L., Zhang, S., Chen, P., Liu, H., Yin, H., & Li, H. (2012). Magnetotactic bacteria, magnetosomes and their application. Microbiological research, 167(9), 507-519.

You, K., Flemings, P.B., Malinverno, A., Collett, T.S., Darnell, K. (2019). Mechanisms of methane hydrate formation in geological systems. Rev. Geophys. 57 (4), 1146–1196.

Yu, X., Wang, J., Liang, J., Li, S., Zeng, X., & Li, W. (2014). Depositional characteristics and accumulation model of gas hydrates in northern South China Sea. Marine and Petroleum Geology, 56, 74–86. https://doi.org/10.1016/j.marpetgeo.2014.03.011

Zonneveld, K. A. F., Versteegh, G. J. M., Kasten, S., Eglinton, T. I., Emeis, K.-C., Huguet, C., Koch, B. P., de Lange, G. J., de Leeuw, J. W., Middelburg, J. J., Mollenhauer, G., Prahl, F. G., Rethemeyer, J., Wakeham, S. G (2010): Selective preservation of organic matter in marine environments; processes and impact on the sedimentary record, Biogeosciences, 7, 483–511, https://doi.org/10.5194/bg-7-483-2010